

Cleared: August 8th, 1973

Clearing Authority: Air Force Flight Dynamics Laboratory

## FOREWORD

This report was prepared by Solar, a Division of International Harvester Company, San Diego, California on Air Force Contract No. AF 33(616)-8497, under Task No. 136804 of Project No. 1368, "Development of Frontal Section for Super-Orbital, Lifting, Re-entry Vehicle." The work was administered under the direction of the Flight Dynamics Laboratory, Research and Technology Division. S M/Sgt. Jesse Ingram, Jr. was project engineer for the Laboratory.

The studies presented began in July 1961, were concluded in May 1964. Solar was the prime contractor and Lockheed Missiles and Space Company (LMSC) was subcontractor in the field of trajectory analyses and vehicle design.

Solar, as prime contractor, retained overall program management and orientation, and performed the majority of the materials development, producibility studies, composite system development, materials property measurements, and materials and structures test programs. The program was managed by the Aerospace Activity of Solar with Mr. M. R. Licciardello as Program Manager. All materials development, testing, and structural fabrication was performed by the Solar Research Laboratories. Acknowledgement is given to Dr. A. G. Metcalfe and Mr. A. R. Stetson, whose advice and guidance throughout the contract period was instrumental in maintaining a technically sound program. Major contributors to the contract work, and to the body of this are Messrs. L. Fredlund, now deceased, B. Ohnysty, V. S. Moore, and F. K. Rose. Particular acknowledgement is given to Mr. R. Polvitz, who shouldered the demanding task of fabricating test specimens and final structural forms with eminent success.

Trajectory and vehicle analyses, nose cone structural and thermal analyses, and early oxidation tests on tungsten and tantalum were performed by Lockheed Missiles and Space Company under subcontract to Solar.

The program at LMSC was concentrated within, but not confined to, the Mechanical and Mathematical Sciences Laboratory of the research organization.

Mr. W.E. Jacobsen of Solid Mechanics served as project leader and directed the structural analyses; Messrs. A.C. Buckingham and R.G. Wilson of Fluid Mechanics provided the thermodynamics analyses; Messrs. D.A. Price and L.A. Manning of Flight Mechanics provided vehicle aerodynamic characteristics, trajectories, and environments. In the earlier phases of the study, Mr. R.A. Perkins of the Materials Sciences Laboratory, Metallurgy and Ceramics, supplied pertinent data concerning high-temperature mechanical and thermo-physical properties of refractory materials (especially their oxidation characteristics) and comparative properties of protective coatings. Able assistance was also contributed toward performing the structural studies by Messrs. C.E. Stuhlman and P. Stern. Mr. F.L. Guard assisted in the area of transient temperature distribution. Final designs were prepared by Messrs. R.V. Beck and A.D. Daniel of Experimental Engineering.

The ASSET nose cap work was conducted by Solar, with analysis performed by LMSC. Acknowledgement is given to Messrs. C.C. LaMaster, P. Beardsley, and W. Giddings of McDonnell Aircraft Company, ASSET Project, who kept their sense of humor under trying circumstances, and to Mr. C.J. Cosenza, ASSET Program Manager for the Air Force, for his cooperation and guidance.

This report is the final report and it concludes the work on Contract No. AF 33(616)-8497, Task No. 136804, Project No. 1368. Solar's report number is ER 1115-30.


**ABSTRACT**

In support of the development of composite structures for super-orbital re-entry vehicles, a series of vehicle studies and nose cap analyses was conducted. The results of these analyses are presented.

A survey of the anticipated range of parameters for super-orbital lifting re-entry vehicles was conducted. For a particular re-entry pattern, vehicle designs were postulated for a range of L/D from 0.5 to 2.0 and  $W/C_D A$  from 50 to 500. Complete trajectories were calculated to provide environmental data for nose cap design.

Thermodynamic and structural analyses of ablative-radiative and radiative systems were conducted, leading to the final tungsten-thoria composite nose cap. Reinforced thoria overlay and tungsten structure weight averaged  $12.7 \text{ lb/ft}^2$  for a peak heating rate of  $670 \text{ Btu/ft}^2 \text{ sec}$ .

This technical documentary report has been reviewed and is approved.

  
W. A. Sloan, Jr.  
Colonel USAF  
Chief, Structures Division

# *Contrails*

## TABLE OF CONTENTS

Section		Page
I.	INTRODUCTION	1
II.	SELECTION OF VEHICLES	3
	2.1 General Super-Orbital Trajectory Analysis	3
	2.2 Selection of Typical Classes of Lifting Vehicles	17
	2.3 Preliminary Design - Nose Structure and Body Configurations	21
	2.4 Entry Trajectory Relationships	35
III.	THERMAL INVESTIGATIONS	49
	3.1 General Considerations	49
	3.2 Thin Radiation-Cooled Structures	63
IV.	ANALYSIS OF ABSORPTION-RADIATION SYSTEMS	73
	4.1 Magnesia Ablation-Radiation System	73
	4.2 Nylon-Phenolic and Quartz Ablators	77
	4.3 Thoria-Tungsten High Heat Capacity-Radiative System	92
V.	STRUCTURAL INVESTIGATIONS	129
	5.1 Strength and Stiffness of a Thin Monocoque Shell	129
	5.2 Thermal Stresses in a Free Composite Slab	134
	5.3 Thermal Stresses in Composite Axisymmetric Thin Shells	137
VI.	SELECTION AND DESIGN OF FRONTAL SECTION	145
	6.1 Selection of Final Design Thermal Protection System	147
	6.2 Design of Frontal Section	150
	6.3 Unit Weight Comparisons	163
VII.	CONCLUSIONS	165
VIII.	REFERENCES	167

# *Contrails*

## LIST OF ILLUSTRATIONS

Figure		Page
1.	Model Trajectory Used for Lifting Re-entry	5
2.	Range from Super-Orbital Re-entry	
3.	Super-Orbital Re-entry Time	10
4.	Stagnation Point Maximum Heating Rate	12
5.	Stagnation Point Total Input Heating	13
6.	Stagnation Point Input Heating; Entry to Radiation Equilibrium Condition	14
7.	Entry Flight Path Boundaries and Angular Width of Entry Corridor	15
8.	Maximum Deceleration	16
9.	Heat Absorption for 10-g Limit Trajectories with Superposed Characteristics of Three Classes of Re-entry Bodies	19
10.	Medium Wing Loading Glider	24
11.	Medium Wing Load Glider; Three-View	25
12.	Winged Glider Nose Section	26
13.	Blunt Elliptic Cone	28
14.	Blunt Elliptic Cone; Three-View	29
15.	Blunt Elliptic Cone Nose Section	30
16.	Blunt Semi-Cone	31
17.	Blunt Semi-Cone; Three-View	32
18.	Light Wing Loading Glider	33
19.	Light Wing Loading Glider; Three-View	34
20.	Altitude-Velocity Contours; $L/D = 2.0$ , $W/C_{DA} = 200$ psf	36
21.	Convective Heating History; $L/D = 2.0$ , $W/C_{DA} = 200$ psf	37
22.	Dynamic Pressure History; $L/D = 2.0$ , $W/C_{DA} = 200$ psf	37
23.	Altitude-Velocity History; $L/D = 2.0$ , $W/C_{DA} = 200$ psf	38
24.	Altitude-Velocity Contours; $L/D = 1.0$ , $W/C_{DA} = 100$ psf	39
25.	Convective Heating History; $L/D = 1.0$ , $W/C_{DA} = 100$ psf	40

## LIST OF ILLUSTRATIONS (Cont)

Figure		Page
26.	Dynamic Pressure History; $L/D = 1.0$ , $W/C_{DA} = 100$ psf	40
27.	Altitude-Velocity History; $L/D = 1.0$ , $W/C_{DA} = 100$ psf	41
28.	Altitude-Velocity Contours; $L/D = 0.5$ , $W/C_{DA} = 50$ psf	42
29.	Convective Heating History; $L/D = 0.5$ , $W/C_{DA} = 50$ psf	43
30.	Dynamic Pressure History; $L/D = 0.5$ , $W/C_{DA} = 50$ psf	43
31.	Altitude-Velocity History; $L/D = 0.5$ , $W/C_{DA} = 50$ psf	44
32.	Altitude-Velocity Contours; $L/D = 2.0$ , $W/C_{DA} = 50$ psf	46
33.	Convective Heating History; $L/D = 2.0$ , $W/C_{DA} = 50$ psf	47
34.	Dynamic Pressure History; $L/D = 2.0$ , $W/C_{DA} = 50$ psf	47
35.	Altitude-Velocity History; $L/D = 2.0$ , $W/C_{DA} = 50$ psf	48
36.	Heat Transfer Distribution; Hemisphere-Cones	50
37.	Effect of Nose Bluntness on Stagnation Point Convective Heat Pulse; Laminar Boundary Layer	50
38.	Effect of Nose Bluntness on Distribution of Convective Heat Pulse; Laminar Boundary Layer	52
39.	Laminar Heating Distribution of a 0.4 Aspect Ratio Ellipsoidal Blunted 20-Degree Cone	54
40.	Transition Function; Lifting Re-entry Trajectory	56
41.	Heat Transfer Histories for Composite Slab; Ceramic over Refractory Metal Substrate	64
42.	Temperature Histories for Composite Slab; $\epsilon_w = 0.6$	66
43.	Temperature Histories for Composite Slab; $\epsilon_w = 0.8$	67
44.	Maximum Temperature Drop Across Ceramic	68
45.	Variation of Maximum Surface Temperature and Temperature Drop Across Ceramic with Emittance; Ceramic Thickness 0.02 Inch	69
46.	Temperature Histories for a Composite Slab; 0.03-Inch Ceramic Over Refractory Metal Substrate	70
47.	Magnesia Ablator Requirements	76
48.	Stagnation Point Ablator Weight Requirements	78
49.	Stagnation Point Ablator Requirements for $(\epsilon_w^{1/4} T_w)$ of 4000 R	79
50.	Convective Heat Rate and Ablation Thickness; Nylon Phenolic and Quartz — $L/D = 2.0$ , $W/C_{DA} = 200$ psf	82



## LIST OF ILLUSTRATIONS (Cont)

Figure		Page
51.	Convective Heat Rate and Ablation Thickness; Nylon Phenolic and Quarts — $L/D = 0.5$ , $W/C_{DA} = 50$ psf	83
52.	Temperature Response; Nylon-Phenolic Ablator — $L/D = 2.0$ , $W/C_{DA} = 200$ psf	86
53.	Temperature Response; Quartz Ablator — $L/D = 2.0$ , $W/C_{DA} = 200$ psf	87
54.	Temperature Response; Nylon-Phenolic Ablator — $L/D = 0.5$ , $W/C_{DA} = 50$ psf	88
55.	Temperature Response; Quartz Ablator — $L/D = 0.5$ , $W/C_{DA} = 50$ psf	89
56.	Error Analysis in Ablator Erosion for Changing Effective Heat of Ablation	90
57.	Heating Rates for Lifting Re-entry Trajectory	94
58.	Temperature Response of Lithium Sink Structure	96
59.	Stagnation Region Temperature Response; Capacitive-Radiative Composite Structure	98
60.	Heat Flux into Beryllium Sink; 0.3-Inch Thoria Composite Structure	100
61.	Winged Vehicle Refractory Nose Cone	102
62.	Thoria Thickness Required to Limit Tungsten Substrate to 4500 F	104
63.	Thoria Surface Temperature Versus Distance from Stagnation Point	105
64.	Tungsten Shell Temperature Versus Distance from Stagnation Point	106
65.	Temperature Difference Across Thoria Coating	108
66.	Node Locations in Composite Structure	109
67.	Temperature Response of Composite Structure at Stagnation Point ( $s = 0$ )	110
68.	Temperature Response of Composite Structure at Shoulder Area ( $s = 1.05$ ft)	111
69.	Temperature Response of Composite Structure at Intermediate Position ( $s = 2.1$ ft)	112
70.	Temperature Response of Composite Structure at Cone Base ( $s = 4.2$ ft)	114
71.	Thermophysical Properties of Thoria	115

## LIST OF ILLUSTRATIONS (Cont)

Figure		Page
72.	Thermophysical Properties of Tungsten	116
73.	Thermophysical Properties of Zirconia	117
74.	Basic Thermal Circuit	119
75.	Temperature Response of Various Nodes for Unshielded Targets of Different Volumes	120
76.	Summary of Target Capacity Effects	123
77.	Temperature Response; Multiple Radiation Baffles	126
78.	Temperature Response; Frontal Section Filled with Zirconia Fibers	127
79.	Glider Nose Shell; Tungsten Monocoque Construction	132
80.	Description of Shell Laminae	142
81.	Winged Glider Frontal Shell; Cumulative Surface Area	148
82.	Winged Glider Frontal Shell; Area of Normal Sections	149
83.	Final Design Frontal Structure; Detailed Drawing	151
84.	Target Temperature Increase for Various Internal Insulation	158
85.	Tungsten Oxidation Behavior at Low Pressure and High Temperature	159
86.	Conical Section Temperature-Pressure History	160
87.	Conical Section Tungsten Oxidation Recession	162

**LIST OF TABLES**

<b>Tables</b>		<b>Page</b>
1.	<b>Hypersonic Glider Entry Parameters</b>	<b>3</b>
2.	<b>Representative Configurations</b>	<b>20</b>
3.	<b>Vehicle Aerodynamic Characteristics</b>	<b>22</b>
4.	<b>Summary of Nylon-Phenolic and Quartz Ablation</b>	<b>85</b>
5.	<b>Air Loads at Elevated Temperatures</b>	<b>133</b>
6.	<b>Comparative Frontal Section Weights</b>	<b>163</b>

# *Contrails*

## NOMENCLATURE

a	speed of sound, fps; semi-major axis of frontal body ellipsoid, ft; semi-major axis of Kepler ellipse, ft
c	specific heat, Btu/lb-deg R
g	acceleration of gravity, ft/sec <sup>2</sup>
h	flight altitude above mean sea level, ft
$\Delta h$	enthalpy difference ( $h_g - h_w$ ) across the boundary layer, i. e., total enthalpy minus wall enthalpy, Btu/lb
k	thermal conductivity, Btu/ft-sec-deg F
$\dot{m}$	mass rate of ablation, lb/ft <sup>2</sup> -sec
$\dot{q}_c$	convective heating rate per unit area, Btu/ft <sup>2</sup> -sec
$\dot{q}_R$	radiative heating rate per unit area, Btu/ft <sup>2</sup> -sec
$\bar{q}$	dynamic pressure, $\rho V^2/2$ , psf
s	meridional surface distance from the apex of a body of revolution, ft
t	time, sec
$t_F$	entry time, final, sec
A	reference area (e.g., planform wing area) upon which vehicle aero- dynamic characteristics are based, sq ft
$C_D$	vehicle drag coefficient, $D/\bar{q}_\infty A$ (assumed as independent of Mach number), dimensionless
$C_L$	vehicle lift coefficient, $L/\bar{q}_\infty A$ (related to $C_D$ through the drag polar curve), dimensionless
D	vehicle drag, lb
F	radiation geometrical shape factor, dimensionless

## NOMENCLATURE (Cont)

J	mechanical equivalent of heat, Btu/778 ft-lb
L	vehicle lift, lb
M	Mach number, $V/a$ , dimensionless
N	permissible deceleration limit, or load factor, g's
$P_{O_2}$	partial pressure of oxygen, Torr
$Q^*$	effective heat of ablation, Btu/lb
$Q_{RE}$	partial heat load from the start of entry, through peak heating, and to the time when a $\dot{q}_c = 233$ Btu/ft <sup>2</sup> -sec is attained (at which heat rate a radiation equilibrium temperature of 4500 F is not exceeded), Btu/ft <sup>2</sup>
$Q_c$	heat load per unit area (time integral of $\dot{q}_c$ ), Btu/ft <sup>2</sup>
R	universal gas constant, 1.987 gm-cal/deg K-mol; geocentric distance of the entry body, ft
$R_E$	entry range along the trajectory trace on the earth's surface, nautical miles
$R_n$	nose radius, ft
$R_o$	radius of the earth, ft
$R_w$	oxidation recession rate, by weight, gm/cm <sup>2</sup> -min
$R_e$	Reynolds number
T	temperature, F, C
V	flight velocity, fps
W	vehicle weight, lb
$W_{abl}$	unit weight of ablator, lb/ft <sup>2</sup>
$W/C_D^A$	ballistic parameter, a function of vehicle wing load (W/A) and drag coefficient ( $C_D$ ), psf

## NOMENCLATURE (Cont)

$\alpha$	vehicle angle of attack (positive for flow impingement upon the lower surface), degrees; heat stored plus heat due to phase change, chemical reactions, etc., Btu/lb
$\beta$	transpiration or "blowing" factor, dimensionless
$\gamma$	flight path angle, positive upward from the local horizontal, degrees
$\delta$	slab thickness, in.
$\epsilon$	eccentricity of Kepler ellipse dimensionless; total normal radiation emittance, dimensionless; strain, in./in.
$\mu$	dynamic viscosity, lb-sec/ft <sup>2</sup>
$\nu$	Poisson's ratio, dimensionless
$\rho$	mass density of air, slugs/ft <sup>3</sup> ; density of a solid (e.g., in the heat conduction equation), lb/ft <sup>3</sup>
$\sigma$	Stefan-Boltzmann radiation constant for a black body, $3.303 \times 10^{-15}$ Btu/in. <sup>2</sup> -sec-(deg R) <sup>4</sup> ; normal stress, psi

### Subscripts:

abl	ablation
c	coating
f	final condition
i	initial condition
m	pertaining to the metallic substrate; melting
o	sea-level condition
s	substrate; shock
w	wall
A	pertaining to an ablative material
E	evaluated at atmospheric entry, here arbitrarily established at 400,000-ft altitude
$\infty$	evaluated at free-stream conditions

# *Contrails*



## I. INTRODUCTION

This volume of the report summarizes the thermal and structural studies conducted by Lockheed Missiles and Space Company in support of prime contract AF 33(616)-8497 awarded to Solar, a Division of International Harvester Company. The analytical investigations were performed at various times during the contract effort, and incorporated data on material properties, composite designs, and structural configurations which were available at the particular point in time. There is, therefore, no planned continuity between each analytical task. Rather, the thermal and structural analyses were designed to develop general ground rules, establish trends, and on the whole to "get a feel" for the magnitude of the task. In each case, analyses were geared to treat materials or composites which were behaving favorably in the development work in progress at Solar. These analyses must therefore be interpreted in the light of the materials development work reported in Volume II, Materials and Composite Structure Development, of this report.

The analyses presented in this volume are summarized as follows:

- Trajectory Analyses: Parametric analyses of lifting re-entry from super-orbital velocities were run. Conditions investigated were L/D 0.5 to 2.0, W/C<sub>D</sub>A 50 psf to 500 psf, and re-entry angle from skipout limit to 10-g deceleration limit. Typical trajectories were selected covering complete re-entry range.
- Vehicle Configurations - Vehicle geometries were selected for each trajectory of interest. Frontal section geometry was specified for each vehicle. Thermal environment was specified for each frontal section.
- Thermal Analyses - Thermal analyses were performed for several candidate composites, resulting in temperature gradient calculations for the most promising system.

---

Manuscript released by the authors May 1964 for publication as an FDL Technical Documentary Report.

# Contrails

- Structural Analyses - Stability analyses were conducted to determine the required thickness of structural shell for the selected frontal section.
- Design Analyses - A detailed design was conducted of the most promising frontal section, and weight estimates were compared with those anticipated for an ablator system.

Each of these analyses is presented in the following sections of this volume.

## II. SELECTION OF VEHICLES

The development of material systems for super-orbital frontal sections has significance only if the inputs to which they are designed are realistic. A general trajectory analysis for super-orbital lifting re-entry vehicles was therefore performed. Realistic estimates of the aerodynamic characteristics of several classes of re-entry shapes were then made, and integrated with the trajectory study. The result was the selection of several vehicles and their corresponding re-entry trajectories to be used as guides in the choice of environmental parameters for design of frontal sections. The results of the vehicle configuration and trajectory analyses are included in the following sections.

### 2.1 GENERAL SUPER-ORBITAL TRAJECTORY ANALYSIS

For a preliminary performance analysis, re-entry trajectories were determined for typical classes of lifting vehicles characterized by the aerodynamic parameters indicated in Table 1.

TABLE 1  
HYPERSONIC GLIDER ENTRY PARAMETERS

L/D	W/C <sub>D</sub> <sup>A</sup> (psf)	Re-entry Angle, $-\gamma_E$		
		Skip-Out Limit (Min) (deg)	Intermediate (deg)	Deceleration Limit, 10 g (Max) (deg)
±0.5	50	5.5	6.5	7.55
	100	5.7	6.7	7.7
	200	5.8	6.8	7.9
±1.0	50	5.4	6.6	7.8
	100	5.6	6.8	8.0
	200	5.8	7.0	8.3
±2.0	50	4.9	6.8	8.1
	200	5.6	7.8	8.9
	500	6.3	-	9.3

# Contrails

The coefficient  $L/D$  is the ratio of lift-to-drag maintained by the vehicle at a specific angle of attack in hypersonic flight;  $W/C_D A$  is the ballistic parameter at the given  $L/D$  ratio,  $W/A$  signifying the glider wing loading and  $C_D$  representing the drag coefficient based upon the reference area  $A$ ;  $\gamma_E$  is the flight path angle at the instant of entry into the sensible atmosphere (negative downward, entry altitude  $h_E = 400,000$  feet). Above an altitude of 400,000 feet, lift and drag forces upon the vehicle were assumed to be negligible. The 1959 ARDC atmosphere was selected as the standard for air density definition. For numerically integrating the equations of motion, a five-degree-of-freedom lifting point mass computer program was utilized. It assumed a spherical, non-rotating earth model with radius of 20,902,900 feet and sea level gravitational acceleration of  $32.228 \text{ ft/sec}^2$ .

The model re-entry trajectory invoked for all lifting cases studied is presented in Figure 1. The trajectory was divided into four convenient phases. The super-orbital vacuum approach to the outermost limits of the atmosphere was denoted by Phase I. The designation Phase II applied to that portion of the trajectory between the 400,000-foot altitude and initial pull-out altitude. When a zero flight path angle was attained, a trimmed-roll maneuver which held the vehicle at constant altitude was initiated. This constant altitude portion of the trajectory was classified as Phase III. Considerable dissipation of kinetic energy occurs during Phase III flight; the vehicle aerodynamically decelerates from super-orbital to sub-orbital velocities during this phase of the trajectory. The final sub-orbital descent at constant  $L/D$  to minimum altitude was labeled Phase IV flight. The minimum altitude of interest from structural heating considerations was 50,000 feet.

The vacuum approach course from missions in outer space was selected such that the entry velocity ( $V_E$ ) in all cases was 36,000 fps (relative, atmospheric) at an altitude of 400,000 feet. Midcourse guidance corrections would determine the Phase I path. Since aerodynamic forces are zero in Phase I, a closed-form conic solution (Keplerian) may describe the approach trajectory, dependent upon the lunar transfer trajectory.

The entry angle is that angle between the vehicle flight path and the local horizontal at 400,000 feet, and is negative for a descending vehicle. For all but one of the vehicles analyzed, trajectories were determined for sets of three specific entry flight paths. The steepest (most negative) angle was limited by peak deceleration,

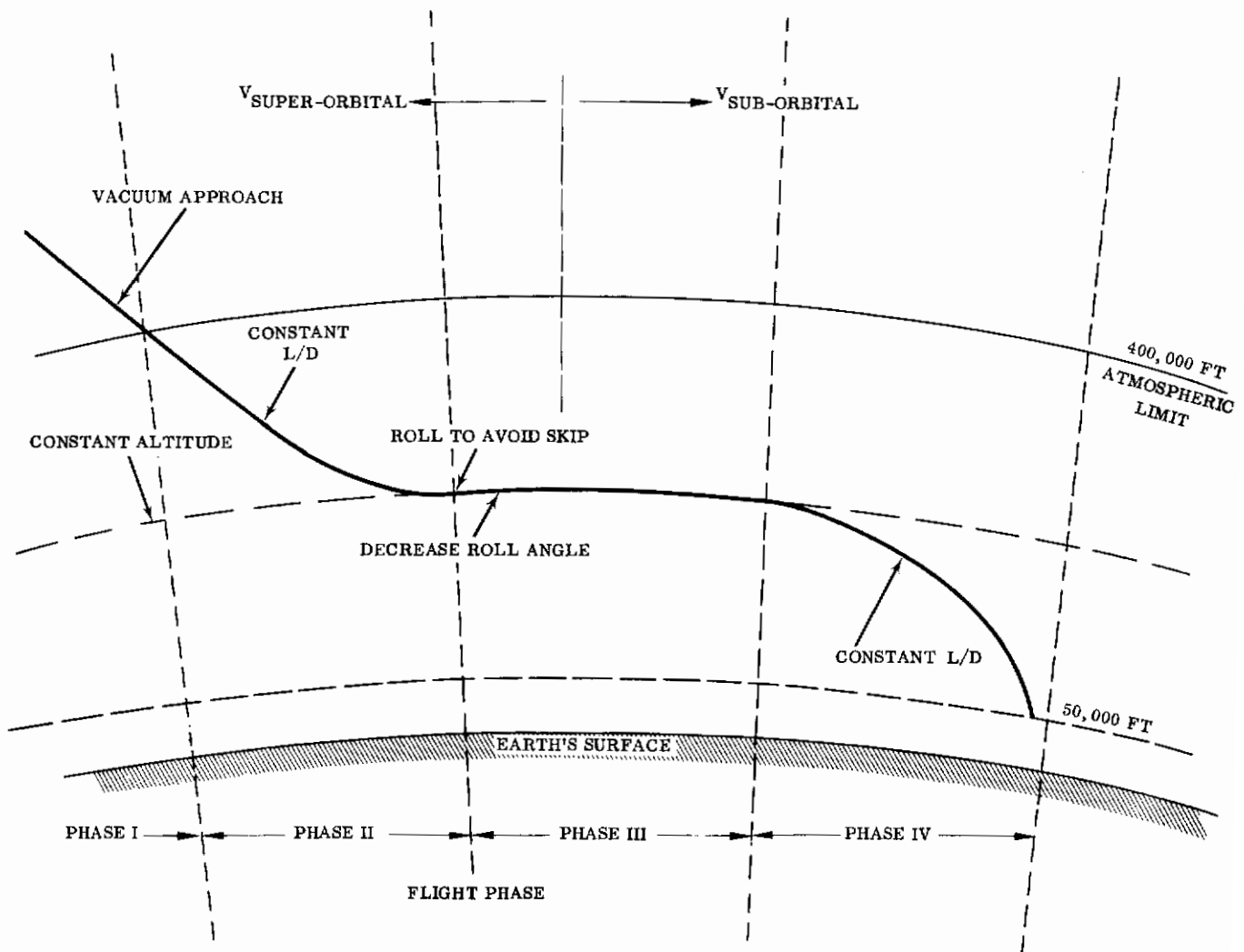


FIGURE 1. MODEL TRAJECTORY USED FOR LIFTING RE-ENTRY

set at 10 g's for manned glider configurations. The shallowest re-entry angle was limited by the peak negative lift which could be obtained at the end of Phase I to maintain constant altitude flight, i.e., to accomplish single-pass entry without skipping back out of the atmosphere. These two initial angles define the lower and upper boundaries of a lifting re-entry corridor with associated boundary heating rates, integrated total heat inputs to the structure, and dynamic pressure environments. The third entry angle considered was intermediate between the skip-out and deceleration limits.

# Contrails

During Phase II descent flight, commencing at atmospheric entry, a constant L/D (maximum positive) was held in order to accomplish pull-up. The Phase II pull-up maneuver is maintained until achieving horizontal flight. The choice of a constant L/D has the advantage of reduced deceleration and heating without the complexity of lift programs which are dependent upon such parameters as time, flight path angle, or air density. Maximum dynamic pressure and the related maximum deceleration, as well as peak heating rates (convective and radiative), occur shortly before the termination of Phase II flight.

Upon reaching the lowest point of the initial descent path, Phase III commences with a roll maneuver which results in a high negative vertical component of lift sufficient to maintain flight at a constant altitude. The effective negative lift must be imposed at an altitude below that defined by the equilibrium force line for the particular negative  $(L/D)_{\max}$  being investigated; otherwise, the air density is insufficient for control, and the vehicle will escape from the atmosphere in spite of any control efforts attempted. Equilibrium flight occurs when the combination of velocity, altitude, and lift is such that the weight of the craft, the lift force, and the centrifugal force are all in equilibrium. For this balanced condition, the rate of change of altitude in the equations of motion is sensibly zero. The Phase III modulation to high negative L/D could not, from a structural standpoint, have been accomplished by pitching the vehicle to a high negative angle attack; such a maneuver would expose the upper surface of the vehicle to an excessive thermal environment.

In Phase III flight, approximately 50 percent of the range capability accrues (Ref. 1). Also, with optional maneuver techniques, the lateral range control can be approximately 40 percent of the maximum linear range. The linear-range can be increased significantly by a slight increase in Phase III constant altitude prior to attaining orbital velocity. The constant angle-of-attack lifting scheme employed, although about 10 percent more severe in its effect upon total thermal input, exhibited structural advantages because the input heating distribution about the vehicle remained fixed with time, and the location of the stagnation point also remained unchanged. The vehicle was rolled in such a manner that the direction of the lift vector rotated continuously, but the absolute magnitude of L/D was invariant. A simple programmed maneuver technique yielded an effective vertical component of lift which satisfied the constant altitude boundary condition. With the rotating longitudinal axis of the vehicle describing a conical surface about the flight path, the resultant fixed angle of attack was obtained. By rolling the glider sequentially from side to side (causing a variation in azimuth as well as a slight perturbation in altitude), any de-

sired course may be followed. The mean projection of the moving lift vector viewed in forward or aft elevation commenced vertically downward at the start of Phase III; thence it rotated upward, becoming horizontal at orbital velocity (centrifugal force and weight in balance) and finally became oriented vertically upward at the conclusion of Phase III.

The final descent portion of the trajectory, Phase IV, commences automatically at the time of intersection of the horizontal flight path with the particular sub-orbital equilibrium glide line which corresponds to design  $(L/D)_{\max}$ . A relatively smooth transition to the glide line occurred when the effective  $L/D$  attained at the end of Phase III was held constant. Phase IV terminated at the preassigned altitude, 50,000 feet, below which structural heating, because of prior energy expenditure, became insignificant.

The following information was obtained for each of the characteristic vehicles listed in Table 1:

1. Altitude vs velocity. The permissible upper and lower bounds of altitude for each velocity (dependent upon negative  $(L/D)_{\max}$  capability and a deceleration of 10 g's, respectively) were superposed upon the flight profiles. Equilibrium glide velocities for the positive and negative values of  $L/D$  (pertaining to sub-orbital or super-orbital flight) were determined from the expression

$$V = \frac{R_o/R}{\sqrt{\frac{\rho}{2} \frac{L/D}{W/C_D A} + \frac{1}{g_o R}}} \text{ fps}$$

where  $R_o$  = radius of the earth, ft

$R$  = geocentric distance of the entry body, ft

$g_o$  = gravitational acceleration corresponding to  $R_o$ , ft/sec<sup>2</sup>

$\rho$  = air density corresponding to  $R$ , slug/ft<sup>3</sup>.

The deceleration limit was determined from the relationship

$$V = \frac{\sqrt{2N (W/C_D A)}}{\sqrt{\rho} \sqrt{1 + (L/D)^2}} \text{ fps}$$

where  $N$  = maximum permissible g-limit, here, 10 g's.

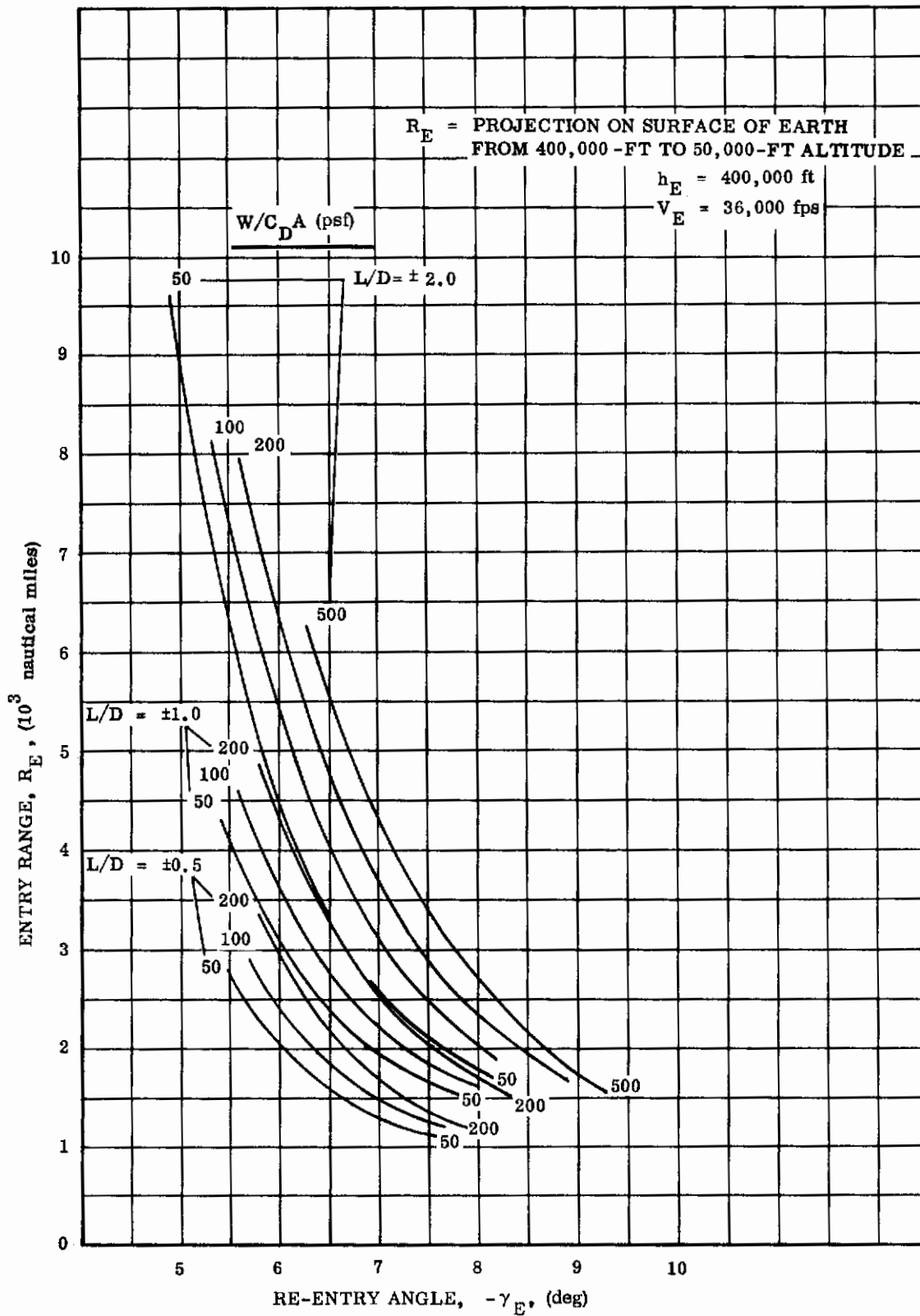


FIGURE 2. RANGE FROM SUPER-ORBITAL RE-ENTRY



2. Entry time (to 50,000-ft altitude), entry range ( $R_E$ ), and total convective heat input ( $Q_C = \int \dot{q}_C dt$ ) for the limiting entry angles which define the re-entry corridor.  $R_E$  is the total range along the trajectory trace on the earth's surface, including the integrated lateral flight distance accrued during descent from 400,000 to 50,000 feet.  $Q_C$  pertains to the unit area (1 square foot) heating at the stagnation point of a 1 foot-radius frontal hemisphere.
3. Time history of heating rate and the integrated heating rate at the stagnation point. For flight speeds greater than 1000 fps, the laminar convective heating rates (cold wall) were determined from the modified correlation equation of Detra, Kemp, and Riddell (Ref. 2) and Zierten (Ref. 3).

$$\dot{q}_C = 17,800 \left( \frac{V}{10^4} \right)^{3.15} \frac{\sqrt{\rho_\infty}}{\sqrt{R_n}} \text{ Btu/ft}^2 \text{-sec}$$

where  $\rho_\infty$  = free stream air density at altitude, slug/ft<sup>3</sup>

$R_n$  = radius of curvature at the stagnation point, ft.

With the ordinate on the convective heating rate curves normalized as  $\dot{q}_C (R_n)^{1/2}$ , the stagnation point heating rates for frontal sections having any specified radius of curvature may be obtained by dividing the presented heating parameter by  $(R_n)^{1/2}$ . Cumulative heat input will be of some importance in subsequent studies involving heat absorption. Subsonic convective heating was assumed to be zero.

4. Time history of dynamic pressure. The values obtained were free stream pressures ( $\bar{q}_\infty = 1/2 \rho_\infty V_\infty^2$ ), with compressibility effects through the bow shock, appreciable in the hypersonic flight regime, having been excluded.
5. Time history of velocity and altitude. Zero time was set at 400,000 foot altitude.

Summary plots of trajectory information as dependent functions of the entry angle ( $-\gamma_E$ ) and with L/D ratios and ballistic coefficients as the significant parameters were utilized in developing general conclusions regarding super-orbital vehicle entry environment. Total range along the trajectory trace on the earth's surface ( $R_E$ ) and re-entry times ( $t_F$ ) as functions of entry angle at 400,000 foot altitude are given in Figures 2 and 3, respectively. Either case pertains to descent from 400,000 feet to the lower bound (50,000 feet). As indicated in Figure 2, a slight decrease in entry angle results in a considerable increase in range. Also, the increase in entry time

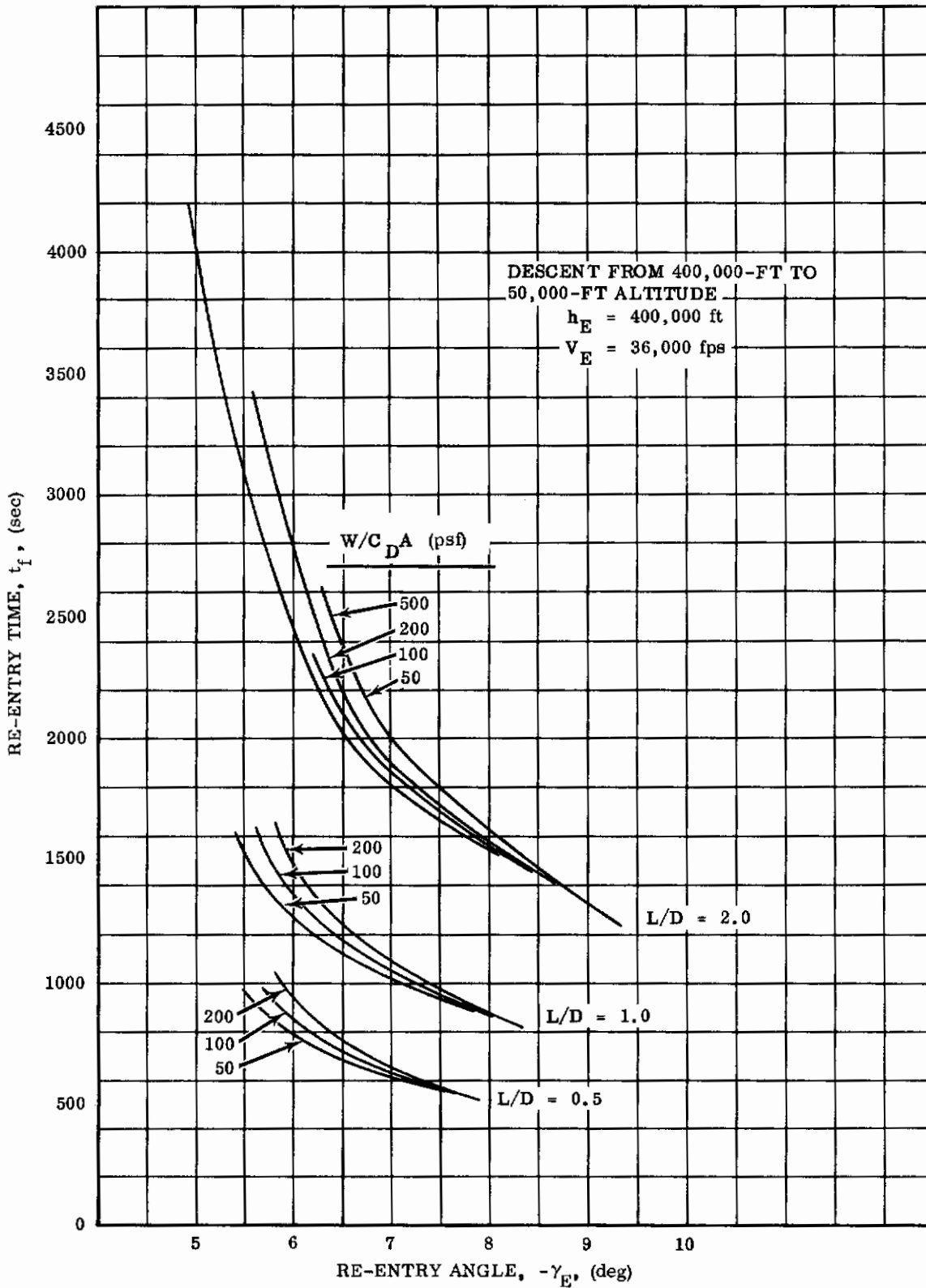


FIGURE 3. SUPER-ORBITAL RE-ENTRY TIME

(Fig. 3) is quite pronounced for atmospheric entry at shallower angles. Entry time and range for a specific entry angle and  $L/D$  are rather insensitive to changes in  $W/C_D A$ , especially at the steeper entry angles. The total ranges were obtained from a zero roll angle throughout Phase IV flight. The fraction of the total range distributed among the three phases of atmospheric flight is affected primarily by vehicle  $L/D$ ; the entry angle with  $W/C_D A$  variation introduced a maximum deviation of only  $\pm 4$  percent in total range. Approximately 15 percent of the total range was traversed in Phase II flight, 55 percent in Phase III flight, and 30 percent in Phase IV flight ( $L/D = 1.0$ ). An increase in  $L/D$  decreased the percent of range in Phase II and increased the percent range travelled in Phase IV. The significant effect of lift-drag ratio upon range distribution results from the increased velocity and altitude at pull-out and the higher altitude and lift capability at the start of sub-orbital equilibrium glide.

Maximum laminar convective heating rate ( $\dot{q}_{c_{\max}}$ ) incident upon a stagnation point of general radius is presented in Figure 4. Similarly, the total input heating load ( $Q_c$ ) is given in Figure 5. Conclusions derived from an examination of these figures which pertain to a group of vehicles having uniform nose radii are:

1. For a given  $L/D$  and  $W/C_D A$  a steeper entry angle results in a higher instantaneous heat pulse ( $\dot{q}_{c_{\max}}$ ) and a lower total heat input ( $Q_c$ ).
2. For a given  $L/D$  and entry angle, an increase in  $W/C_D A$  increases both  $\dot{q}_{c_{\max}}$  and  $Q_c$ .
3. For a given  $W/C_D A$  and entry angle, an increase in  $L/D$  decreases  $\dot{q}_{c_{\max}}$  and increases  $Q_c$ .

Curves of integrated heating between penetration of the outermost atmosphere and the instant that convective heat flow inward just equals reradiation flux out are presented in Figure 6. The heat rate specified for the balanced thermal state (radiation equilibrium) for this early study was  $233 \text{ Btu/ft}^2\text{-sec}$ , corresponding to a surface emittance of 0.8 and a wall temperature of 4500 F on a 1-foot radius frontal body. To prevent equilibrium wall temperatures exceeding the upper limit of 4500 F, supplemental absorptive heat protection structure must be provided during the portions of the trajectories displaying the higher input heating rates. This additional thermal protection comprises either permanent or expendable systems (heat sink or ablative, respectively) or combinations of each.

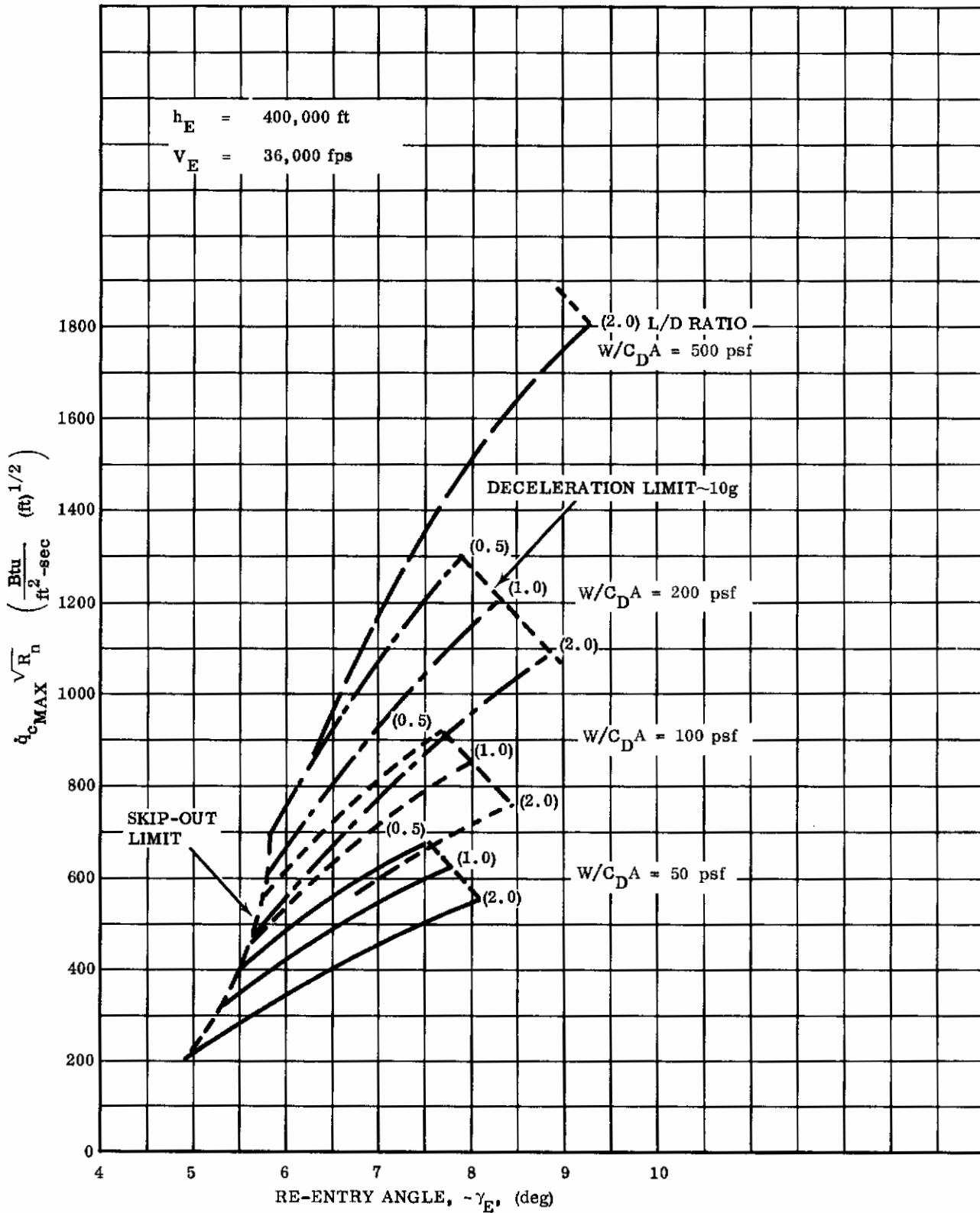


FIGURE 4. STAGNATION POINT MAXIMUM HEATING RATE

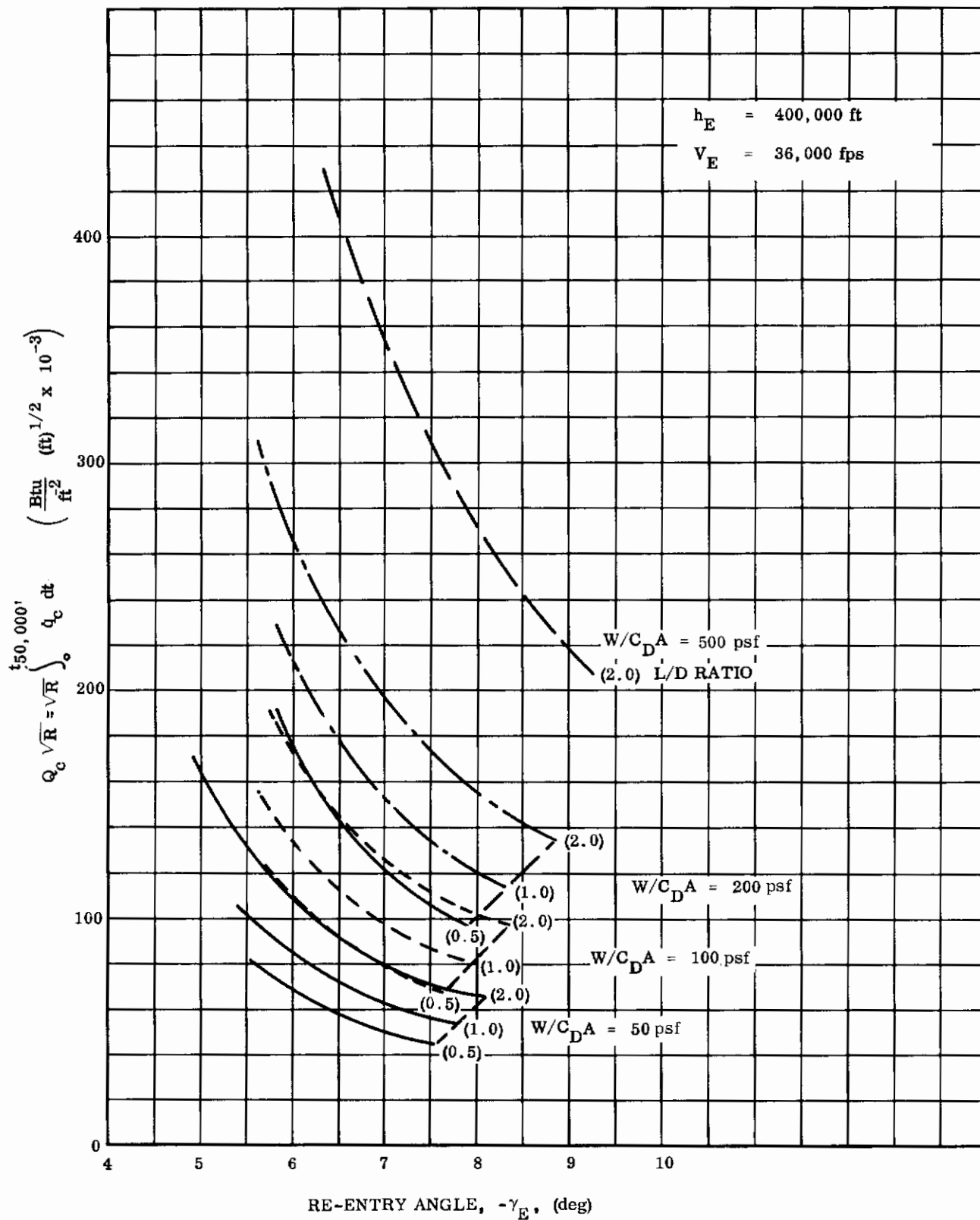


FIGURE 5. STAGNATION POINT TOTAL INPUT HEATING

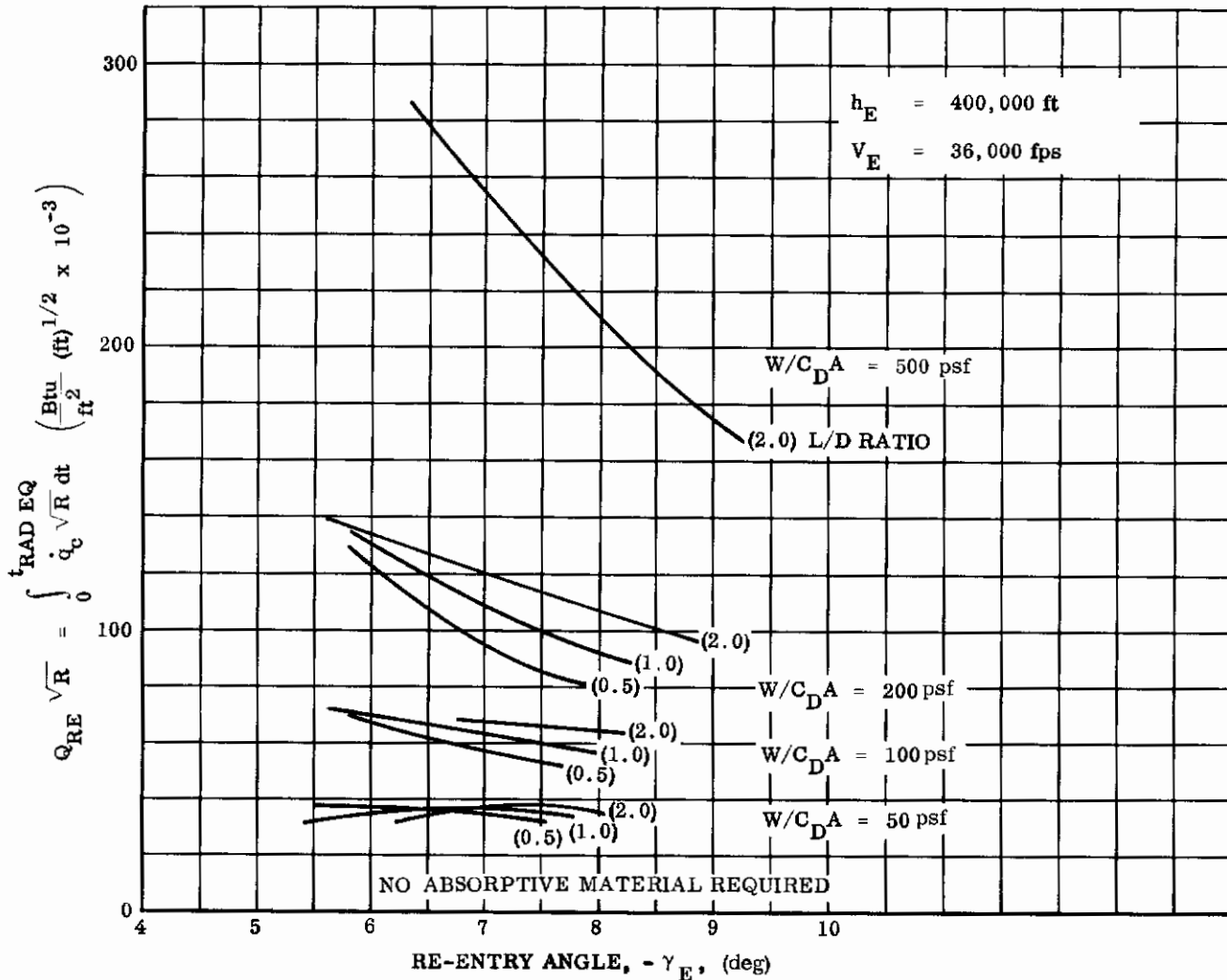


FIGURE 6. STAGNATION POINT INPUT HEATING; Entry to Radiation Equilibrium Condition

From the corridor limits, skip-out, and deceleration indicated in Figure 4, a curve of corridor boundaries as a function of vehicle L/D and as influenced by ballistic parameter was plotted (Fig. 7). Both the maximum and minimum limits on entry angle, as well as the angular differential or actual width of entry corridor was shown in the plot. The lower curve emphasizes the characteristic importance of L/D upon corridor width and the relative insensitivity of  $W/C_{D A}$ . A maximum dispersion of 3.6 degrees in flight path angle is permissible at entry for a vehicle having an L/D of 2.0 and a  $W/C_{D A}$  of 200 psf. By applying an alternative maneuver technique during Phase II flight, modulating the L/D to values less than  $(L/D)_{max}$ , the corridor width could be increased a maximum of 25 percent. With a reduced L/D, the vehicle can enter at a shallower angle and still maintain constant altitude after pull-out.

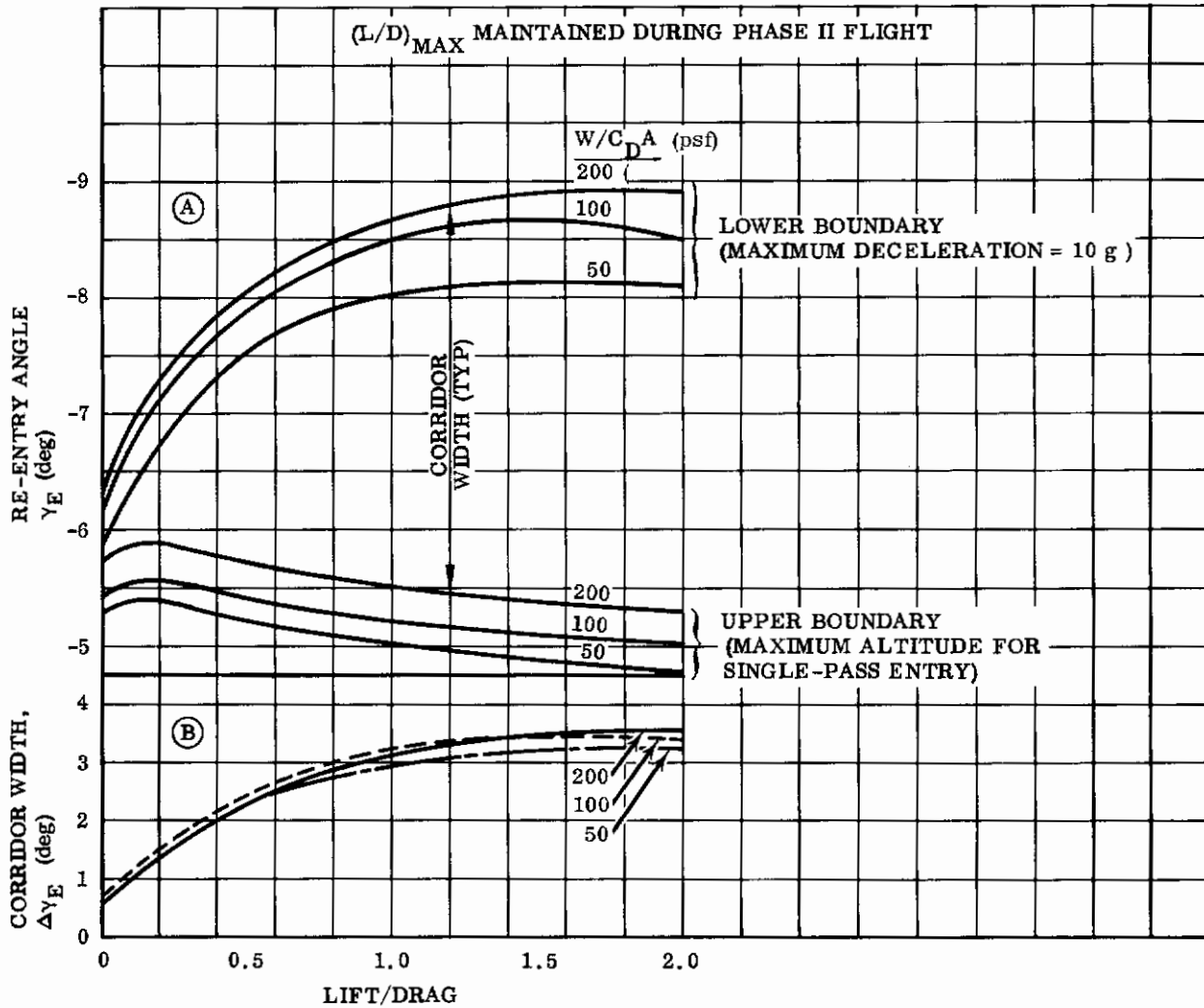


FIGURE 7. ENTRY FLIGHT PATH BOUNDARIES AND ANGULAR WIDTH OF ENTRY CORRIDOR

No summary plot was prepared for peak dynamic pressure  $\bar{q}_{\infty \max}$ , because dynamic pressure and glide deceleration (Fig. 8) are related through the expression

$$N = \sqrt{\frac{1 + (L/D)^2}{W/C_D A}} \bar{q}_{\infty}, \text{ g's.}$$

Therefore, maximum total deceleration and peak dynamic pressure occur simultaneously. As indicated in Figure 8, entry angle steepness has the predominant influence upon peak deceleration. From the foregoing relationship between dynamic pressure and deceleration and from the relative insensitivity of  $N_{\max}$  to either  $L/D$  or  $W/C_D A$ ,

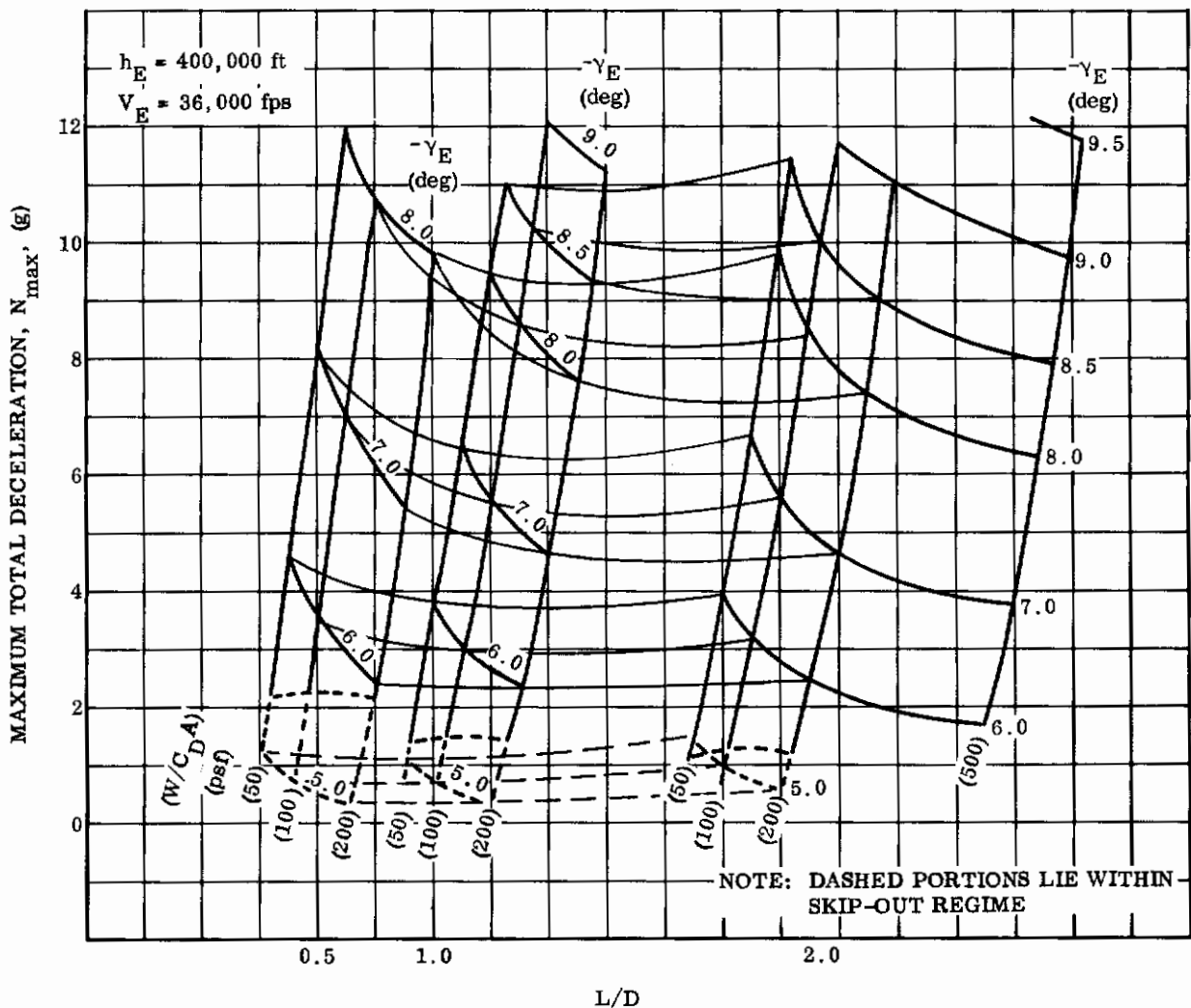


FIGURE 8. MAXIMUM DECELERATION

the following conclusions regarding maximum dynamic pressure were formulated:

1. For a constant L/D and  $W/C_{DA}$ , a steeper entry angle results in a more severe aerodynamic pressure.
2. For a constant L/D and  $\gamma_E$ , increasing  $W/C_{DA}$  increases the dynamic pressure.
3. For a constant  $W/C_{DA}$  and  $\gamma_E$ , increasing L/D decreases the maximum instantaneous  $\bar{q}_\infty$ .



## 2.2 SELECTION OF TYPICAL CLASSES OF LIFTING VEHICLES

The aerodynamic analyses of Section 2.1 indicated general trajectory variables and heating problems associated with a super-orbital plunge from space for a range of manned vehicles; also, a simple lifting maneuver program to be performed within the atmosphere was recommended. Lift-to-drag ratios were varied between 0.5 and 2.0; ballistic coefficients ranged between 50 and 200 psf with isolated check runs having been made at a  $W/C_D A$  of 500 psf; extremes in entry angle were considered (shallow skip-out limit to steep deceleration or overall vehicle heating limit). Lift capability provided extensive down-range and lateral-range for selection of landing sites. Minimum range comprised between a third and two-thirds the east-west span of the U.S.; maximum range at shallow entry encompassed nearly half the circumference of the earth. Least interest recently has been indicated in operating hypersonic winged vehicles at the higher ballistic coefficients, obtained at low angles of attack. For a glider displaying a hypersonic  $(L/D)_{\max}$  of 2.0, operation at a  $W/C_D A$  of 200 psf would correspond to a flight attitude of approximately 10 degrees, at which point shielding of a cabin on the upper surface from the high kinetic energy air stream becomes questionable. The trend is toward operating within the portion of the corridor established between  $(L/D)_{\max}$  and  $C_{L_{\max}}$  flight for increased range as well as decreased severity of peak convective heating rate and integrated heat load. Also, gas cap radiation becomes relatively high for high  $W/C_D A$ 's and steep entry angles.

From among the preceding general super-orbital trajectories, four representative vehicles were selected as a basis for adjudging feasibilities and practicabilities of various frontal structure to be mounted thereon. It was considered important to select, at this point, a broad range of dissimilar classes of lifting vehicles which offered foreseeable potential for future Air Force applications.

The general approach in establishing four trajectories for further study in this program was that of determining those combinations of  $L/D$ ,  $W/C_D A$ , and  $\gamma_E$  that lead to near minimum weight of absorptive heat protection material provided the combinations of the three aerodynamic parameters were consistent with trajectory requirements. The four candidate trajectories are thus intended to be representative of groups of vehicles having adequate entry capability along with a low absorptive heat protection weight in the nose sections, while at the same time possessing sufficient structural latitude to allow compromise with other demands such as

1. Mission requirements (aside from re-entry)
2. Inert weight requirements affecting  $W/C_D A$
3. Limitations imposed by realistic  $C_L$  and  $C_D$  characteristics of re-entry vehicles.

Cumulative heating to the commencement of thermal relief by significant reradiation was of considerable importance in evaluating the heat protection systems (Fig. 6). Assuming that the weight of the absorptive system is proportional to  $Q_{RE}$ , minimization of that partial heat load parameter should be emphasized. Heat load for an insulative system, however, is far less significant (Ref. 4).

A range of lift-to-drag ratios to satisfy re-entry lifting maneuver requirements (e.g., attaining a given longitudinal or lateral range, or achieving touchdown in a predetermined time) may be covered reasonably by  $L/D$ 's of 0.5, 1.0, and 2.0. Determining characteristic trajectory parameters ( $\gamma_E$  and  $W/C_D A$ ) corresponding to these  $L/D$ 's then remains. Thermal or aerodynamic effects of nose radii were not quantitatively considered in the preliminary trajectory selection. A choice of the steepest entry angle in each instance results in minimum  $Q_{RE}$  and least weight of the absorptive component of a composite radiative-absorptive system.

Preliminary curves, descriptive of vehicle classes studied further, are plotted in Figure 9. Partial heat load values were derived for an effective fixed radius of one foot. With vehicle geometry defined, effective radii and their quantitative effect upon  $Q_{RE}$  can be ascertained. Using drag polars derived by Newtonian impact theory (such polars being applicable at the higher Mach numbers and angles of attack), lines of typical  $W/C_D A$ -vs- $L/D$  variation are superimposed upon the  $Q_{RE}$  plot. These represent three possible vehicle configurations:

1. Low  $L/D$ ; a blunted semi-cone
2. Intermediate  $L/D$ ; a blunted elliptic cone
3. High  $L/D$ ; a winged glider.

The associated vehicle aerodynamic characteristics (hypersonic  $L/D$  and corresponding  $W/C_D A$ ) are approximate, but representative, values and are therefore shown as broad lines rather than by points in Figure 9. The maximum  $L/D$  values are slightly higher than it was felt could be achieved in an actual vehicle, and

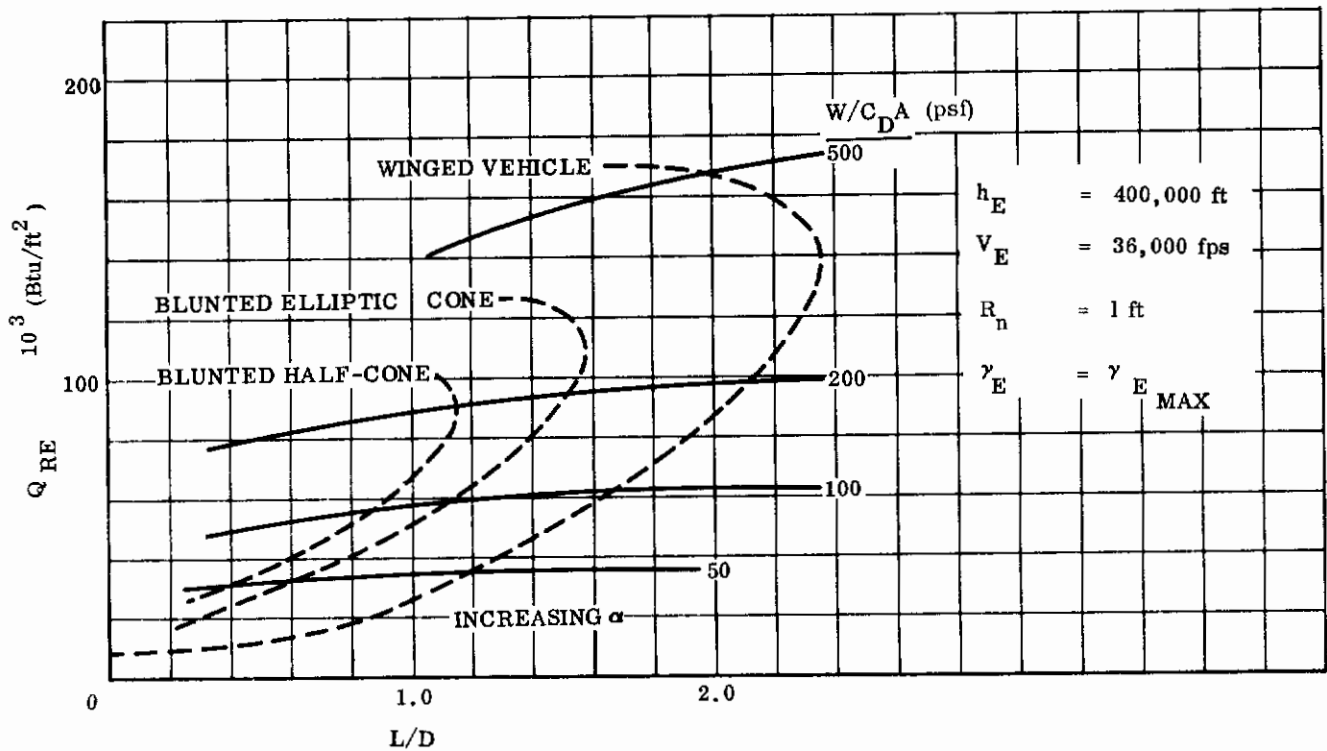


FIGURE 9. HEAT ABSORPTION FOR 10-g LIMIT TRAJECTORIES WITH SUPERPOSED CHARACTERISTICS OF THREE CLASSES OF RE-ENTRY BODIES

definitely higher than values recommended for the subsequent studies; with such the case, vehicle operation may be envisioned at design points slightly off  $(L/D)_{\text{max}}$  and toward  $C_{L_{\text{max}}}$ , i. e., at higher attitudes ( $\alpha$ ).

For  $L/D = 2$ , the relatively high value of  $W/C_D A$  of 200 psf (occurring at a moderate flight attitude and above  $(L/D)_{\text{max}}$ ) was selected for investigating most severe thermal environment in the subsequent nose structure analyses. For  $L/D = 1$ , a  $W/C_D A$  of 100 psf was selected because this set of parameters resulted in trajectories representative both of the elliptic cone entering at lower angles of attack (only slightly greater than  $(L/D)_{\text{max}}$ ) and the winged vehicle entering at intermediate angles of attack between  $(L/D)_{\text{max}}$  and  $C_{L_{\text{max}}}$ . At  $L/D = 0.5$ , a  $W/C_D A$  of 50 psf was selected because this combination of parameters yielded trajectories nearly representative of all three classes of lifting bodies: the blunted semi-cone at small flight attitudes; the elliptic cone at medium attitudes; and the winged vehicle at its largest angles of attack short of aerodynamic instability.

Since Figure 9 was derived for general qualitative comparisons of heat input to absorptive media, it does not depict true magnitudes of thermal input to either the blunted or winged vehicles. The blunted vehicles could conceivably have effective nose radii significantly in excess of one foot at all attitudes, reducing the heat load. A frontal section of a winged vehicle at intermediate-to-large angles of attack would probably also present a larger effective nose radius to the air stream. Figure 9 does, however, relate typical candidate vehicles to  $Q_{RE}$  ( $R_n = 1$  foot) showing trends to be observed if  $Q_{RE}$  is to be minimized.

A fourth class of vehicle, namely a glider characterized by an exceedingly light wing loading, was added to the study because it depicted a structure for which no heat absorption ability was required for a simple tungsten shell to survive the re-entry environment. This type of structure (hot wall) fully utilizes the high-temperature capability of refractory metals throughout atmospheric entry.

Vehicles and trajectory characteristics selected are shown in Table 2.

TABLE 2  
REPRESENTATIVE CONFIGURATIONS

Class of Vehicle	L/D	$W/C_D A^{(1)}$	$-\gamma_E^{(2)}$	$t_F^{(3)}$	$R_E^{(4)}$	$\dot{q}_c \sqrt{R_n}^{(5)}$ max	$Q_c \sqrt{R_n}^{(6)}$
I Winged glider	2.0	200	8.9	1387	1744	1085	136,010
II Blunt elliptic cone	1.0	100	8.0	866	1634	850	81,940
III Blunt semi-cone <sup>(7)</sup>	0.5	50	7.55	557	1122	675	47,280
IV Light wing-load glider	2.0	50	4.9	4184	9571	205	171,700

1. Ballistic coefficient, psf
2. Re-entry angle, degrees
3. Re-entry time, seconds
4. Re-entry ranges, nautical miles
5. Max. convective heat flux,  $Btu(ft)^{1/2}/ft^2$ -sec
6. Total heat input,  $Btu(ft)^{1/2}/ft^2$
7. These parameters may also typify a symmetric cone

Configurations I, II, and III enter the atmosphere at the steepest angle allowable short of exceeding the 10-g deceleration bounds. The peak heat fluxes at the stagnation point are of severity requiring absorptive heat protection. Configuration IV re-enters at the skip-out limit and follows a trajectory indicative of a structure utilizing hot-wall radiation to dissipate the relatively long-duration, low-level pulse. For this latter case the nose structure would consist of a refractory metal shell overlaid with a thin oxidation-protective coating.

Entry times (to 50,000-foot altitude) varied between 10 minutes for the low-lift, steep-entry body to more than one hour for the high-lift craft approaching the atmosphere near its shallowest permissible entry angle. Maximum laminar cold wall heating rate near the nose cap region ( $R_n = 1$  foot) ranged from approximately 1100 Btu/ft<sup>2</sup>-sec for the glider displaying a medium wing loading, downward to 200 Btu/ft<sup>2</sup>-sec for the glider with low wing loading. High magnitudes of total heat load are not necessarily critical since prolonged radiation from a high-temperature-capability frontal structure can reradiate much of this energy back to the air stream.

### 2.3 PRELIMINARY DESIGN - NOSE AND BODY CONFIGURATIONS

Pictorial likenesses and dimensioned views of the four conceptual vehicles were prepared to aid in identifying specific entry craft as they are subsequently discussed. The representative early-generation lifting shapes selected provide an insight into the range of possible attachment bodies for candidate frontal sections. The selected vehicles, sized, equipped, and supplied for a two-man crew, have weights at entry ranging to 15,000 pounds.

Flight attitudes at which the various vehicles would be operated to attain the desired lift-drag characteristics were first determined. Hypersonic flight properties were obtained both from tunnel test data and analytically determined drag polar diagrams based upon modified Newtonian flow theory. Comparisons of the two methods, where model data were available, were generally good, especially for the thin-winged gliders which resemble flat plates flown at moderate angles of attack.

The pertinent aerodynamic characteristics associated with the four lifting vehicles, values held fixed throughout entry, are summarized in Table 3.

TABLE 3  
VEHICLE AERODYNAMIC CHARACTERISTICS

Type Vehicle	L/D	W/A (psf)	$\alpha$ (deg)	$C_D$	$C_L$
Winged glider (medium wing load)	2.0	25	22	0.125	0.250
Blunt elliptic cone	1.0	54	31	0.54	0.54
Blunt semi-cone	0.5	60	5	1.20	0.60
Light glider	2.0	5	20	0.1	0.2

The lift and drag coefficients ( $C_L$  and  $C_D$ ) were based upon planform areas. The wing-loading expression (W/A) is the ratio of entry weight of the vehicle to planform area. The angle of attack ( $\alpha$ ) is the angle between the vehicle reference line and velocity vector. Trimmed flight at constant  $\alpha$  is utilized throughout the entire re-entry, i.e., during initial super-orbital descent, throughout the constant-altitude roll maneuver, and finally, during sub-orbital equilibrium glide to touchdown. Such an entry scheme is indicative of a fixed stagnation point and fixed flow distribution.

To make the stagnation point fall near the axis of symmetry of a frontal section of revolution, the nose centerlines of the preliminary design vehicles were aligned approximately at angle  $\alpha$  from the body centerlines. Such drooped alignment produces thermal relief at the stagnation point (assuming a blunted body of revolution for the nose cap) as well as a rotationally symmetric temperature and load distribution about the nose. Temperature relief at the stagnation point follows an increase in the radius of curvature at that point, since convective input heating decreases with a larger effective radius. Utilizing shapes which are partially flattened or blunted at the frontal point is thus thermally advantageous. To confine the aft size of the nose to a realistic value (for attachment to the vehicle support structure), the radius of curvature should sharpen aft of the stagnation point, resulting in somewhat higher operating temperatures in the shoulder region compared with those for a hemisphere. Two advantages of a resultant more-uniform input heating are:

- Thermal stresses due to temperature gradients along the shell are minimized
- The refractory metal cap will be more efficiently utilized as a consequence of the augmented surface area radiating heat at a uniformly high temperature.

Based upon the preceding observations, oblate ellipsoidal shells were used for the frontal geometry.

The selected vehicles were assumed to have re-entry weights ranging between 7500 pounds for the blunt semi-cone and light glider configurations to 15,000 pounds for the glider of medium wing loading and the blunt elliptic cone.

### 2.3.1 Medium Wing Loading Glider

A rendering of the winged glider of medium wing loading is shown in Figure 10. A plan view, side elevation, and front view are shown in Figure 11. Details of the corresponding nose section are shown in Figure 12 (plan view, side elevation, and rear view). This particular external nose geometry was recommended for both this glider and for the light glider configuration. Since the trimmed flight attitudes are nearly the same for each glider (Table 3) the applicable frontal structure would be attached to the given vehicle at a droop angle of 20 degrees from the body center-lines. The frontal cap is an ellipsoid of revolution (oblate spheroid) with ratio of semi-minor to semi-major axes  $b/a$  equal to 0.4, and with an effective radius of curvature at the stagnation point

$$\rho_{\text{stag pt}} = a^2/b = 0.994^2/0.398 = 2.48 \text{ ft.}$$

At the connection station of nose section to body, the structure is 2.4 feet high by 4.0 feet wide and is roughly triangular in cross section. One-foot-diameter wing leading edges extend from the lower side edges of the frontal section. An arrow planform rather than a delta reduces the undesirable center-of-pressure shift near unity Mach number. The lower wing surface is flat, whereas a diamond shape camber is provided on the upper surface. The aft-mounted cabin on the upper surface should be well protected from heat impingement at operating attitudes.

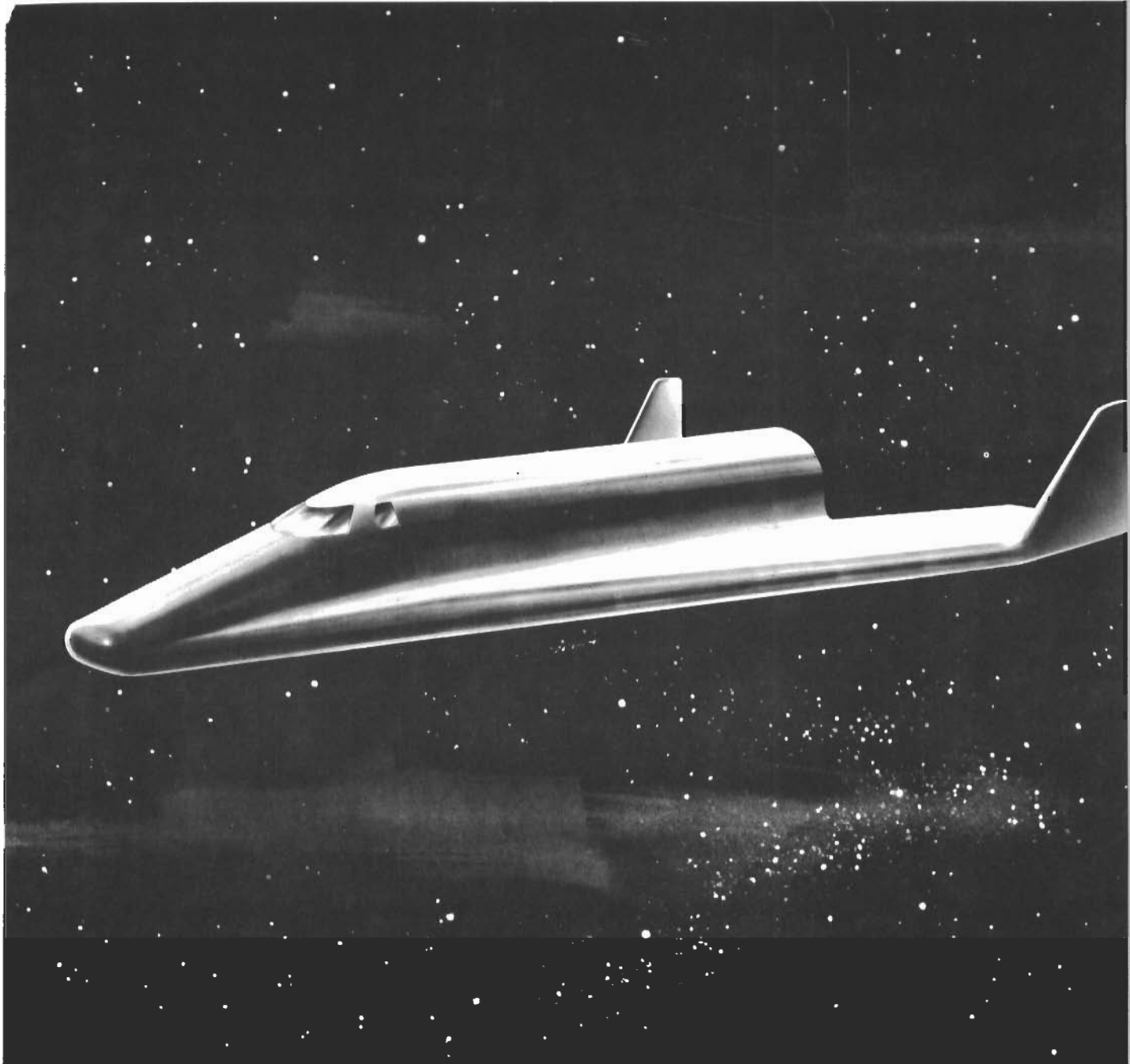
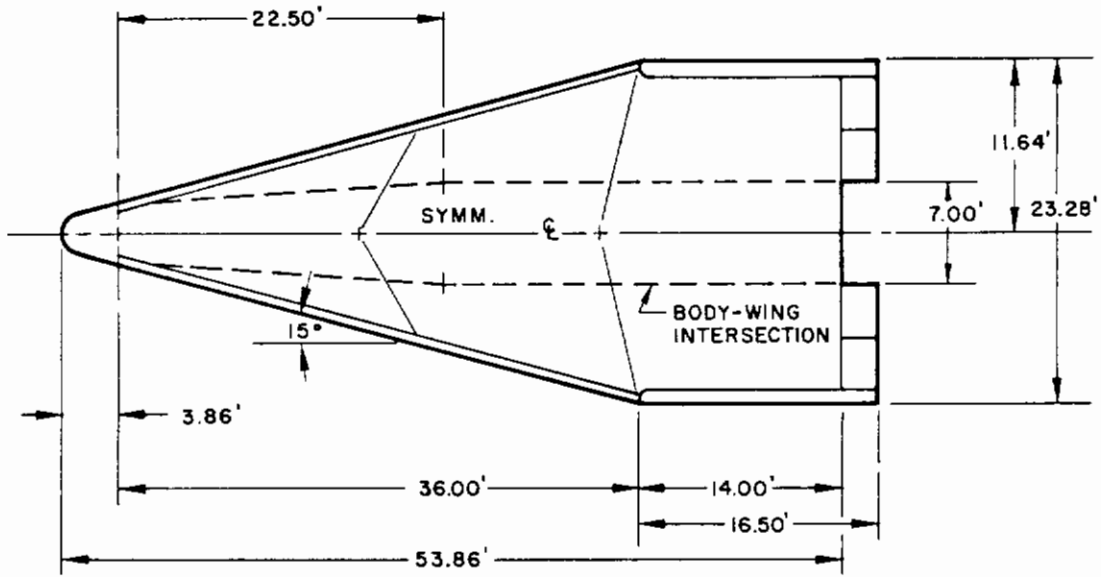


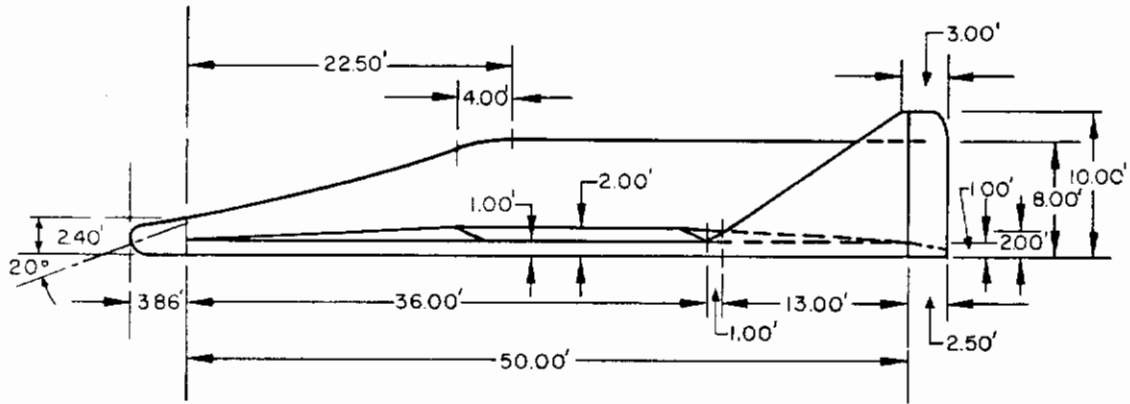
FIGURE 10. MEDIUM WING LOADING GLIDER



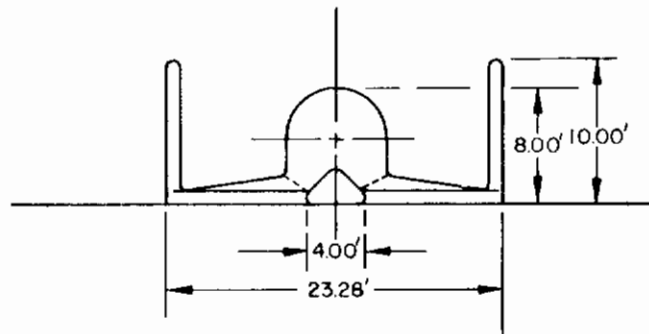
# Contracts



**PLAN VIEW**



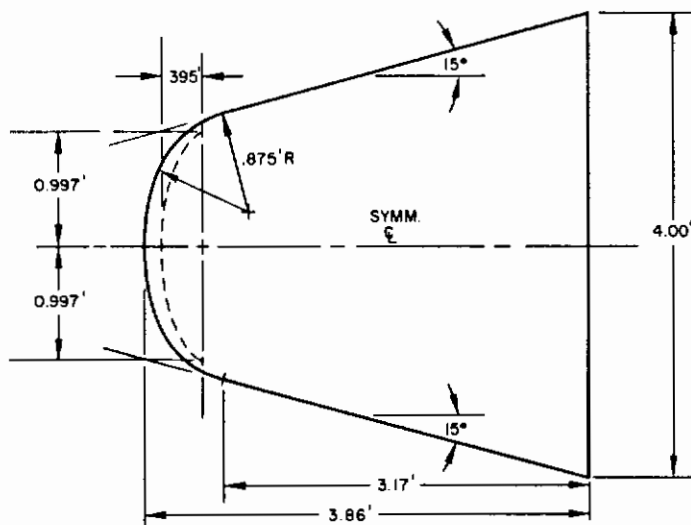
**SIDE ELEVATION**



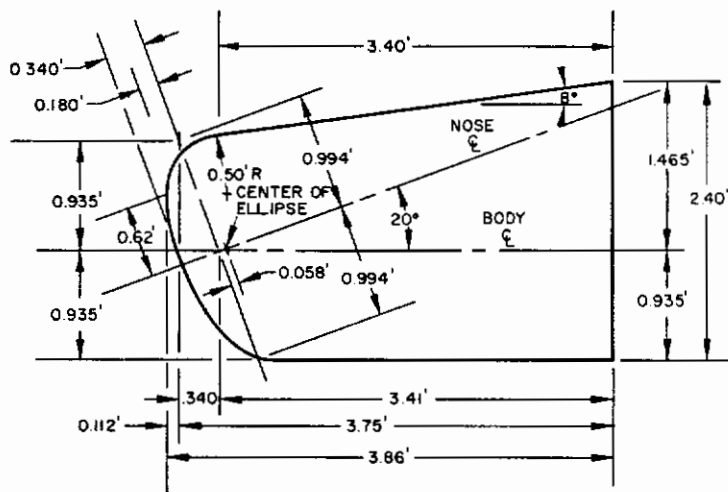
**FRONT VIEW**

FIGURE 11. MEDIUM WIND LOADING GLIDER; Three-View

# Contours

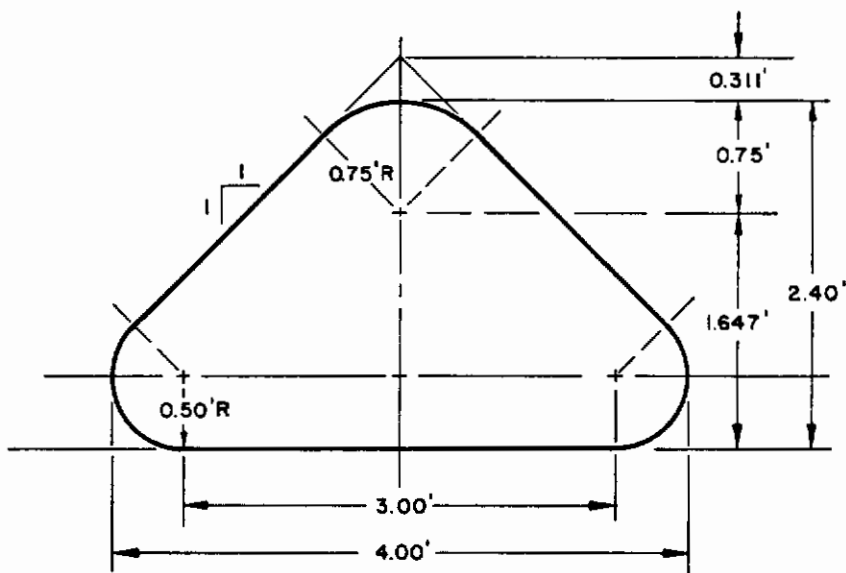


**PLAN VIEW**



$a = 0.994'$   
 $b = 0.398'$   
 $k = 0.40$   
 $f_{STAG PT} = \frac{a^2}{b} = 2.48'$

**SIDE ELEVATION**



**REAR VIEW**

**FIGURE 12. WINGED GLIDER NOSE SECTION**

## 2.3.2 Blunt Elliptic Cone

A rendering of the blunt elliptic cone configuration is shown in Figure 13. All sections normal to the centerline of the blunt elliptic cone are 2:1 ellipses (Fig. 14). The nose is inclined 30 degrees relative to the body. The shape of the non-axisymmetric frontal ellipsoid recommended for this configuration is shown in Figure 15. Of the various nose sections, this shape would be the most complex to fabricate because of the transitions required for attachment to the flattened afterbody. Trailing edge flaps and rotavons provide maneuver control.

## 2.3.3 Blunt Semi-Cone

A rendering of the blunt semi-cone configuration is shown in Figure 16. The blunt semi-cone (Fig. 17) is a modified ballistic shape of relatively low L/D at hypersonic speeds. It is formed by slicing a plane (offset from the axis) through the cone. Due to its side elevation asymmetry, the desired L/D is attained at a relatively low angle of attack,  $\alpha = 5$  degrees. In view of the small flight attitude, the nose centerline for this configuration was made coincident with the body centerline. The frontal shape is described as an oblate spheroid, with b/a of 0.5 in both the plan and elevation views. The radius of curvature at the body centerline is

$$\rho = a^2/b = 1.56^2/0.78 = 3.1 \text{ ft.}$$

## 2.3.4 Light Wing Loading Glider

A rendering of the light glider ( $W/A = 5$  psf) configuration is shown in Figure 18. Details of the delta wing planform, a sectional elevation view through the centerline and a rear view are shown in Figure 19. The base shape of the wing is a slender quadrangular pyramid with all sections perpendicular to the centerline rhombic (diamond) shaped. Trailing edge control flaps and dual fins are located inboard of the wing tips. A bubble cabin is placed centrally on the upper surface. A leading edge radius of 3 inches is possible with a lower intensity heating environment for this vehicle. The nose cap (same geometric configuration as for the glider of medium wing loading) is entirely radiative for the anticipated environment. The extremely light wing loading prescribed for the light glider presents a challenge, structurally, to achieve in a rigid re-entry vehicle. Moreover, with large fixed aerodynamic surfaces placed atop a multi-stage booster, stabilization during ascent flight is expected to be extremely difficult.

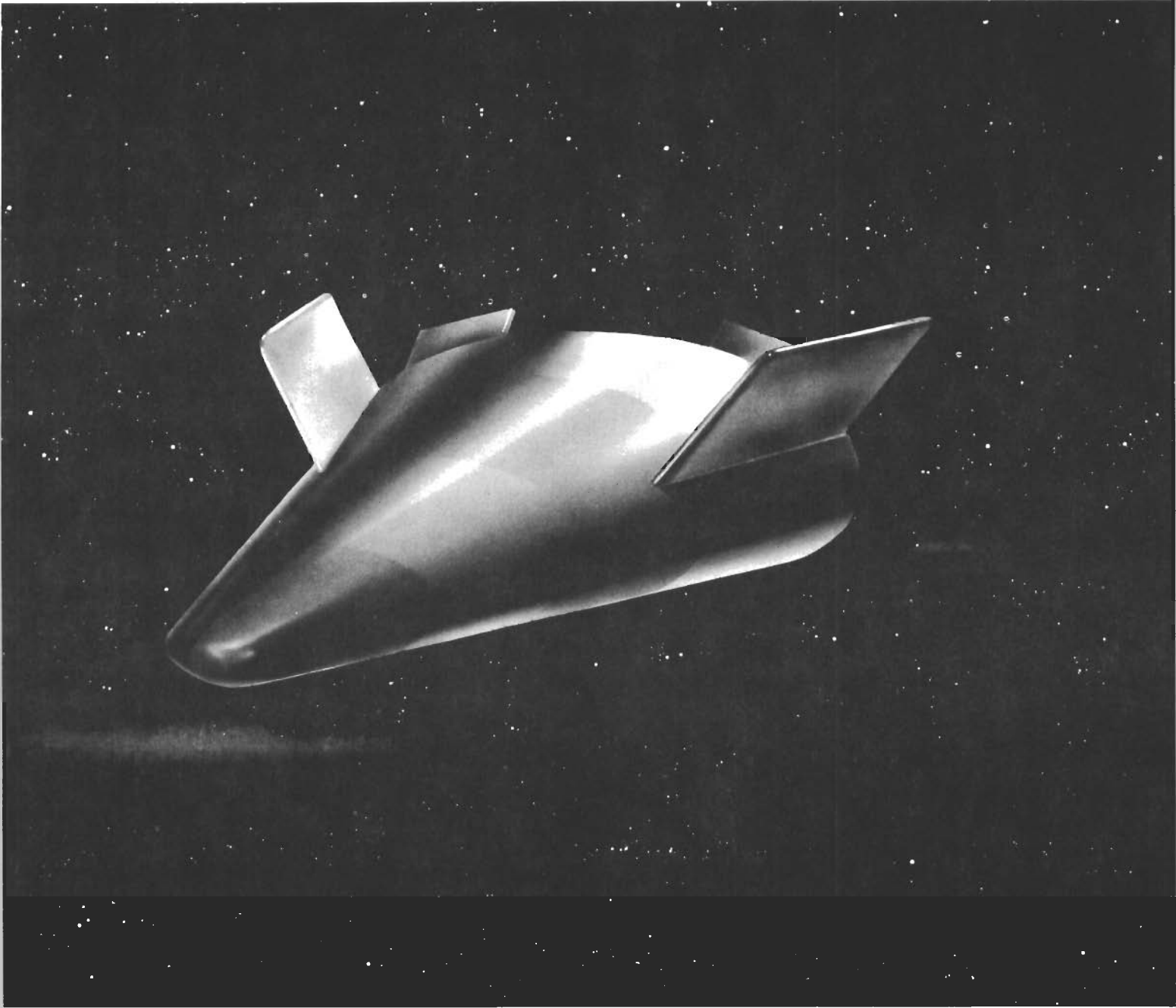


FIGURE 13. BLUNT ELLIPTIC CONE

# Contraails

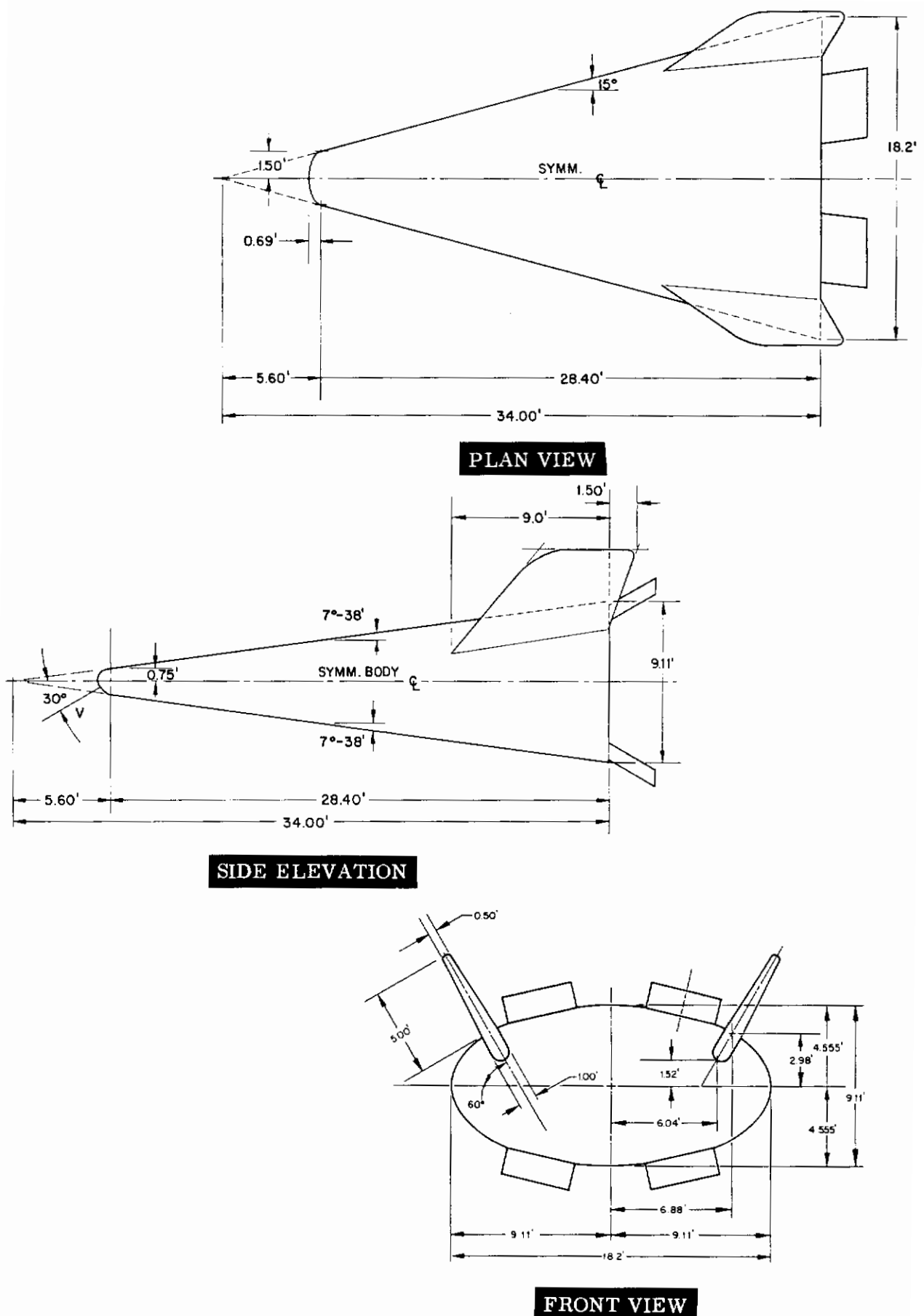
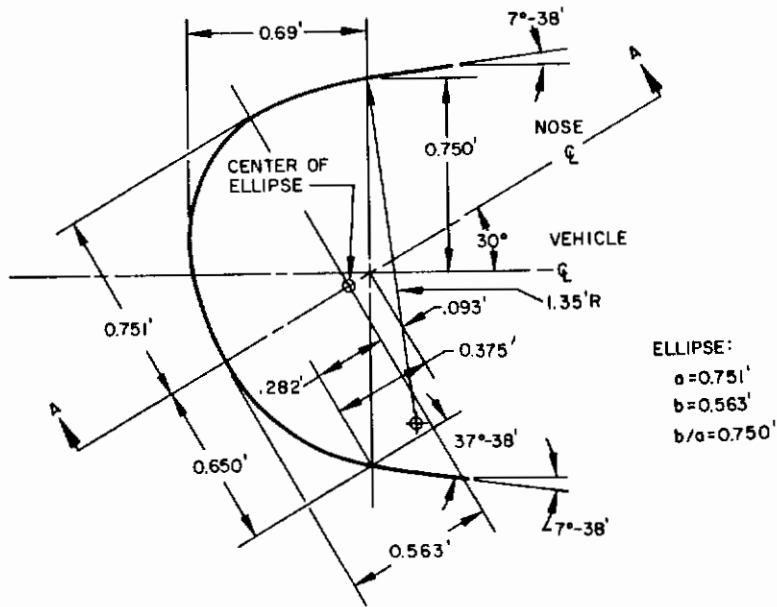
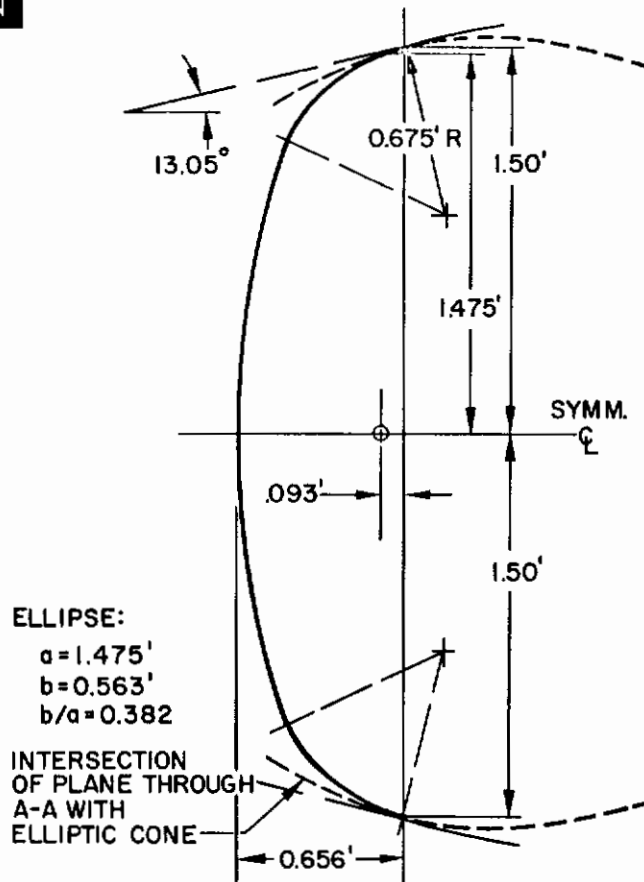


FIGURE 14. BLUNT ELLIPTIC CONE; Three-View



**SIDE ELEVATION**



**SECTION AA**

**FIGURE 15. BLUNT ELLIPTIC CONE NOSE SECTION**

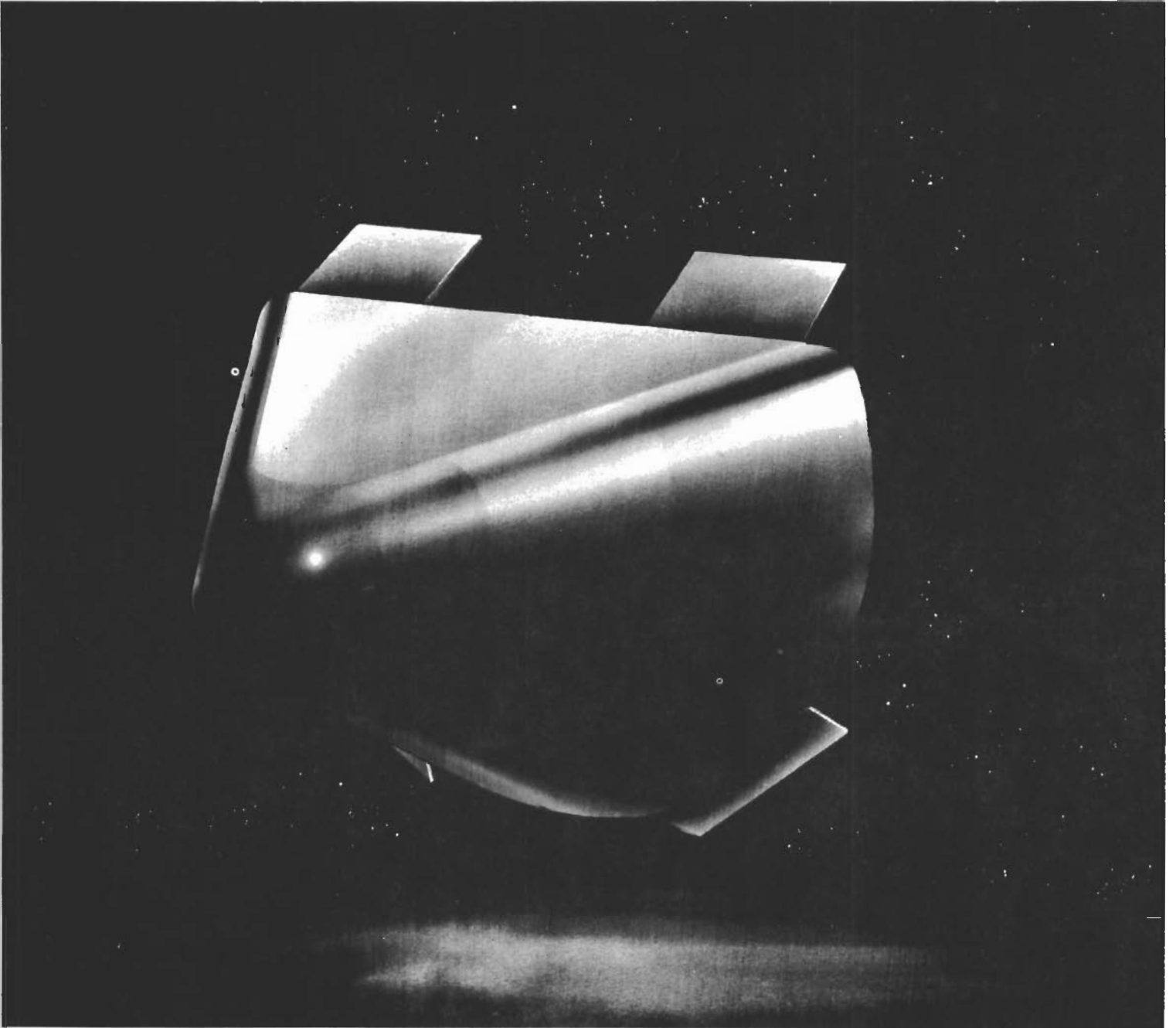


FIGURE 16. BLUNT SEMI-CONE

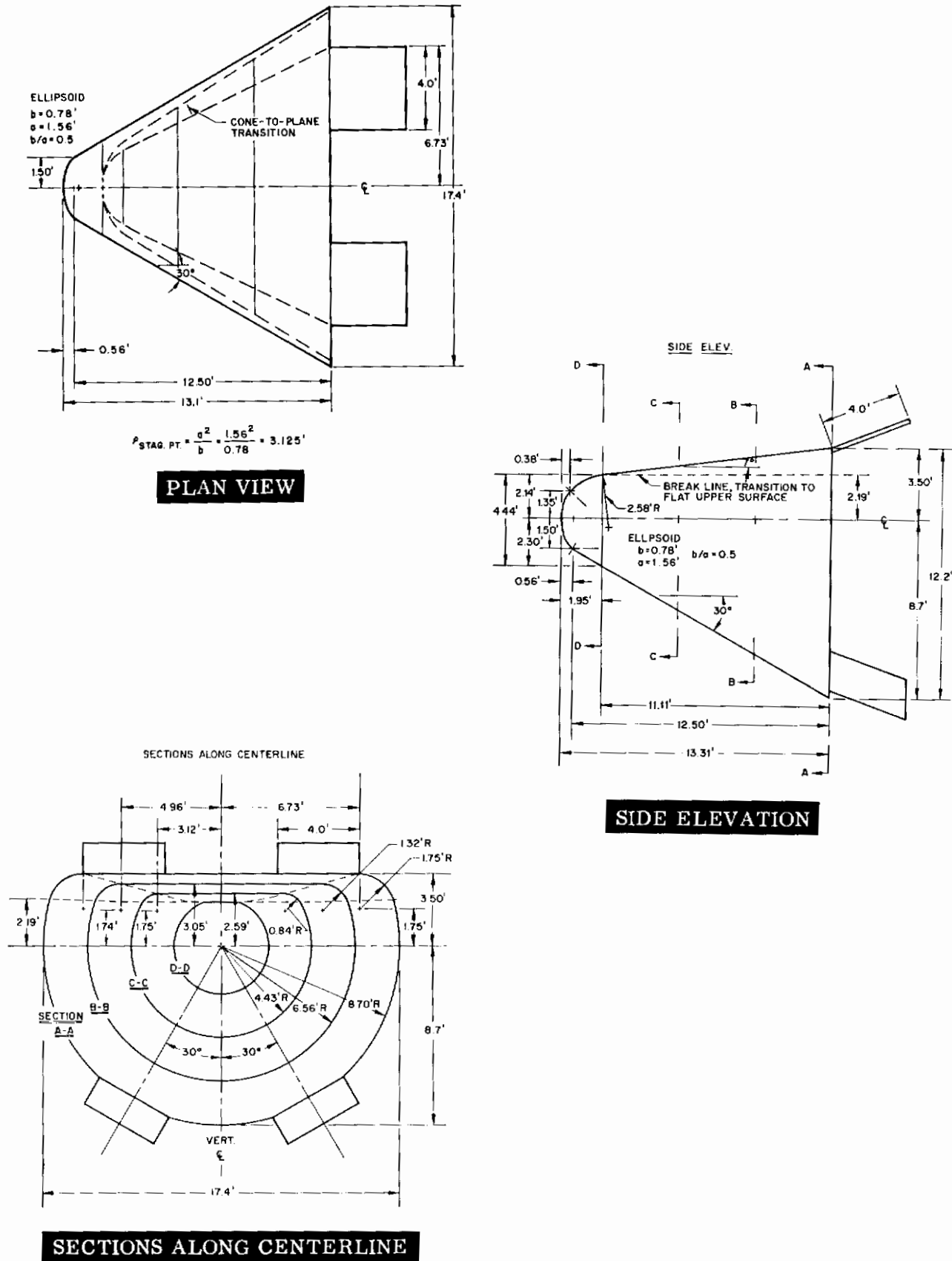


FIGURE 17. BLUNT SEMI-CONE; Three-View



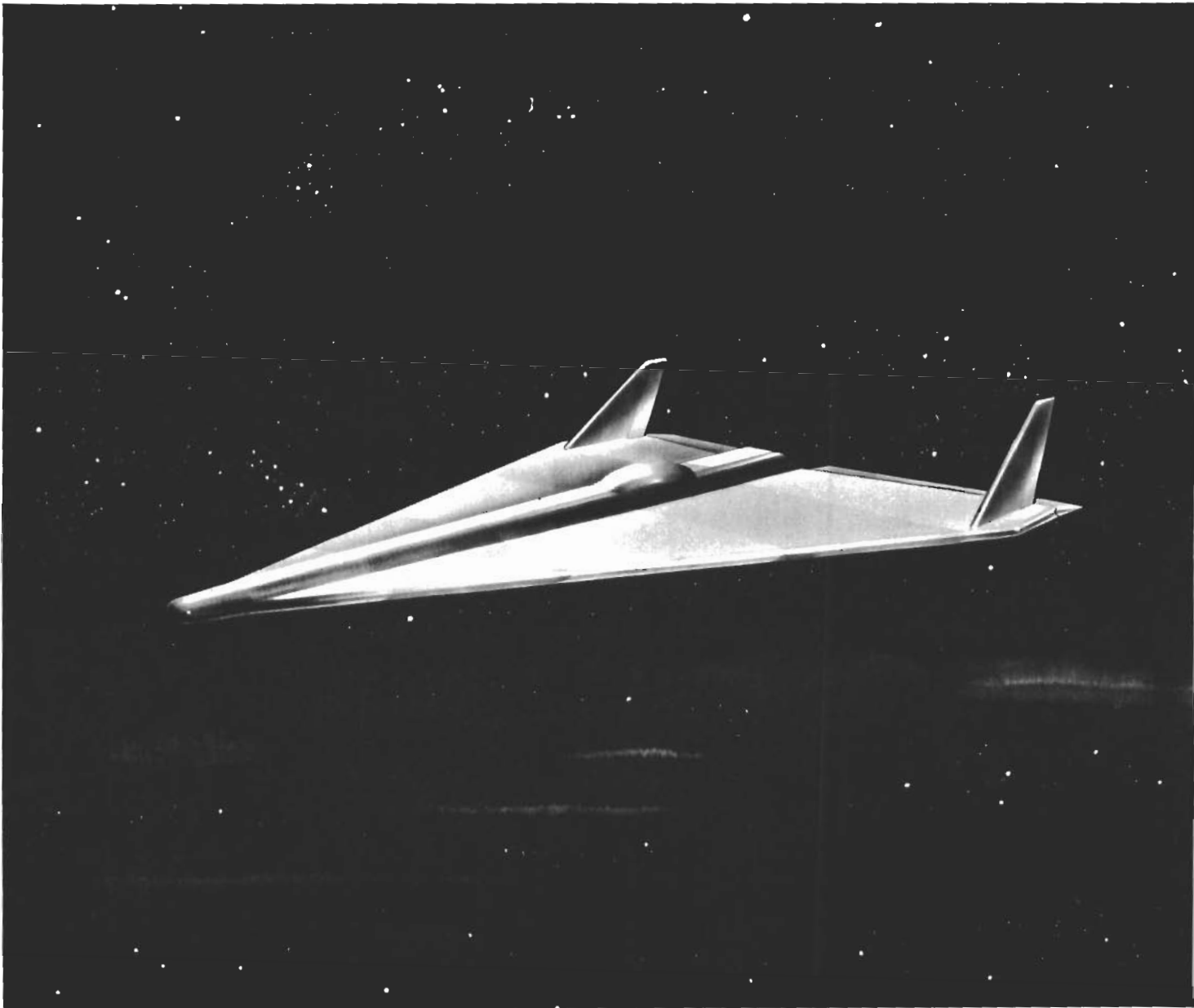


FIGURE 18. LIGHT WING LOADING GLIDER

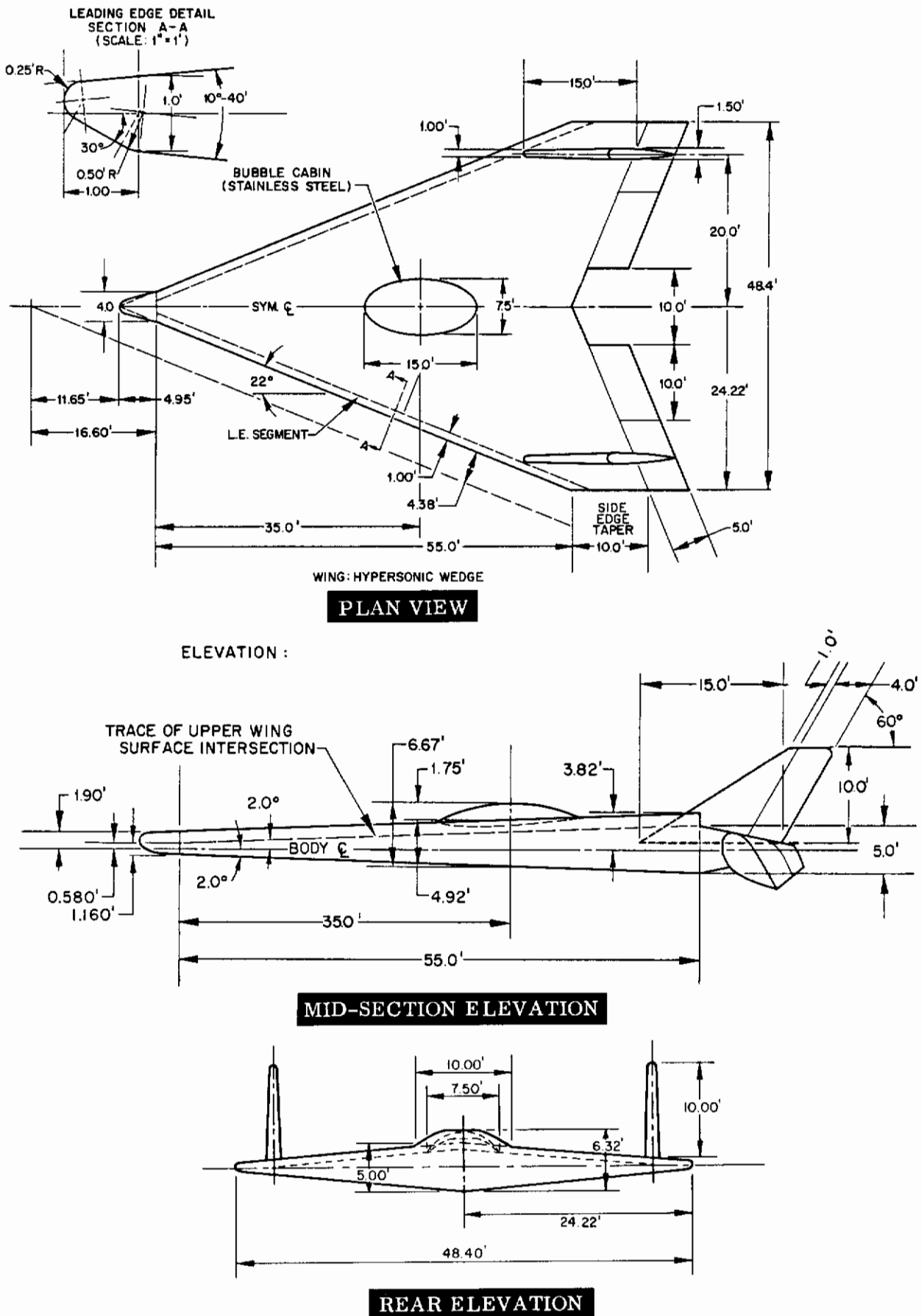


FIGURE 19. LIGHT WING LOADING GLIDER; Three-View

Of the four selected vehicles, only the light glider is subjected to peak heating inputs sufficiently low (approximately 200 Btu/ft<sup>2</sup>-sec) that thin-wall radiation structure at the nose will suffice. Throughout entry, wall temperatures remain below permissible operating temperatures of a combined tungsten shell and thin ceramic protective overlay. The remaining three vehicles, entering at their steepest allowable angles, would be subjected to an initial thermal pulse of amplitude requiring limited protection by thermal absorption (thin ablator or sufficient heat storage capacity) for a short period near peak heating. In this latter system as in the purely radiative, the refractory metal substructure subsequent to peak heating operates under high total heat loads; at high operating temperatures, the nose structure will reradiate a considerable portion of the moderate-level long-duration input heating. Such a thermal protection plan is characterized as an absorptive-radiative system while that pertaining to the light glider is concisely termed a hot-wall or radiative structure.

Each of the configurations, while felt to be representative of early generation super-orbital re-entry craft, is presented to assist in providing realistic overall attachment structure for the candidate frontal sections.

## 2.4 ENTRY TRAJECTORY RELATIONSHIPS

Graphical trajectory information is presented for the four specific classes of lifting re-entry vehicles selected for additional analysis. The altitude-velocity contours, the convective heating history, the dynamic pressure history, and the altitude-velocity history for the medium wing loaded glider ( $L/D = 2.0$ ,  $W/C_{DA} = 200$  psf) are presented in Figures 20 through 23. On the velocity altitude contours (Fig. 20), lines denoting circular orbital and escape velocities are added for reference purposes.

Similar data are presented for the parameters denoting the blunt elliptic cone ( $L/D = 1.0$ ,  $W/C_{DA} = 100$  psf) in Figures 24 through 27. Similarly, Figures 28 through 31 show the trajectory plots for the body which may be described as either a flat or symmetrical cone ( $L/D = 0.5$ ,  $W/C_{DA} = 50$  psf). Finally, similar data are presented for the light wing loaded glider ( $L/D = 2.0$ ,  $W/C_{DA} = 50$  psf) in Figures 32 through 35.

Trajectory information for all vehicles was evaluated within the lifting entry corridor and near the skip-out and deceleration limits. The convective heating history curves (both instantaneous cold-wall rates and cumulative incident heating) pertain to the stagnation point of a 1-foot-radius frontal hemisphere. The correlation equations

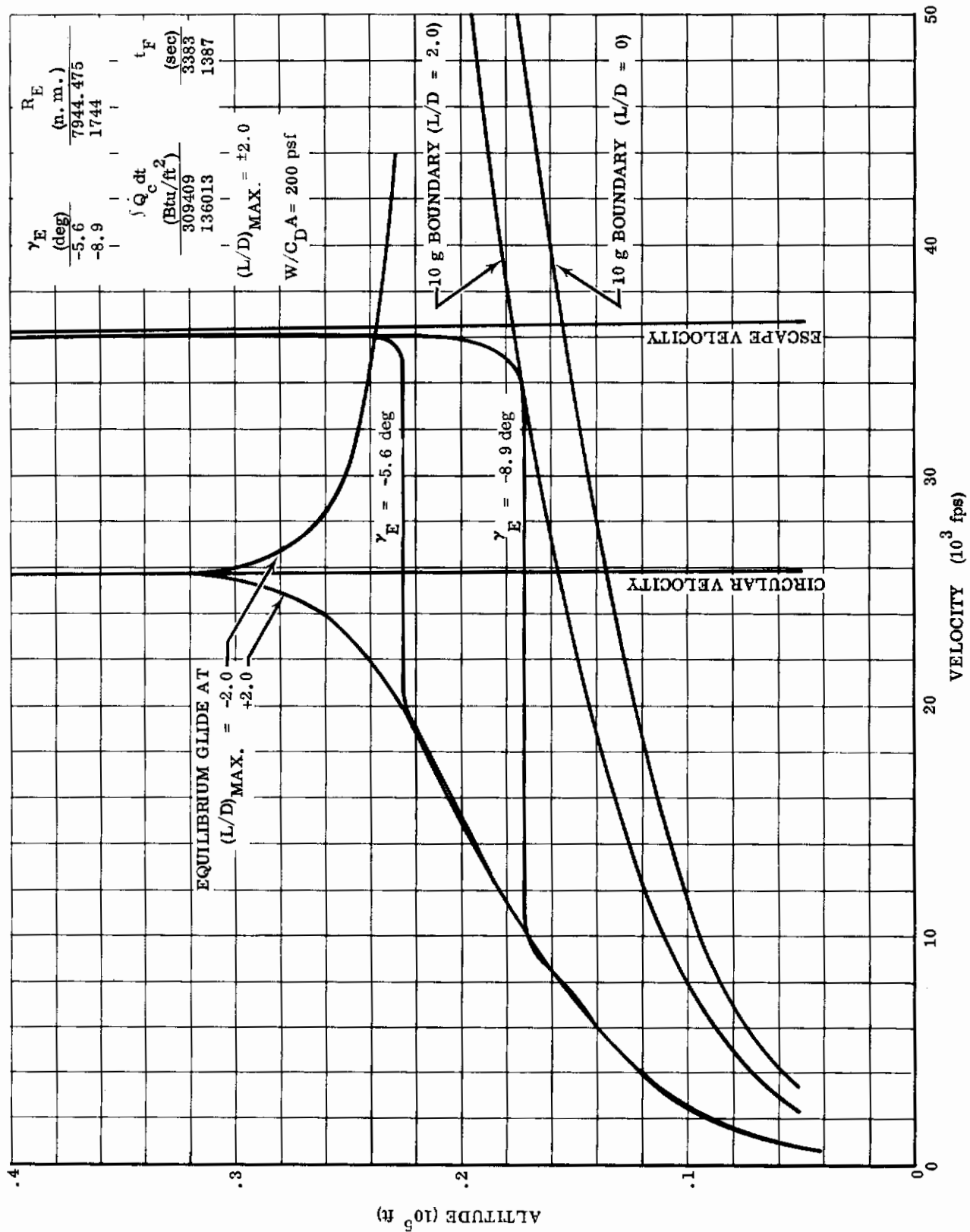


FIGURE 20. ALTITUDE-VELOCITY CONTOURS;  $L/D = 2.0$ ,  $W/C_{D,A} = 200$  psf

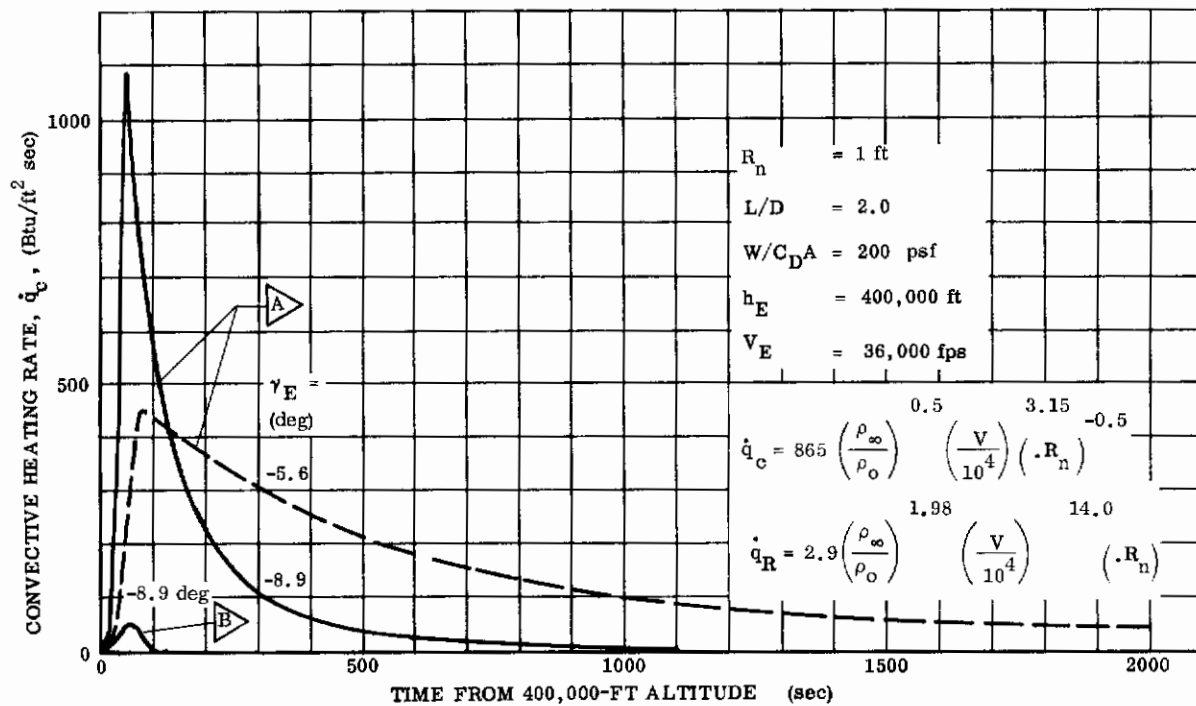


FIGURE 21. CONVECTIVE HEATING HISTORY;  $L/D = 2.0$ ,  $W/C_D A = 200 \text{ psf}$

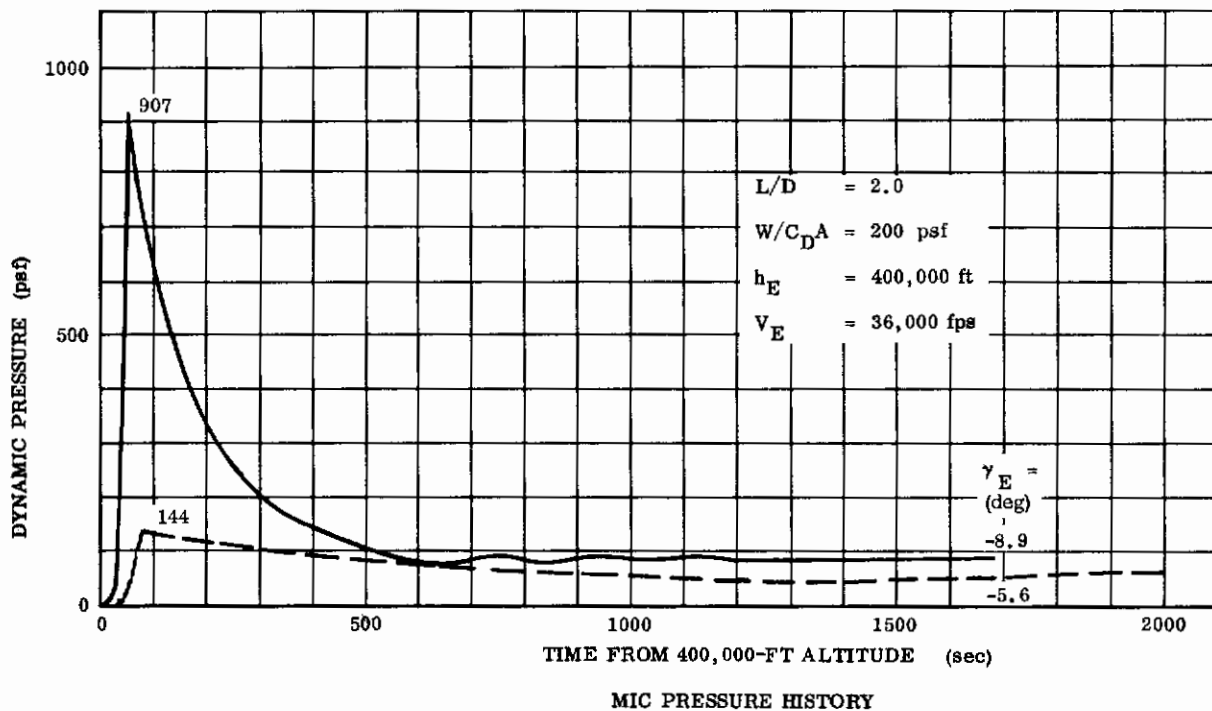


FIGURE 22. DYNAMIC PRESSURE HISTORY;  $L/D = 2.0$ ,  $W/C_D A = 200 \text{ psf}$

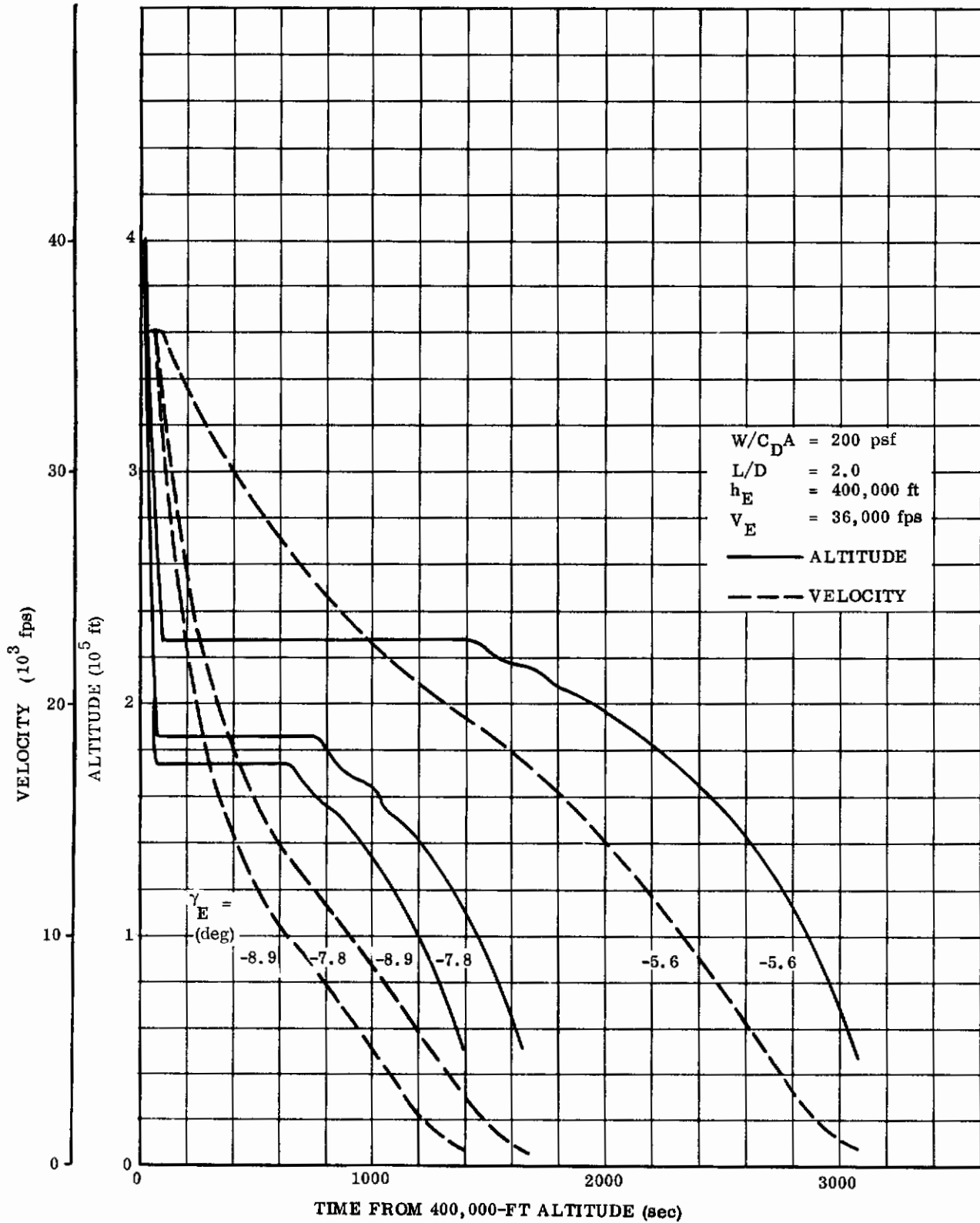


FIGURE 23. ALTITUDE-VELOCITY HISTORY;  $L/D = 2.0$ ,  $W/C_D^A = 200 \text{ psf}$

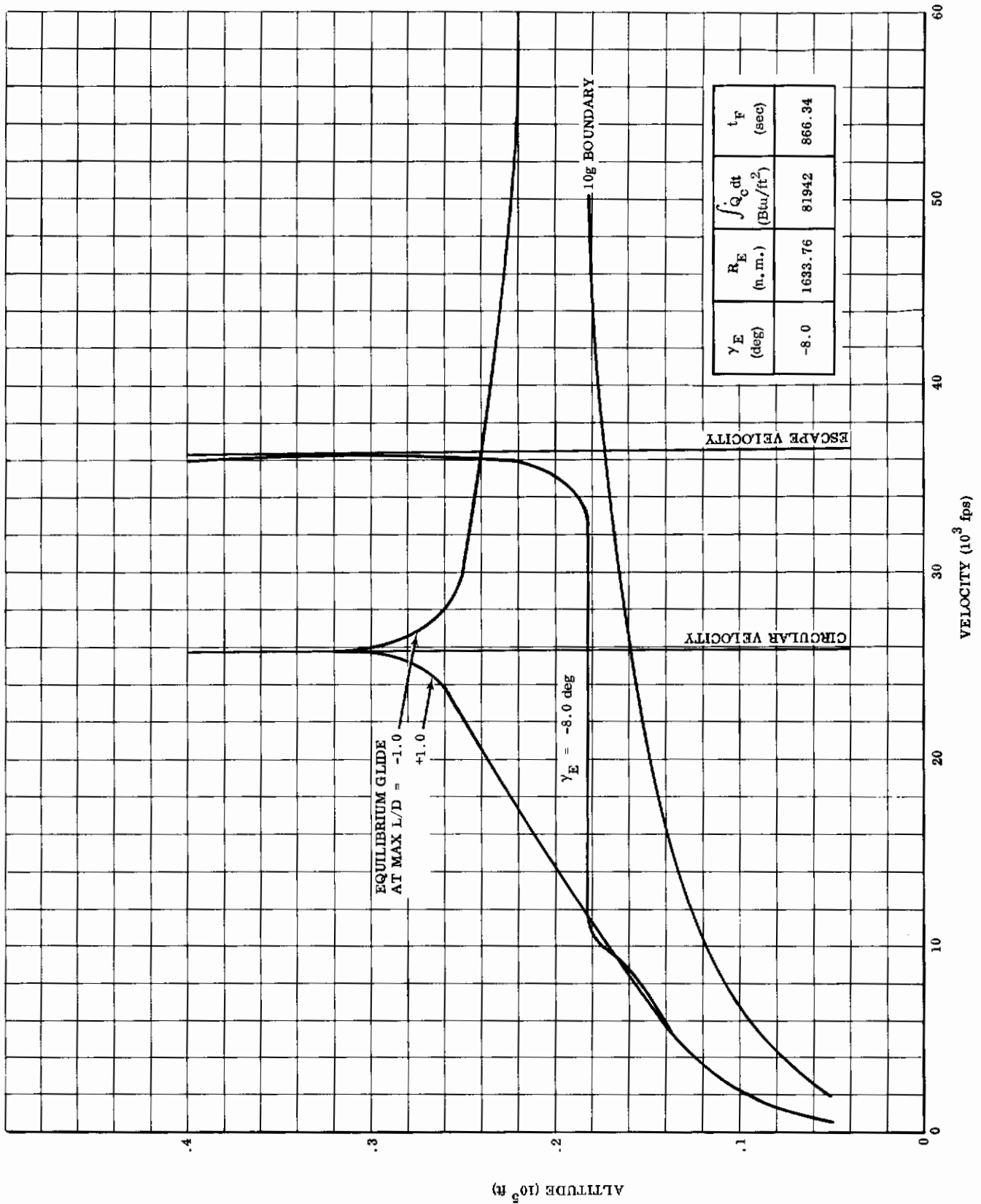


FIGURE 24. ALTITUDE-VELOCITY CONTOURS; L/D = 1.0, W/C<sub>D</sub>A = 100 psf

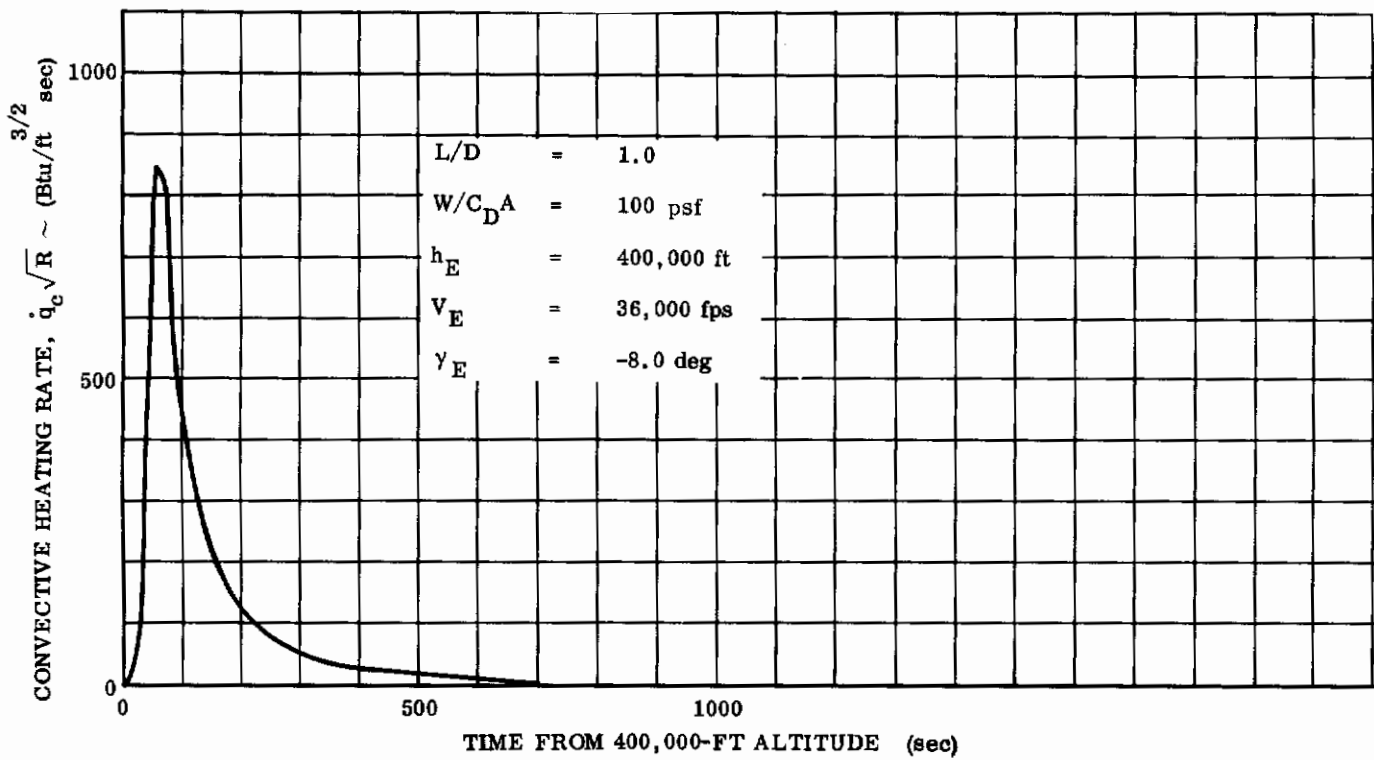


FIGURE 25. CONVECTIVE HEATING HISTORY; L/D = 1.0, W/C<sub>D</sub>A = 100 psf

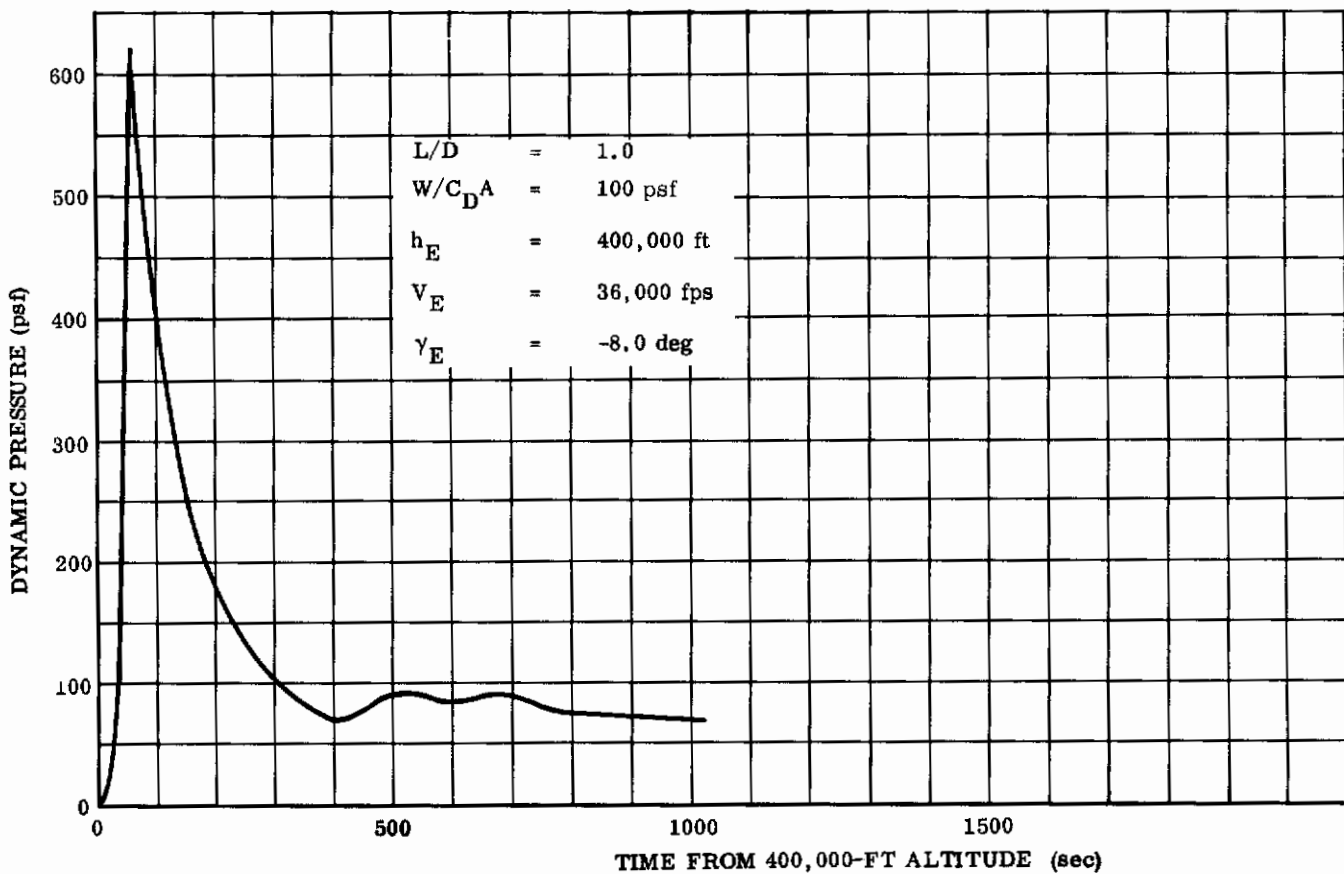


FIGURE 26. DYNAMIC PRESSURE HISTORY; L/D = 1.0, W/C<sub>D</sub>A = 100 psf



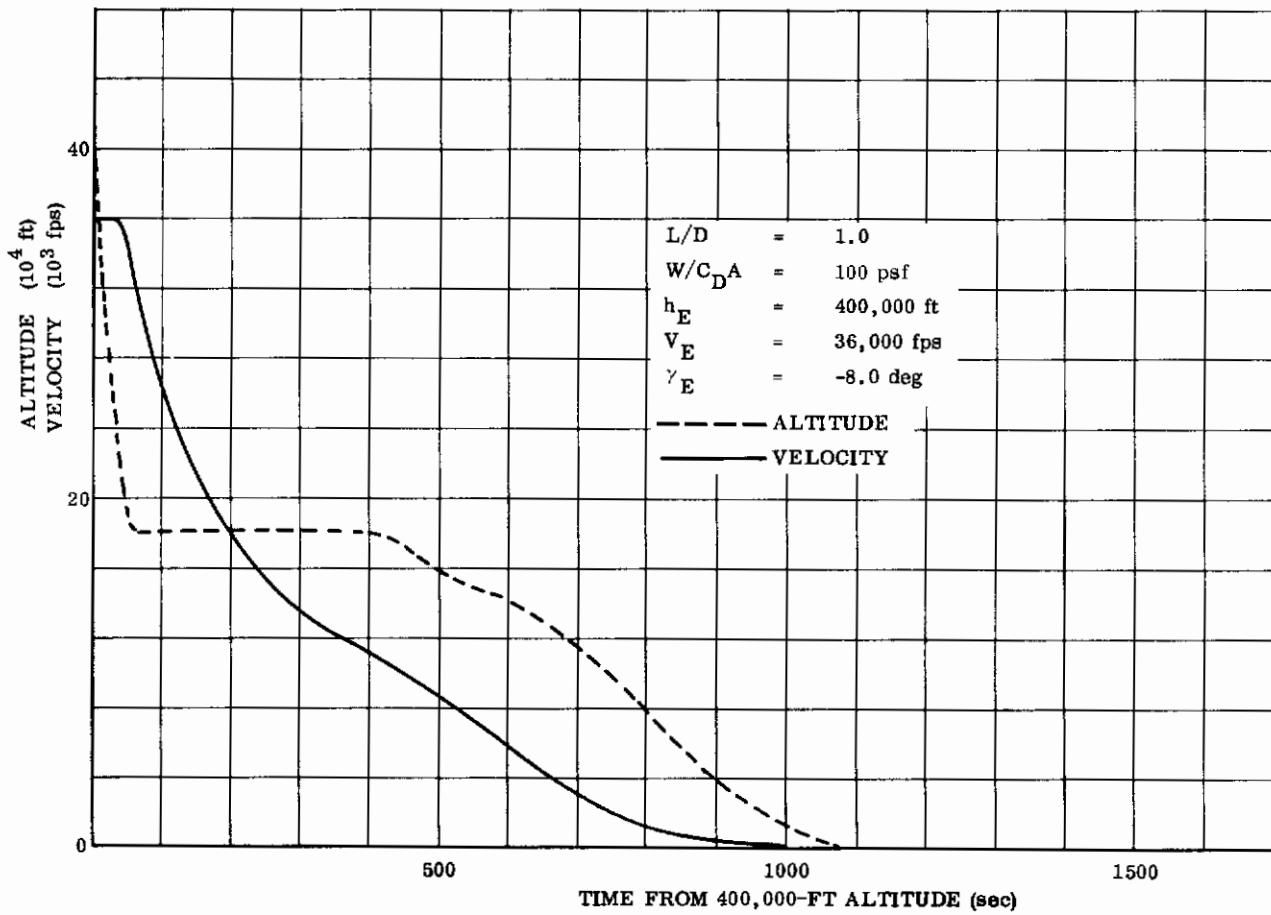


FIGURE 27. ALTITUDE-VELOCITY HISTORY;  $L/D = 1.0$ ,  $W/C_{D^A} = 100$  psf

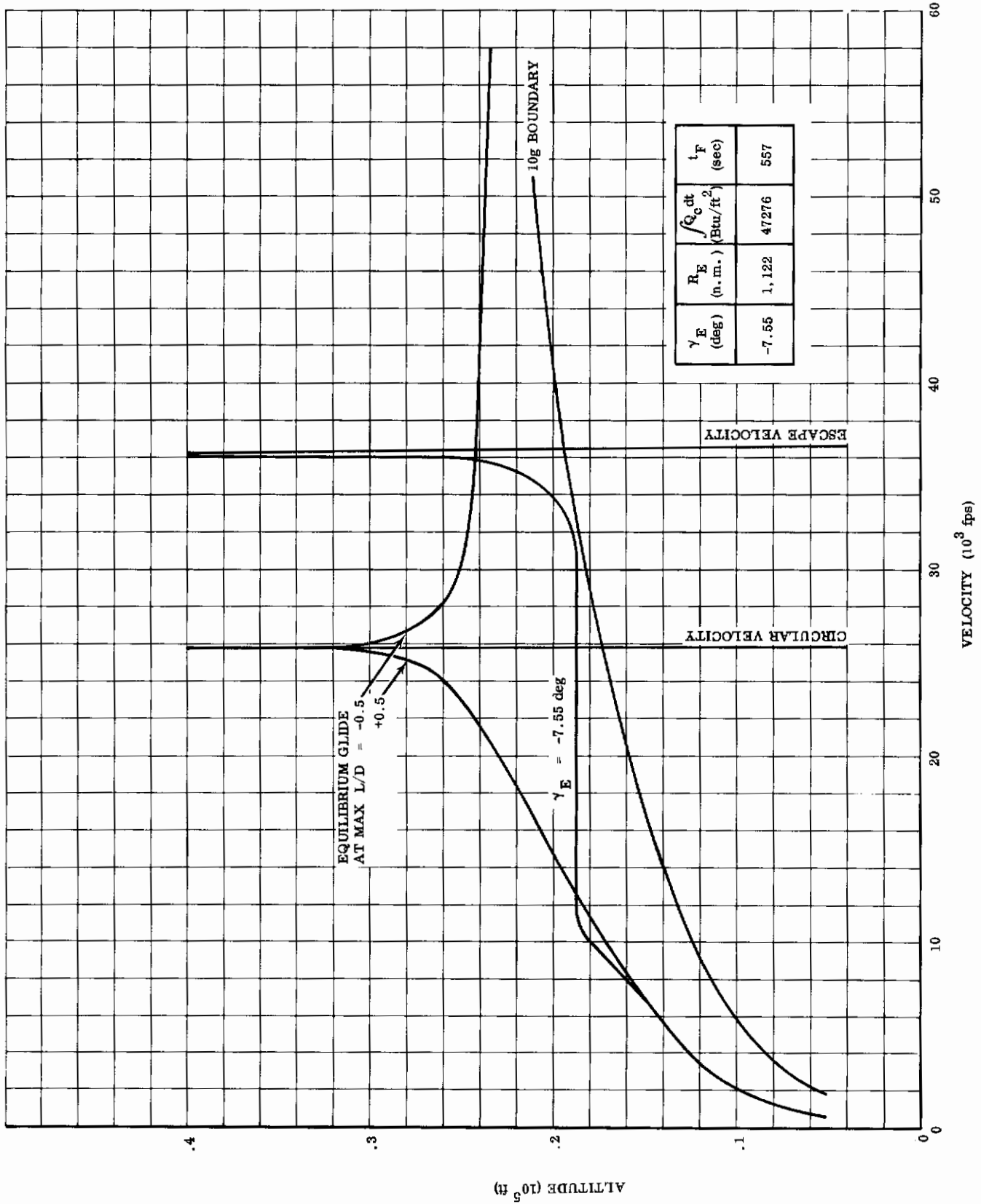


FIGURE 28. ALTITUDE-VELOCITY CONTOURS; L/D = 0.5, W/C<sub>D</sub>A = 50 psf

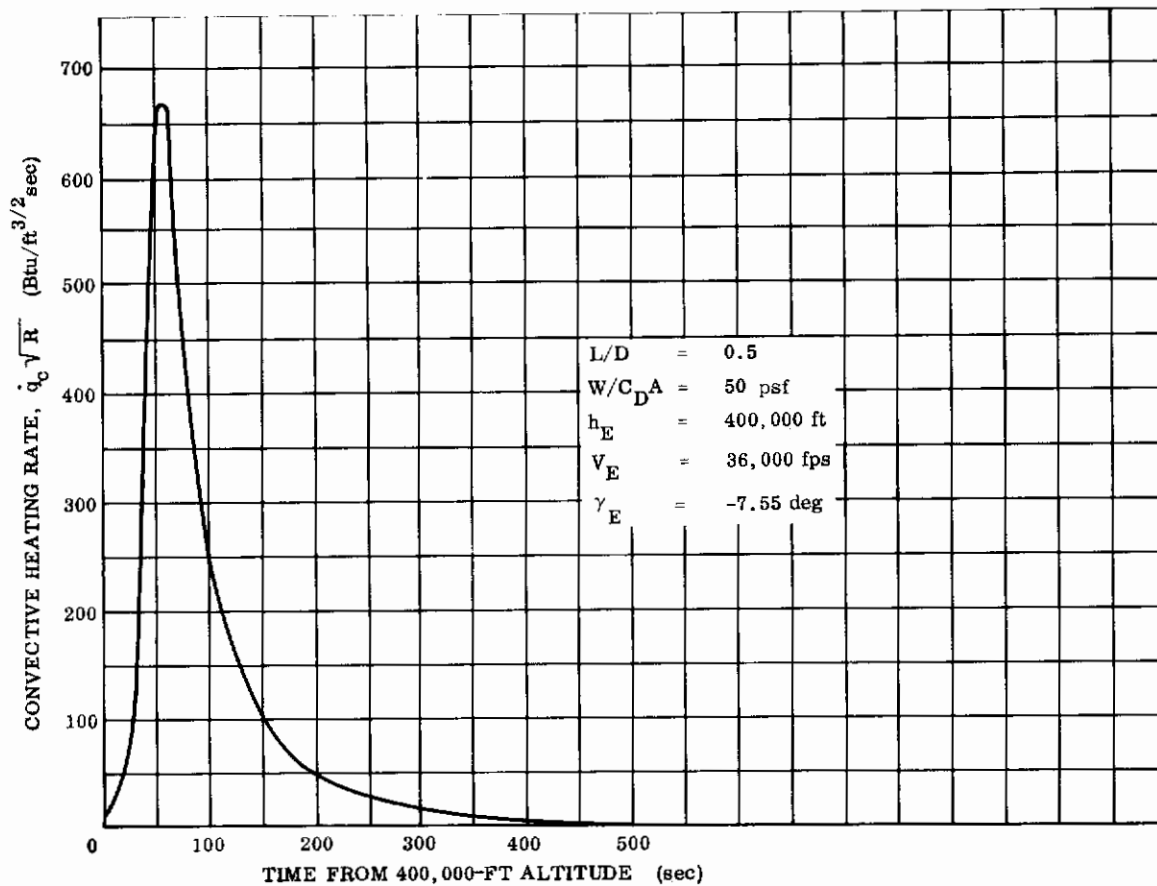


FIGURE 29. CONVECTIVE HEATING HISTORY; L/D = 0.5, W/C<sub>DA</sub> = 50 psf

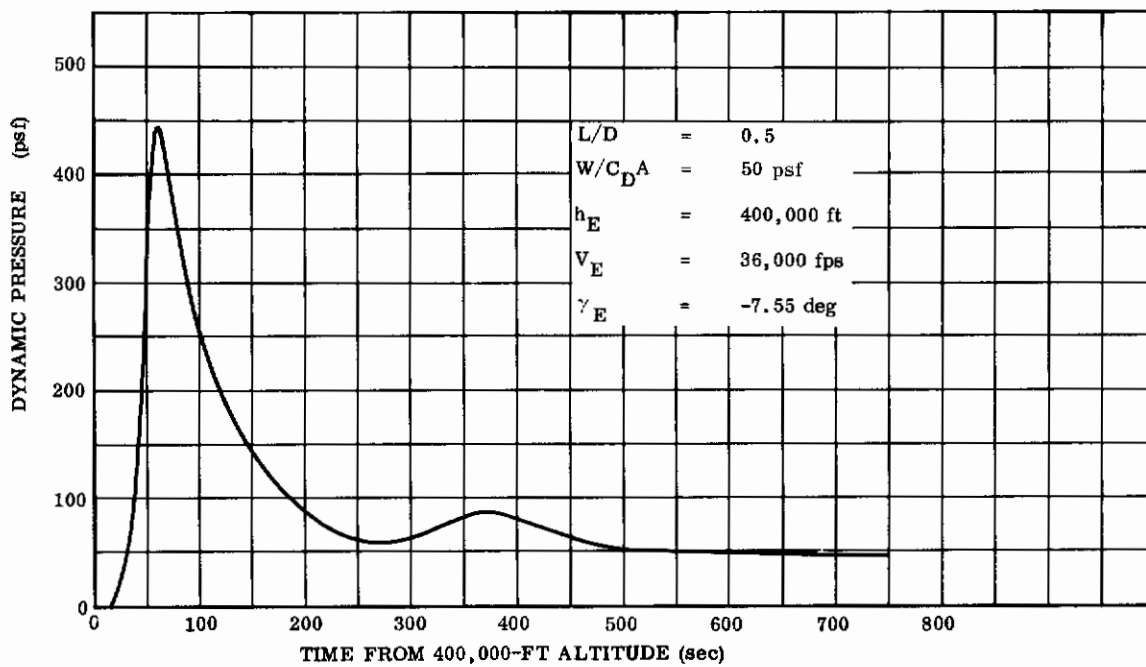


FIGURE 30. DYNAMIC PRESSURE HISTORY; L/D = 0.5, W/C<sub>DA</sub> = 50 psf

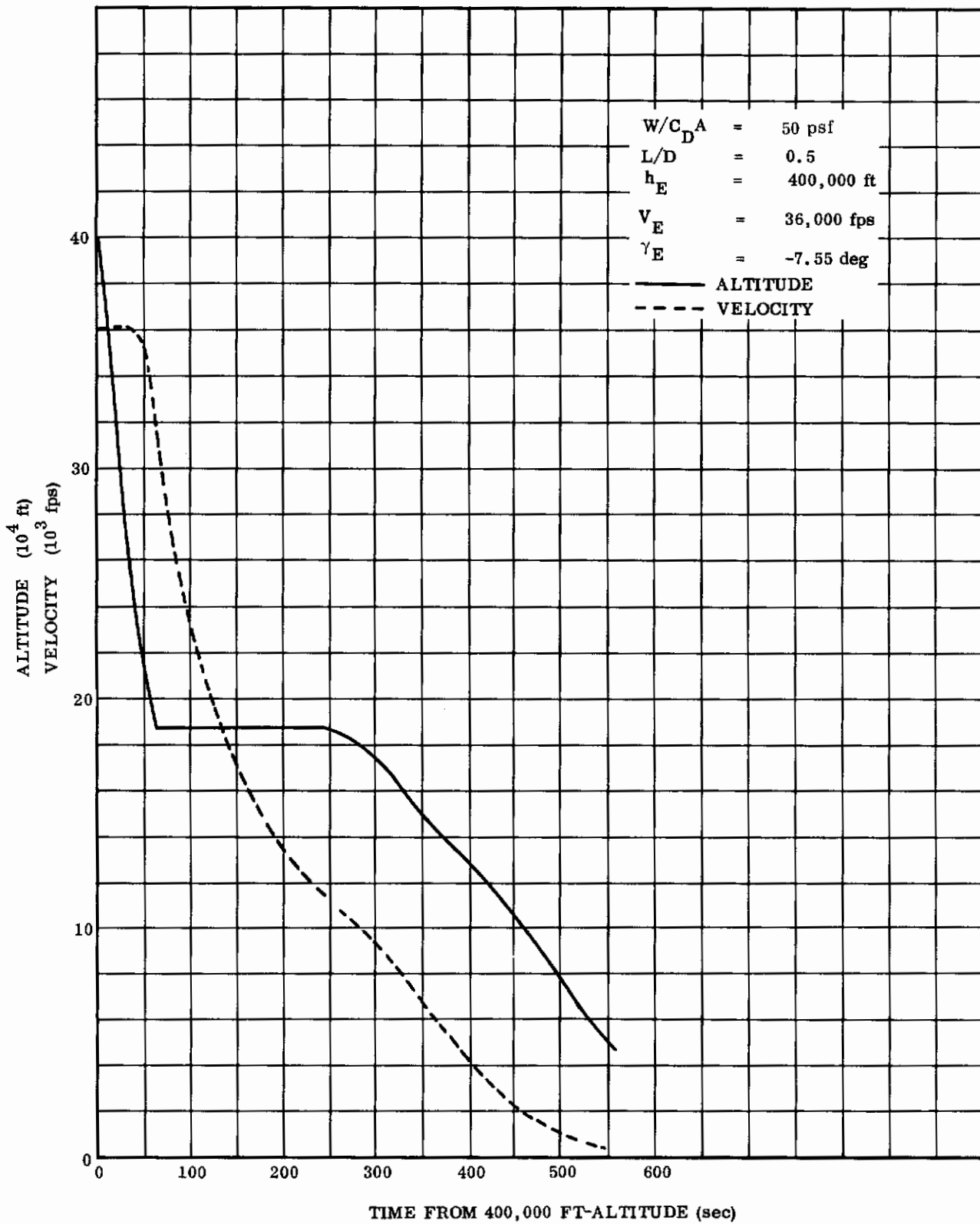


FIGURE 31. ALTITUDE-VELOCITY HISTORY; L/D = 0.5, W/C<sub>D</sub><sup>A</sup> = 50 psf

accompanying Figure 21 are for convective and radiative incident heat flux. The expression for cold-wall convective rate is in a slightly altered form but corresponds identically with that given in Section 2.1. The comparatively insignificant gas cap radiative flux, also shown, is about 5 percent of the peak magnitude of the convective ( $R_n = 1$  ft), as would be expected for lifting trajectories of low  $W/C_D A$  which do not penetrate deeply into the atmosphere during initial descent. The supplemental correlation equation presented in Figure 21 for estimating stagnation point radiant energy transfer is derived in Reference 5. The specific constant shown pertains to an ellipsoidal nose cap having an aspect ratio ( $b/a$ ) approximately equal to 0.4.

The winged glider peak stagnation heating rate of 1100 Btu/ft<sup>2</sup>-sec was higher than that for the other three selected vehicles. The severe heat pulse (greater than 200 Btu/ft<sup>2</sup>-sec) is maintained for over 3 minutes. The dynamic pressure variation for free stream conditions (Fig. 22) was derived for entry along the upper and lower bounds of the permissible flight corridor.

The trajectory data for the blunt elliptic cone are presented in Figures 24 through 27, and for the blunt cone and semi-cone in Figures 28 through 32. Stagnation point convective heating rates were lower for these vehicles than for the winged glider, even though the  $L/D$  ratio was lower in both cases. The strong dependence of stagnation point maximum heating rate on  $W/C_D A$  is demonstrated by this fact.

Similar trajectory data depicting entry conditions for the light glider ( $L/D = 2.0$ ,  $W/C_D A = 50$  psf) are shown in Figures 32 through 35. The dashed curves superimposed on Figure 32 denote various levels of cold wall convective heating rate. The shallow trajectory becomes tangent to the heating curve representing a flux of 200 Btu/ft<sup>2</sup>-sec. A simple hot-wall structure should prove adequate to resist the environment associated with this particular trajectory. The entry path is such that deceleration occurs under low-density conditions at high altitude, dependent upon the vehicle's light weight, large wing area, and shallow flight path angle. To be emphasized, however, is the fact that realization of such an exceedingly light wing loading as 5 psf, if possible in a rigid structure, would be most challenging from a design standpoint. Of the four representative lifting entry bodies, the winged glider, the blunt elliptic cone, the semi-cone, and the light glider, only the light glider required no supplemental absorptive thermal protection during peak nose heating.

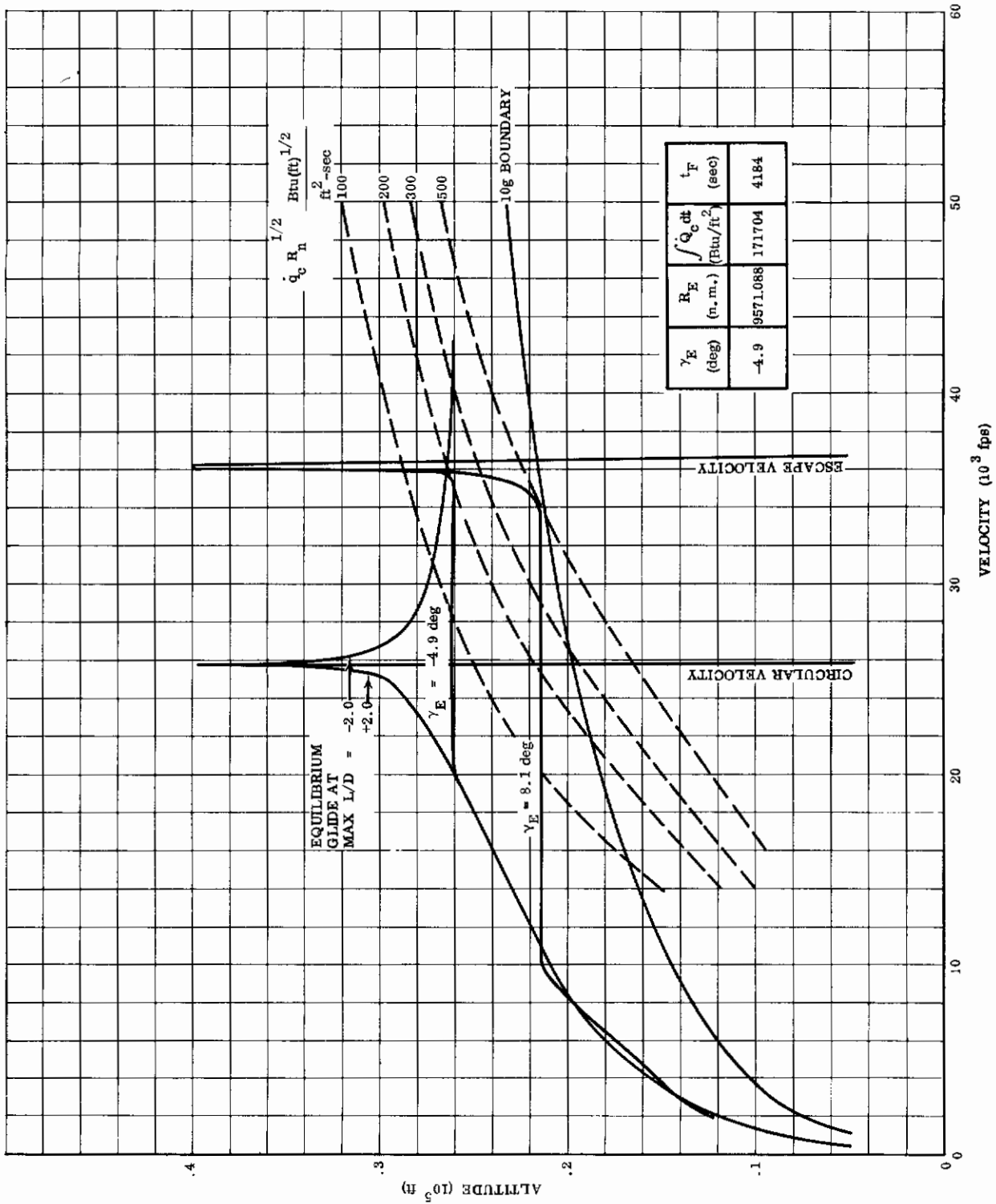


FIGURE 32. ALTITUDE-VELOCITY CONTOURS; L/D = 2.0, W/C<sub>D</sub>A = 50 psf

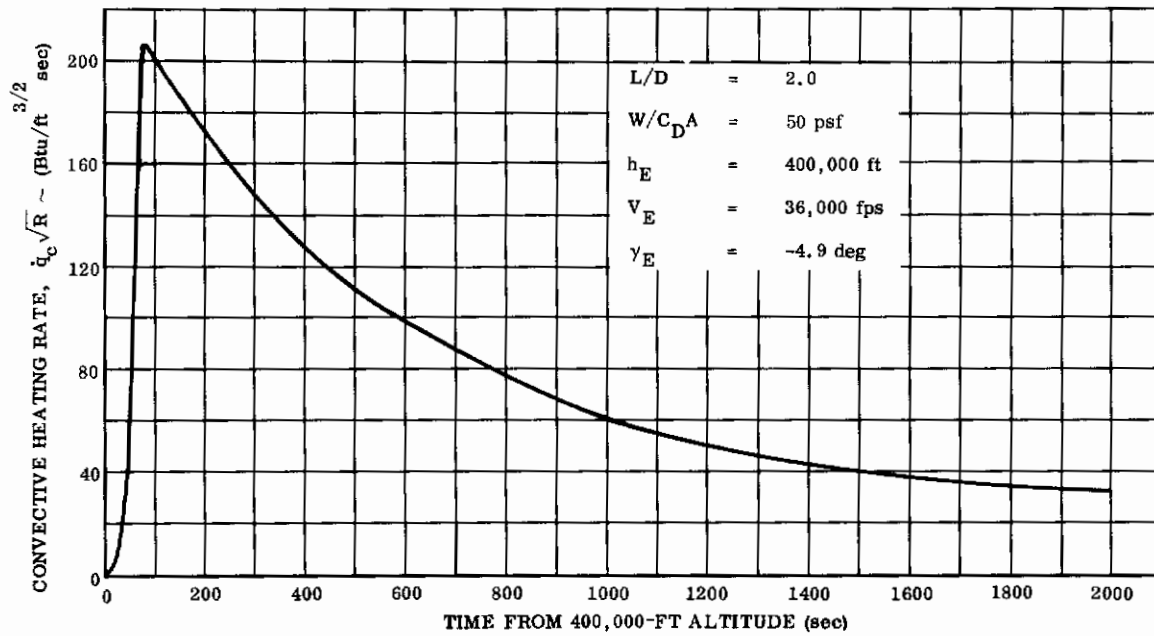


FIGURE 33. CONVECTIVE HEATING HISTORY;  $L/D = 2.0$ ,  $W/C_{D^A} = 50$  psf

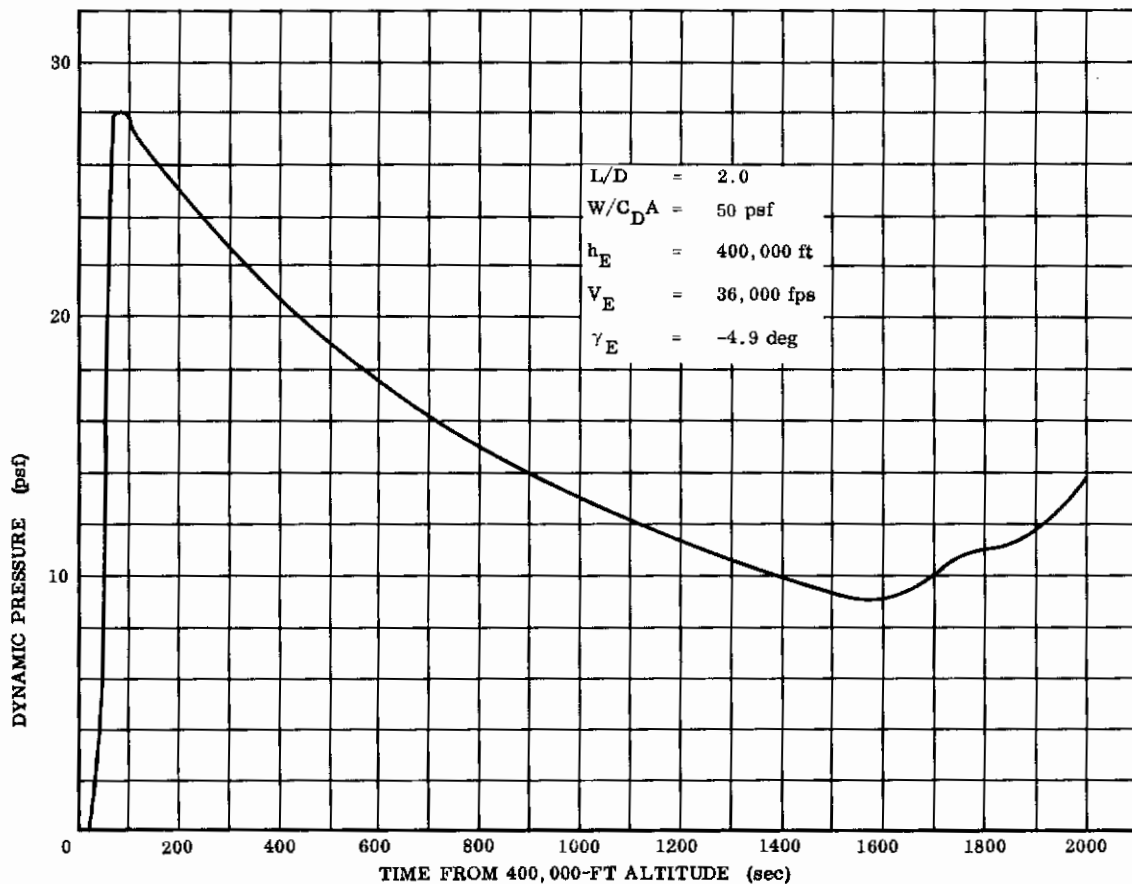


FIGURE 34. DYNAMIC PRESSURE HISTORY;  $L/D = 2.0$ ,  $W/C_{D^A} = 50$  psf

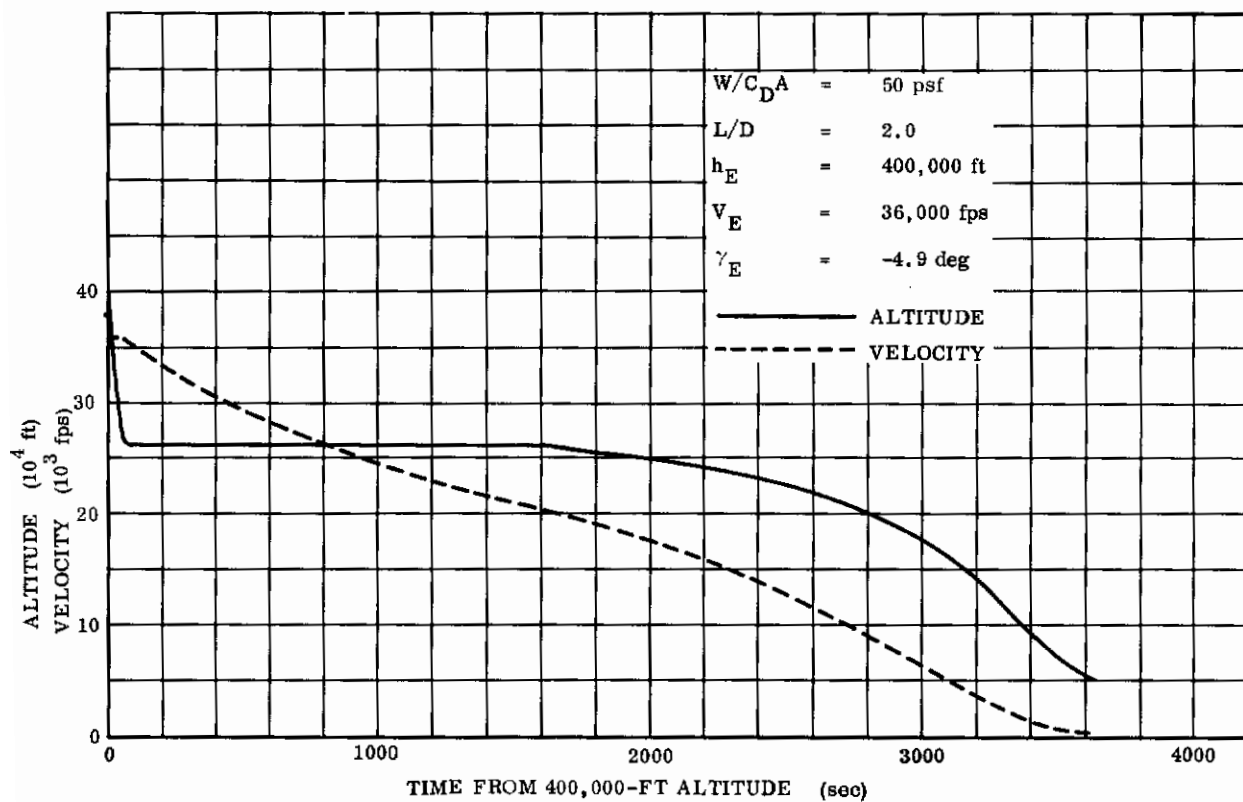


FIGURE 35. ALTITUDE-VELOCITY HISTORY;  $L/D = 2.0$ ,  $W/C_{D^A} = 50$  psf



### III. THERMAL INVESTIGATIONS

#### 3.1 GENERAL CONSIDERATIONS

Having selected representative lifting vehicles for parabolic entry into the earth's atmosphere, the transient thermal problem was next investigated for different nose geometries and material systems. Important considerations included defining resultant temperature responses and temperature distributions throughout the structure and determining material degradation or recession. Parametric studies, including broad ranges of anticipated thermo-physical properties of materials, were conducted for both absorptive and dissipative thermal protection systems, as well as for required combinations of the two. One- and two-dimensional transient heat conduction solutions included, where applicable, moving boundaries and variable thermal diffusivity.

Structurally simplest and lightest in weight was the thin, hot-wall nose section of the light glider ( $L/D = 2.0$ ,  $W/C_{DA} = 50$  psf,  $\gamma_E = -4.9$  degrees). Successful usage of this system hinged upon achieving an efficient outer radiator surface to dissipate the prolonged thermal pulse; devising a suitable high-temperature inner insulator to block the rearward flow of heat from the back surface of the refractory metal nose shell; and retention of a thin, brittle protective overlay on the refractory shell.

The other nose section given primary consideration was that of the winged glider ( $L/D = 2.0$ ,  $W/C_{DA} = 200$  psf,  $\gamma_E = -8.9$  degrees). Transitory thermal absorption capability was required for this particular frontal body as it would be subjected to the highest peak heat rates, sufficient to melt and oxidize any thin-wall refractory structure, even with a most optimum total surface emittance. Such capability could be provided by various ablative, heat sink, or transpirative systems.

Since a combination of the two winged gliders typified or encompassed a range of hyperthermal structure characteristics, the ensuing frontal section heat flow studies concentrated upon the basic shell configuration common to both (Fig. 12). The basic body was expected to endure an environment, in one instance, for which a hot-wall

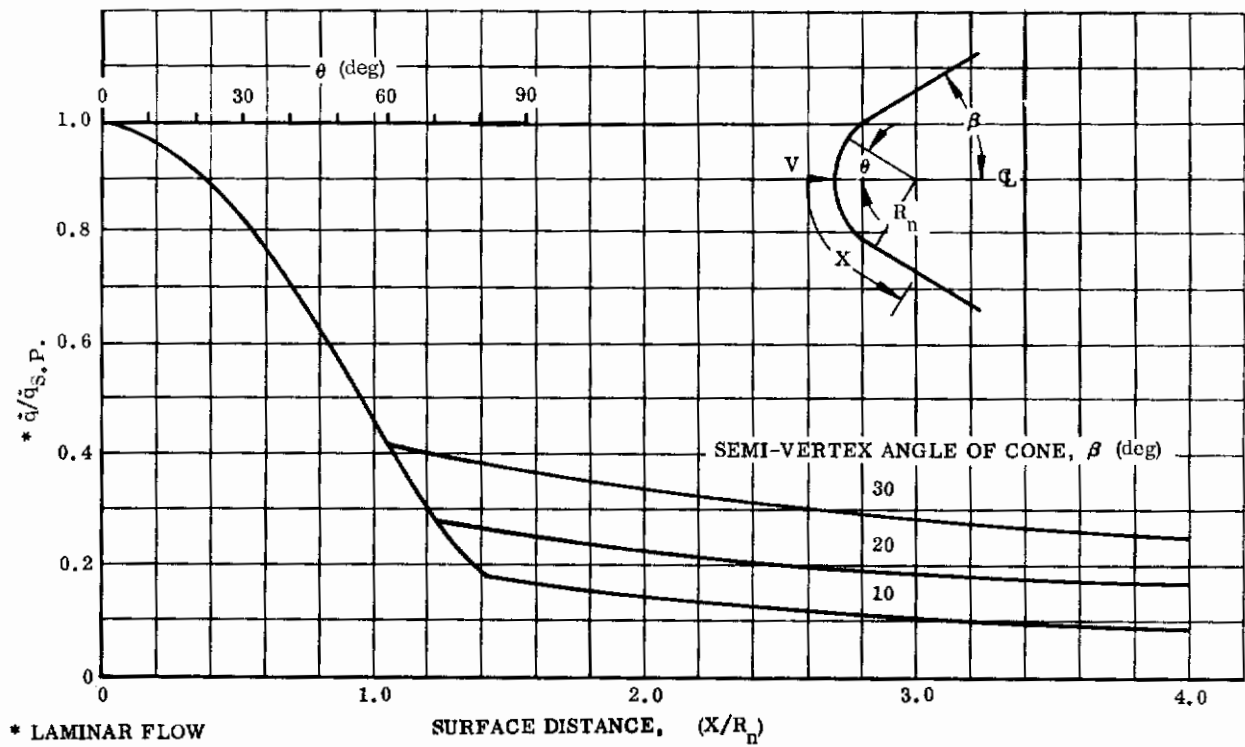


FIGURE 36. HEAT TRANSFER DISTRIBUTION; Hemisphere-Cones

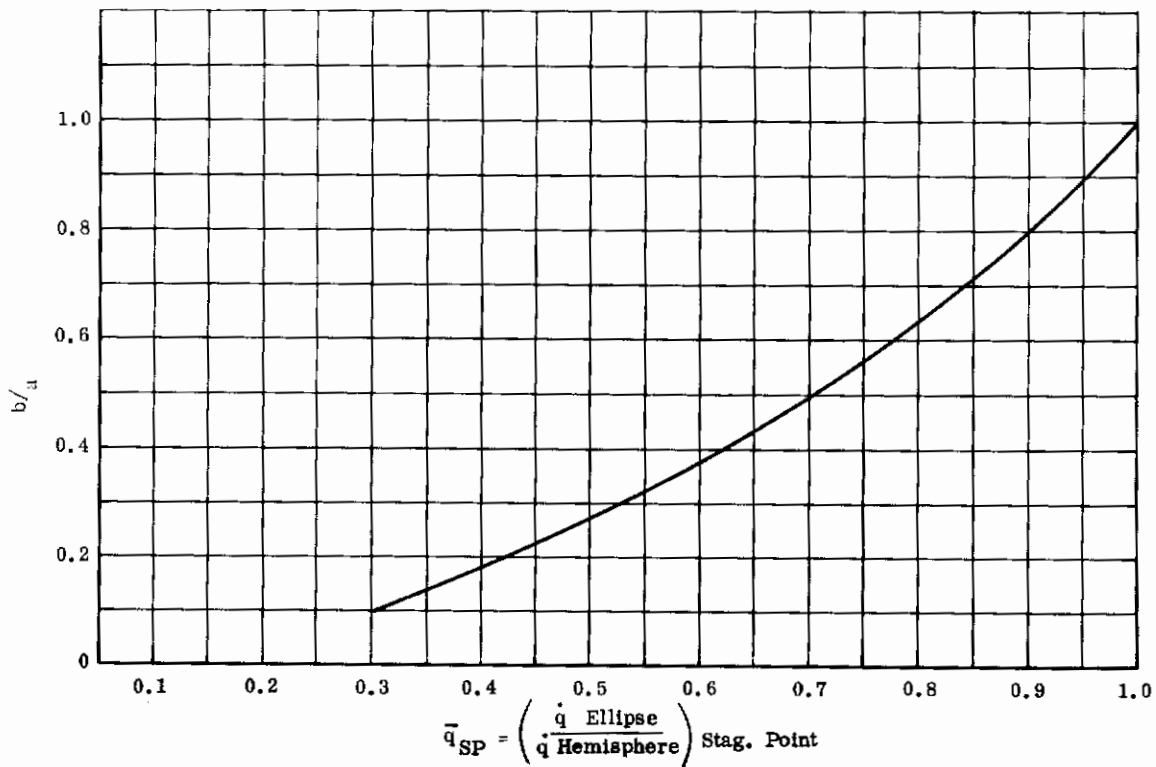


FIGURE 37. EFFECT OF NOSE BLUNTNES ON STAGNATION POINT CONVECTIVE HEAT PULSE; Laminar Boundary Layer

radiative structure would suffice and, in the other instance, a peak heating environment requiring a combined absorptive-radiative approach. The configuration was roughly an oblate ellipsoid-cone, the ellipsoidal cap being a body of revolution with a rotationally symmetric temperature-load distribution based upon the 20-degree drooped mounting which aligned the cap with the velocity vector throughout entry flight. The skirt region was an unsymmetric transition section permitting nose section attachment to the respective vehicles; however, it approximated a frustum of a cone. For simplicity of design and ease of fabrication, an unstiffened (monocoque) tungsten alloy shell of a uniform 0.040-inch thickness was selected as the standard substrate for the thermal analyses. The shell thickness requirement was determined from structural strength and buckling analyses (Section V).

### 3.1.1 Incident Heating Distribution About Various Frontal Shapes

Preliminary design values of heat distribution for hemisphere-cones based upon heat rate at the stagnation point are presented in Figure 36. Distance aft of the stagnation point is normalized with respect to the nose radius. The conical afterbody values pertain to shapes having semi-vertex angles of 10, 20, and 30 degrees. A Newtonian pressure distribution and laminar flow conditions about the body were assumed.

The significance of nose bluntness upon convective heat transfer was also determined. Stagnation point incident heating variation and the meridional convective heating distribution for a family of ellipsoids bounded by a hemisphere are shown in Figures 37 and 38. The analysis is based upon existence of a laminar boundary layer in the domain depicted. Higher convective rates due to flow transition were investigated subsequently for selected configurations.

The variation in stagnation point heating appears in Figure 37. This variation indicates the comparative relief for more blunt shapes versus the hemisphere. The result is based upon an explicit set of solutions to the Lees' integral (Ref. 6) for various ellipsoidal shapes, a half-power viscosity-temperature dependence, Newtonian-Prandtl-Meyer pressure distribution, and an isentropic exponent ( $\gamma_e$ ) assumed as 1.2. For an elliptic nose with a ratio of semi-minor to semi-major axis of 0.3, the heat transfer is reduced to approximately half that for a hemispherical frontal section with radius equal to semi-major axis. In addition to reducing the peak absolute temperatures by nearly 12 percent, the heat transfer distribution over the nose surface is nearly uniform

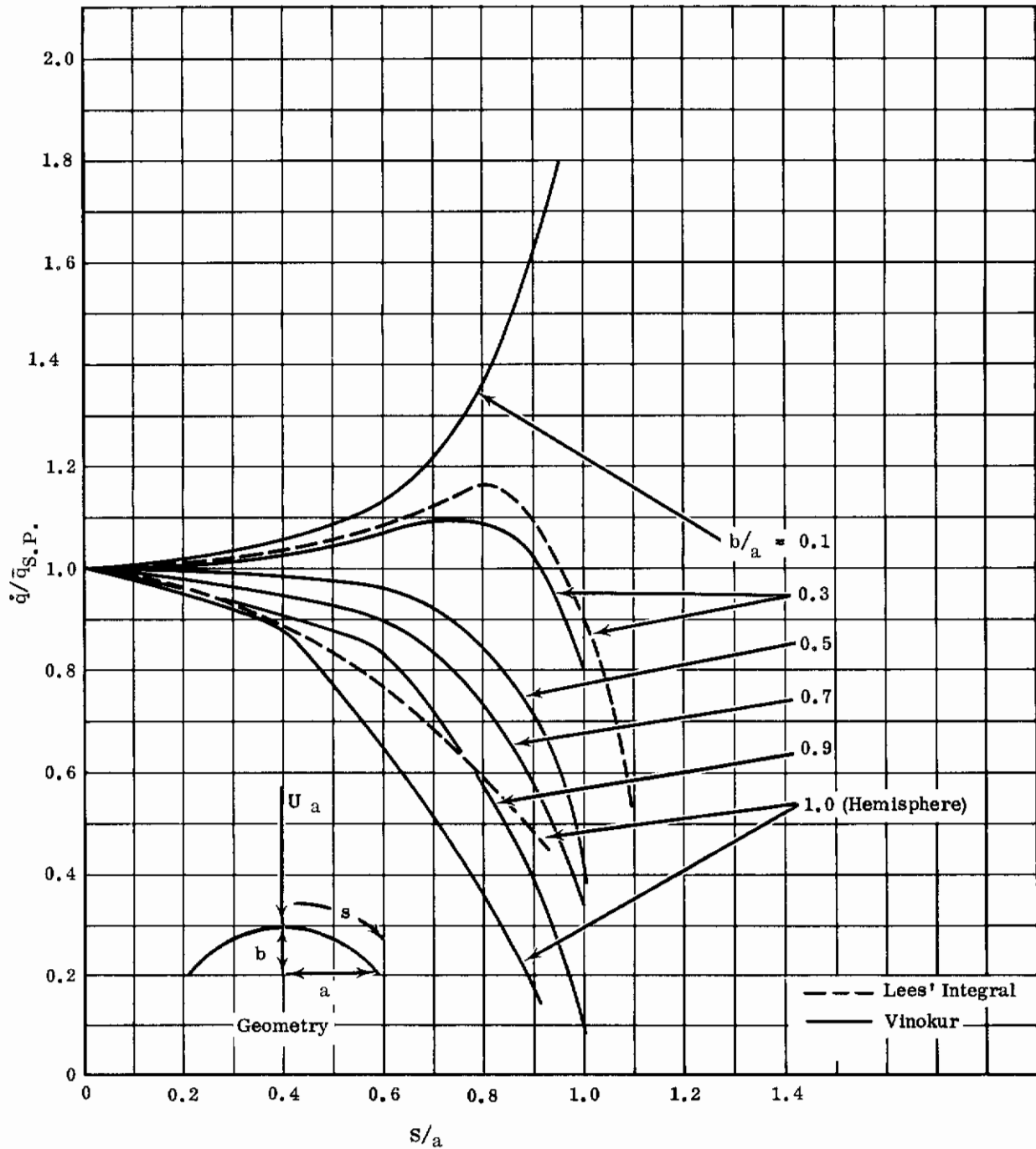


FIGURE 38. EFFECT OF NOSE BLUNTNESS ON DISTRIBUTION OF CONVECTIVE HEAT PULSE; Laminar Boundary Layer

except in the shoulder region (Fig. 38). The Newtonian-Prandtl-Meyer assumption to the pressure distribution, while reasonable for hemispheres, becomes less valid for more blunt configurations. A corrective procedure was established, utilizing actual flight pressure distributions and modifying the corresponding contribution to the Lees' integral. This work was accomplished and is described in detail in Reference 7.

Further comparisons were based upon a theoretical analysis of Vinokur (Ref. 8). This solution involved a constant density shock layer and was thus limited to the subsonic domain (bounded by the shock wave and the locus of sonic points for the particular configuration). The Vinokur distribution is known to be highly accurate for very blunt bodies ( $b/a \rightarrow 0$ ) where the Newtonian assumption loses all semblance of validity. As an illustration, the curve for  $b/a = 0.3$  (Fig. 38) obtained from the Lees' integral method using flight-test pressure distributions compares well with the corresponding Vinokur solution. Considerably wider variation is noticed at the  $b/a$  value of 1.0; however, the Vinokur distribution is not intended to supplant the Newtonian for the hemisphere or near-hemisphere. For the blunt shapes, the Vinokur distribution was utilized, while for near hemispheres the LMSC-modified Lees' integral was applied.

The integral depicted in Reference 7 has the form, for the purposes of this analysis:

$$\frac{\dot{q}}{\dot{q}_{SP}} = \frac{1}{2} \left( \frac{R_{EFF}}{a} \right)^{1/2} \left( \frac{\gamma_E}{\gamma_E - 1} \right)^{1/4} \frac{\left( \frac{P_E}{P_0} \right)^{\frac{5\gamma_E + 1}{6\gamma_E}} \left[ 1 - \left( \frac{P_E}{P_0} \right)^{\frac{\gamma_E - 1}{\gamma_E}} \right]^{1/2} \left( \frac{r}{a} \right)}{\left[ \int_0^{5/a} \left( \frac{P_E}{P_0} \right)^{\frac{5\gamma_E + 1}{6\gamma_E}} \left[ 1 - \left( \frac{P_E}{P_0} \right)^{\frac{\gamma_E - 1}{\gamma_E}} \right]^{1/2} \left( \frac{r}{a} \right)^{1/2} d \left( \frac{r}{a} \right) \right]^{1/2}}$$

- where  $R_{EFF}$  = effective radius of curvature of the nose
- $\gamma_e$  = isentropic exponent
- $r$  =  $r(s/a)$ , normal distance from axis of symmetry to the solid boundary
- $p_e/p_0$  = boundary-to-stagnation point pressure ratio (experimental for blunt bodies; Newtonian-Prandtl-Meyer match for hemispheres)
- $a$  = semi-major axis of ellipse
- $b$  = semi-minor axis of ellipse

Heating distribution was determined about a body of revolution which approximates the non-axisymmetric nose shape common to the two entry gliders ( $L/D = 2.0$ ,  $W/C_{DA} = 200$  psf;  $L/D = 2.0$ ,  $W/C_{DA} = 50$  psf). Laminar rates, normalized to the stagnation point value for the 0.4-aspect ratio ellipsoid-cone combination, are shown in Figure 39. This curve is a combination of Vinokur's oblate ellipsoid results (Ref. 9) with those of Lees (Ref. 6) for hemispherically blunted cones. Due to nose bluntness, the heating remains nearly constant over the cap region. Expansion of fluid around the shoulder area causes a sizable reduction in local heating.

### 3.1.2 Boundary Layer Transition

Possible boundary layer transition during re-entry was examined. For the parabolic entry environment, the transition phenomenon is, unfortunately, ill-defined. One deduced criterion for transition is based upon the assumption that a critical value of local momentum thickness Reynolds number exists below which the flow is always turbulent. For this investigation, the critical momentum thickness Reynolds number was taken as 200, as suggested in Reference 6. The momentum thickness Reynolds number may be expressed as

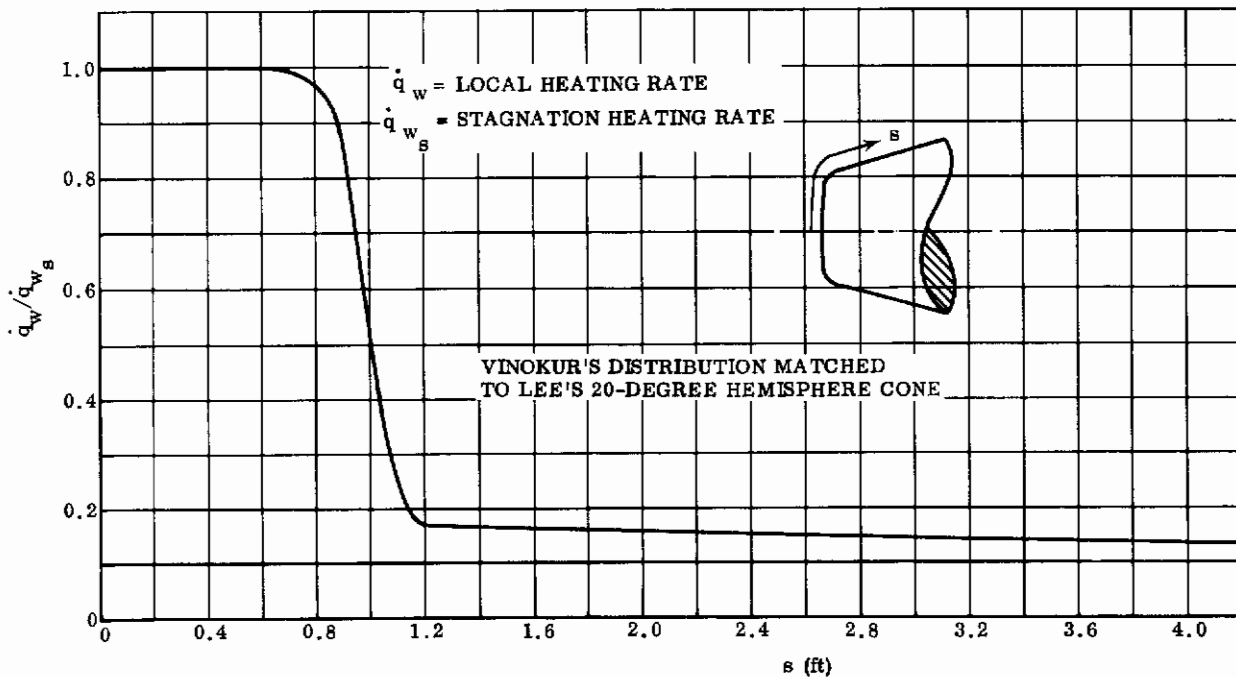


FIGURE 39. LAMINAR HEATING DISTRIBUTION OF A 0.4 ASPECT RATIO ELLIPSOIDAL BLUNTED 20-DEGREE CONE

$$Re_{\theta} = 0.61 R_B^{1/2} F_R S_R \left[ \frac{\rho_{\infty} a_{\infty}}{\mu_{\infty}} \right]^{1/2}$$

where  $R_B$  = body cylinder radius

$F_R$  = body shape function

$$S_R = \left[ \frac{\rho_o}{\rho_{\infty}} \frac{\rho_o}{\rho_{\infty}}^{1/2} \frac{\mu_{\infty}}{\mu_o} \right]^{1/2}$$

p = pressure

$\rho$  = density

$\mu$  = viscosity

a = sonic velocity

#### Subscripts

o = stagnation

$\infty$  = free stream

Assuming that the nose stagnation streamline passes through a normal shock, both  $S_R$  and the quantity  $(\rho_{\infty} a_{\infty} / \mu_{\infty})$  are functions only of the vehicle trajectory, i. e., the Mach number and altitude. The transition function  $\left[ Re_{\theta} / (R_B^{1/2} F_R) \right]$  versus time for the portion of re-entry during which heating is significant is shown in Figure 40. In the case of laminar heating, the net surface heating rate for the winged glider becomes negative at approximately 120 seconds; transition to turbulent flow would delay the surface cooling somewhat. Figure 40 indicates a maximum value of transition function of approximately 150, occurring at 80 seconds. For the ellipsoidal portion of the nose structure,  $R_B$  was on the order of 1 foot. Extending the hemisphere-cylinder and 0.3 ellipsoid-cylinder results of Reference 11 to the present configuration ( $b/a = 0.4$ ),  $F_R$  was found to be less than unity. It followed that maximum  $Re_{\theta}$  was a number less than 150. Transition of the flow from laminar to turbulent thus appeared not to occur on the ellipsoidal nose cap during re-entry.

The transition analysis neglected the effects of surface roughness and possible flow disturbance due to ablation. A check for flow transition on the conical portion of the nose was not made; convective heating rates are greatly decreased in this region for turbulent as well as laminar flow. Also, the conical skirt structure is somewhat over-protected due to a "practical" minimum depth of ceramic coating to provide imbedment for a required reinforcement.

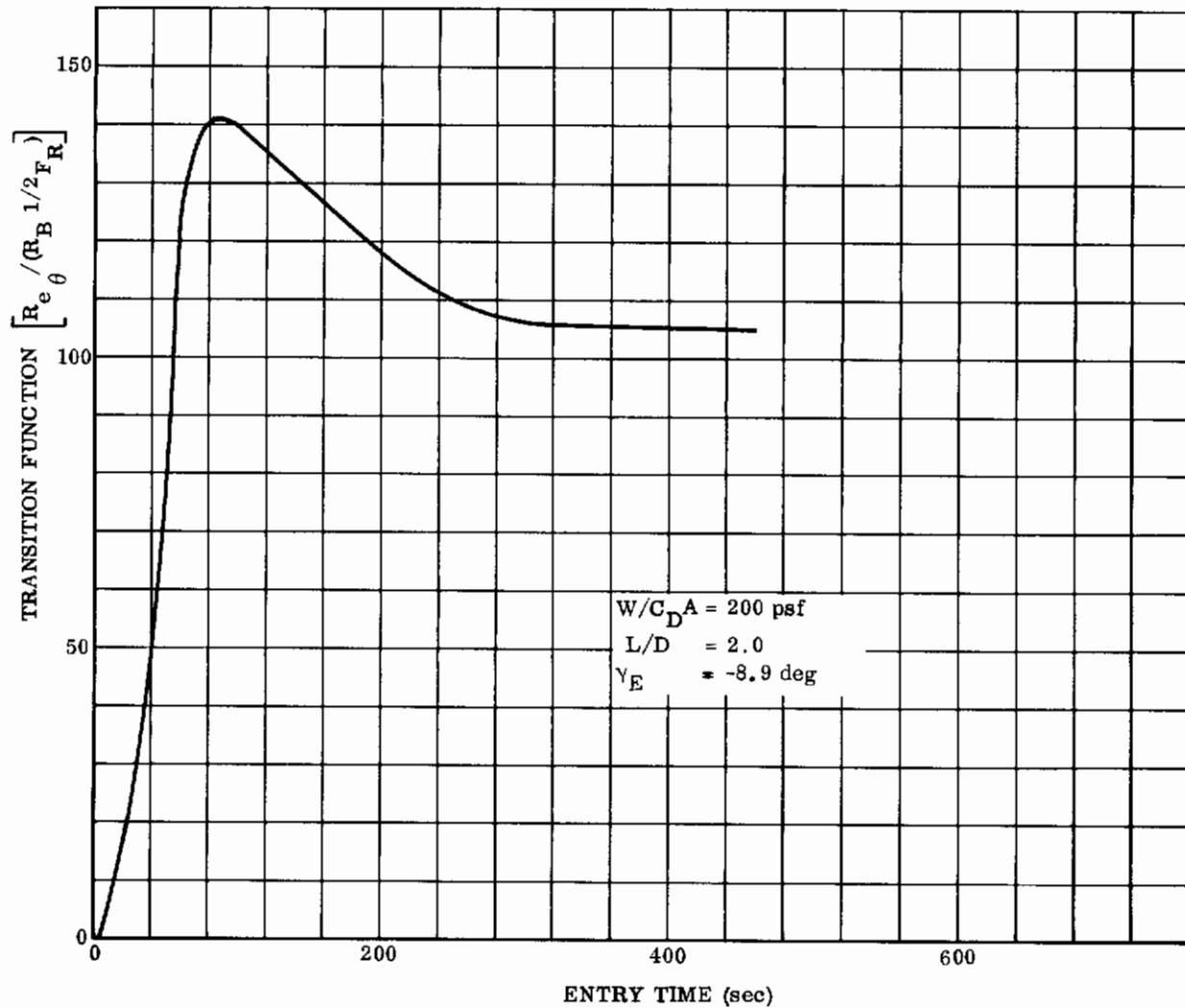


FIGURE 40. TRANSITION FUNCTION; Lifting Re-entry Trajectory

### 3.1.3 Programs for Transient Heat Flow Solutions

Two basic, but operationally versatile, forms of digital computer programs were utilized for calculating transient temperature distributions. The selection of a program for a specific case depended upon the nature of the boundary conditions as well as the extent and accuracy of the temperature response sought.

The stationary boundary treatment heat flow program is capable of solving heat balance equations for an arbitrary nodal arrangement throughout a general three-dimensional system of many materials. Temperature responses of non-ablating structural composites were evaluated primarily by this type of program. Descriptions of the program format and solutions developed at Lockheed Missiles and Space Company for solving by an IBM 7090 computer, appear in References 10 and 11. The program



provides for temperature-dependent thermal properties of materials. Also, there is provision for optional modes of heat input (internally calculated from trajectory information or solved from given heat transfer data).

A one-dimensional moving boundary program utilized in this study (Ref. 12 and 13) solves the heat balance equations for a known heat transfer to a composite slab undergoing recession of the exposed surface. Again, temperature-dependent thermal properties are included. The same thermal program, due to its generality, adequacy, and economy, was also employed for evaluating heat conduction in certain simple non-ablating cases.

The following discussion describes the basic equations and finite difference techniques incorporated into the digital computer solution. The method solved for transient heat conductions of a one-dimensional composite slab, accounting for a moving boundary and variable diffusivity.

The Newtonian derivation of heating through a differential element yields the "heat equation":

$$c \rho \frac{\partial T}{\partial \theta} = \sum_{i=1}^3 \frac{\partial}{\partial x_i} \left( k \frac{\partial T}{\partial x_i} \right)$$

Two basic assumptions were made to develop the governing equation: (1) each element is thermally homogeneous ( $k(x_i, T)$  is a constant with respect to  $x_i$  which implies  $\partial k / \partial x_i = 0$  and  $\partial k / \partial T = dk/dT$ ); (2) one-dimensional variations alone influence the solution. The governing equation is then the Fourier unsteady equation for heat conduction in a solid:

$$c \rho \frac{\partial T}{\partial \theta} = k \frac{\partial^2 T}{\partial x^2} \tag{1}$$

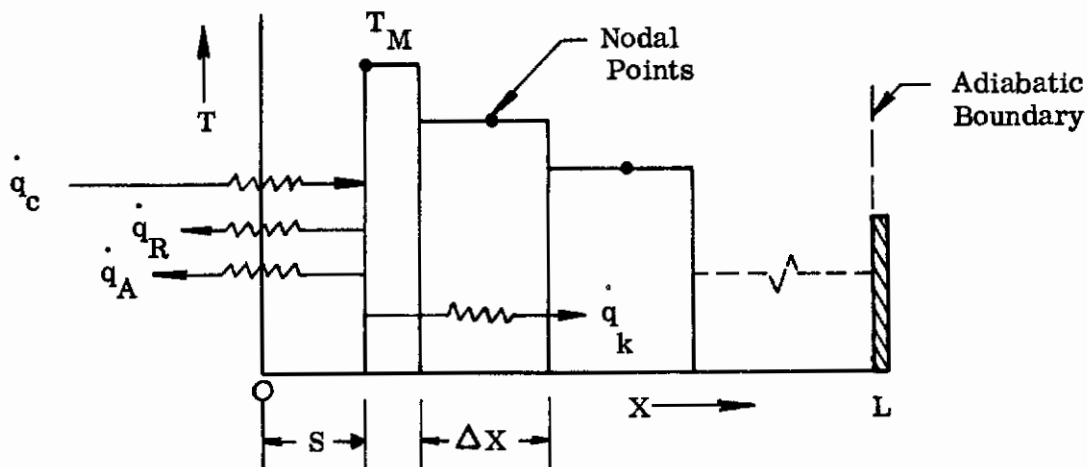
where

- $c$  = heat capacity of the element,  $c = C(T)$ , Btu/lb-deg R
- $\rho$  = density of the element,  $\rho = \rho(T)$ , lb/ft<sup>3</sup>
- $k$  = thermal conductivity of the element,  
 $k = k(T)$ , Btu/ft-sec = deg R
- $\theta$  = time, seconds
- $x$  = spatial coordinate, feet
- $T$  = temperature, degrees R.

The formulation of a numerical solution was based upon usual finite difference procedures applied to the governing differential equations, e.g., References 12 and 14.

The system was subdivided into a number of geometrical subvolumes. Next, the thermal properties of each subvolume were considered to be concentrated at the central node of each volume (so-called "lumped parameters"). Heat conduction was computed to and from each node in the network. The unsteady conditions were specified by the governing equations in finite difference form with appropriate boundary restraints. Physically, the program was constructed to handle the concentrated nodal parameters  $c$ ,  $\rho$ , and  $k$  as varying functions of  $T$ ; all parameters were implicitly functions of  $\theta$ .

The geometry of the solution was:



where:

- $T_M$  = Melting temperature of the decomposing ablator
- $S$  = Recession distance of the outer surface
- $\dot{q}_c$  = Convective heat pulse (aerodynamic)
- $\dot{q}_R$  = Radiation heat pulse from the solid wall
- $\dot{q}_A$  = Increment of heat relief due to ablation process
- $\dot{q}_k$  = Increment of heat conducted through material

The boundary conditions to Equation (1) are:

$$\begin{aligned}
 \theta &\geq \theta_M & S < x < L & & c \rho \frac{\partial T}{\partial \theta} &= k \frac{\partial^2 T}{\partial x^2} & (1) \\
 T &= T(x) < T_M & x > 0 & & & & \\
 T &= T_M & x = 0 & & \theta &= \theta_M & \\
 S &= 0 & & & & & \\
 -k \frac{\partial T}{\partial x} &= 0 & x = L & & & &
 \end{aligned}$$

When the surface node temperature reaches  $T_M$  the heat balance is:

$$\dot{q}_c - \dot{q}_A - \dot{q}_R - \dot{q}_k = 0 \quad (2)$$

It is convenient to the problem to put  $\dot{q}_A$  in terms of an effective heat of ablation ( $Q^*$ ):

$$\dot{q}_A = \frac{\partial S}{\partial \theta} \rho_A Q^*$$

Where  $Q^* = Q^* [ Q_{Fu}, \beta (\Delta h) ]$ ,  $Q_{Fu}$  is the heat of fusion of the ablator, and  $\beta (\Delta h)$  is the contribution from the energy absorbed in the ablator resulting in the diffusion of particles from the ablation surface.  $\beta$  is the so-called "blowing parameter" and is a function of the molecular weight of the diffusion species and the incident energy. An analysis was used to determine the variation of  $Q^*$  with  $\Delta h$  for a given trajectory and ablator material.  $\Delta h$  was the enthalpy difference across the boundary layer, and  $\rho_A$  was the mean density of the products of ablation.

The heat balance at the surface then yielded the differential equation describing the surface recession or surface erosion rate of an ablator subjected to an incident heat pulse and simultaneously cooled by surface radiation and internal conduction:

$$\frac{\partial S}{\partial \theta} = \left[ \dot{q}_c - \sigma \epsilon F (T_w^4 - T_o^4) - k \frac{\partial T}{\partial x} \right] \frac{1}{\rho_A Q^*} \quad (3)$$

where:

- $\sigma$  = Stefan-Boltzman constant
- $\epsilon$  = effective total emissivity of the solid surface
- $F$  = radiation geometrical shape factor
- $T_o$  = radiation sink temperature
- $T_w$  = wall temperature.

In the usual manner, the temperature of a given node, governed by Equation (1), was formulated by a finite difference scheme, involving adjacent network points explicitly. The explicit development of the appropriate finite difference approximations for partial derivatives in the governing equations is a tedious development. To avoid excessive redundancy, the methods incorporated for development of the working equations are outlined only.

Assuming that the characteristic changes in thermal response are small over small spatial divisions ( $\Delta x$ ), a Taylor series expansion was made at each node in the network to determine explicitly the form of the equations for the partial derivatives in Equation (1) and (3). The response of the central node was weighted with respect to the contributing nodes, however many and whatever pattern the contributing nodes may form about the central node of interest. The difference form of the partial derivatives was determined from the sum or difference of the Taylor series expansions along the network. The formulation was then completed by substitution into the governing equation, subject to the boundary conditions depicted for the problem and the heat balance constraint of Equation (3).

The difference formulation for Equation (1) at the wall can be written:

$$c \rho \frac{\Delta x}{2} \frac{T_w' - T_w}{\Delta \theta} = \dot{q}_c - \epsilon \sigma F (T_w^4 - T_o^4) - \frac{k}{\Delta x} (T_w - T_{w+1}) \quad (4)$$

where:

- $T_w'$  =  $T_w$  at time  $\theta + \Delta \theta$
- $T_{w+1}$  = first adjacent nodal point in the direction of heat flow.

Using the lumped properties of the nodes  $\left[ k = k(x), c = c(x), \text{ and } \Delta x = \Delta x(x) \right]$ , a rearrangement of Equation (4) yielded the difference form programmed for the outermost node on the moving boundary:

$$T_w' = \frac{\Delta \theta}{(\rho c \Delta x)_w} \left[ \dot{q}_c - \sigma \epsilon F (T_w^4 - T_o^4) - \frac{T_w - T_{w+1}}{\left(\frac{\Delta x}{k}\right)_w + \left(\frac{\Delta x}{2k}\right)_{w+1}} \right] \quad (5)$$

An internal node is subject only to the governing Equation (1); constraints due to surface heat balance appear only indirectly through the driving temperature ( $T_{N-1}$ ), so that the following equation is evolved:

$$T_N' = \frac{\Delta \theta}{(\rho c \Delta x)_N} \left[ \frac{T_{N-1} - T_N}{\frac{1}{2} \left( \left(\frac{\Delta x}{k}\right)_{N-1} + \left(\frac{\Delta x}{k}\right)_N \right)} - \frac{T_N - T_{N+1}}{\frac{1}{2} \left( \left(\frac{\Delta x}{k}\right)_N - \left(\frac{\Delta x}{k}\right)_{N-1} \right)} \right] \quad (6)$$

recalling, that in finite difference formulation, the step back to the driving term ( $T_{N-1}$ ) appears as a negative term in the spatial coordinate ( $\Delta x$ ).

The final node in the net was bounded in the forward marching direction by an adiabatic boundary, so that  $T_F'$  was described completely by the balance between nodal capacitance and the driving energy of the previous adjacent node:

$$T_F' = \frac{\Delta \theta}{(\rho c \Delta x)_F} \left[ \frac{T_{F-1} - T_F}{\frac{\Delta x}{2k}_{F-1} + \frac{\Delta x}{k}_F} \right] \quad (7)$$

The surface recession was coupled to the surface temperature ( $T_w$ ) and the boundary conditions through the finite difference approximation to Equation (3):

$$\frac{\Delta s}{\Delta \theta} = \left[ \dot{q}_c - \sigma \epsilon F (T_w^4 - T_o^4) - \frac{T_w - T_{w+1}}{\left(\frac{\Delta x}{k}\right)_w + \left(\frac{\Delta x}{2k}\right)_{w+1}} \right] \frac{1}{\rho_A Q^*} \quad (8)$$

The solution of Equations 5, 6, 7, and 8, dropping the surface node for  $T_w \geq T_M$  and re-calculating a corresponding  $\Delta \theta$ , was handled by an IBM 7090 digital computer program with varying thermal properties and ablation cooling ( $Q^*$ ) over a heat pulse history for any given trajectory.

### 3.1.4 Incident Gas Cap Radiation

A study was conducted of the supplemental heating from an incandescent gas cap which forms about the frontal body at hypervelocities in the dense lower atmosphere. Vehicles characterized by higher ballistic coefficients and steeper entry angles are thus more subject to such radiant heating. Furthermore, shock layer radiation increases with shock and stand-off distance, a factor which is amplified by body size and bluntness. Equilibrium gas cap radiation was included in the final design temperature analyses of the winged glider entering the atmosphere at the 10-g deceleration limit. The remaining candidate lifting vehicles received disproportionately little radiation compared with aerodynamically convected energy.

No attempt was made to evaluate the contribution of radiation from chemical and thermodynamic non-equilibrium. Little is as yet understood concerning such factors as non-equilibrium energy distribution in the gas stream and particle degeneracy.

Reference 5 presents a stagnation point radiant-energy transfer expression for an ellipsoidal nose cap ( $b/a = 0.4$ ) of the approximate form

$$\dot{q}_R = 3.00 R_n (\rho_\infty/\rho_0)^{1.98} (V_\infty/10^4)^{14} \text{ Btu/ft}^2\text{-sec.}$$

The peak heating rate for the winged glider occurred at an entry of 50 seconds, which is approximately the beginning of Phase III flight, where the free stream velocity was 34,000 fps and the altitude was 173,000 feet. Substituting the corresponding density ratio ( $6.39 \times 10^{-4}$ ) and the effective nose radius (2.5 feet) into the above equation gives a  $\dot{q}_R$  of 100 Btu/ft<sup>2</sup>-sec, a value included in the final design thermal analysis. This heat rate was less than 20 percent of the hot-wall incident convective value subsequently presented. Also, due to the short duration, the heat load from the shock layer radiation was less than 10 percent of the total heat to the time of radiation equilibrium conditions. With  $\dot{q}_R$  decreasing rapidly aft of the stagnation region, gas cap heating was considered only to the sonic point of the glider nose ( $s \approx 0.9$  foot).

Recent investigations (Ref. 15), accounting for shock curvature, indicated slightly lower values of radiation heat transfer, making the above maximum of 100 Btu/ft<sup>2</sup>-sec somewhat conservative.

## 3.2 THIN RADIATION COOLED STRUCTURES

A parametric analysis was undertaken to determine one-dimensional transient temperature variation at the stagnation point of simple hot-wall frontal structure. This generalized structure was a thin composite consisting of a refractory metal substrate coated (e.g., by plasma-arc spraying) with a protective, relatively dense ceramic overlay which would operate at temperatures sufficient to return a major portion of the energy to the air stream by radiation, but which would possess little heat capacity.

Use of the hot-wall structural concept was restricted exclusively to the glider presenting an exceedingly light wing loading ( $L/D = 2.0$ ,  $W/C_{DA} = 50$  psf) and entering the atmosphere at such a shallow angle that it traversed the portion of the corridor near skip-out. Hot-wall structure such as described, which has no provision for transitory absorption during peak heating, would not qualify for the other selected configurations, i.e., those exposed to maximum heating rates exceeding  $200 \text{ Btu/ft}^2\text{-sec}$ , a limiting value for a thin radiation-cooled structure. The peak heating value for a radiation shield depends upon its melting point and surface radiation characteristics. Some of the more desirable ceramic overlay materials which were compatible with tungsten alloy substrates had melting points as low as  $5100 \text{ F}$  and wall emittances as low as  $0.3$  to  $0.4$  at elevated temperature. Trajectories associated with the acceptable hot-wall glider are characterized by a long-duration heat pulse, a high integrated heat load, and a moderately high peak heat transfer rate.

Convective and net heat transfer histories are presented in Figure 41 for a hemispherical nose of 1-foot radius and entry conditions stated above. A peak value of  $190 \text{ Btu/ft}^2\text{-sec}$  was achieved at approximately 70 seconds from the 400,000-foot altitude and then underwent slow decay. This thermal pattern is typical for vehicles of high  $L/D$  ratio. The peak rate was less than previous values, because hot-wall effects were taken into account. Based on the net heat transfer, i.e., incident convective less reradiation to space, radiation equilibrium conditions were achieved at a later time than maximum aerodynamic heating, a result of slight capacity effects of the ceramic overlay and substrate.

Lightweight systems employing thin ceramic overlays, of the order of  $0.03$  inch, have a maximum temperature drop across the ceramic of about  $200 \text{ F}$  with radiation equilibrium achieved soon after peak convective heat transfer. The low

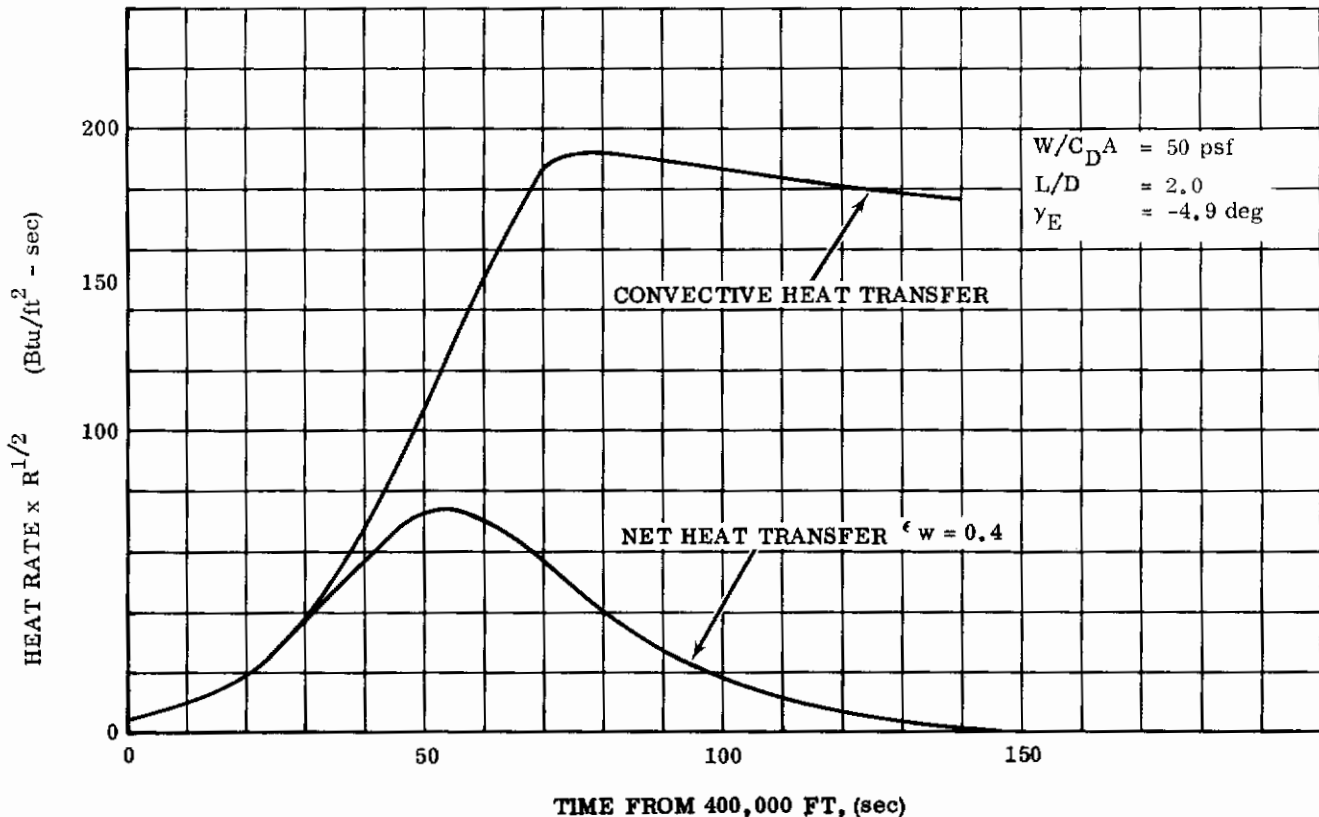


FIGURE 41. HEAT TRANSFER HISTORIES FOR COMPOSITE SLAB; Ceramic Over Refractory Metal Substrate

gradients are a result of the small thickness chosen for ceramic coating materials. Increases in ceramic overlay thickness to the order of 0.2 inch result, during initial descent, in substantial temperature differentials across the ceramic, of the order of 2000 F, and in peak operating temperatures of 4500 to 5000 F. For thicker overlays for use in reinforced systems, substantial thermal stresses could arise.

Uncertainties in high-temperature thermal properties of the candidate materials imposed limitations on the accuracy with which the thermal response of a given structure could be evaluated. Necessary properties include conductivity ( $k$ ), specific heat ( $c$ ), and total normal surface emittance ( $\epsilon_w$ ). Because of the limited materials information in the high-temperature regime, a parametric study of a refractory substrate - ceramic overlay was made. Wall emittance ( $\epsilon_w$ ), thermal diffusivity ( $k/\rho c$ ), and capacity parameter ( $\rho c$ ) were varied to depict a range of overlay thicknesses and materials selections. The calculated results, therefore, may be applied to general ceramic-refractory composite systems, even accounting for such effects as ceramic porosity.



The ranges of parameters incorporated in the hot-wall transient temperature determination were:

Wall emittance,  $\epsilon_w$ : 0.4, 0.6 and 0.8

Diffusivity,  $k/\rho c$ : 0.01 to 0.08 ft<sup>2</sup>/hr

Heat capacity parameter,  $\rho c$ : 24, 48 and 72 Btu/ft<sup>3</sup>-deg F

Ceramic thickness,  $\delta$ : 0.03 and 0.20 inch

Two typical temperature responses for selected composite systems incorporating 0.2-inch ceramic over 0.04-inch refractory alloy base are shown in Figures 42 and 43. The results for  $\epsilon_w = 0.4$  are summarized in Figure 44, which shows the maximum temperature drop across the ceramic coating as a function of the capacity parameter  $(\rho c \delta)/(\rho c \delta)_m$  and the thermal diffusivity. The strong effect of the diffusivity and minor influence of the relative ceramic-substrate heat storage capacities are indicated. These results are based upon temperature-dependent values of conductivity and specific heat. To account for the higher diffusivities at temperatures below 3000 F, typical of the families of ceramic overlays of special interest, temperature-dependent values of  $k/\rho c$  characteristic of thoria were assigned to depict the average characteristics of the ceramic materials (Ref. 16). High-temperature diffusivities ( $T_w > 3000$  F) were considered constant at either 0.01, 0.03, 0.05, or 0.08 ft<sup>2</sup>/hr. Figure 44 may be generalized to accommodate variations in ceramic thickness from 0.2 inch by interpreting the absolute numerical values on the abscissa as the modulus  $k/\rho c \delta^2, \text{sec}^{-1}$ , where  $\delta$  has the units of feet.

The effects of wall emittance upon maximum temperature drop across the ceramic and maximum surface temperature were determined. The results are summarized in Figure 45. For a value of  $k/\rho c = 0.03$  ft<sup>2</sup>/hr, the maximum temperature drop across the ceramic decreased from approximately 1680 to 1320 F for an increase in  $\epsilon_w$  from 0.4 to 0.8. The effect was much less dramatic for  $k/\rho c = 0.05$  ft<sup>2</sup>/hr; for this diffusivity, the maximum temperature differential was approximately 950 F for  $\epsilon_w = 0.4$ , and decreased to 820 F for  $\epsilon_w = 0.8$ . With radiation equilibrium attained at levels of heat transfer corresponding approximately to peak convection (Fig. 41) and with minimal heat storage, the peak absolute surface temperatures were expected to vary inversely as the fourth root of  $\epsilon_w$ . Results presented in Figure 45 show that an increase in  $\epsilon_w$  from 0.4 to 0.8 was in fact accompanied by a reduction in surface temperature from approximately 5050 to 4200 F.

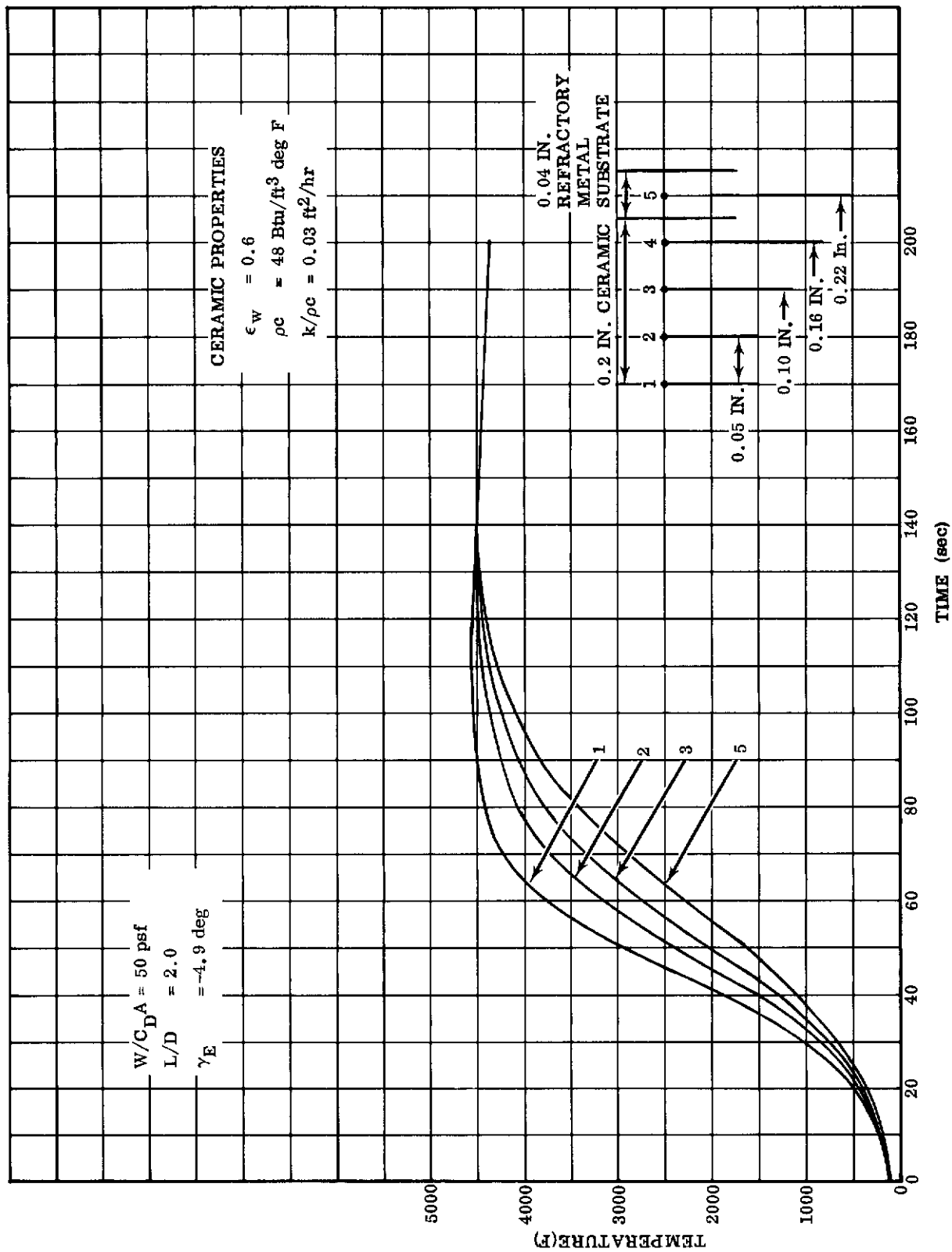


FIGURE 42. TEMPERATURE HISTORIES FOR COMPOSITE SLAB;  $\epsilon_w = 0.6$

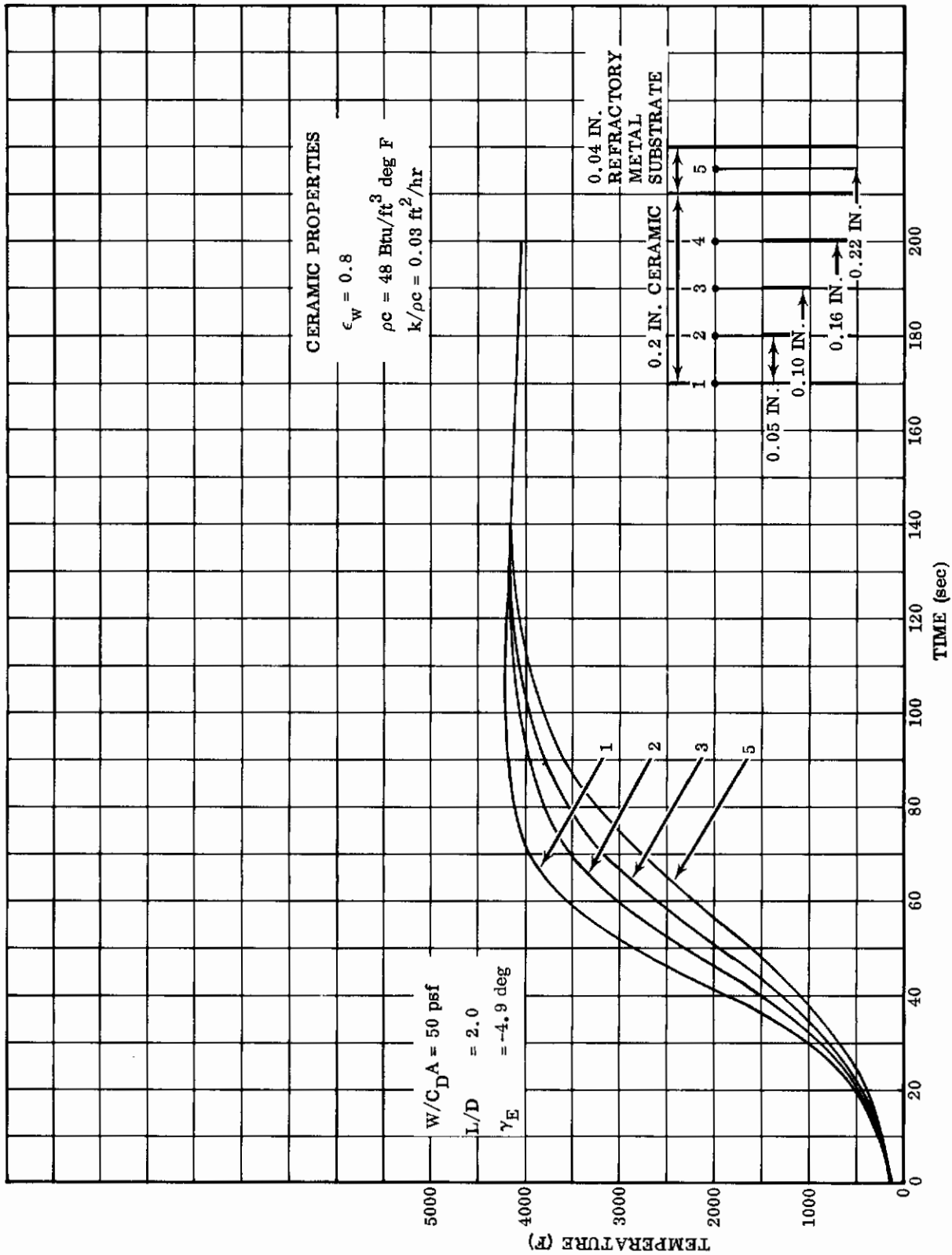


FIGURE 43. TEMPERATURE HISTORIES FOR COMPOSITE SLAB;  $\epsilon_w = 0.8$

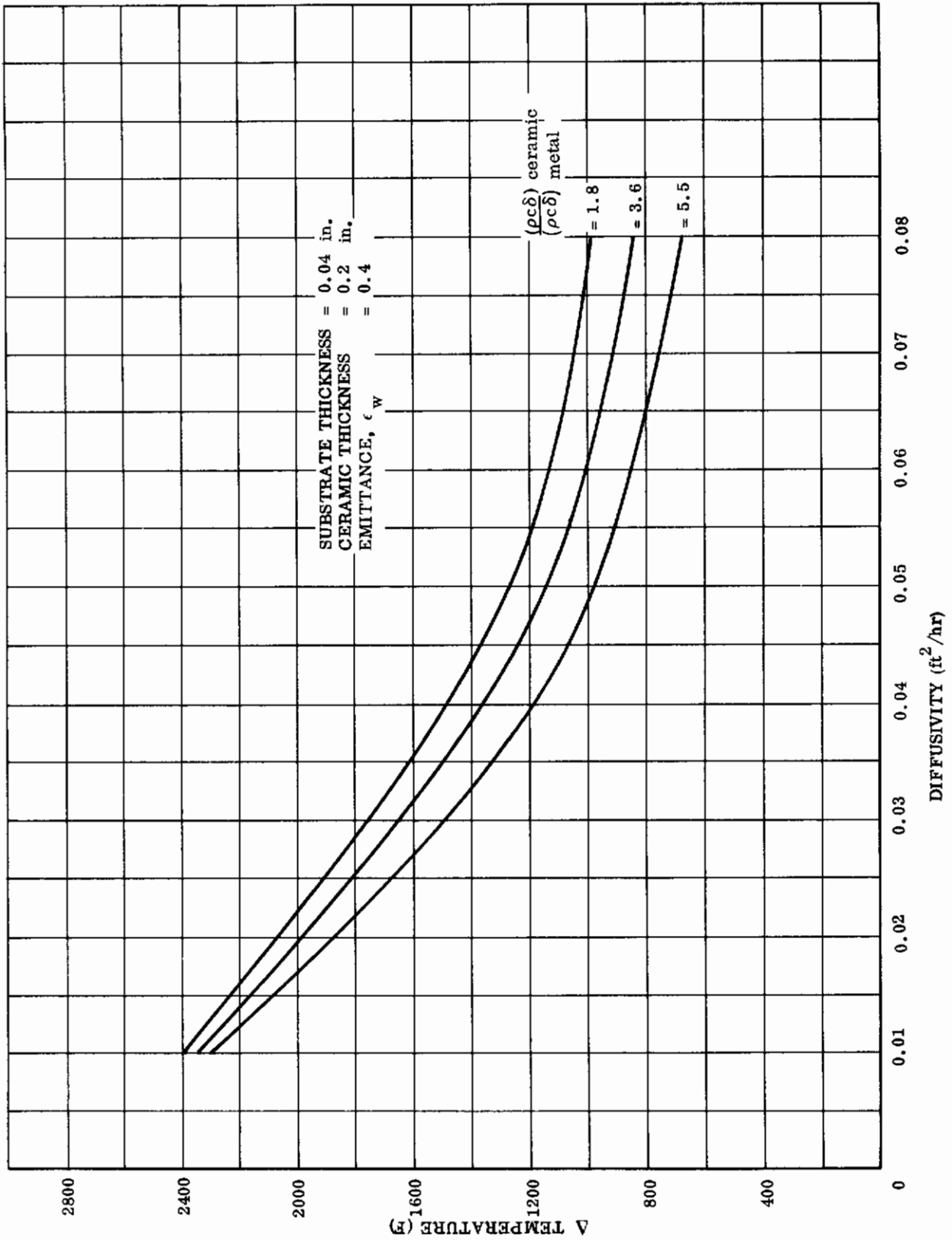


FIGURE 44. MAXIMUM TEMPERATURE DROP ACROSS CERAMIC

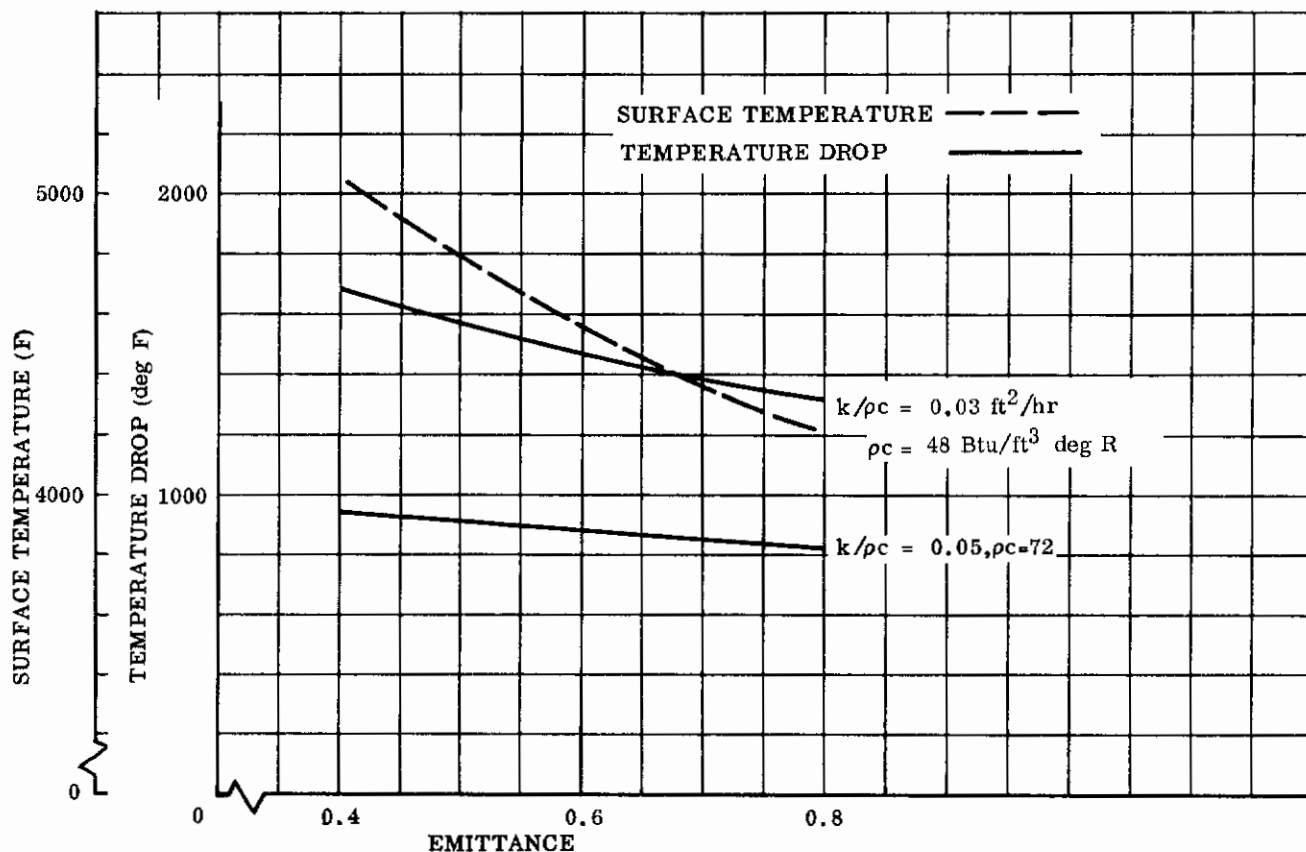


FIGURE 45. VARIATION OF MAXIMUM SURFACE TEMPERATURE AND TEMPERATURE DROP ACROSS CERAMIC WITH EMITTANCE; Ceramic Thickness 0.02-Inch

For those ceramics having a  $k/\rho c$  greater than  $0.05 \text{ ft}^2/\text{hr}$  (e.g., magnesia), the maximum temperature drop through a 0.2-inch thickness is less than 1000 F (Fig. 44). The diffusivity of magnesia at 3000 F is nearly  $0.05 \text{ ft}^2/\text{hr}$ . Operating at temperatures in excess of 3000 F may tend to reduce further the temperature gradients in the system because of an increased value of apparent conductivity (increased internal radiation). The diffusivities for thoria and zirconia between 2000 and 3000 F are approximately  $0.03 \text{ ft}^2/\text{hr}$  and  $0.023 \text{ ft}^2/\text{hr}$ , respectively. Maximum temperature drops of less than 1700 F for thoria and 1900 F for zirconia are indicated by Figure 44.

Another series of hot-wall solutions was investigated for a reduced overlay thickness of 0.03 inch. For the thin ceramic coating, Figure 46 shows a maximum temperature drop of less than 200 F, corresponding to the specific values of diffusivity and heat capacity of  $0.03 \text{ ft}^2/\text{hr}$  and  $48 \text{ Btu/ft}^3\text{-deg F}$ , respectively. A slight reduction in depthwise temperature gradient was generally discerned for the thinner overlays.

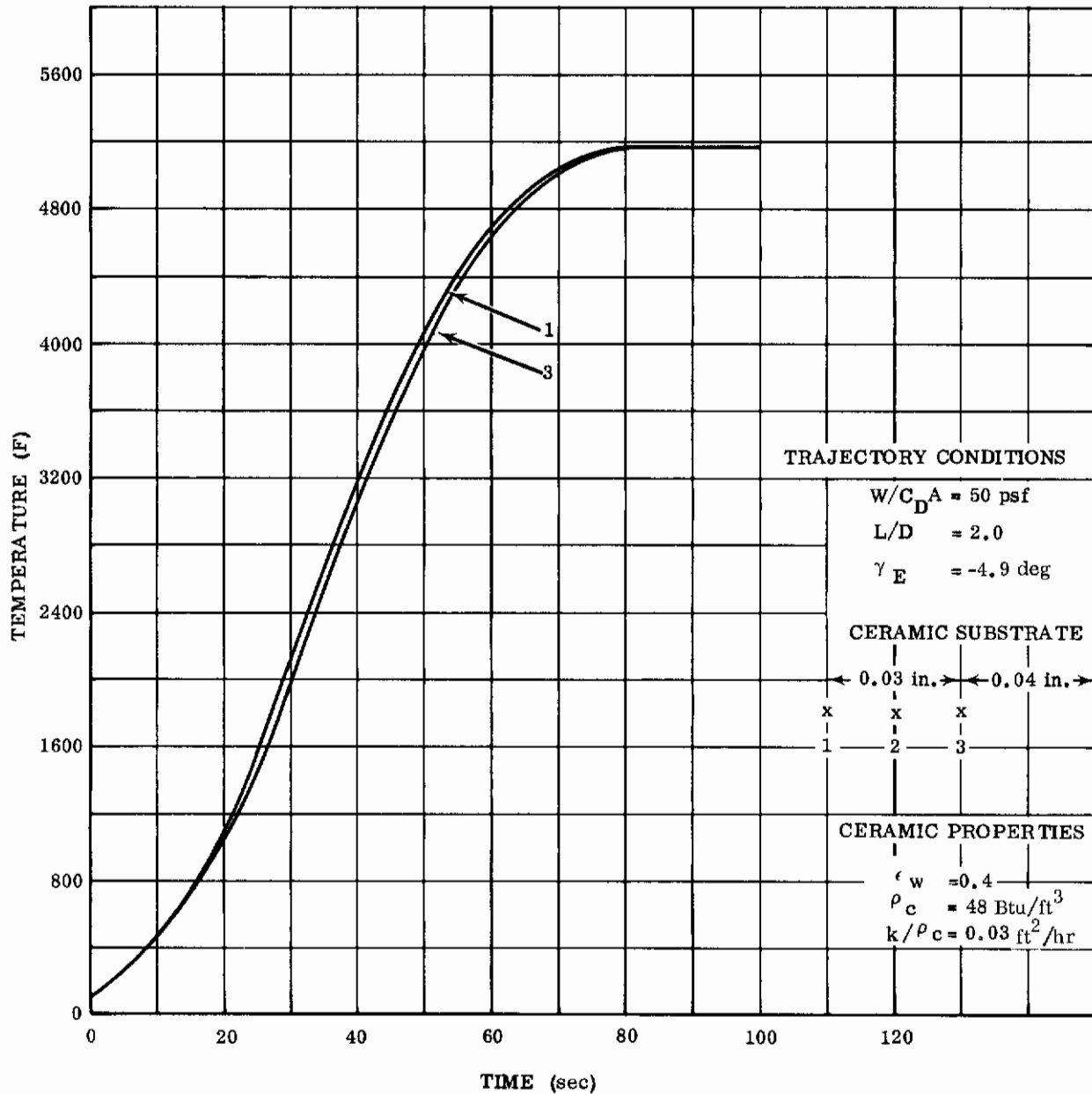


FIGURE 46. TEMPERATURE HISTORIES FOR A COMPOSITE SLAB; 0.03-Inch Ceramic Over Refractory Metal Substrate

The preceding results were based upon perfect insulation at the inner face of the metallic substrate wall, i. e. , zero heat transfer to the interior of the frontal section. The heat transfer predictions pertained to a hemispherical nose radius of one foot. Some relief in temperature would follow an increase in nose radius or bluntness since peak temperatures vary inversely with  $R_n^{1/8}$ .

Reduced density (increased porosity) will effect a reduction in conductivity, particularly at lower temperatures (Ref. 23). Limited available data from other sources, as well, appeared to substantiate this observation. The result is an essentially constant diffusivity and an accompanying reduction in capacity parameter ( $\rho c$ ). The effects of reduced density may be inferred from the preceding results and Figure 44.

# *Contrails*



## IV. ANALYSIS OF ABSORPTION-RADIATION SYSTEMS

Analysis of the low heat capacity radiative frontal section presented in Section III indicated that such nose caps would have limited capabilities. Restriction of the tungsten shell to operating temperatures of 4500 F limited the nose cap to stagnation point heat flux rates of 200 Btu/ft<sup>2</sup>-sec. This heating rate would imply extremely large nose radii, or unrealistic vehicle design. Evaluation of structural systems with heat capacity was therefore initiated. The system types for early study were:

- Magnesia over tungsten - Magnesia is an efficient high-temperature ablator, which can act as a refractory radiating surface after ablation stops.
- Nylon-phenolic or quartz over tungsten - Both charring and non-charring ablators were evaluated to provide comparative data. The ablators were designed to be completely dissipated when the heat flux dropped to 300 Btu/ft<sup>2</sup>-sec.
- Thoria over tungsten - Thick coatings over insulated tungsten were considered. Since test data indicated that thoria sublimed at reduced pressures, heat absorption by this method appeared attractive when combined with the high surface emittance of thoria.

The philosophy used in each analysis was similar. During the initial passage through the atmosphere the nose heating environment temporarily exceeds, for certain vehicles, permissible temperature limits for radiation structure. For this relatively short interval of time, a temporary or transitory heat-absorptive system was envisioned for the outer surface. When the magnitude of the entry thermal pulse diminishes to suitable levels, the residual structure operates under prolonged aerodynamic exposure as a hot-wall thermal radiator.

The results of these analyses are presented in the following sections.

### 4.1 MAGNESIA ABLATION-RADIATION SYSTEM

A moving-boundary transient temperature analysis of the inorganic protective coating, magnesia, was carried out. To calculate the time variation of temperature

and surface recession, one-dimensional heat balance relationships for composite slabs were employed. For the sake of limiting extensive parametric calculations, two of the three vehicle configurations were selected for ablation determinations: the glider of medium wing loading ( $L/D = 2.0$ ,  $W/C_D A = 200$  psf); and the blunt semi-cone ( $L/D = 0.5$ ,  $W/C_D A = 50$  psf).

Magnesia gave indications of satisfying important requirements of an efficient ablation system for super-orbital lifting entry:

- High heat of ablation (resulting from a high heat of decomposition and high transpiration factor for the decomposed products)
- High surface temperature performance.

Since magnesia also exhibits high conductivity, considerable heat is stored in the nonablated portion of the structure, and temperatures become excessive throughout the thickness of ablative overlay. Ideally, from a minimal weight standpoint, the ablative material of a composite ablation-radiation structure is completely consumed at which time the radiation structure can first be utilized. Consequently, only thin ablator coatings exist just before the radiation structure is employed and the non-ablated portion (normally considered as insulative) operates just short of the ablation temperature. At such temperatures, particularly for non-reinforced systems, large amounts of material may slough away before the heats of decomposition and vaporization or gaseous injection effects can be efficiently utilized. This effect can be minimized by the use of magnesia which can operate both as an ablation material and as a hot-wall structure after ablation is finished.

Estimates of the ablator requirements were based upon optimistic performance of the magnesia ablator relying on complete decomposition of magnesia to gaseous magnesium and oxygen. This assumption has been shown to be reasonably valid by tests described in Volume II. The sum of the heats of decomposition and fusion was assumed to be 8000 Btu/lb, which corresponds to decomposition in the neighborhood of the melting point at one atmosphere. Since the average molecular weight of the injected products is slightly less than that of air (Ref. 17), the laminar transpiration factor is about 0.7, yielding a theoretically efficient heat protection system. The resultant effective heat of ablation was given by

$$Q^* = \alpha + \beta \Delta h \approx 8000 + 0.7 \frac{V^2}{2 gJ} \text{ Btu/lb}$$

where:

- $\alpha$  = heat stored plus heat due to phase change, chemical reactions and other factors
- $\Delta h$  = enthalpy difference across the boundary layer
- $V_{\infty}$  = free stream velocity
- $g$  = gravitational acceleration
- $J$  = mechanical equivalent of heat
- $\beta$  = transpiration factor

In Figure 47, the weight requirements for such an ideal performance are presented as a function of the cold-wall integrated heat input (to the time of reradiation capability) with  $\epsilon_w = 0.4$ . These results find general application to the stagnation region of various shape and size frontal sections. These results are based upon the following trajectory conditions:

$W/C_D A$ (psf)	$L/D$	$\gamma_E$ (deg)	$Q_{R.E.}$ (Btu/ft <sup>2</sup> ) (1)
50	0.5	-7.55	34,000
200	2.0	-8.9	100,000

For a frontal hemispherical section of 1-foot radius, the ablator weight requirements in the stagnation region are 0.8 and 2.9 lb/ft<sup>2</sup>, respectively, for  $W/C_D A = 50$  and 200 psf.

Thermal conductivity of magnesia may be decreased by foaming or loading, i. e., supplementing the basic ceramic with materials of lower conductivity. Reductions in conductivity that may be achieved by increasing the ablator porosity by as much as 50 percent by volume do not appear to be sufficient to maintain the back wall at temperatures substantially below the melting point of magnesia. The temperature gradients in thin overlays of MgO were negligible throughout the critical thermal period early in descent. Also, high temperatures prevailed uniformly through the slab thickness. Material softening and degradation which accompanies intense and prolonged hyperthermal operation points out a definite requirement for ceramic reinforcement to prevent catastrophic ablation. Further, chemical incompatibility between MgO and most other materials at elevated temperatures can be a seriously limiting factor.

1. Integrated heat input to a 1-foot-radius stagnation point which requires thermal absorption from the time of atmospheric entry to attainment of  $\dot{q}_c = 200$  Btu/ft<sup>2</sup> sec.

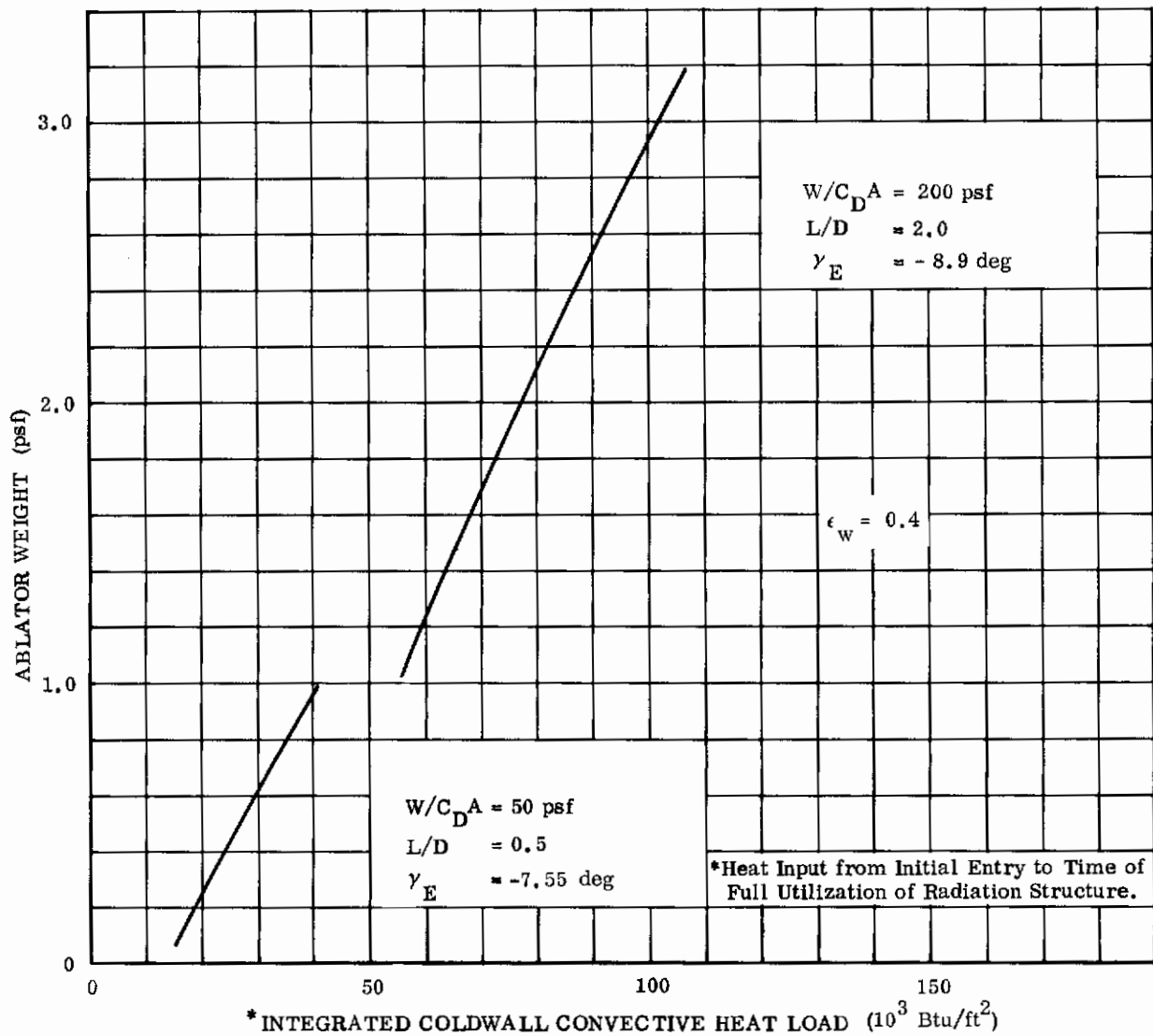


FIGURE 47. MAGNESIA ABLATOR REQUIREMENTS

## 4.2 NYLON-PHENOLIC AND QUARTZ ABLATORS

Prior to detailed study of these ablators, a simplified parametric analysis of ablator requirements was conducted. Illustrations to depict preliminary design ablator weights were formulated. Estimates of ablator requirements were made for specific re-entry conditions including a range of  $W/C_D A$  from 50 to 200 psf and  $L/D$  from 0.5 to 1.0. One of the general plots of stagnation point unit weight of ablative protection is presented in Figure 48 for a 1-foot-radius hemisphere on a vehicle characterized by  $L/D = 1.0$ ,  $W/C_D A = 200$  psf, and  $\gamma_E = -8.3$  degrees. With the laminar heat transfer distribution decaying aft of the stagnation point, the localized heat protection requirements represent a practical maximum. Moreover, since the frontal structure represents only a small percentage of the total vehicle area, the ablative protection in the cap region represents an important but small fraction of the entire heat protection weight (Ref. 18). With the effective nose radii often greater than 1 foot, less heat protection per unit area would suffice, scaling approximately as  $R_n^{-1/2}$ .

To represent a large selection of ablative materials, extensive variations in transpiration factor ( $\beta$ ) and surface emittance-wall temperature product ( $\epsilon_w^{1/4} T_w$ ) were investigated. The significant decrease in weight requirements accompanying the higher surface temperatures and/or higher surface emittances (Fig. 48) indicates the strong influence of these ablative parameters. The variation of heat protection weight with re-entry angle,  $L/D$  ratio, and ballistic coefficient is indicated in Figure 49. A material transpiration factor of 0.4 was invoked for this case as well as the assumed surface condition of constant radiation at  $(\epsilon^{1/4} T_w) = 4000$  R. A similar study based upon the assumption of negligible relief from surface radiation (Ref. 19) was conducted. The resultant ablator weights were, for this latter case, approximately 50 percent higher and showed no tendency to decrease with decreasing entry angle. All results showed characteristic variations of weight with  $\gamma_E$  similar to the indicated total convective heat load ( $Q_{R,E}$ ) to the time of radiation equilibrium heat flux (Fig. 6). The ballistic coefficient for a given entry angle substantially influences the heat load and the resultant ablator weight. For  $W/C_D A \leq 100$  psf, the weight requirements decreased slightly for the shallower entry angles (Fig. 49) because of the reduced peak heat rates and lowering of the average heat transfer rate to a value only slightly above that for radiation to space. However, the assumption of constant surface

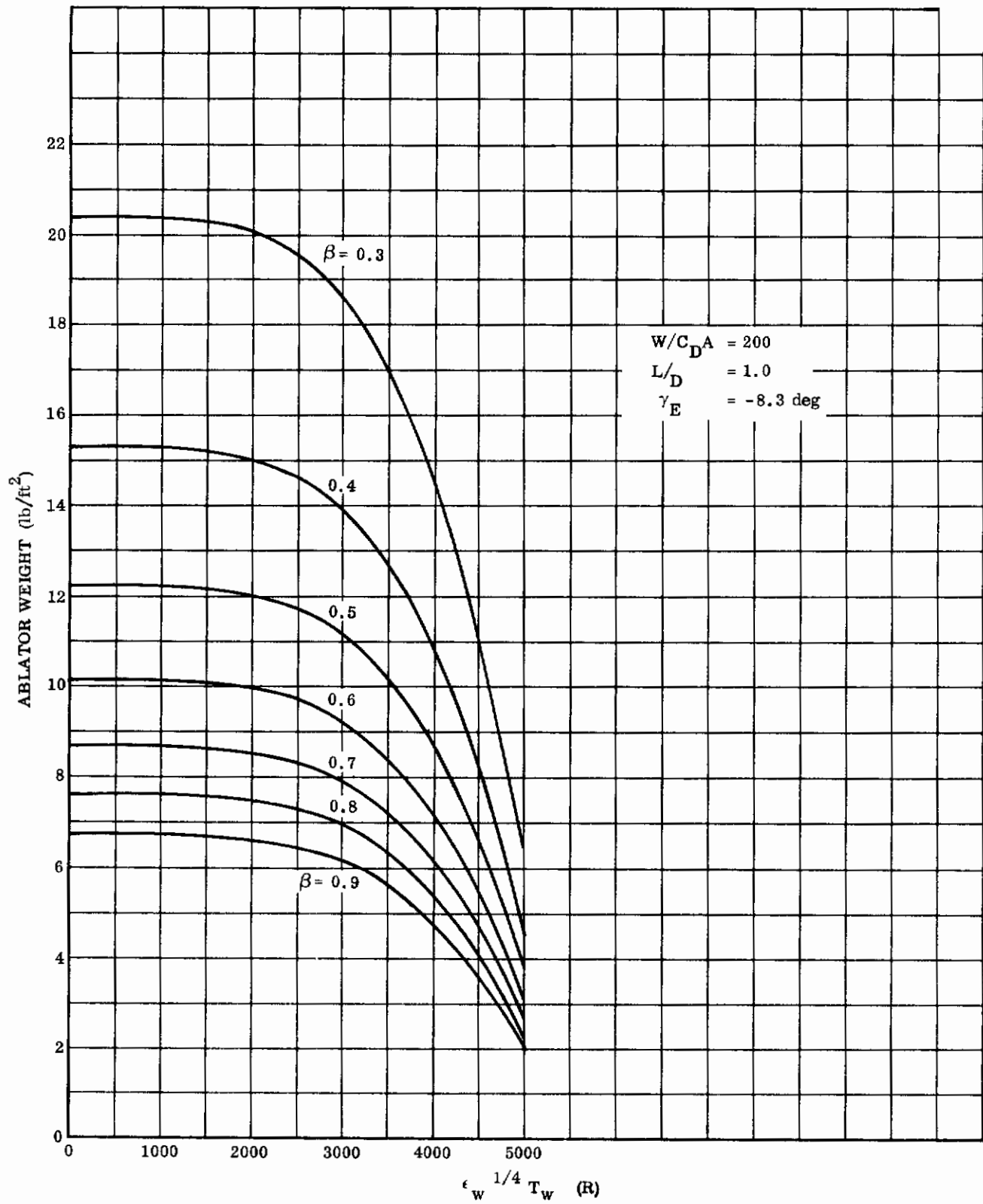


FIGURE 48. STAGNATION POINT ABLATOR WEIGHT REQUIREMENTS

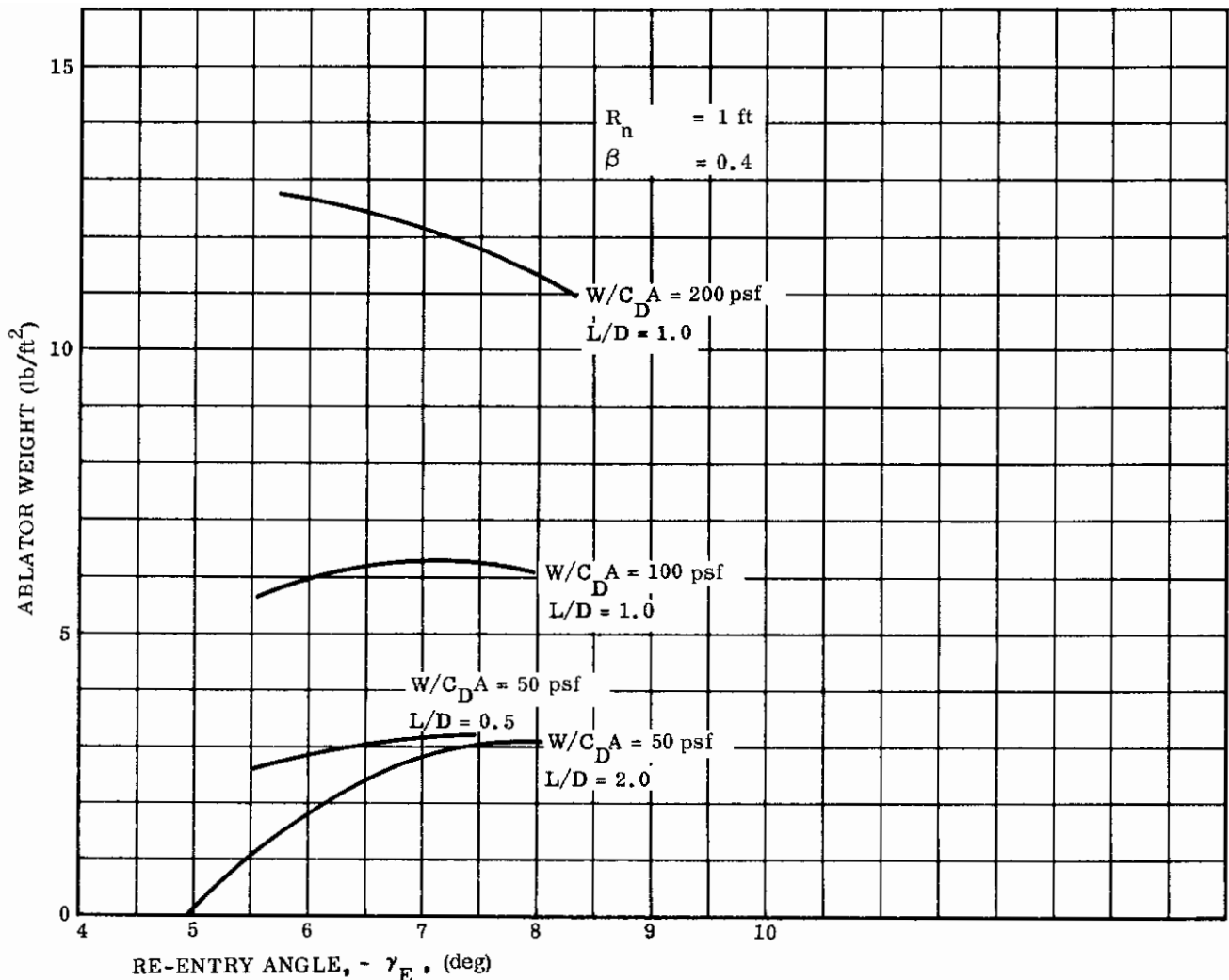


FIGURE 49. STAGNATION POINT ABLATOR REQUIREMENTS FOR  $(\epsilon_w^{1/4} T_w)$  OF 4000 R

radiation corresponding to the given  $(\epsilon_w^{1/4} T_w)$ , used throughout the entire absorp-  
 tive period, resulted in weight requirements being slightly underestimated. Radiation  
 was overrated during the early portion of re-entry. This effect was most pronounced  
 for the smaller re-entry angles and lower  $W/C_D A$  trajectories. Accounting for the  
 latter effect would tend to make the lower  $W/C_D A$  curves more nearly flat. The light  
 glider with an  $L/D$  of 2, and  $W/C_D A$  of 50 psf required essentially no ablator at the  
 shallower entry angles. The calculations were based on the following approximations:

1. The effective heat of ablation is represented by

$$Q^* = \frac{\dot{q}_{net}}{\dot{m}} = \frac{\dot{q}_c - \epsilon_w \sigma T_w^4}{\dot{m}} = \alpha + \beta (h_s - h_w) \approx \frac{\beta V_\infty^2}{2gJ} \text{ Btu/lb}$$

where:  $V_{\infty}$  = free stream velocity  
 $g$  = gravitational acceleration  
 $J$  = mechanical equivalent of heat  
 $\alpha$  = heat absorbed, plus heat due to phase change, chemical reactions, etc. (usually between 1000 and 2000 Btu/lb)  
 $\beta$  = transpiration factor  
 $\dot{m}$  = mass rate of ablation  
 $(h_s - h_w)$  = total enthalpy minus wall enthalpy  
 $\epsilon_w$  = surface emittance  
 $T_w$  = absolute wall temperature

2. Structure reached radiation equilibrium temperature after

$$\dot{q}_c = 200 \text{ Btu/ft}^2\text{-sec}$$

3. Shock layer radiation neglected (Ref. 5 and 20)

4. Negligible heat transfer to substructure.

For most high-temperature ablators, the effective heat of ablation given by the approximation  $Q^* \approx \frac{\beta V^2}{2gJ}$  leads to ablator weights 10 to 15 percent high for  $\alpha = 1500$  Btu/lb,  $\beta = 0.5$ ,  $T_w = 4500$  F, and for the range of free stream velocities of interest.

A detailed analysis of the specific ablation-radiation system is necessary for a more precise evaluation of heat protection weight requirements. Such an analysis should account for transient effects, consider local flow fields resulting from vehicle dynamics, and include a representation of the geometry. In general, the wall temperature and emittance will not be constant; moreover, the effective heat of ablation is not depicted by the above equation for some materials.

#### 4.2.1 Detailed Ablation Analysis

To assess the comparative effectiveness of various absorptive systems for given entry configurations, the heat protection afforded by nylon phenolic and quartz was determined. Quartz (fused silica) is categorized as a glassy type of ablator that demonstrates high viscosity at elevated temperatures but a rapidly decreasing viscosity with only small additional increments in temperature. Melting and partial vaporization are characteristics of the high-temperature behavior of the material. Phenolic nylon, an organic composite, is a low-conductivity, char-forming ablator.



Its complex ablative process may be described by a dual moving boundary. Precise phenomenological knowledge of reinforced-plastic charring ablators is severely restricted, especially for a super-orbital and transitory application. Information in question includes surface temperature conditions along with mechanical, thermal, and chemical interactions between char surfaces and flowing gas in the boundary layer. Phenolic nylon ablative behavior for this study was derived principally from surface erosion information (limited available flight data) and surface energy balance calculations.

This extension to the thermal absorption studies -- determining erosion and transient temperatures of nylon phenolic and fused quartz -- again presupposed a coating of just sufficient thickness to protect the given nose cap only during the period of most intense heating. The ablative coating, as in the case of the magnesia, was to be completely consumed when the heat rate subsided from the peak to the stated level of 200 Btu/ft<sup>2</sup>-sec. Iterative calculations were required to determine initial thicknesses of ablative coating for each trajectory. The coatings were stipulated to be in direct contact with, and supported by, an 0.04-inch tungsten shell substructure.

The lifting entry trajectories of 36,000 fps examined in this ablative study pertained to the medium glider ( $L/D = 2.0$ ,  $W/C_D A = 200$  psf,  $\gamma_E = -8.9$  degrees) and to the blunt semi-cone ( $L/D = 0.5$ ,  $W/C_D A = 50$  psf,  $\gamma_E = -7.6$  degrees) each entering the earth's atmosphere at the steepest flight path angle (10-g deceleration limit). The comparatively hot trajectory exhibited a maximum heat rate roughly twice that of the cooler trajectory; the elapsed time between start of entry, through  $\dot{q}_{max}$ , to the instant of functioning in the passive radiation mode was also nearly in the ratio 2:1. For similar-shaped heating pulses, the total heat load for the relatively hot trajectory was approximately four times larger than that for the less severe entry environment. Resultant curves of hot-wall heat rate versus flight time from the 400,000-foot altitude are presented in Figures 50 and 51. Erosion histories were determined as were comparative temperature histories at three nodal locations ranging between the ablator mid-depth and the substructure. Approximate temperature gradients over a defined thickness for any given time were obtained from the known locations on the temperature response curves.

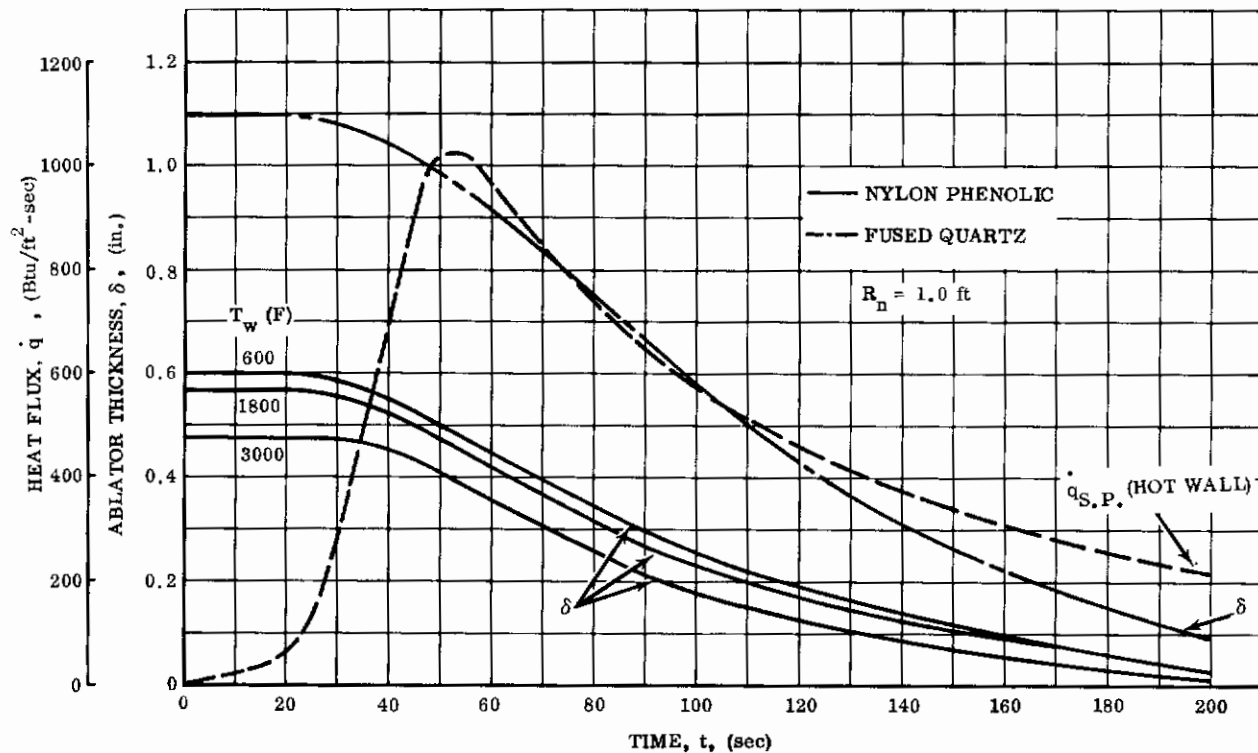


FIGURE 50. CONVECTIVE HEAT RATE AND ABLATION THICKNESS; Nylon Phenolic and Quartz --  $L/D = 2.0$ ,  $W/C_D A = 200$  psf

Thermo-physical properties for an equal mixture of nylon fibers and phenolic resin were developed from References 16, 21, and 22. The most pronounced uncertainty in material properties was the response of the nylon phenolic, i.e., its "effective" heat of ablation. The difficulty was due primarily to an imperfect description of the basic erosion process, and secondarily to the lack of consistent property data at elevated temperatures. A particularly restrictive assumption was neglecting that the final ablator thickness might literally be torn from the substrate near the end of the ablation period.

After reducing and comparing the LMSC internal flight test data and the information of Reference 22, instantaneous char removal at the specific outer wall temperatures of 600, 1500, and 3000 F was assumed. Surface temperatures with a char coating present may, for some conditions, approach the 3000 F value. The intermediate temperature selection was arbitrary. The lower temperature ( $T_w = 600$  F) represented virgin material (complete char removal). With a probability of significant radiation from the surface of a carbonaceous formation, a total normal emittance of 0.8 was chosen.

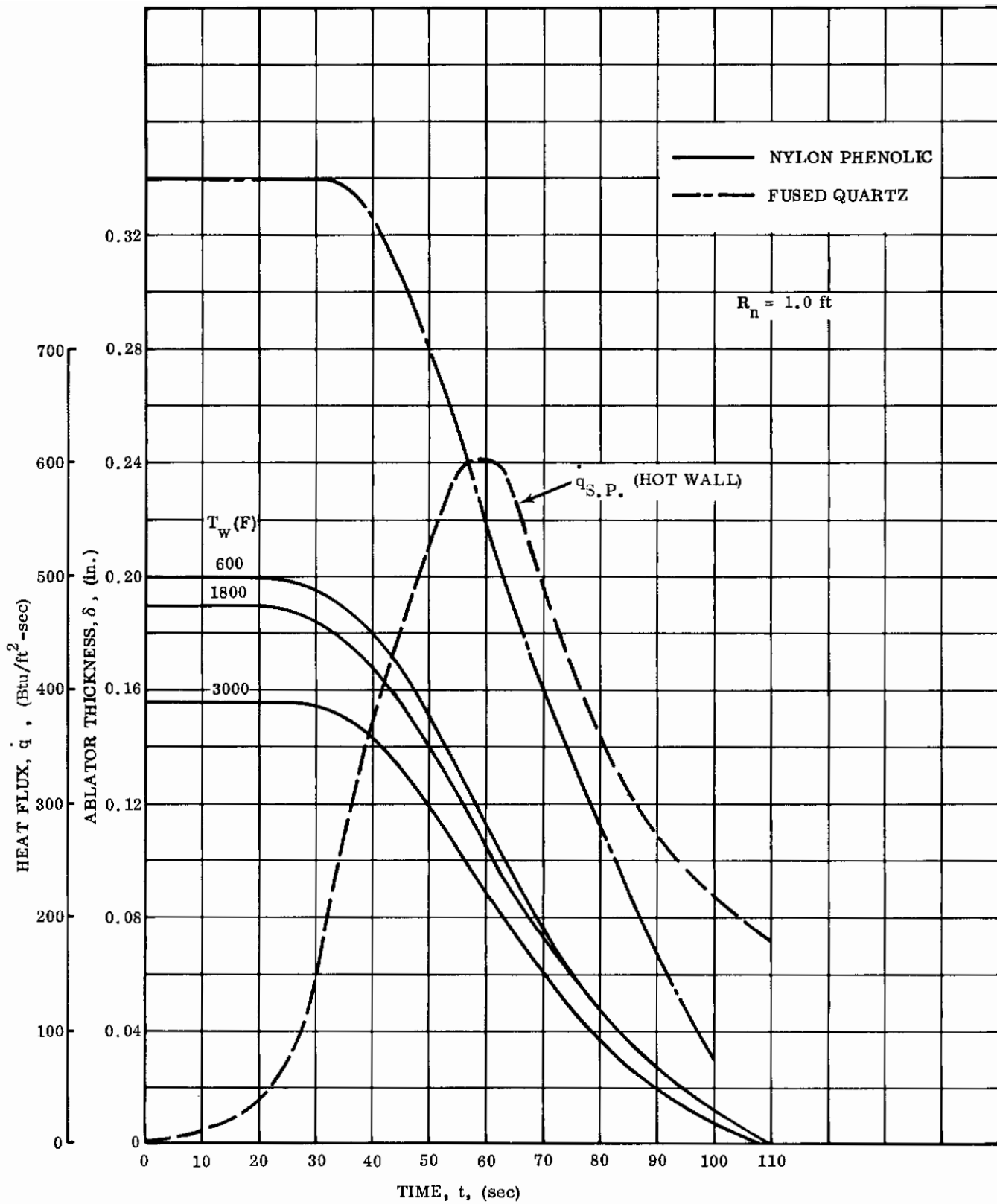


FIGURE 51. CONVECTIVE HEAT RATE AND ABLATION THICKNESS; Nylon Phenolic and Quartz --  $L/D = 0.5$ ,  $W/C_D A = 50 \text{ psf}$

Quartz thermal properties were better defined. The most favorable data were selected for the study, namely, fused silica infused with carbon black, which provided a total emittance,  $\epsilon_w = 0.5$ . The effects of surface radiation entered the program only through the governing equations. Necessary modification was required for the Avco analytical approach - defining total effective heat of ablation as including both the material ablation and total radiation; in this study, an effective heat of ablation ( $Q^*$ ), was calculated neglecting internal and surface radiation.

The program utilized computed the external surface radiation, but did not account for the possibility of lowering the internal temperature and raising the ablator viscosity during ablation as a result of internal radiation through the glassy material. The Avco technique can be constructed to yield more favorable ablator responses than was evident for the quartz analysis presented here. Fused quartz materials data were calculated from information available in Reference 16, 22, 23, and 24.

In addition to heat rates, Figures 50 and 51 show the time-variation of stagnation point ablator thicknesses for the two vehicle configurations. For the winged glider (Fig. 50), the required coating of nylon phenolic for the lowest node-removal temperature assumed was 0.60 inch. This coating is approximately half the necessary thickness of fused silica, 1.10 inches. Similar observations may be made for the semi-cone vehicle (Fig. 51), where the corresponding thicknesses of nylon phenolic and fused silica were 0.20 and 0.34 inch, respectively. The non-zero thicknesses at the end of the heat pulse noted on the curves arose from the time steps in the finite difference technique. These residual thicknesses induce only a small error in the analysis.

A summary of recessions and unit ablative weights is presented in Table 4. The phenolic nylon density was taken as 90 lb/ft<sup>3</sup>, and that for virgin quartz as 144 lb/ft<sup>3</sup>.

The ratios of required unit ablator weights for the glider of medium wing loading and for the blunt semi-cone frontal cap were approximately in the ratio 3:1.

**TABLE 4**  
**SUMMARY OF NYLON-PHENOLIC AND QUARTZ ABLATION**  
 $R_n = 1.0$  foot

Material	$T_w$ (F)	Vehicle Configuration			
		Medium Wing Load Glider		Semi-Cone	
		$\delta_{abl}$ (in.)	$W_{abl}$ (psf)	$\delta_{abl}$ (in.)	$W_{abl}$ (psf)
Nylon-phenolic	600	0.600	4.5	0.200	1.5
	1800	0.570	4.3	0.190	1.4
	3000	0.480	3.6	0.156	1.2
Quartz	3400	1.100	13.2	0.340	4.1

The respective temperature responses of nylon phenolic and quartz are compared in Figure 52 and 53 for the winged vehicle. Two temperature nodes are presented for each ablator, and their locations are shown on the figures. The third and innermost nodal position represented the average temperature within the thin-wall tungsten substrate. The temperature response for the blunt semi-cone vehicle is repeated in Figure 54 and 55 for each ablator.

As the ablator thickness approached zero, the nylon phenolic showed the more severe temperature response  $\partial T/\partial t$ , an indication of thermal shock conditions. Even though the quartz response was less steep, thermal shock could understandably be a problem here, too. The thermal conductivity of nylon phenolic was roughly an order of magnitude lower than that for quartz. Thus, as the rapidly moving ablation surface approaches a particular node, an abruptly rising temperature pulse is imposed locally. As the node in question reaches the ablation temperature, it is discontinued in the computation. The program, upon executing nodal removal, continues calculations on the next nodal interval.

The nylon phenolic specific heat capacity was roughly twice that of the quartz. Insulating effectiveness of the two materials may be related through the parameter  $\rho k/c$ . A comparison of insulator quality for a given thickness of the phenolic nylon and quartz shows that the former was about thirty times more efficient.

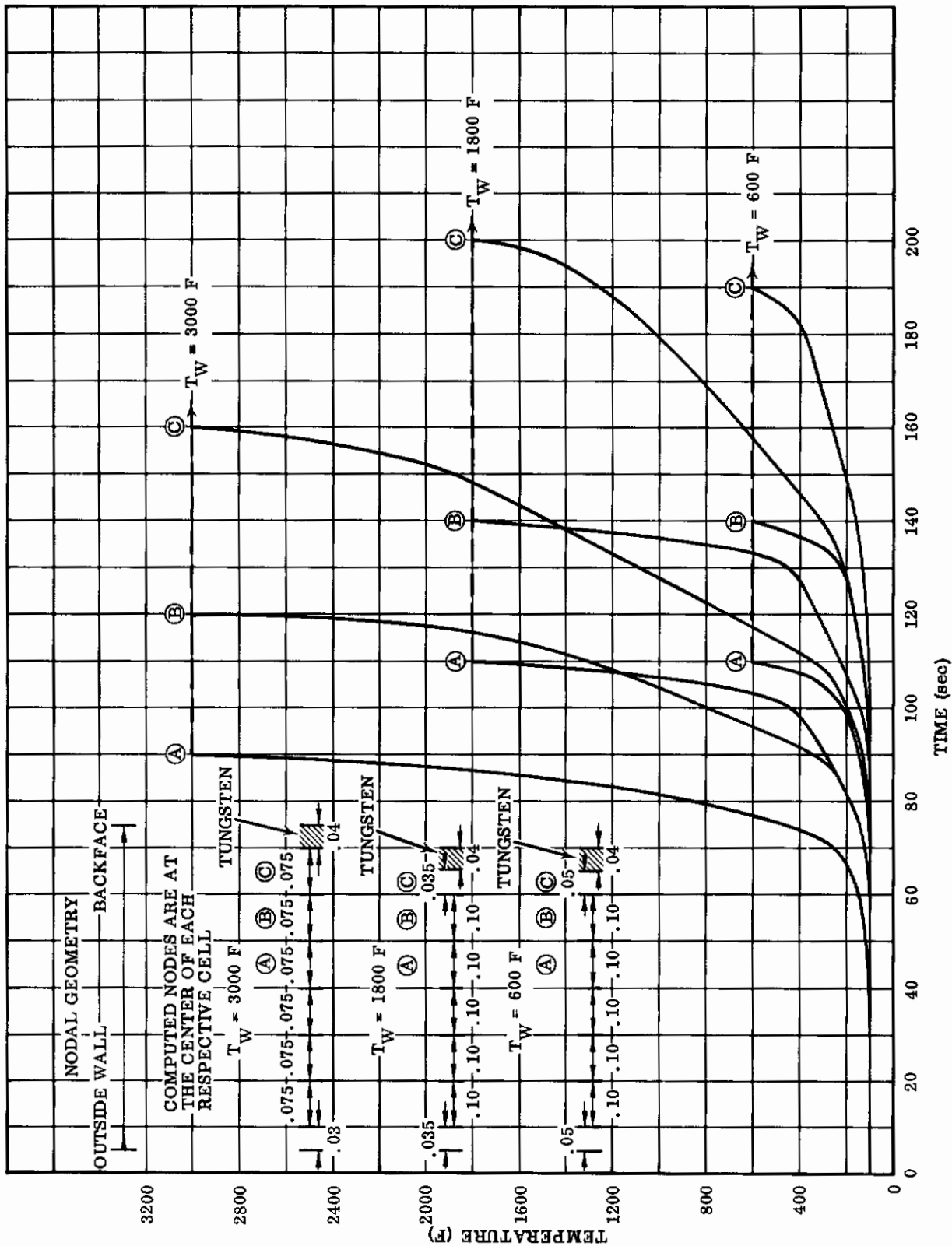


FIGURE 52. TEMPERATURE RESPONSE; Nylon-Phenolic Ablator --  
 $L/D = 2.0$ ,  $W/C_D A = 200$  psf

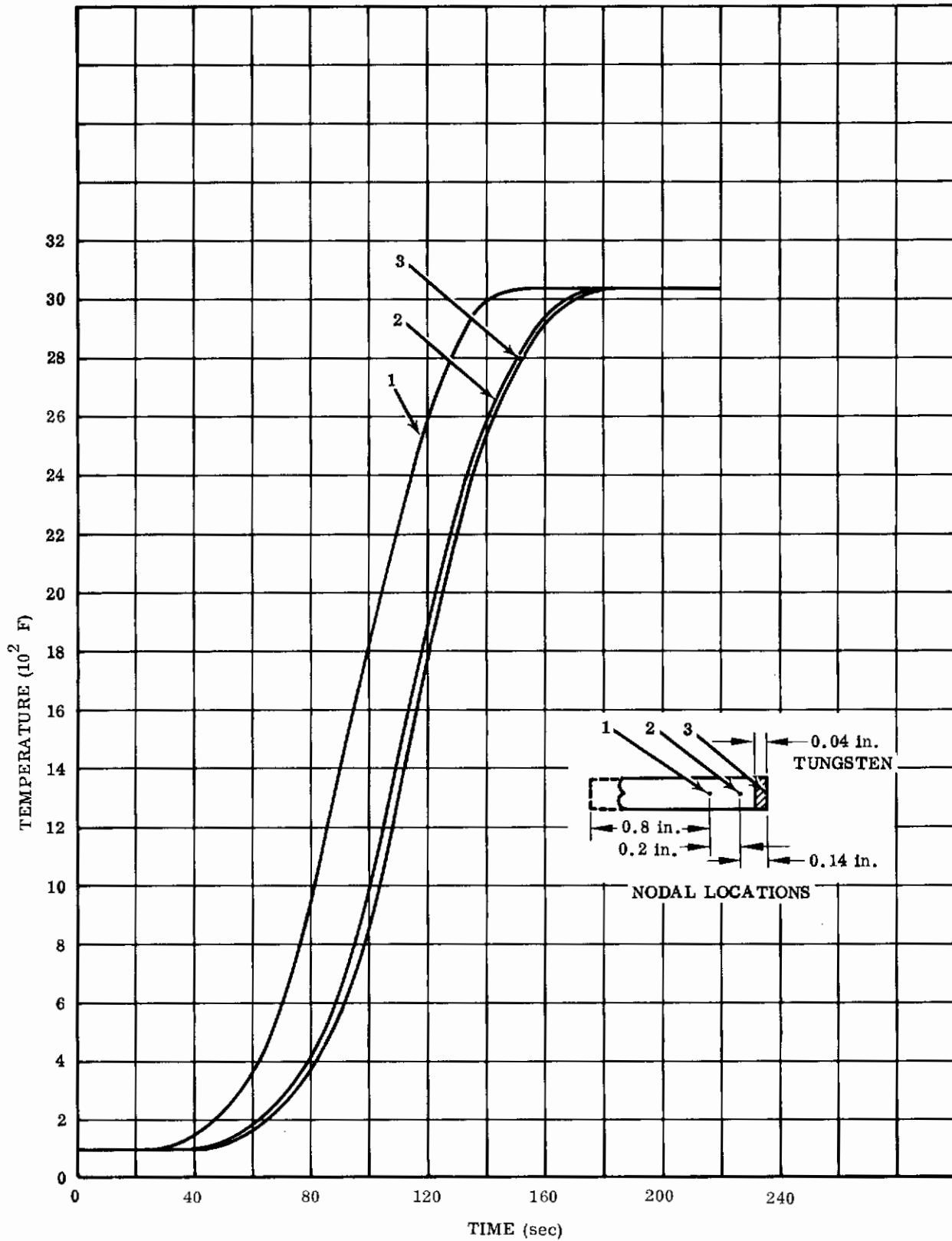


FIGURE 53. TEMPERATURE RESPONSE; Quartz Ablator-- L/D = 2.0,  $W/C_D A = 200$  psf

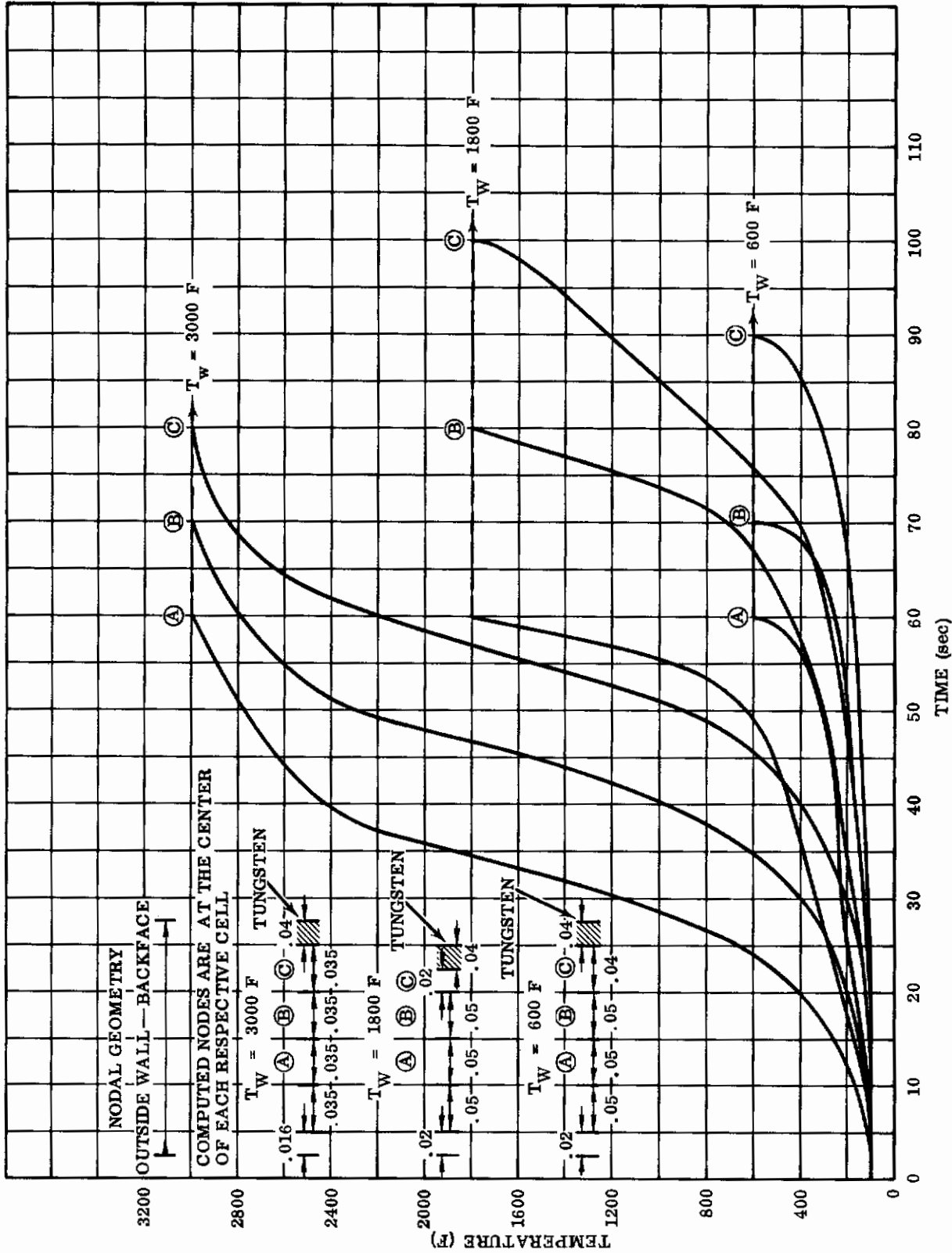


FIGURE 54. TEMPERATURE RESPONSE; Nylon-Phenolic Ablator --  
 L/D = 0.5, W/C<sub>D</sub>A = 50 psf



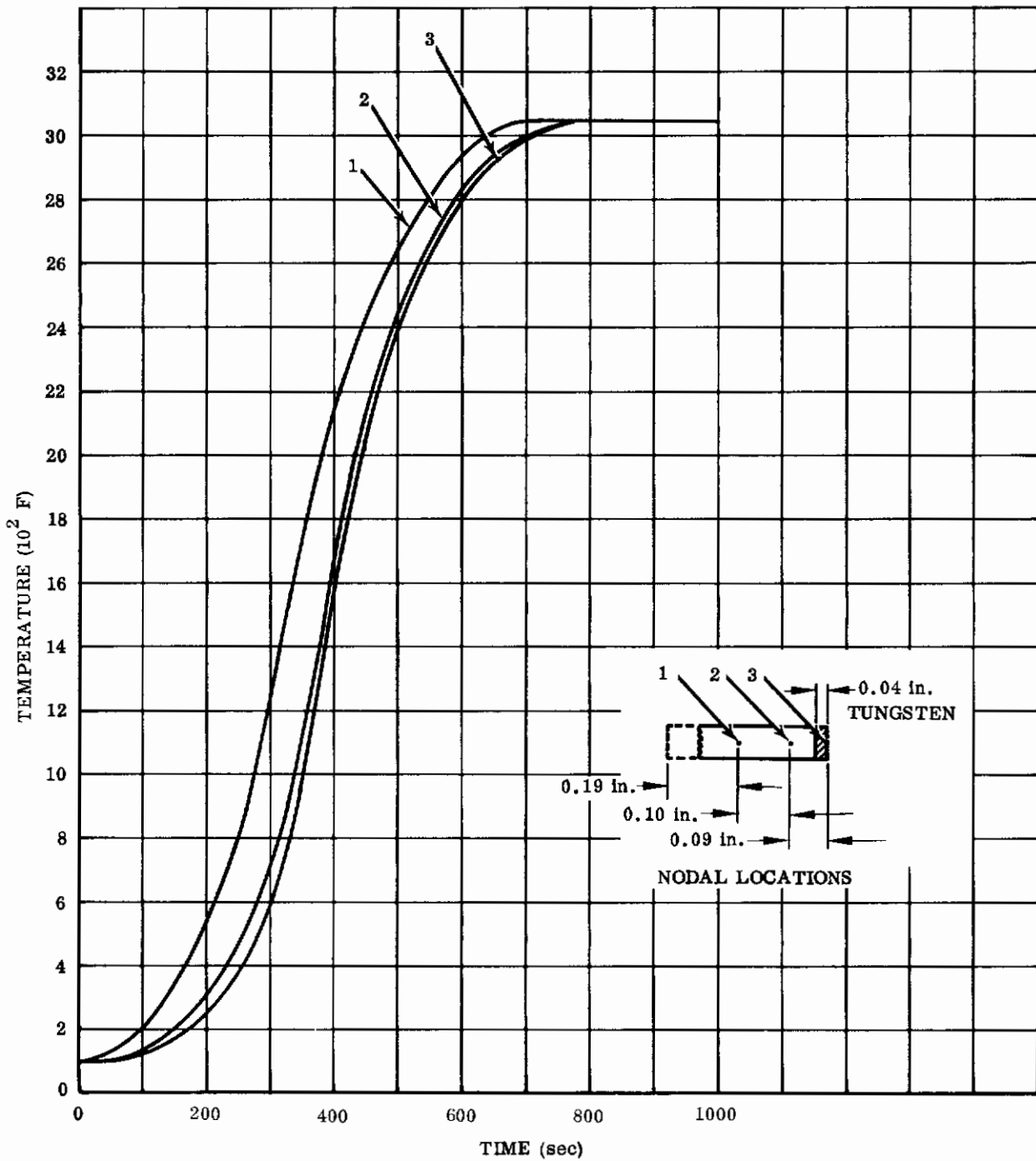


FIGURE 55. TEMPERATURE RESPONSE; Quartz Ablator --  $L/D = 0.5$ ,  $W/C_D A = 50$  psf

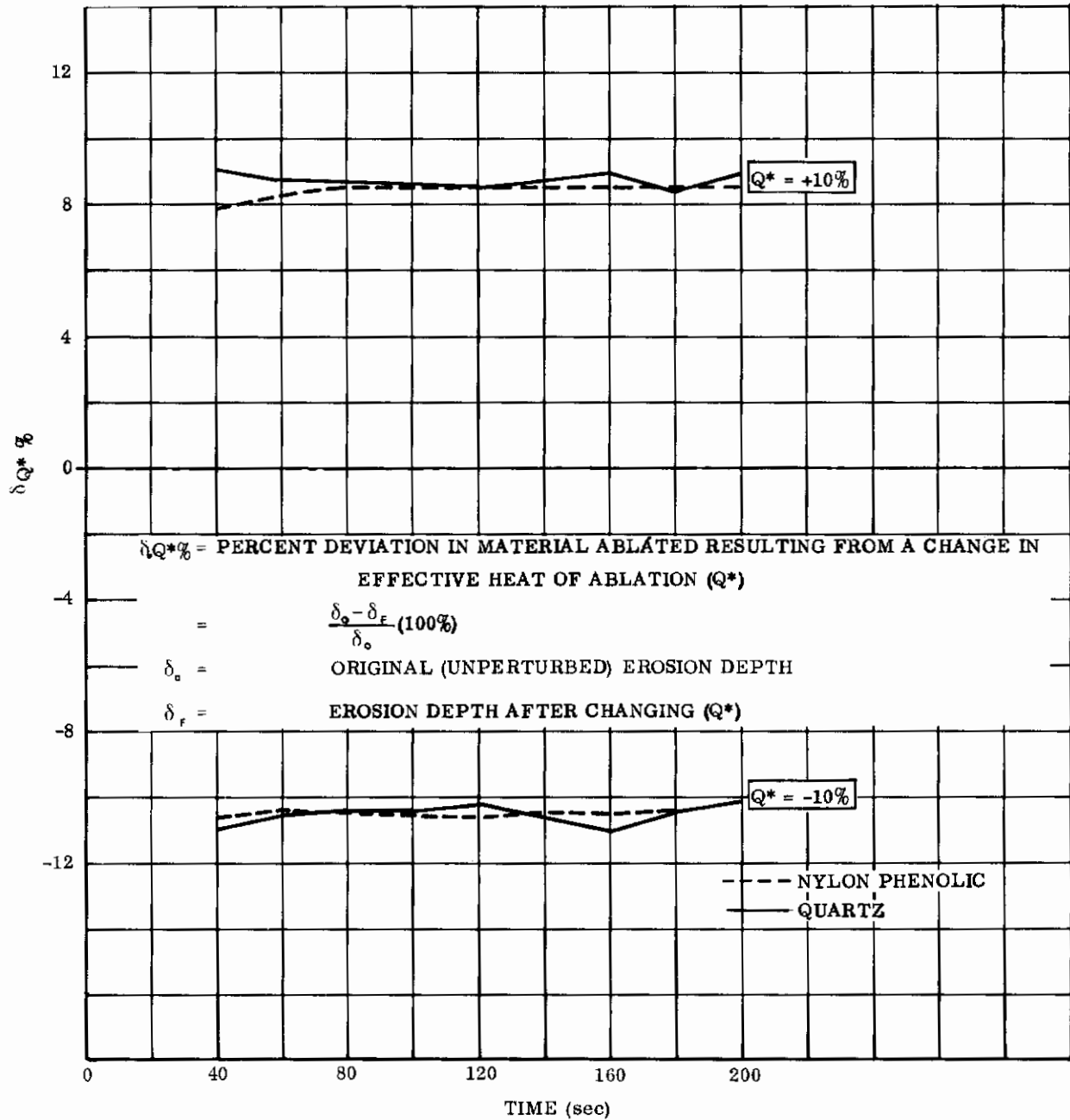


FIGURE 56. ERROR ANALYSIS IN ABLATOR EROSION FOR CHANGING EFFECTIVE HEAT OF ABLATION

## 4.2.2 Uncertainty in Thermal Properties

An error analysis of nylon phenolic and fused silica was undertaken to determine effects of uncertainties in thermal properties. The properties to be evaluated,  $k$ ,  $c$ , and  $Q^*$ , were each perturbed in magnitude by assigned fixed percentages of the original established values used in the previous ablation calculations:  $\pm 20$  percent deviation in thermal conductivities of the two materials;  $\pm 20$  percent in specific heats;  $\pm 10$  percent in effective heats of ablation. The presented results of these incremental variations, impressed one at a time, were the histories of erosion deviation and temperature deviation. In addition to showing thermal property influences in the solutions, the uncertainty analysis illustrated degree of accuracy of the numerical results through symmetry (or repetition) of positive and negative deviations about the zero value (Ref. 25).

Deviations in erosion of both nylon phenolic and quartz were only weakly dependent upon changes in thermal conductivity. The same conclusion was apparent for effects of variable specific heat, especially for nylon phenolic where the capacity effects were effectively "shielded" by the insulation capability. As might be expected in a surface erosion analysis, the influences of changes in effective heat of ablation were of greatest significance. The deviation in ablated material was approximately 1:1 for both nylon phenolic and quartz (Fig. 56).

Property errors had a much more significant effect upon temperature response than upon erosion. Temperature deviations were investigated at two nodal locations - one situated at nearly half the total depth of the cap, and the other at the back face of the substrate. Indications of temperature deviation were delayed in the substrate, but eventually proved to be higher in magnitude than for the node near the center of the ablator. The nodal temperature response, as indicated in Reference 25, was less influenced by an error in effective heat of ablation than by errors in conductivity or capacity.

## 4.2.3 Conclusions on Ablation Analysis

Basic shortcomings were revealed in the proposed method of combining transitory ablation with subsequent substructural radiation protection for trajectories that develop large heat rates. One of the more important restrictions was the lack of

precise knowledge concerning fundamental mechanics of ablator systems; the investigator cannot predict with confidence the complete disappearance of the ablating surface when a pre-established heat rate is achieved. In addition to trajectory oscillations and atmospheric variations which could produce large fluctuations in incident heat, there remains the uncertainty in ablator performance due to material inhomogeneity. An ablative system could, as a result, conceivably fail earlier in the trajectory and at a more destructive heat rate. The conventional ablative system is customarily over-designed; reasonable uncertainties in the analysis are thus balanced by a reserve of ablation material which serves as insulation. From the standpoints of lower weight (Table 4) and relief in temperature response (influencing ablator retention), the nylon phenolic appeared more favorable than the fused quartz. Recognizing the small incremental weight contributed by an ablative overlay compared with the total weight of the refractory nose structure, then allowing at the termination of the severe heat pulse a slight residual of nylon phenolic (or a coating with similar ablation characteristics), a favorable external heat protection system is obtained for the trajectories investigated. Quartz ablation, in lieu of nylon phenolic, is predominantly characterized by melting and flowing rather than by vaporization and carbonaceous erosion. Melting of the quartz and its possible deposition on rearward portions of the structure could detrimentally alter the vehicle geometry and operation. At the highest temperature regimes, silica vapor may chemically attack the tungsten substrate causing a harmful oxidation and degradation of the primary shell structure. For either material utilized in the transitory (complete-consumptive) manner evaluated, severe gradients were indicated at late times, commencing about the last 10 seconds before nose removal, with expected high thermal stresses and acute problems of retaining thin oxidation-protective coatings on a refractory-metal nose shell.

#### 4.3 THORIA-TUNGSTEN HIGH HEAT CAPACITY - RADIATIVE SYSTEM

Transient application of the ablators magnesia, phenolic nylon, and quartz were considered. Each served primarily as a heat absorber, making use of the respective erosive characteristics of the materials; any insulative qualities they contributed were purely secondary. Also evaluated was a thin hot-wall concept which rapidly attained radiation equilibrium conditions due to its negligible heat storage capacity. Another thermal protection system considered possesses minimal erosive tendencies and embodies sufficient storage capacity (heat sink) to withstand peak

heating conditions prior to its functioning in a radiative mode. This concept was termed a capacitive-radiative structure and consisted of multi-layer (composite) elements.

One-dimensional transient temperatures were calculated for the frontal section cap and skirt regions of the winged glider, chosen because it was exposed thermally to the most severe lifting entry trajectory. Convective and gaseous radiative heat rates invoked are shown in Figure 57. All possible sources of thermal relief were considered: a high-temperature total normal emittance of 0.8 or better on a surface coating of thoria was assumed; an effective nose radius of 2.5 feet applied; an effective heat of ablation of 10,000 Btu/lb was assumed for the coating at a surface temperature of 5000 F minimum. Tungsten alloy shell analyses had indicated that a peak operating temperature of 4500 F should not be exceeded in the primary structure, such a limit imposed by the maximum permissible degradation of structural strength and stiffness. This series of exploratory studies was conducted basically to determine whether or not the composite non-ablative system was plausible.

The initial composite investigated consisted of a thorium oxide outer protective surface applied to a tungsten alloy frontal shell which, in turn, was backed by a non-structural insulative mat of fibrous ceramic in combination with a beryllium retaining shell. The internal beryllium shell, in addition to providing support for the fibrous insulative layer, contributed a small sink capacity to the system. A light ( $5 \text{ lb/ft}^3$ ) fibrous mat of zirconium oxide filaments ( $T_m = 4850 \text{ F}$ ) was evaluated as a potential barrier to the inward passage of heat from the high-temperature tungsten shell.

During the course of the investigation, a question arose as to what surface temperature could be sustained by an outer coating of thoria. Initial material evaluation studies indicated slight erosion at a limiting temperature of 5500 F; in subsequent plasma-arc tunnel tests, peak temperatures in the neighborhood of 5000 F were measured. Effects of the decreased surface temperature during ablation were determined by comparative solutions. In addition to only minor thermal erosion observed for thoria (less than 0.03 inch for all cases considered), its moderate thermal resistance and high thermal capacitance were advantageous in maintaining the temperature of the tungsten substructure within the 4500 F upper bound. Final specimen tests have indicated that temperatures of 5500 F are reasonable for low-pressure sublimation

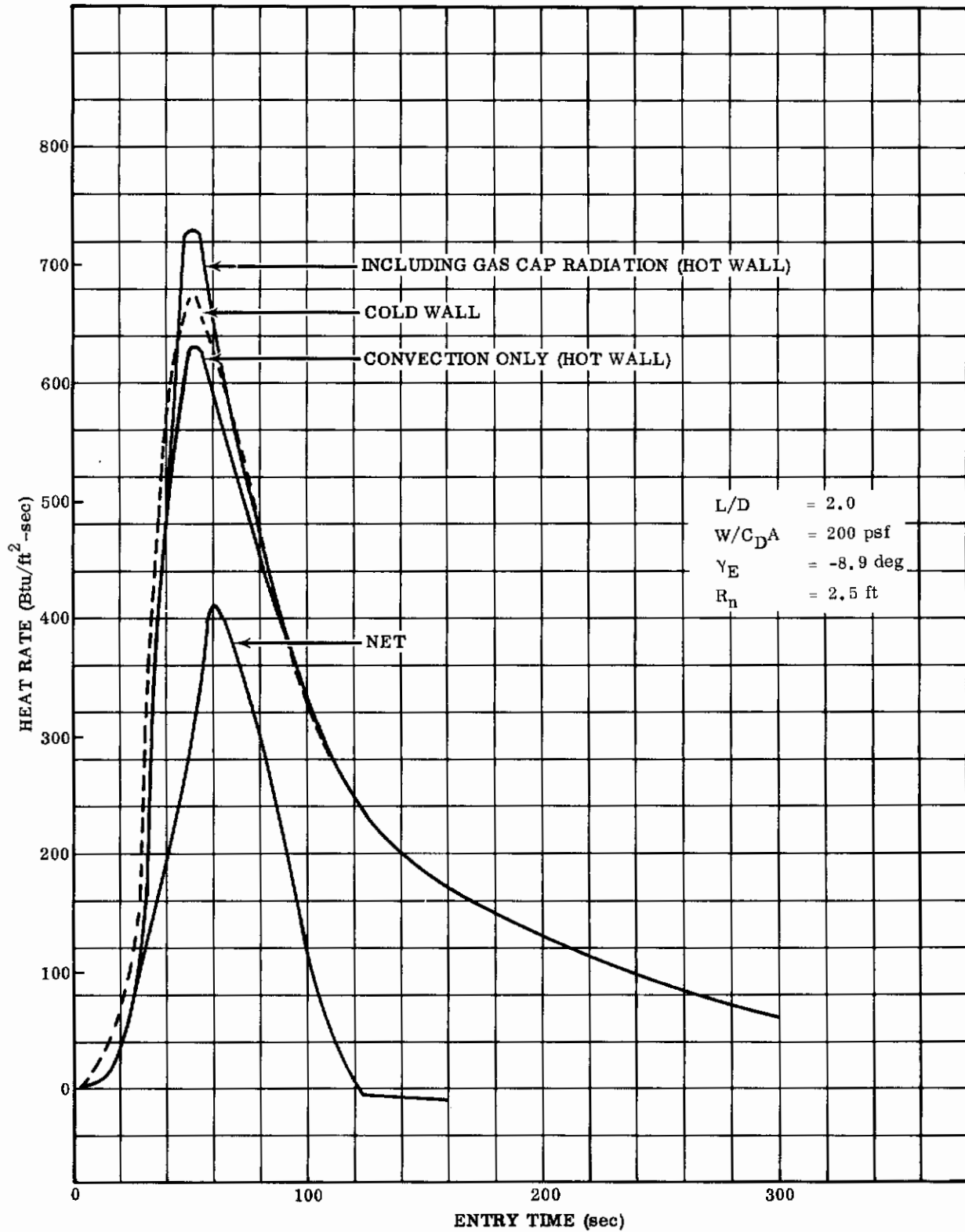


FIGURE 57. HEATING RATES FOR LIFTING RE-ENTRY TRAJECTORY

of thoria. Required thicknesses of thoria were determined for several internal thermal control systems, but temperatures attained throughout the primary structural system (protective ceramic coating and supporting tungsten shell) were insensitive to type of internal system. One internal cooling concept evaluated employed a boiling lithium heat sink; but, because of severe design implications associated with the transpiration approach, the low-density backface insulative layer received principal attention.

The cold-wall convective heat rate compared for a 2.5-foot nose radius is shown in Figure 57 for the period of maximum flux. Values were based upon laminar stagnation point relations of Fay and Riddell. Recent work by H. Hoshizaki at Lockheed Missiles and Space Company (Ref. 26) has resulted in a more precise correlation expression. A comparison between the Fay and Riddell values and those calculated from Hoshizaki's expression indicates that a maximum conservatism in convective heating of approximately ten percent may be implicit in the present analysis. Also shown in Figure 57 are hot-wall heat rates and combined hot-wall convection plus shock radiation rates, the latter having been the basis for the thermal analyses. The hot-wall reduction in energy transfer to the thoria was established from a surface temperature of 5000 F. For a particular ablation temperature, hot-wall heat rate was nearly independent of the coating thickness. The computed net heat rate to the surface - defined as incident hot-wall flux minus reradiation flux - is also given. Temperature-dependent emittance data were employed in solving for surface re-radiation. Radiation equilibrium was established at approximately 120 seconds of re-entry flight. For later times, the net rate was negative, indicating surface cooling. The cumulative net heating was 18,000 Btu/ft<sup>2</sup> at 120 seconds after atmospheric entry, compared with an integrated hot-wall heat input of 86,000 Btu/ft<sup>2</sup> for the entire 1387-second trajectory.

The high heat capacity composite structure initially evaluated consisted of the following components in order of their location from the outer surface:

- A 0.3-inch thoria overlay
- A 0.04-inch tungsten primary shell
- An air gap
- A 0.2-inch zirconia fibrous insulation
- A 0.04-inch tungsten secondary shell
- A Boiling lithium heat sink backed by a tungsten or tantalum support structure.

The temperature responses of the thoria surface, tungsten substrate, and lithium sink are shown in Figure 58. The flat portion of the surface temperature corresponds to thorium oxide sublimation of about 0.025 inch over a 60-second period. The limited recession indicated that the function of the coating in this design is primarily insulative. Changes in ablation temperatures or emittance had only slight effect on internal temperatures.

The system described above appeared impractical for several reasons:

1. Obtaining adequate structural integrity was questionable - fasteners to support the multi-element metallic structure are a source of heat "leaks" and localized thermal stress problems.

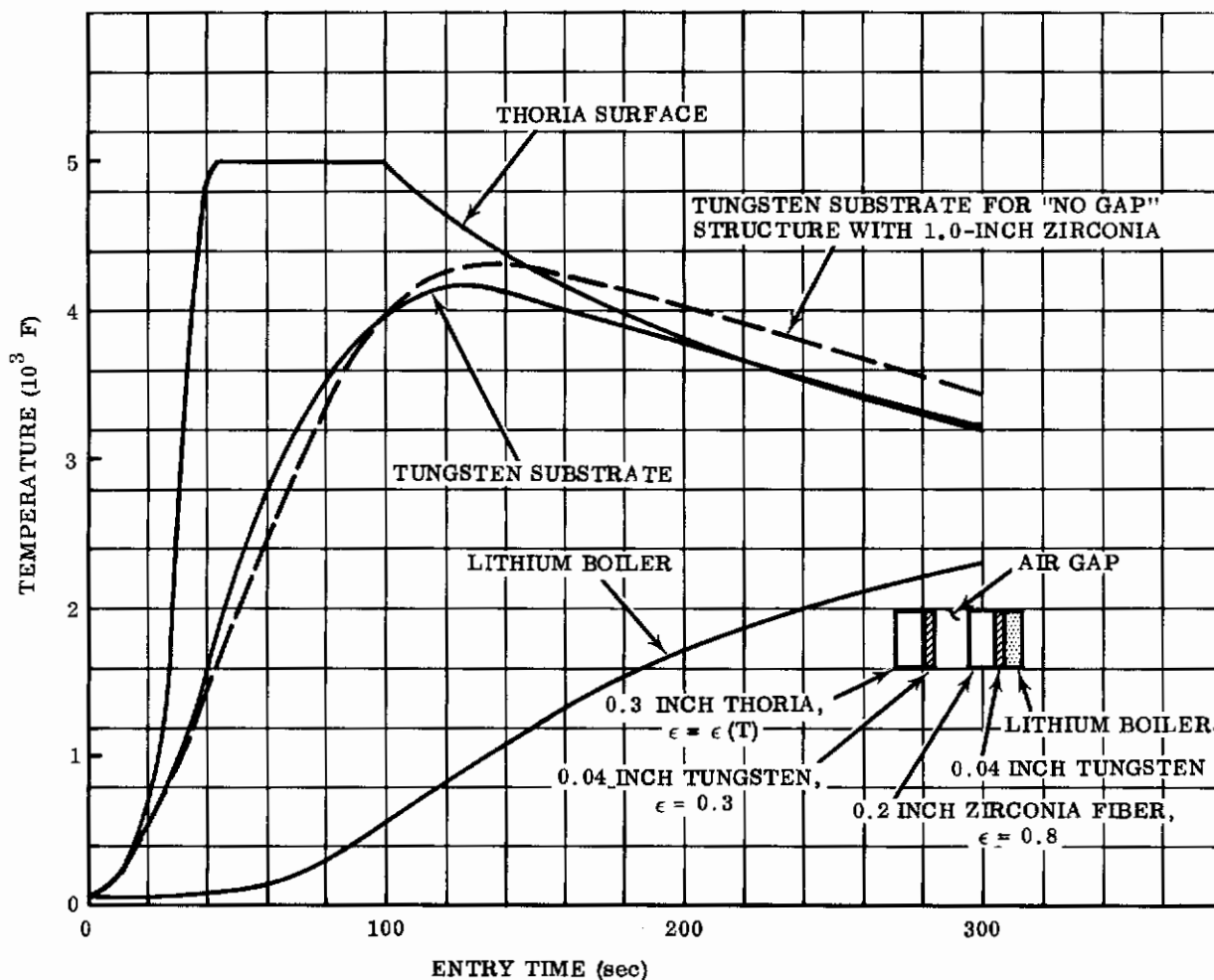


FIGURE 58. TEMPERATURE RESPONSE OF LITHIUM SINK STRUCTURE



2. Heat blockage to the back wall of the cap appears inadequate.
3. The internal placement of a lithium boiler may be dangerously ineffective. Transpiration benefits customarily associated with lithium phase-change cooling are practically unobtainable unless the lithium is placed adjacent to a porous exterior wall. Phase changes, moreover, with resulting high vapor pressures, act to the detriment of the internal structure unless venting methods are incorporated.

A simplified composite structure, incorporating a beryllium backing for a layer of insulative fibrous zirconia, was thus adopted. A section through this structure (external-to-internal) is described as:

- A thorium oxide overlay
- An 0.04-inch tungsten alloy shell
- A layer of fibrous zirconia insulation
- A beryllium sink

Surface heating conditions identical to those experienced by the original lithium-cooled composite were applied to a structure revised to include no air gap or lithium sink, but with thickness of zirconia matte increased to 1 inch. The dashed curve of Figure 58 shows the resulting tungsten substrate temperature. The configurational change lowered the tungsten shell temperature slightly early in re-entry because thermal radiation resistance across the previous air gap had exceeded the pure conduction resistance of fibrous zirconia. Later, at higher tungsten temperatures, the gap radiation resistance decreased, causing a decrease in tungsten temperature of some 200 F below that exhibited by the structure with rearward insulation contacting the shell. The zirconia fiber temperature response was similar for either composite structure.

High-capacity continuous (all adjacent layers in contact) structural composites, which involved protective thoria coatings less than 0.3-inch thick, were next investigated to ascertain the effects of overlay thickness upon tungsten substrate temperature. For thoria thicknesses of 0.1 and 0.2 inch, the tungsten substrate temperature exceeded the established 4500 F limit.

Minimization of temperature at the rear wall of the continuous composite shell (beryllium backface) was of concern because this temperature history influences the radiation and conduction heat transfer to the interior of the nose cap. Calculations

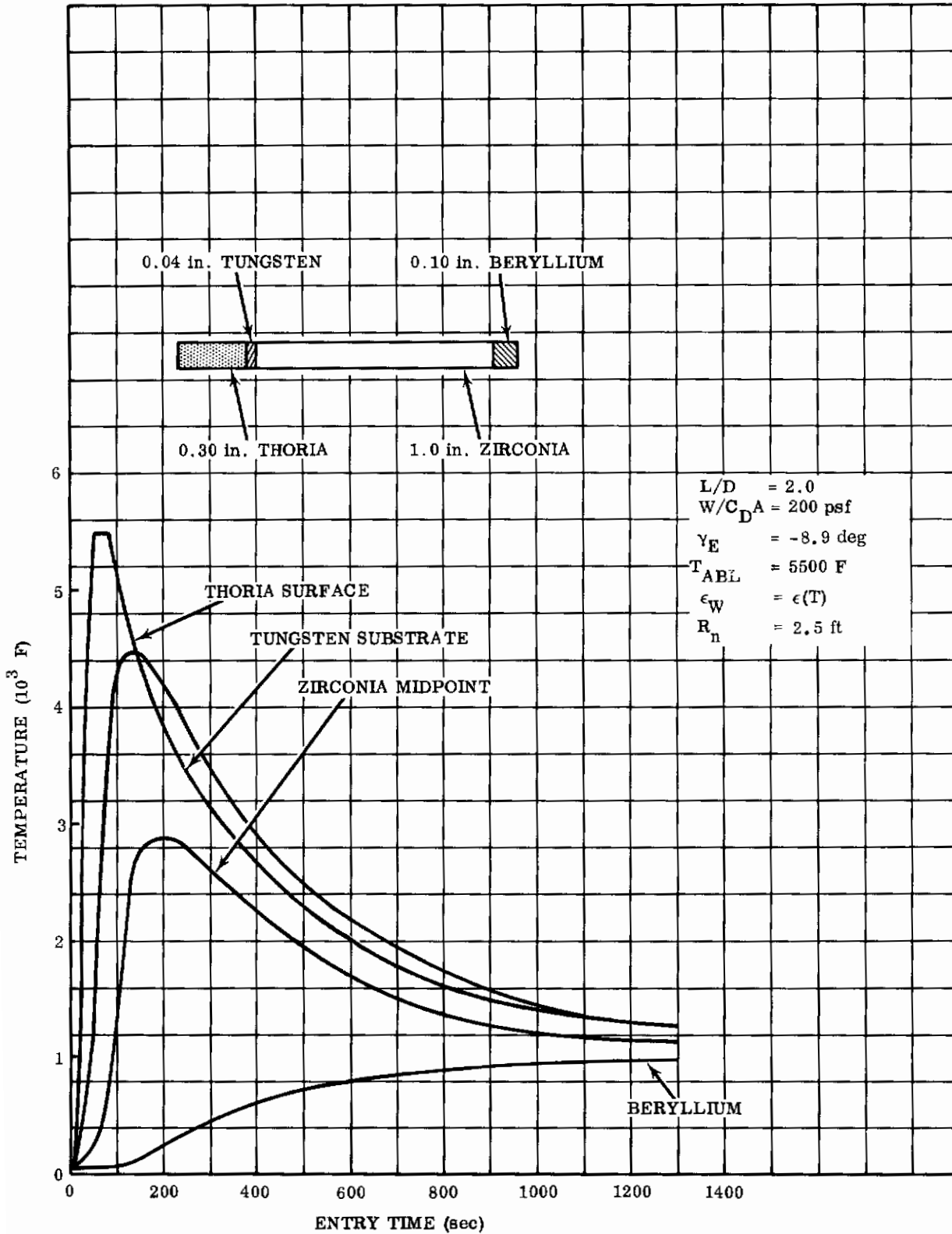


FIGURE 59. STAGNATION REGION TEMPERATURE RESPONSE; CAPACITIVE-Radiative Composite Structure

were made to determine relative effects of zirconia thickness versus beryllium thickness (Ref. 27). Two cases were compared: 0.4-inch  $ZrO_2$ , 0.2-inch Be; and 0.2-inch  $ZrO_2$ , 0.4-inch Be. Differences in temperature response at the rear surface were less than 100 F, and at 800-second flight time, a near-peak temperature of approximately 1000 F was attained in either case. With a beryllium-to-zirconia fiber density ratio of 22, a lighter weight insulation is provided by utilizing relatively greater thicknesses of the ceramic fiber. The maximum temperature at the beryllium backface was less than 1100 F for the entire 1387-second trajectory. The temperature response calculations were based upon a 0.3-inch external coating of thoria operating at a constant surface emittance of 0.8. Comparative temperature response calculations were performed to weigh the effects of incorporating into the solution either a constant value of total normal surface emittance ( $\epsilon_w = 0.8$ ) or temperature-dependent values for thoria. These latter variable values were provided in Reference 28 and ranged from 0.75 at 2700 F to 0.87 at 3600 F and above. For the constant and variable emittances, temperature responses were checked at corresponding structural locations: on the surface of a 0.2-inch thick thoria coating; within the tungsten substrate; and at the rear surface of the beryllium retaining shell. Temperatures were similar for both cases. The tungsten reached a maximum temperature of 4800 F when constant emittance was assumed; the  $\epsilon(T)$  values decreased the peak shell temperature to 4750 F. Beryllium temperatures were nearly identical for either set of surface emittance values.

Since in the foregoing evaluation the tungsten substrate exceeded its maximum design temperature of 4500 F, the thoria thickness was increased from 0.2 to 0.3 inch. Resultant temperature responses of the ceramic surface, tungsten substrate, the middle of the zirconia fiber insulation, and the beryllium sink are shown in Figure 59. The solution incorporated temperature-dependent emittance data and an ablation temperature of 5500 F. The 1-inch thickness of zirconia fiber insulation shown in Figure 59 should provide satisfactory thermal protection to the interior while contributing an almost negligible portion to the total system weight, 0.42 lb/ft<sup>2</sup>. The 0.3-inch thickness of thoria restricted the tungsten temperature to 4500 F while ablating only 0.01 inch.

The upper curve of Figure 60 depicts the heat rate into the 0.1-inch thick beryllium sink sketched in Figure 59 and located in the cap region, i. e., receiving

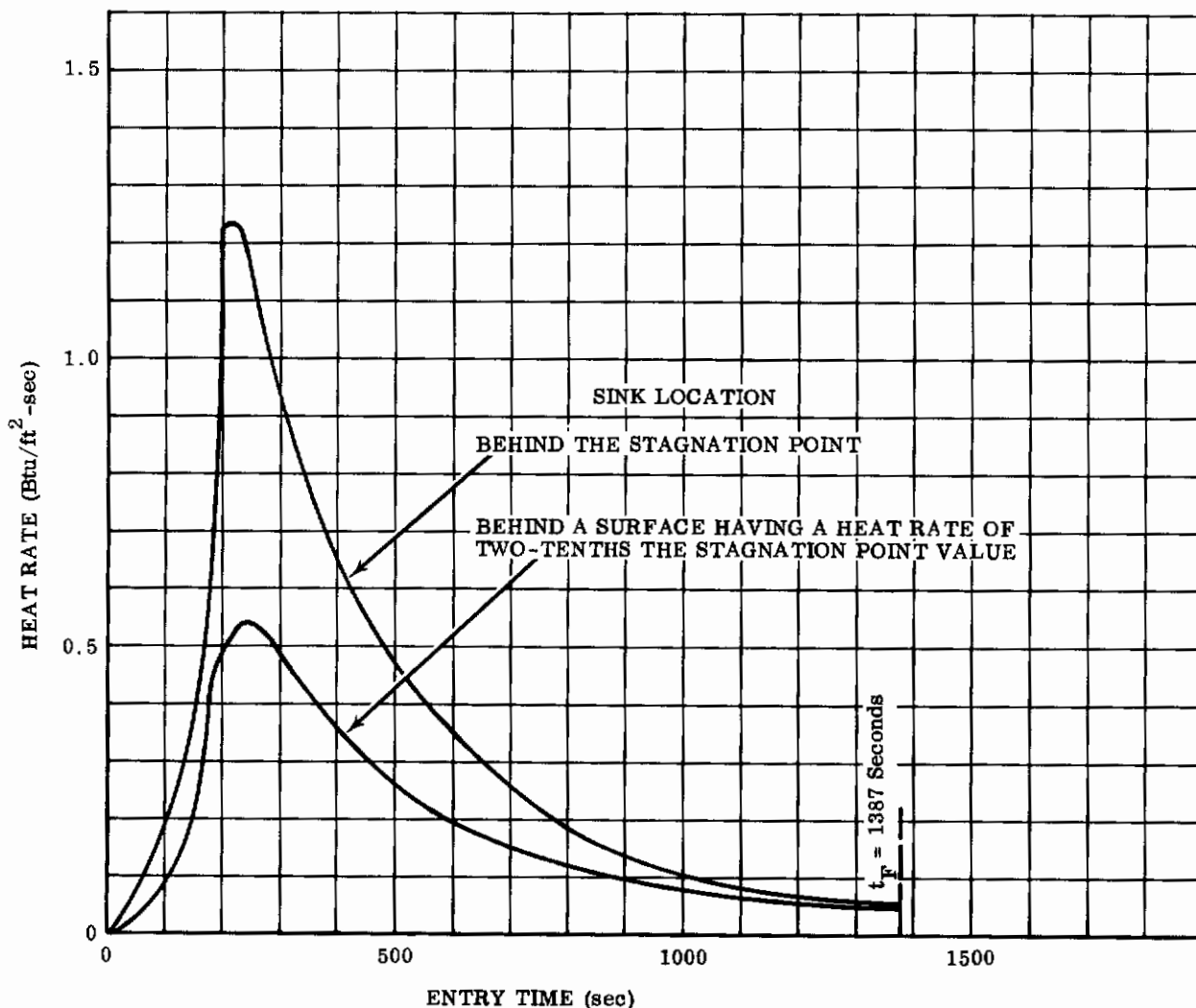


FIGURE 60. HEAT FLUX INTO BERYLLIUM SINK; 0.3-Inch Thoria Composite Structure

heat from the stagnation point. To approximate conditions to which an area of beryllium situated at a rearward conical skirt section would be exposed, additional heat flow calculations were made. The same composite slab configuration was assumed, but it was now subjected to an incident heat rate on the outer surface reduced to two-tenths the stagnation value. The aft-situated beryllium structure experienced heat absorption at a rate shown by the lower curve of Figure 60. These heat fluxes were used subsequently to describe the nose interior thermal environment.

Due to reduced heat rates on the skirt section, no thoria surface recession occurred, and a peak outer temperature of 3650 F was observed. With a peak tungsten operating temperature of 2840 F, structural weight reduction could be obtained by de-

creasing the coating thickness at points removed from the frontal section cap. A two-dimensional transient heating analysis with assumed laminar heating distribution was completed with the intended goal of establishing a tapered thickness of ceramic overlay.

The effects of reducing the ablation temperature from 5500 to 5000 F were examined for the same composite system coated with 0.3-inch thick thorium oxide; of particular interest were the insignificant reductions in maximum tungsten and beryllium temperature of 130 and 20 F, respectively. Ablation at the 5000 F surface temperature was of prolonged duration, extending from 25 to 60 seconds; the surface recession increased from 0.010- to 0.025-inch thickness for the lower ablation temperature.

The heating analysis on high heat capacity-radiative composites indicated the following conclusions:

1. A continuous composite structure (no inter-layer air gaps), consisting of a ceramic oxide coating protecting a tungsten alloy shell and insulated on the inside by a layer of fibrous zirconia, retained by a beryllium sink, performed satisfactorily in the combined modes of absorption and radiation.
2. Approximately an 0.3-inch coating of thoria was required on the frontal cap to limit the primary refractory structure temperature to 4500 F.
3. At the higher ablation temperature of thoria, 5500 F, less than 0.01 inch of surface recession occurred. Should ablation occur at 5000 F, approximately 0.025 inch of surface recession results.

The proposed capacitive-radiative configuration appeared practical and adequate from the standpoint of thermal protection afforded, structural simplicity, and reliability. Several considerations, however, yet remained, notably strength, fabrication limitations, allowable temperature response in the nose cap interior, and weight, any one of which may indicate a need for further modification in the basic structure. The 0.3-inch thickness of 70 percent dense thorium oxide ( $\rho = 437 \text{ lb/ft}^3$ ) results, for instance, in a stagnation region coating weight of 10.5 psf .

#### 4.3.1 Two-Dimensional Heat Transfer in Composite Structure

Two-dimensional heat transfer calculations were made to determine transient temperature distribution throughout the continuous slab for the high-capacity composite glider frontal section just considered. The manner of graduating external coating

thickness, fore-to-aft, to conserve weight was also determined, considering meridional heat flow as well as inward flow. The actual nose configuration was approximated by an axially symmetric conceptual shape (an oblate ellipsoid-cone) to simplify the solution. While expedient to the solution, the body of revolution provided an accurate thermo-structural representation of the critical, high-temperature cap region. An overlay of reinforced thoria, serving as thermal and oxidation protection for a monocoque 4500 F tungsten alloy shell, was continued basically unchanged from previous studies.

The nose shape proposed for use in the medium wing-load glider analysis ( $W/C_D A = 200$  psf,  $L/D = 2.0$ ,  $\gamma_E = -8.9$  degrees) is shown in Figure 61. The axis of symmetry of the frontal section was aligned throughout re-entry with the vehicle flight path, denoted by the free stream velocity vector  $V_\infty$ .

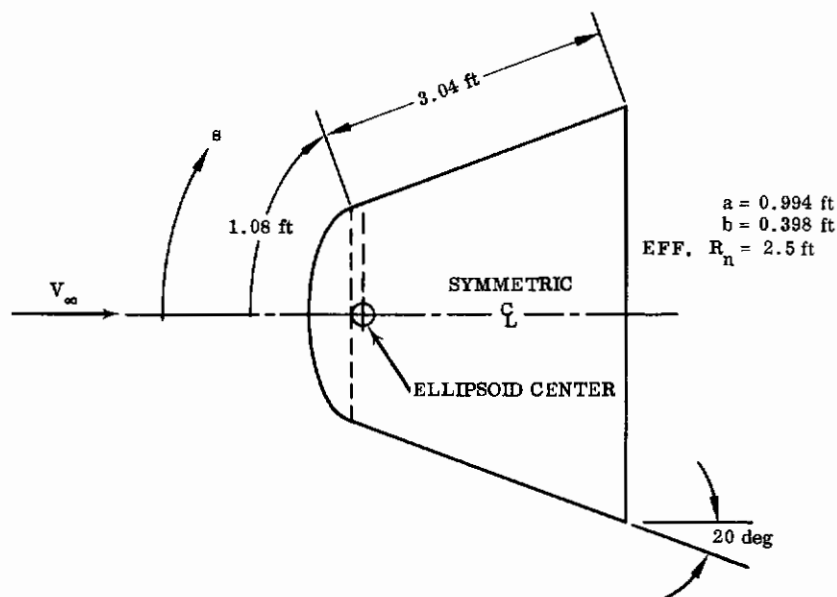


FIGURE 61. WINGED VEHICLE REFRACTORY NOSE CONE

A schematic sectioned view through the composite thickness was presented in Figure 59. In the coating taper analysis, the tungsten substrate, zirconia fiber insulation, and beryllium retaining structure are assumed to have uniform thickness.

Stagnation point convective heating used in the present analysis was obtained from the Hoshizaki correlation equation (Ref. 26). Invoking a constant value of

stagnation-to-free stream density ratio of 17 was found valid (Ref. 7 and 29) for the portion of the trajectory comprising major heat rates, zero to 200 seconds. The cold-wall convective heat rates were then given by the expression

$$\dot{q}_c = 820 (\rho_\infty/\rho_0)^{0.5} (V_\infty/10^4)^{3.19} R_n^{-0.5} \text{ Btu/ft}^2\text{-sec}$$

For velocities below 38,000 fps, this expression gives heat rates slightly less than those obtained formerly (Fig. 57). Again, equilibrium gas cap radiation was included in the subsonic portion of the shock layer. With unlikely transition of the vehicle boundary layer to turbulent (shown in the previous verification of momentum thickness Reynolds number), a laminar heating distribution about the body was presumed throughout entry.

Results are given in terms of composite structure temperature response at various stations and thicknesses of thorium oxide coating to limit the tungsten alloy substrate to 4500 F everywhere on the nose shell. A plot of thoria thickness versus body position is shown in Figure 62. For the updated heat rates, a maximum coating thickness of 0.29 inch throughout the stagnation region, tapering to 0.1 inch on the conical skirt appeared satisfactory. Although diminished heating rates on the conical nose section permitted a further reduction in overlay thickness for surface distances (s) greater than 1 foot, the 0.1-inch thickness was felt to be a minimum based on thoria fabrication requirements, that is, imbedding a reinforcing mesh.

At the start of re-entry (400,000 feet), the entire nose cap was assumed to be stabilized at the uniform temperature of 60 F. The initial temperature has negligible influence on the computed response because of the tremendous energy absorbed by the system throughout subsequent re-entry. Thicknesses of the tungsten substrate, filamentary zirconia matte, and beryllium shell were held constant at 0.04, 1.0, and 0.10 inch, respectively, for ensuing temperature calculations. Ceramic overlay thicknesses were varied as shown in Figure 62.

Thoria surface temperatures as a function of distance from the stagnation point are plotted in Figure 63 with entry flight time as the parameter. At 80-second flight, the thoria surface had reached the ablation temperature of 5000 F in a region from the stagnation point to the sonic point, s nearly 0.9 foot. Ablation occurred within this cap region from approximately 50 through 90 seconds entry time. All rearward thoria surfaces, including the shoulder and conical skirt sections, experienced

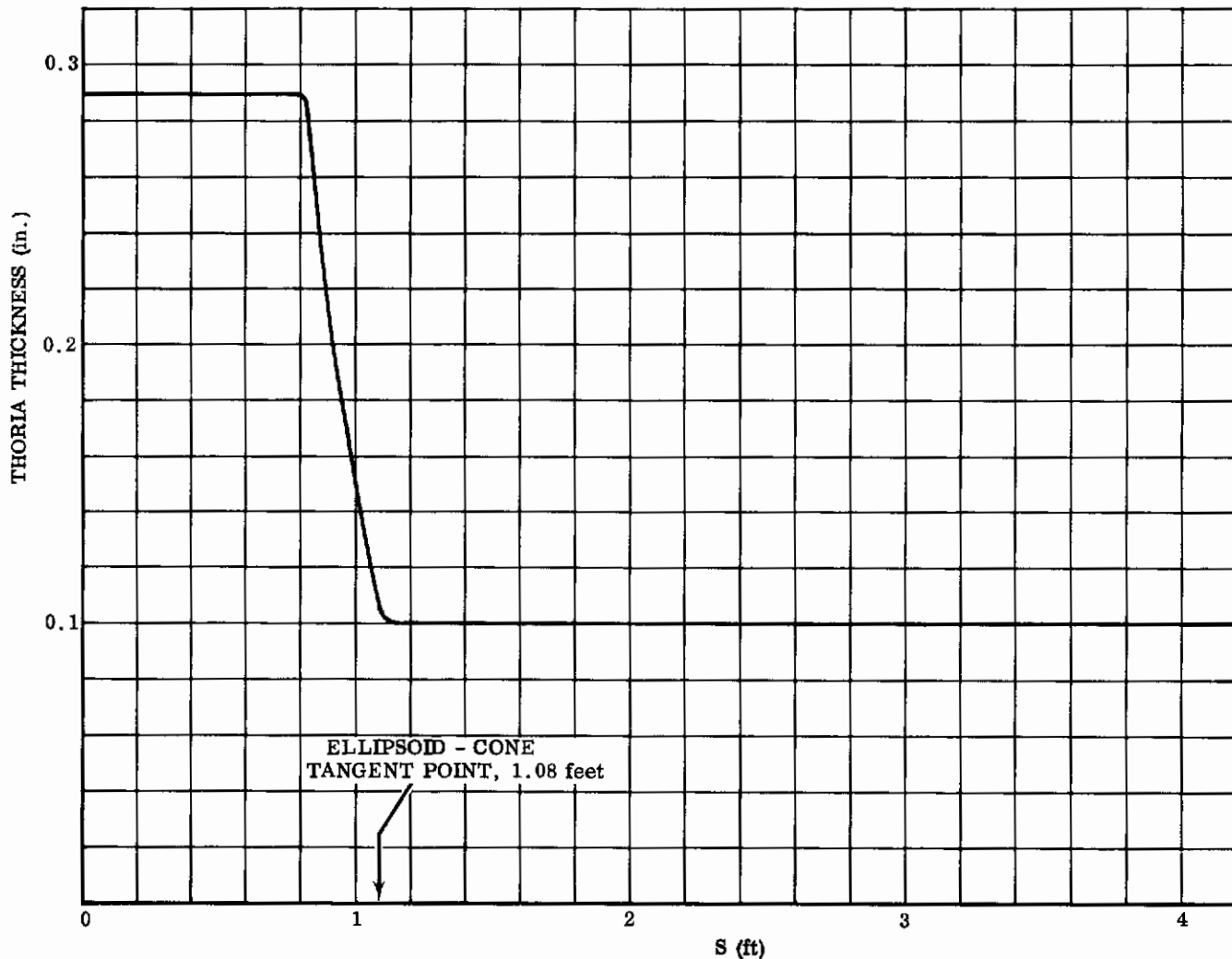


FIGURE 62. THORIA THICKNESS REQUIRED TO LIMIT TUNGSTEN SUBSTRATE TO 4500 F

maximum temperature less than the assumed ablation value. Only one-eighth of the thoria surface absorbed energy in an ablation process; the remainder served only as a somewhat inefficient insulation for the tungsten substrate. At 100 seconds, ablation ceased and the high-temperature ellipsoidal portion of the surface began cooling through reradiation exceeding the aerodynamic input convection. Simultaneously, the conical portion continued to increase in temperature after 80 seconds. By 300 seconds, the entire surface of the frontal body had cooled considerably. As expected, the surface temperature response in Figure 63 had the same form as the heating distribution of Figure 39. Surface temperature gradients were high in the shoulder region. Axial heat con-



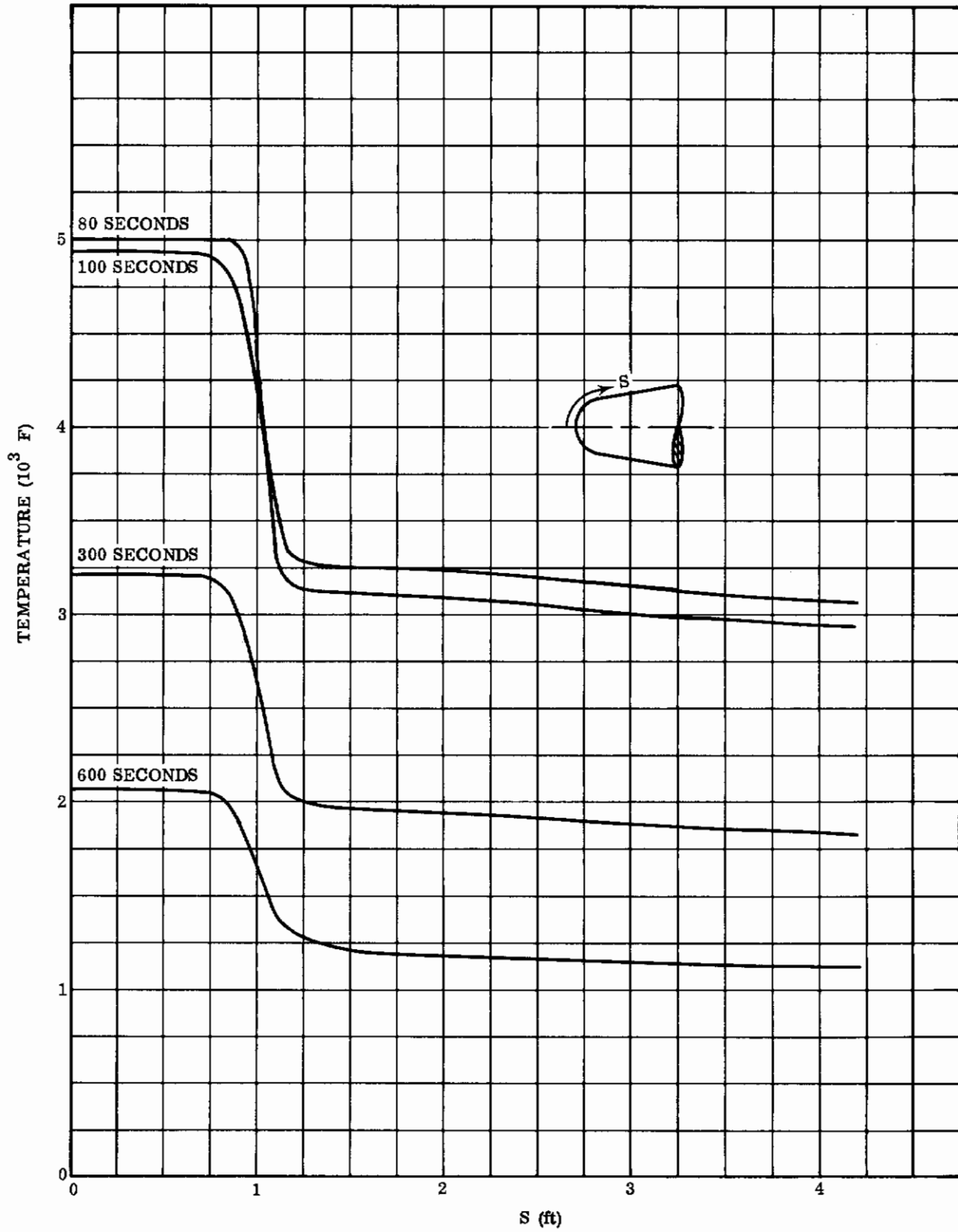


FIGURE 63. THORIA SURFACE TEMPERATURE VERSUS DISTANCE FROM STAGNATION POINT

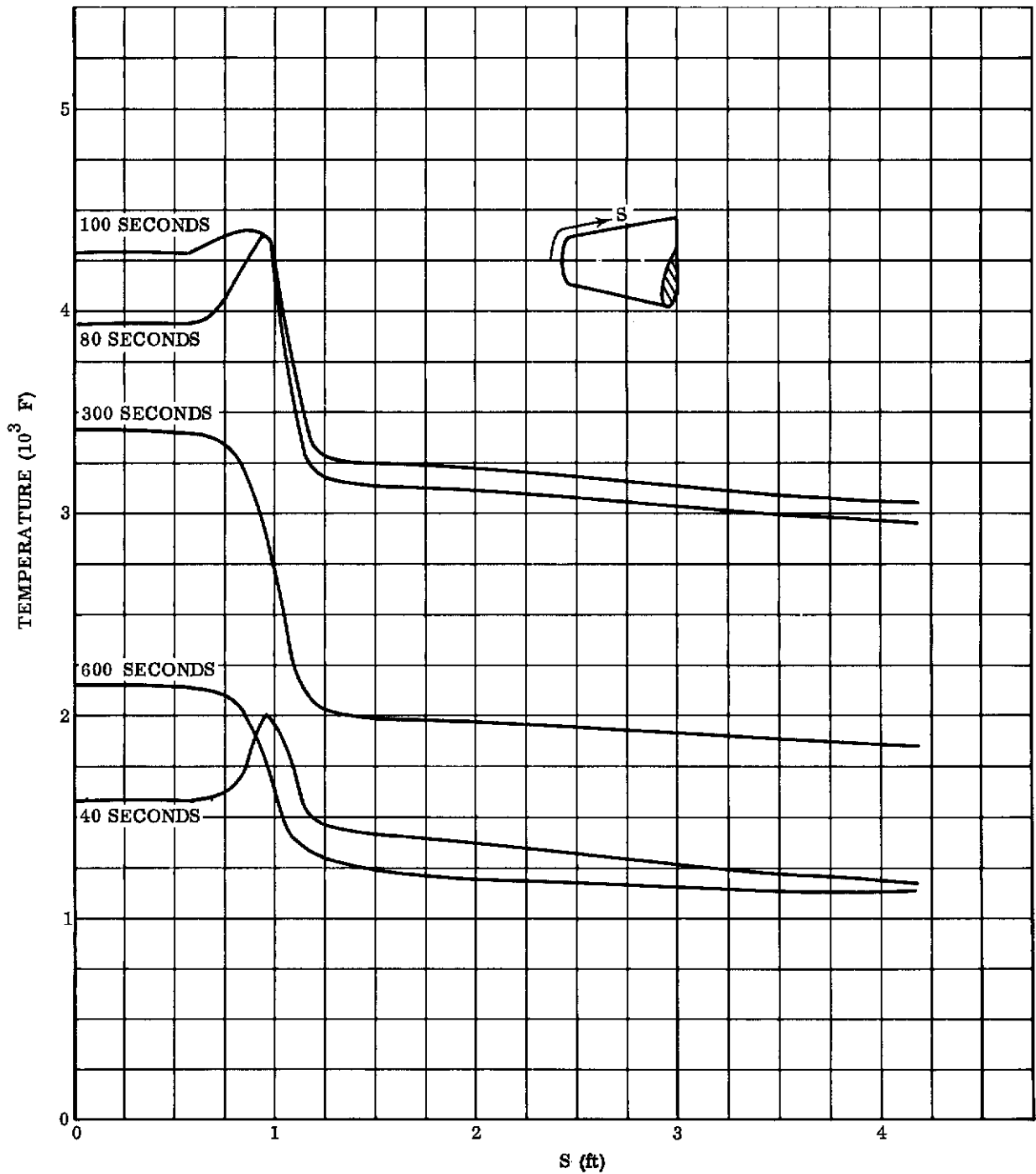


FIGURE 64. TUNGSTEN SHELL TEMPERATURE VERSUS DISTANCE FROM STAGNATION POINT

duction in the thoria did little to decrease meridional temperature gradients because of the steep, short-duration heating pulse and the thermal resistance presented by the coating.

Variation of temperature with meridional distance, similar to the above curves but applicable to the tungsten substrate, is shown in Figure 64. A slight temperature increase near the shoulder ( $s \approx 1$  foot) was observed early in re-entry accompanying the local thinning of the thoria overlay. A more-gradual transition in ceramic coating thickness than that shown in Figure 62 would appreciably lessen the local temperature gradient within the tungsten shell. Temperature differential across the protective thoria coating may be obtained by a subtraction of the results in Figures 63 and 64. With the tungsten shell possessing both good thermal conduction characteristics and a thin section, the temperatures shown in Figure 64 may be assumed nearly identical to those at the rear face of the ceramic coating. The resultant temperature difference across the ceramic is shown in Figure 65. A maximum differential of 3100 F occurred about 40 seconds following entry.

Temperature history (response) was determined at eight depthwise nodal locations within the composite. These nodes are shown in Figure 66.

The term  $\delta$  signifies the variable coating thickness, a function of meridional surface position  $s$ . Figures 67 through 70 show the temperature response for the first ten minutes of entry at four streamwise locations from the apex of the ellipsoid cone:

1. The stagnation point
2. Shoulder
3. Intermediate distance along conical frustum
4. Base of cone

Curves for 1300 seconds of entry flight were presented in Reference 30. The depths of Nodes 2 and 3 are presented on the specific temperature curves and are dependent upon the local coating thickness.

Temperature response at the stagnation point appears in Figure 67 with ablation again indicated in the interval, 50 to 90 seconds. Less than 0.03 inch of the original 0.29-inch thickness of thoria was removed during the erosion process. After 120 seconds, the composite structure commenced losing heat to the surroundings,

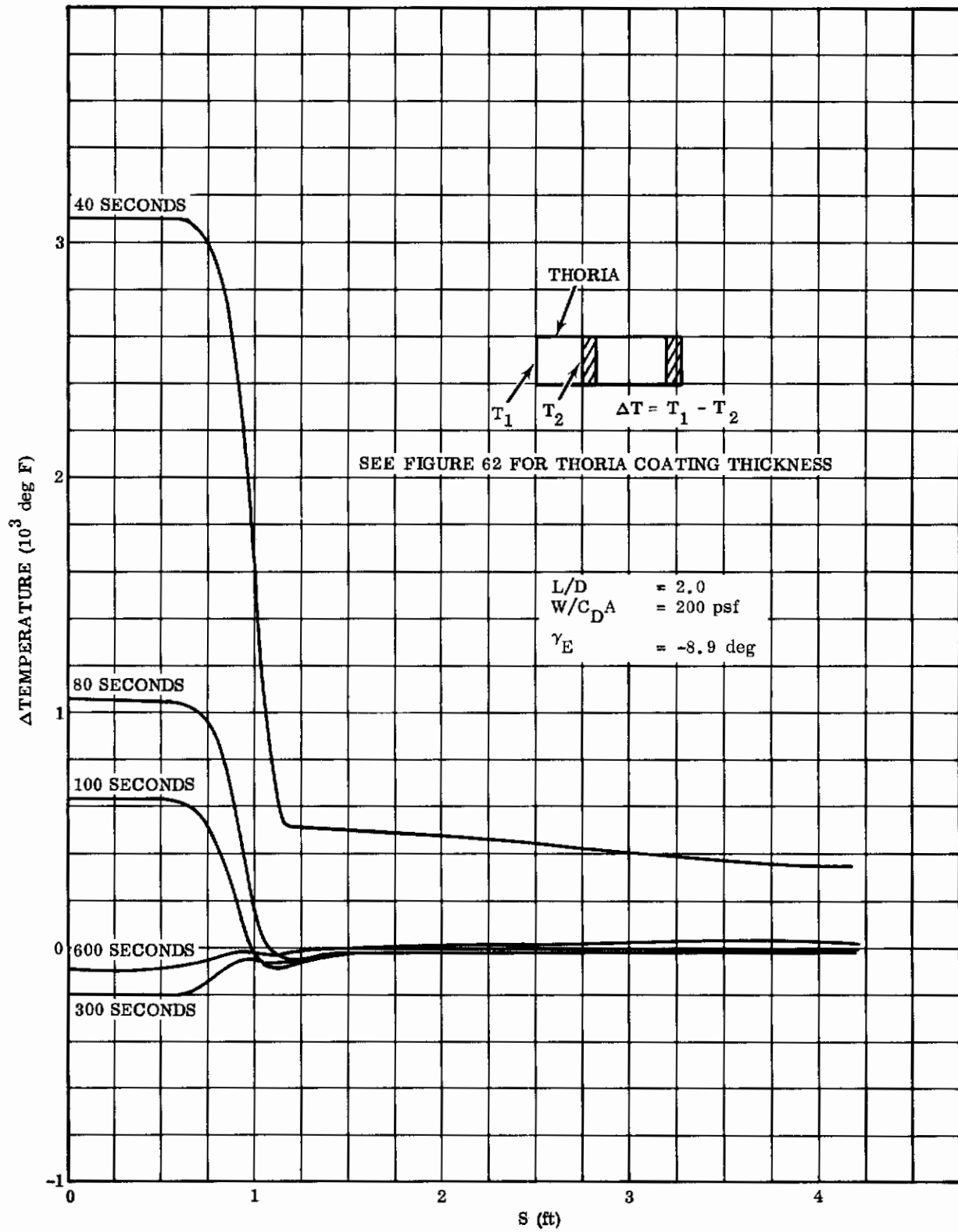
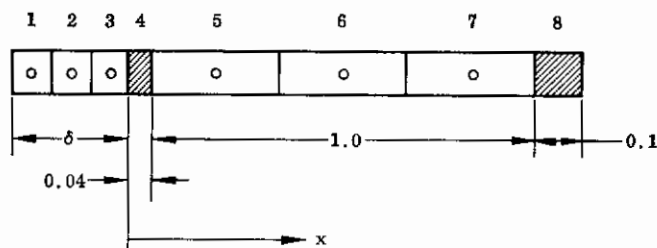


FIGURE 65. TEMPERATURE DIFFERENCE ACROSS THORIA COATING



NODE

- |                  |              |
|------------------|--------------|
| 1 THORIA SURFACE |              |
| 2 THORIA CENTER  |              |
| 3 THORIA REAR    |              |
| 4 TUNGSTEN SHELL | x = 0.02 in. |
| 5 ZIRCONIA FIBER | x = 0.21 in. |
| 6 ZIRCONIA FIBER | x = 0.54 in. |
| 7 ZIRCONIA FIBER | x = 0.87 in. |
| 8 BERYLLIUM SINK | x = 1.09 in. |

FIGURE 66. NODE LOCATION IN COMPOSITE STRUCTURE

since the second thoria node temperature had then exceeded the surface temperature. Later, the entire structure, except the beryllium heat sink, underwent cooling. The beryllium, considered as perfectly insulated at the rear face, continued to increase in temperature to 900 F at 1300 seconds of flight time.

The temperature history of the structure at a station 1.05 feet meridionally aft of the stagnation point is shown in Figure 68. This location corresponds to the shoulder region of the heat shield, the juncture of the ellipsoidal and conical portions. Surface heating from the gas cap was negligible in this area, and convective heating was approximately 30 percent of the stagnation rate. The thoria surface near the shoulder assumed a maximum temperature of approximately 4000 F and hence did not ablate. The tungsten substrate maximum temperature was only slightly less, 3850 F. With the tungsten operating locally some 600 F under the maximum permissible temperature, a further reduction in thoria thickness is possible. Abrupt thickness reductions, however, pose the problem of high-temperature gradients, since significantly thicker coatings are required a slight distance toward the stagnation region. A maximum beryllium temperature of 700 F occurred at the shoulder station compared with 900 F at the stagnation point.

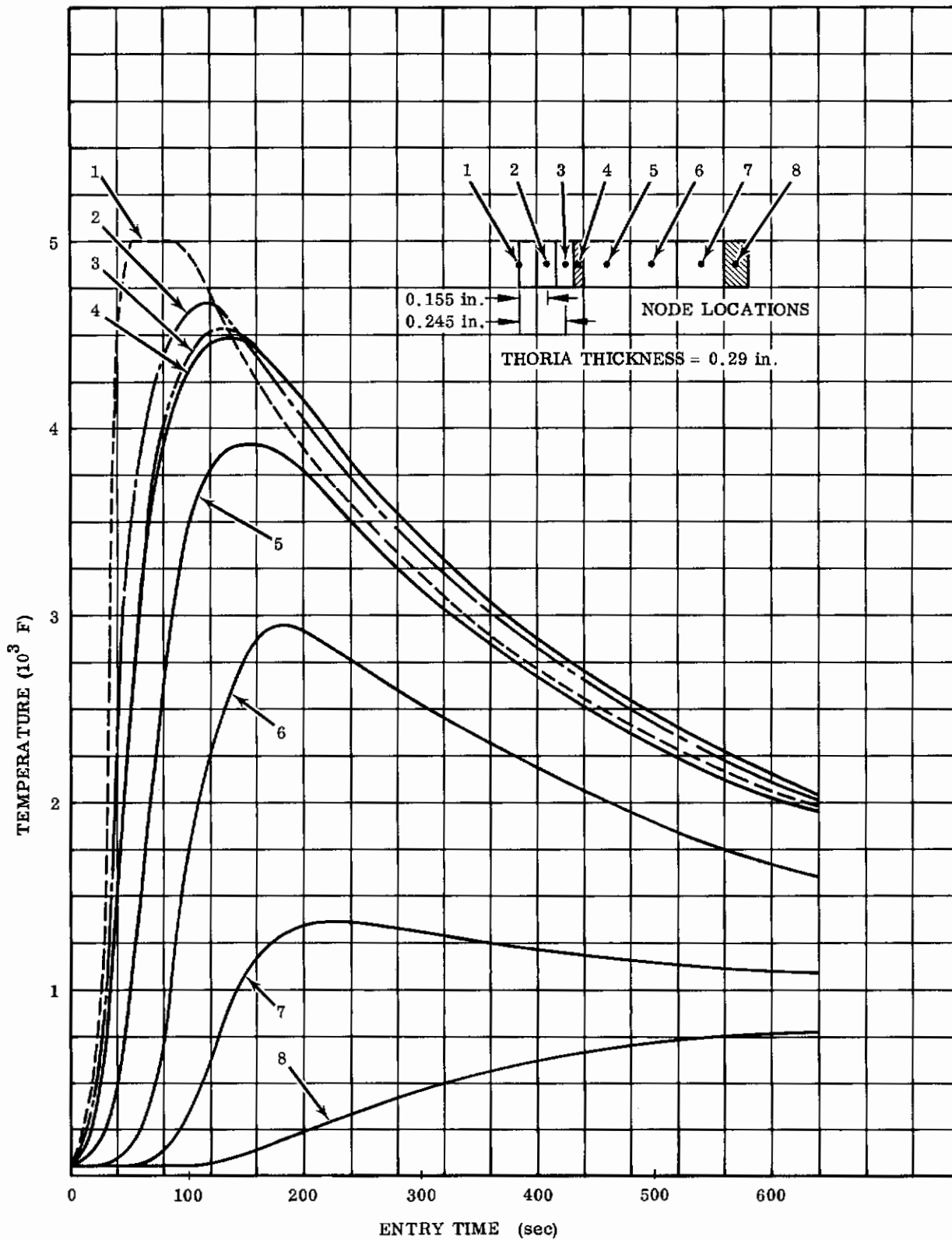


FIGURE 67. TEMPERATURE RESPONSE OF COMPOSITE STRUCTURE AT STAGNATION POINT ( $s = 0$ )

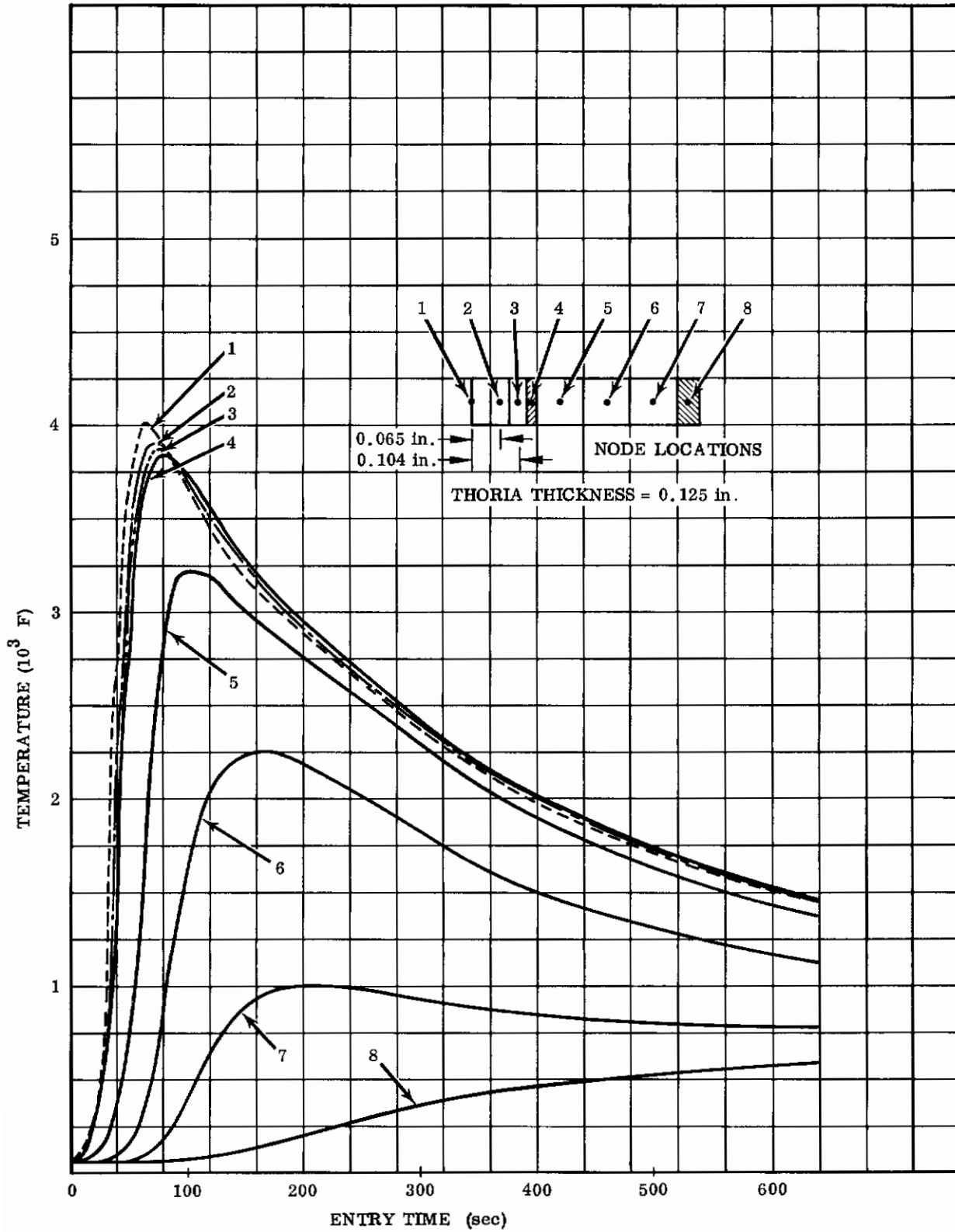


FIGURE 68. TEMPERATURE RESPONSE OF COMPOSITE STRUCTURE AT SHOULDER AREA ( $s = 1.05$  ft)

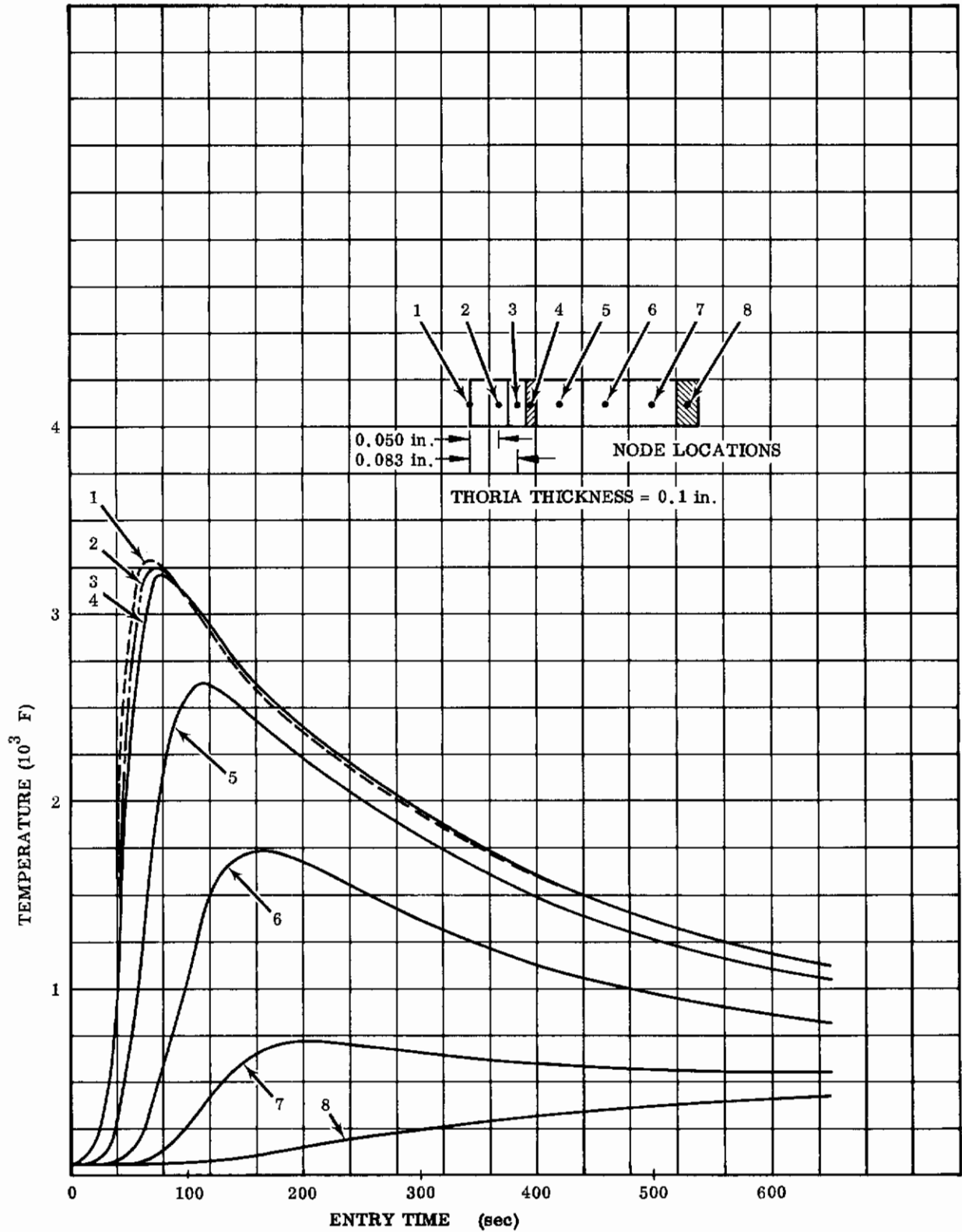


FIGURE 69. TEMPERATURE RESPONSE OF COMPOSITE STRUCTURE AT INTERMEDIATE POSITION ( $s = 2.1$  ft)



The response 2.1 feet aft of the stagnation point, an intermediate position along the cone, is shown in Figure 69. The 0.1-inch thick thoria experienced a maximum surface temperature of only 3300 F. The temperatures of Nodes 3 and 4, the last thoria node and the tungsten shell, respectively, were nearly equal throughout re-entry and are shown as coincident points on the figure. Temperatures at Nodes 1 through 4 also become indistinguishable at later flight times. Figure 70 extends the temperature history results to the base station of the conical skirt. At this station, the maximum temperature was 3125 F on the surface of the 0.1-inch thoria coating.

Temperature-dependent thermal properties of the thorium oxide, tungsten, and fibrous zirconia are given in Figures 71 through 73. The sources of this information are References 31 and 37. Presented properties required for the calculations include density, thermal conductivity, specific heat, emittance, and effective heat of ablation.

The evaluation of heating distribution on the high heat capacity-radiative candidate nose section with tapered protective coating thickness resulted in the following conclusions:

1. Only laminar boundary layer heating is likely to occur on frontal portions of the entry glider under consideration.
2. For the analytical composite structure, an 0.29-inch coating of thoria was required at the stagnation point to limit the underlying tungsten shell temperature to 4500 F. A uniform 0.29-inch thickness of thoria overlay afforded sufficient protection aft to the sonic point on the ellipsoidal portion of the nose cap with essentially a constant convective heating rate in this region.
3. A decrease in thoria thickness to 0.1 inch was possible on the frontal body conical skirt.
4. Since no ablation occurred beyond the sonic point, the use of a thoria covering for the entire nose surface is questionable due to its excessive density.
5. Sizable radial and axial temperature gradients were determined in the ceramic oxide coating.

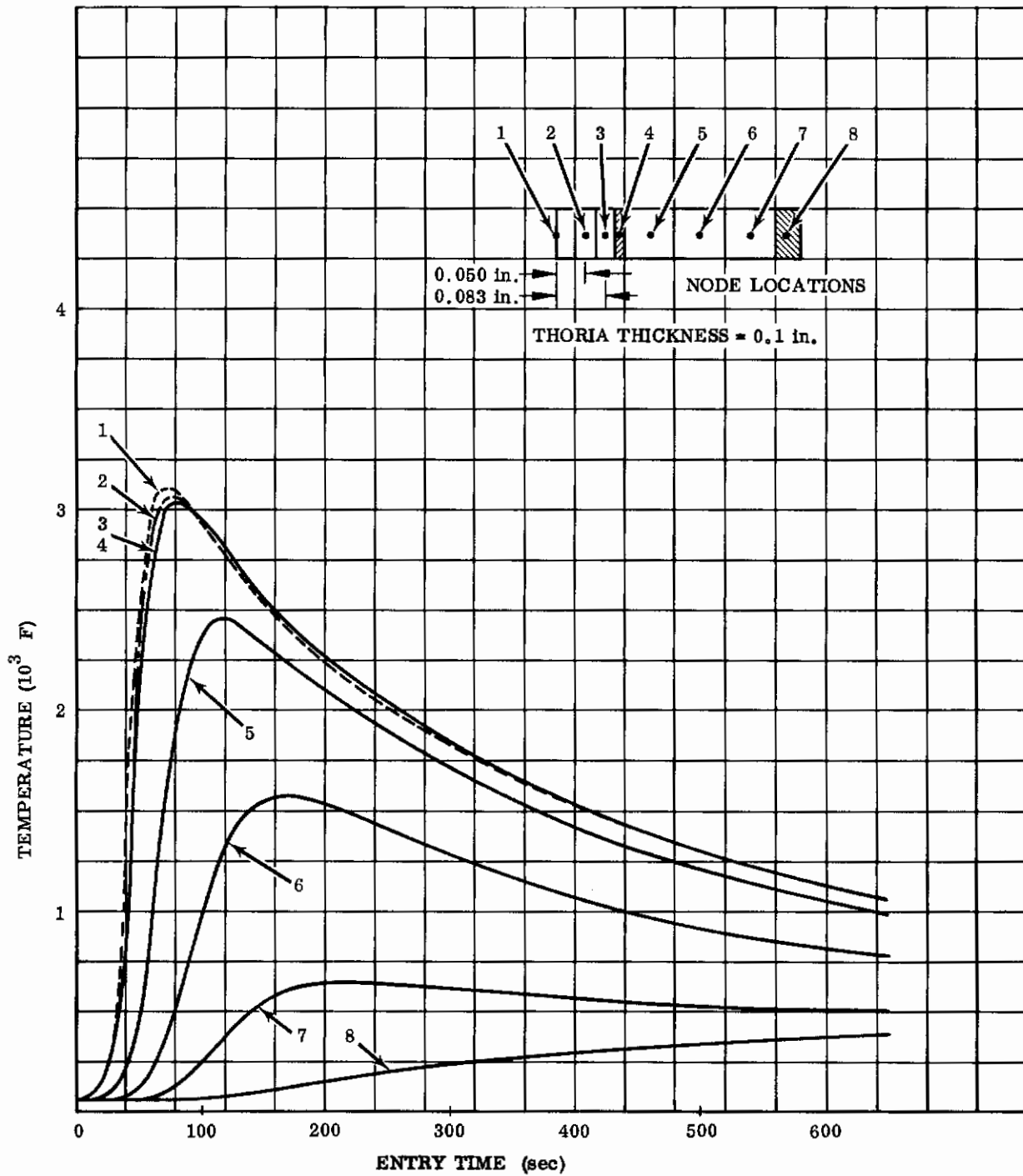


FIGURE 70. TEMPERATURE RESPONSE OF COMPOSITE STRUCTURE AT CONE BASE ( $s = 4.2$  ft)

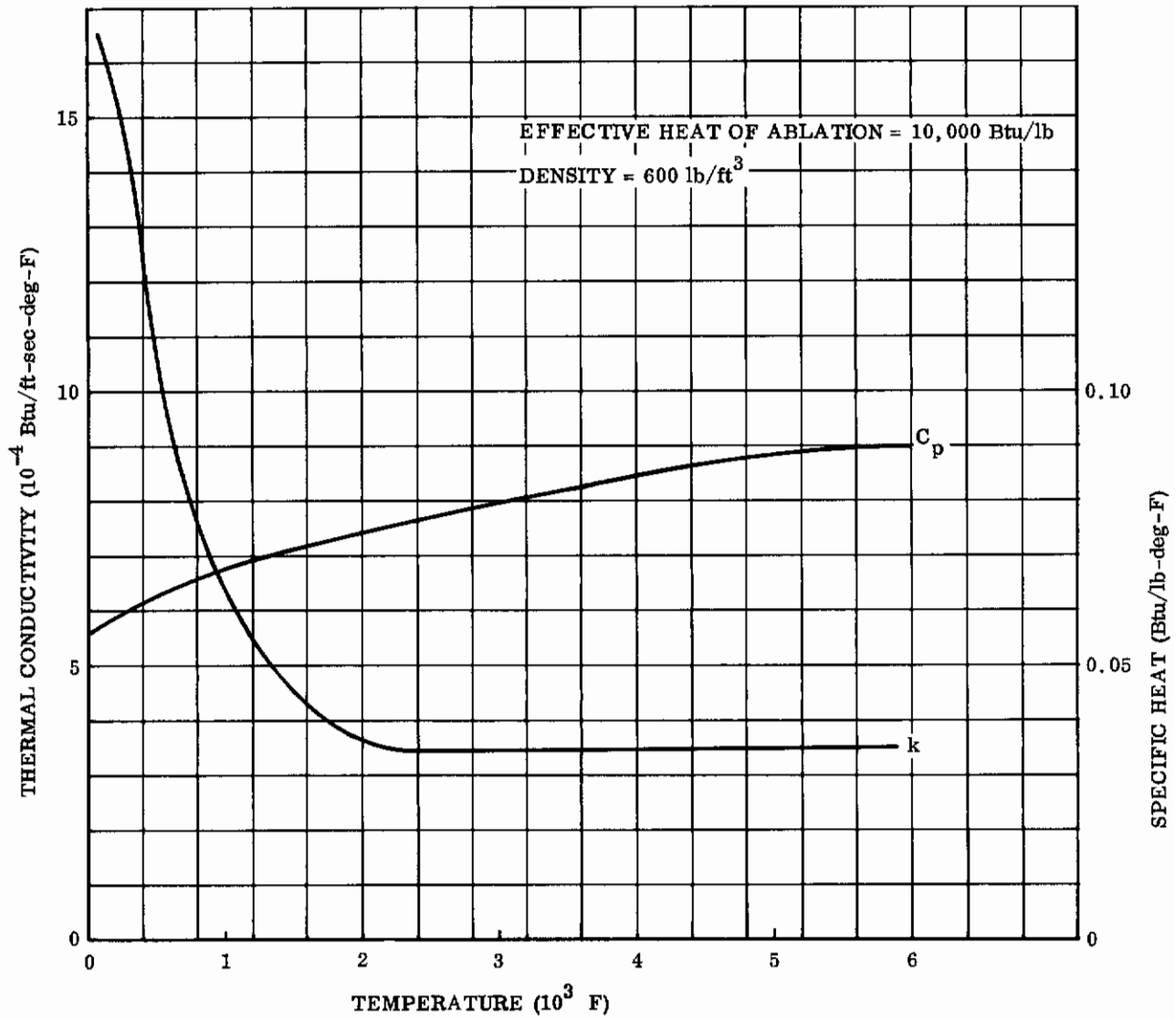


FIGURE 71. THERMOPHYSICAL PROPERTIES OF THORIA

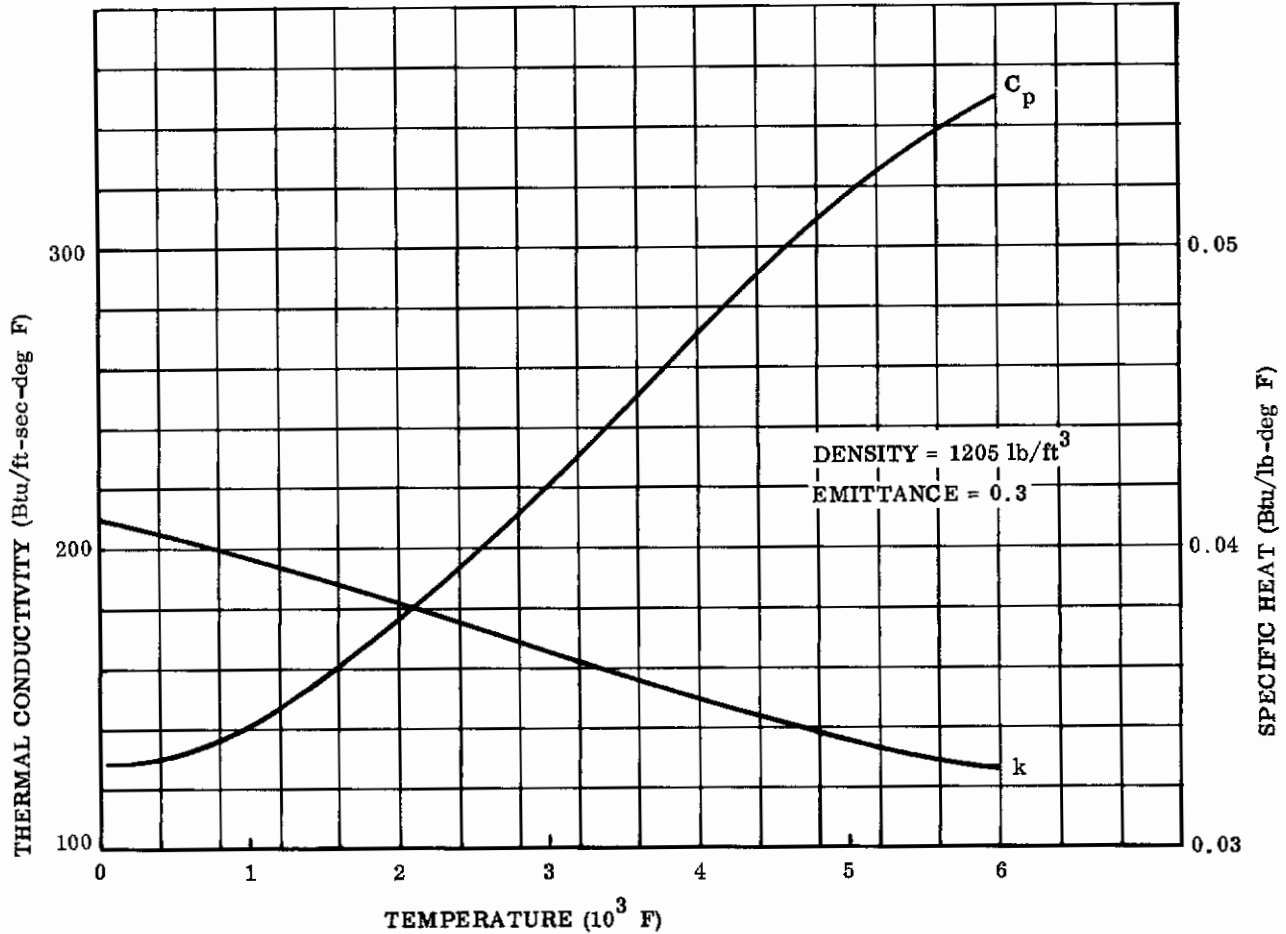


FIGURE 72. THERMOPHYSICAL PROPERTIES OF TUNGSTEN

#### 4.3.2 Internal Heat Blockage

A general analysis of heat flow to the base of the frontal section was conducted for the tungsten thoria composite frontal section. The primary goal was to determine the feasibility to restrict the re-entry temperature rise at the rear of the nose cap to 100 F. Outer composite (primary structure) back-wall heat rates over the total trajectory time were required for this study at two locations - the frontal cap section and a rearward skirt station (Fig. 60). Again, the trajectory selected for analysis pertained to the relatively "hot" winged glider ( $W/C_D A = 200$  psf,  $L/D = 2$ ,  $\gamma_E = -8.9$  degrees) which required 1387 seconds for super-orbital entry. As for the analysis immediately preceding, two-dimensional rotationally symmetric conditions were assumed.

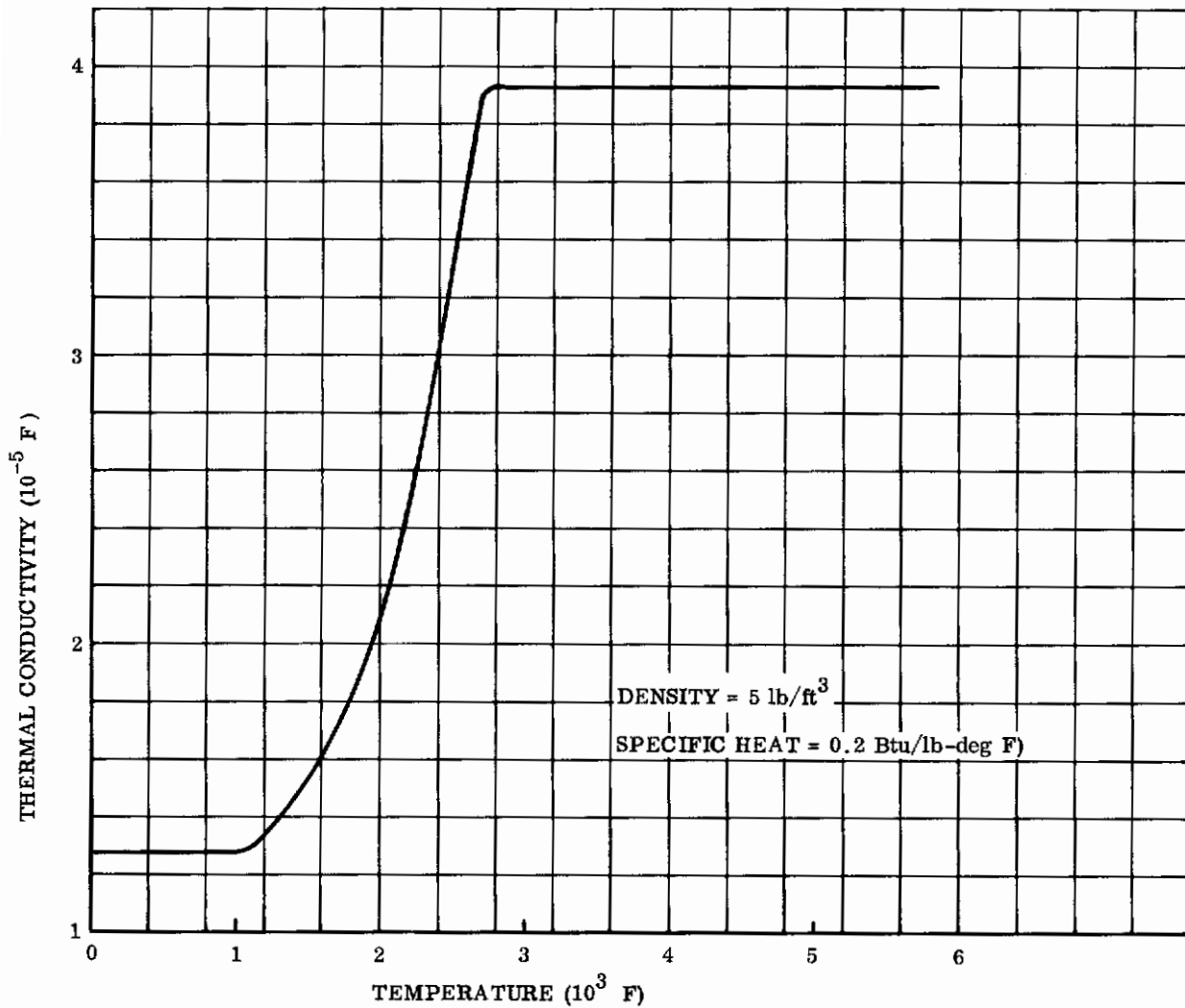


FIGURE 73. THERMOPHYSICAL PROPERTIES OF ZIRCONIA

Discrete material volumes must be provided in the central base of the nose structure to ascertain transient temperature behavior at a specific node in the heating network. This element of mass will be specified as the target or receiver of the heating. Any material in any state (solid, liquid, or gas) may, in principal, represent the target. But, considering interesting modes of heat transfer (conduction and radiation),

realism of results, and programming complexity, the use of a solid element appeared advantageous. Aluminum, having characteristics representative of efficient low-temperature-capability structure which could endure the stated temperature rise, was chosen as the candidate element. Dissimilar internal analytical models were utilized to determine target behavior under two influences:

1. Variation of heat capacity of the target node. Temperature response resulting from changing thermal capacity ( $\rho cV$ ) of the target was determined. The response of an object subjected to energy transfer is a strong function of its capacity to absorb, as well as to receive and transmit, thermal energy.
2. Variation in mode of heat transfer. Various combinations of conduction and radiation were investigated. Alternative systems considered in the study included basic conduction and radiation within a vacant shell containing only the target, pure conduction for an insulator system, and combined conduction and radiation for a more complex case incorporating multiple radiation barriers.

The same fundamental outer shell configuration was used for each thermal solution. Here, as in the outer composite shell analysis, the configuration was an oblate ellipsoidal cap having a maximum effective radius of curvature of 2.5 feet joined at the rear to a conical frustum skirt section. The external heating distribution about the body from the stagnation point through the subsonic region was nearly uniform because of its blunt ellipsoidal shape ( $b/a = 0.4$ ). Internal heating from the nose cap was introduced into the solution by substituting for the actual beryllium back wall of the composite ellipsoidal section a plane disc element with an applied uniform spatial heating rate given in Figure 60 (stagnation point rear wall values). The aft heat source was a narrow radial band situated midway along the conical skirt section. The lower-amplitude internal (back face) heating on the lateral wall of the conical frustum emanated from this band source. Both heat sources were connected analytically by conduction and radiation paths (where the latter were applicable) having areas, path lengths, and geometrical radiation configuration factors associated with the designated internal model. Finally, an aluminum target of specified capacity was placed in the central base of the conical frustum. This thermal receptor was a disc with dimensions varied for different models. The configuration factors were developed from Reference 33, except in those cases where geometrical considerations dictated calculation in the usual manner (intergration of the normal surface intensity vector between source and object). The basic configuration and the thermal paths considered are shown in Figure 74.

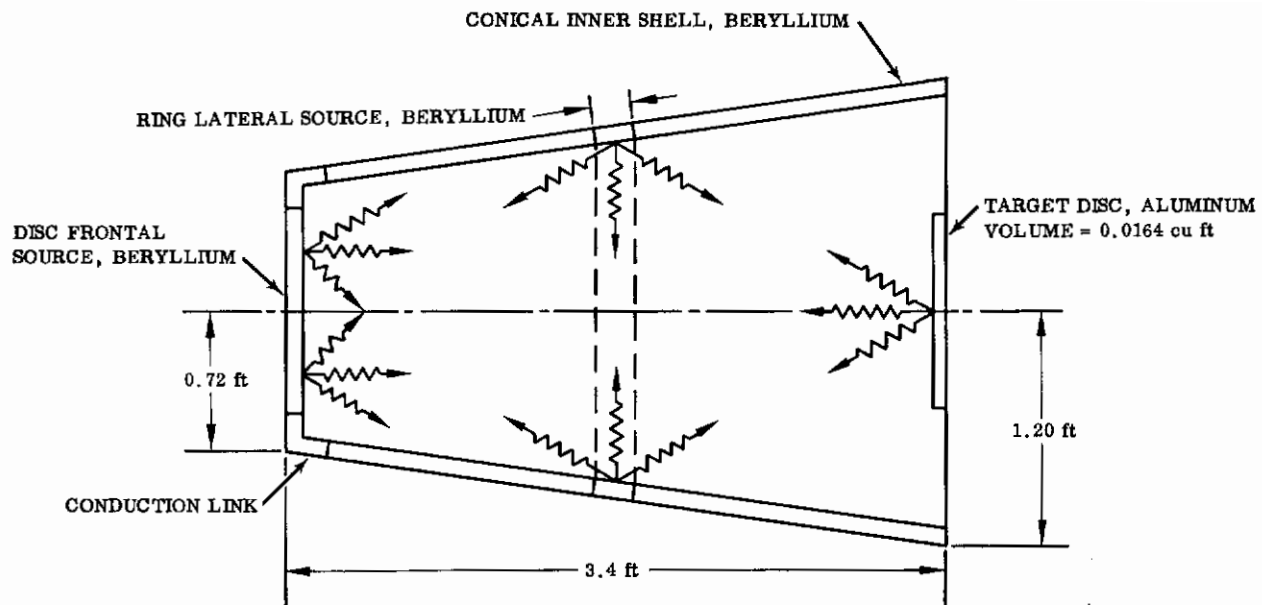


FIGURE 74. BASIC THERMAL CIRCUIT

Frontal and lateral composite back walls were conductively linked, the appropriate interface areas having been calculated as program input. The target was isolated from the source structure by perfect insulators to conduction. An exception was the nose cap interior completely filled with zirconia fiber; for that case, suitable conductance links for the structural combination of beryllium, zirconia fiber, and aluminum target were used. Combinations of temperature-dependent thermal conductivity, associated path lengths, and interface areas were represented for the various thermal models. The effect of internal radiation networks upon target thermal response was determined in further cases. Greater detail in the heat transfer analysis than that afforded by these simple models would have been inconsistent with the knowledge of actual internal structural layout, including bulkheads, stringers, reinforcements, and joints.

The following concepts were evaluated for heat blockage ability:

1. An interior exposed target volume was varied in volume to define the effect of capacitance.

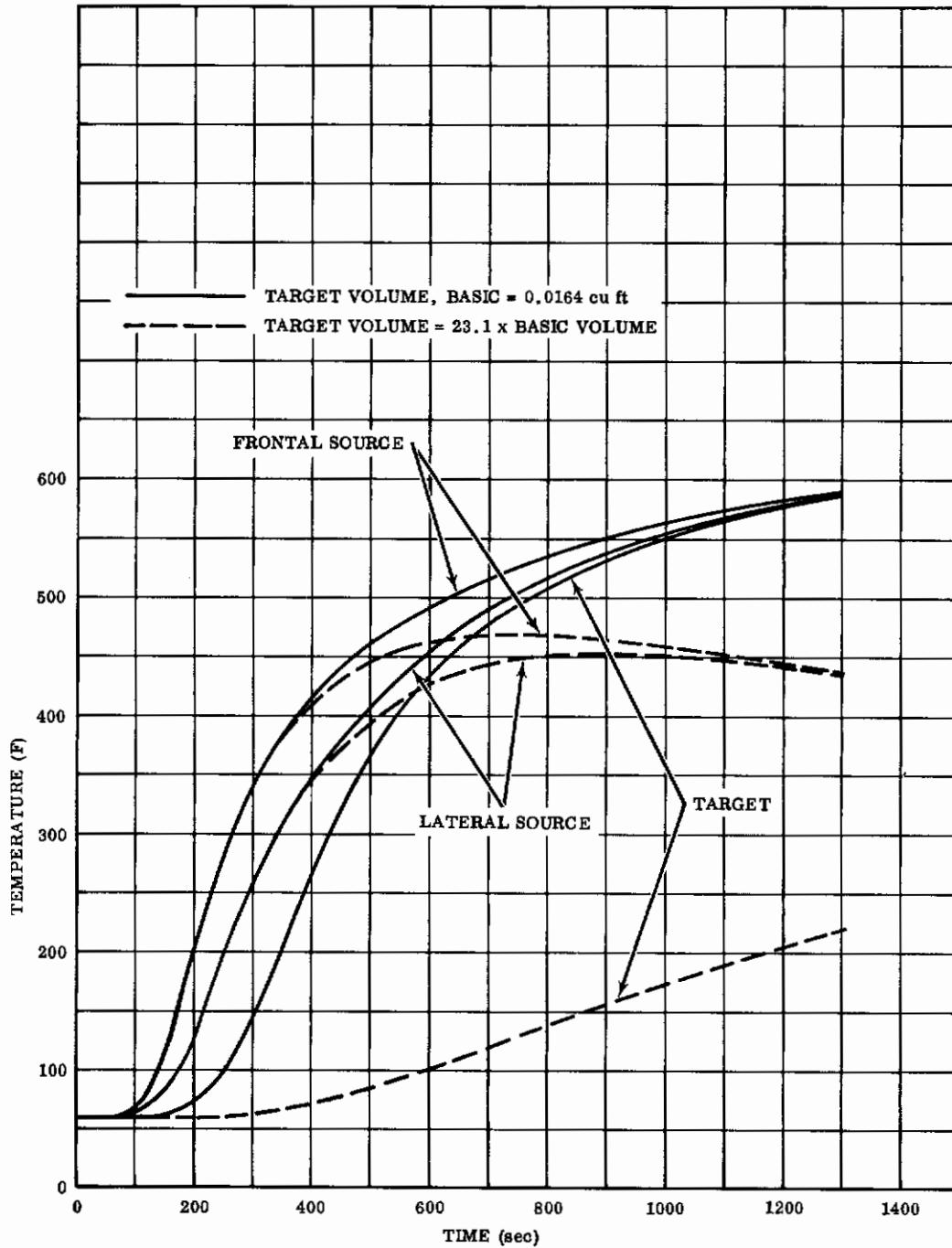


FIGURE 75. TEMPERATURE RESPONSE OF VARIOUS NODES FOR UNSHIELDED TARGETS OF DIFFERENT VOLUMES



2. A target surrounded by a simple aluminum enclosure (radiation barrier) was varied in volume. At this stage a fixed representative target volume was selected for subsequent analyses.
3. A target of selected volume within an aluminum enclosure was shielded by tungsten radiation barriers. Single and triple shields, placed between the aluminum enclosure and the backface of the primary composite wall, were geometrically similar to the outer nose shell.
4. A target was shielded by many internal radiation baffles placed within and in direct view of the tungsten shell (supplemental study).
5. An exposed target of the selected volume was surrounded by and coupled into a conduction network of zirconia fiber insulation which completely filled the nose cap interior.

A previously described arbitrary node program computed, in a step-wise manner, the spatial and temporal distribution of temperature and heat rate. Heat transfer modes, nodal locations, conduction and radiation path lengths, areas, volumes and shape factors were all initially specified. The initial temperature of all nodes, including sources, target, and intervening links was set uniformly at 60 F for time zero (atmospheric entry) with a maximum temperature increase of 100 F permitted for the overall flight. The general flow network consisted of conduction paths along the beryllium inner wall between frontal source and lateral ring source; radiation paths from frontal source to lateral source, sides, and target center; and, finally, radiation paths from lateral source to lateral sides, target center, and target rim. Extended arrangements included networks for a variable number of intervening radiation barriers and for a fiber-filled pure-conduction system.

Figure 75 shows the target temperature response due to a change in target thermal capacity. The basic aluminum target disc had a radius of 3 inches, a thickness of 1 inch, and a corresponding volume of 0.0164 cubic feet. For each volume change, resultant area and configuration factors to and from the target were determined. Also shown is the temperature response for a disc of the same given thickness but a diameter sufficient to cover the base of the configuration. Such a change introduced a volumetric increase of 23:1 over the basic target. Accompanying the increase in volume was a decrease of 370 F in maximum sensible temperature at the target node as well as a considerable reduction in rate of temperature rise. The time to reach the 160 F established upper limit of target temperature increased from 310 seconds for the basic volume to 920 seconds for the larger volume.

Further information in Figure 75 includes temperature response at the heating sources, Frontal Node 1 and Lateral Node 2. All cases displayed a marked decrease in source temperatures for a greater energy "sink" capacity of target node or of intervening material. When the receptor volume was reduced by a factor of 7.54 below the basic volume, a temperature increase of 25 F resulted at 1300 seconds.

Next the functional form of the response was determined for the aluminum target disc enclosed by a close-proximity radiation baffle of 0.1-inch thick aluminum. The enclosure was cylindrical, with a 4-inch radius and a 1-inch depth. It was assumed to be coated with a white silica paint to enhance the surface emittance. Heating characteristics of several such painted coatings have been investigated (Ref. 34), and considerable variation in coating effectiveness results from exposure to high temperature and surface chemical reactions. Here, a mean value of the ratio, material absorptivity-to-emissivity, of 0.5 was considered as representative of the coating. Again selecting the decreased target volume (0.133 x basic value), the radiation enclosure was found to exert considerable control over maximum target temperature. A maximum temperature of 260 F was observed, 450 F below that for the same low-capacity unencased target. The enclosed-target temperature did not reach the cut-off value of 160 F until 910 seconds of trajectory time had elapsed.

The next target selected was an aluminum disc of 1-inch radius and 0.1-inch thickness with a resultant 90:1 reduction in volume from the initial basic volume. This target volume,  $1.82 \times 10^{-4}$  cubic feet, was the most critical, thermally, and remained unchanged for the ensuing studies. Encased by the simple aluminum radiation enclosure, the maximum temperature reached by the object at 1300 seconds in this case was 602 F, and the 160 F level was attained at 420 seconds.

A summary of the effects of aluminum target volume variation (either exposed directly to primary backface radiation or protected by a thin painted enclosure) is presented in Figure 76. Maximum target temperature reached at 1300 seconds of trajectory time, and critical time for the various capacity targets to reach 160 F are given. These curves permit an estimate to be made of the thermal response of an aluminum structure of arbitrary volume located similarly to the target considered herein. Targets of other materials may be investigated by substituting for the abscissa ( $V_{Al}$ ) an effective volume of aluminum ( $V'_{Al} = (\rho c) V / .0225$ ), where the  $(\rho c)$

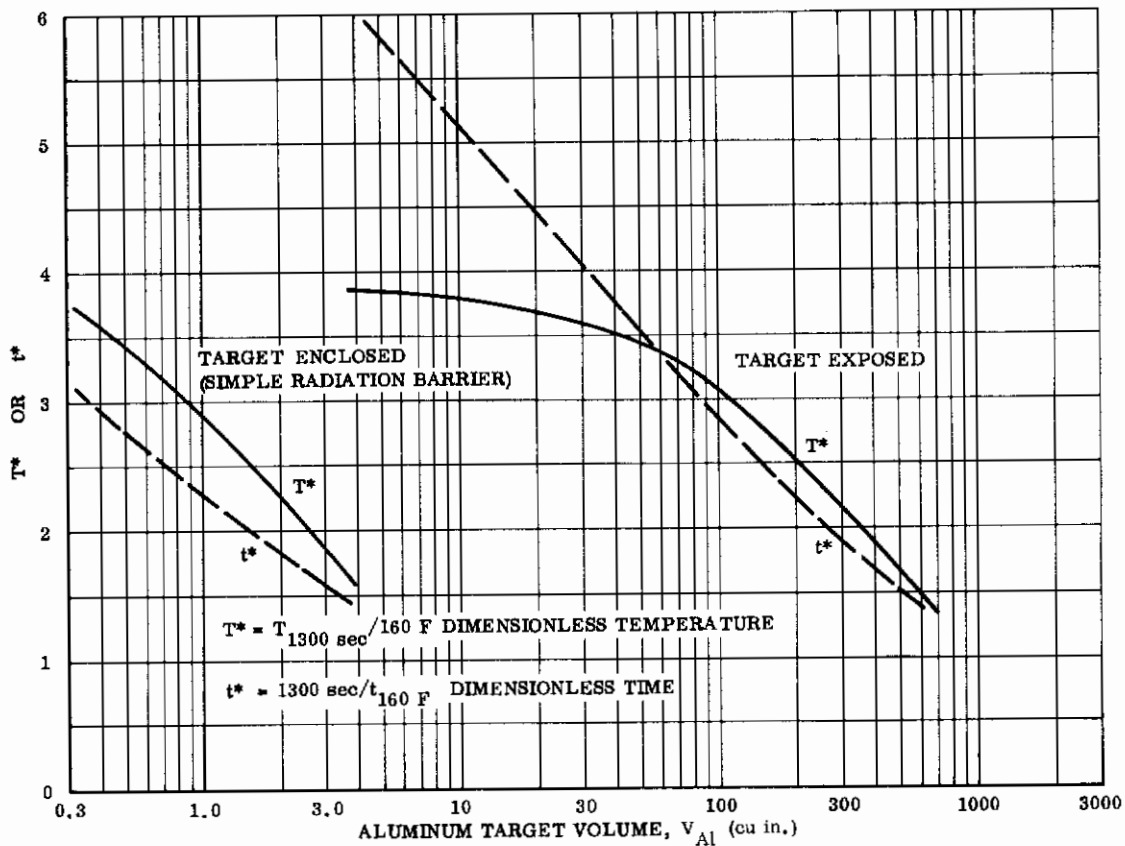


FIGURE 76. SUMMARY OF TARGET CAPACITY EFFECTS

product of the general material is in Btu/deg F-in.<sup>3</sup> and the volume ( $V$ ) is in cubic inches. This substitution of target material presupposes that geometry, emittance, and thermal conductivity of the object are similar to those for the aluminum targets investigated; otherwise, detailed analyses similar to the aforementioned are warranted. For aluminum, an extrapolation of the dimensionless temperature ( $T^*$ ) and time ( $t^*$ ) curves (Fig. 76) to unity value shows that a shielded or encased target of 8 cubic inches would meet the specification for maximum temperature; a target exposed to primary radiation requires a volume of about 1000 cubic inches, though. Respective weights are 0.8 pound and 98 pounds.

Temperature response was also computed for the low-capacity target shielded by an aluminum enclosure but additionally protected from radiation by a single, triple, and twelve intervening baffles of tungsten. For the single intermediate radiation baffle, a shell of 0.04-inch tungsten, geometrically similar to the primary shell structure but displaced 0.5 inch inward, was analyzed. The temperature observed at the target was 487 F in 1300-second flight with a time to critical temperature of 670 seconds. For a tungsten density of 1205 lb/ft<sup>3</sup>, the single radiation shield would contribute a weight of 120 pounds.

Incorporating three intervening radiation shields of similar geometry and mutually separated by 0.5 inch restricted the target temperature to 140 F. Extrapolation of the multiple baffle response data beyond 1300 seconds showed that the receptor node would not reach 160 F until 1370 seconds of flight time. The weight contributed, however, by a three-element internal shield system of 0.040-inch tungsten would approach 350 pounds. With the effect of target volume still important, temperature changes resulting from a different thermal capacity can be estimated from Figure 76.

A supplemental method of providing internal radiation relief at the base of the nose cap was considered: installing an augmented series of thin internal baffles exposed directly to the high-temperature back wall of the primary structural shell throughout total re-entry. Conceptually, the composite outer wall in this latter system lacks the insulative layer (fibrous zirconia) and capacitive layer (rearward retaining structure of beryllium) between the tungsten alloy shell and the outermost radiation baffle. Without the rear layers of the composite structure a significantly more-intense heat flux emanated from the frontal and lateral sources now situated in the refractory alloy primary structure; maximum absolute temperatures on the boundary of the internal heating model were as much as three times higher than those formerly experienced when the insulative layer was incorporated. To counter the high thermal potential of the sources, a set of twelve radiation-shielding elements was employed ahead of the small-capacity ( $V_{Al} = 0.314$  cubic inch) enclosed aluminum receptor. The barriers consisted of overly thick 0.040-inch tungsten progressively displaced at intervals of 0.5 inch inward from the primary nose shell structure. The number of shields selected was arbitrary, subject only to the physical dimensions of the nose interior.

The objective of this supplemental study was primarily to demonstrate the general effectiveness or, conversely, the inadequacy of a multiple barrier system. Outer tungsten shell temperatures applied at the frontal and lateral sources were developed previously (Fig. 67 and 69). A refractory metal was required, at least for the outer shields which faced the extremely hot outer boundary that radiated at a peak temperature of 4500 F. A possible option of mirror-like reflective surfaces on lower-temperature heat sink materials was also considered, but such a system was discarded for two reasons:

1. The severe thermal environment might lead to unfavorable mechanical decay of the surface, including localized warp, erosion, or catastrophic cracking of the mirror surface.
2. Complex chemical interactions at elevated temperatures between a mirror surface and any traces of gas or solid material in the nose cap are a definite probability. Such chemical combination is liable to deteriorate the reflective qualities of a mirror and lead to an over-heating of the substrate material.

With such restrictions, the intervening barriers were conceived as radiators rather than perfect reflectors with their operation restricted to emission of incident thermal energy at a level dependent upon total emittance characteristics of tungsten at high temperatures.

The most significant results — the responses of the target, the coated aluminum enclosure surrounding the target, and the two sources in the thoria-protected tungsten outer shell — are summarized in Figure 77. Peak frontal temperature values ranged between 4200 F for the outer shield to 2550 F for the innermost. The increase in target temperature (Fig. 77) was far in excess of the maximum allowable; the target node reached the melting point of aluminum at 610 seconds following atmospheric entry. No phase change nor other refinement was incorporated since system "failure," by definition, had occurred earlier in flight, at 220 seconds, when the target reached the cut-off temperature of 160 F.

Multiple barrier results for thinner elements with a faster response would be even more disenchanting. Because of the prodigious volume of thermally absorbing material represented by the twelve tungsten shields, heat flow within the network was capacitance-governed for the first several hundred seconds of entry flight. The multi-element radiation network adjoining the high-temperature refractory metal shell proved

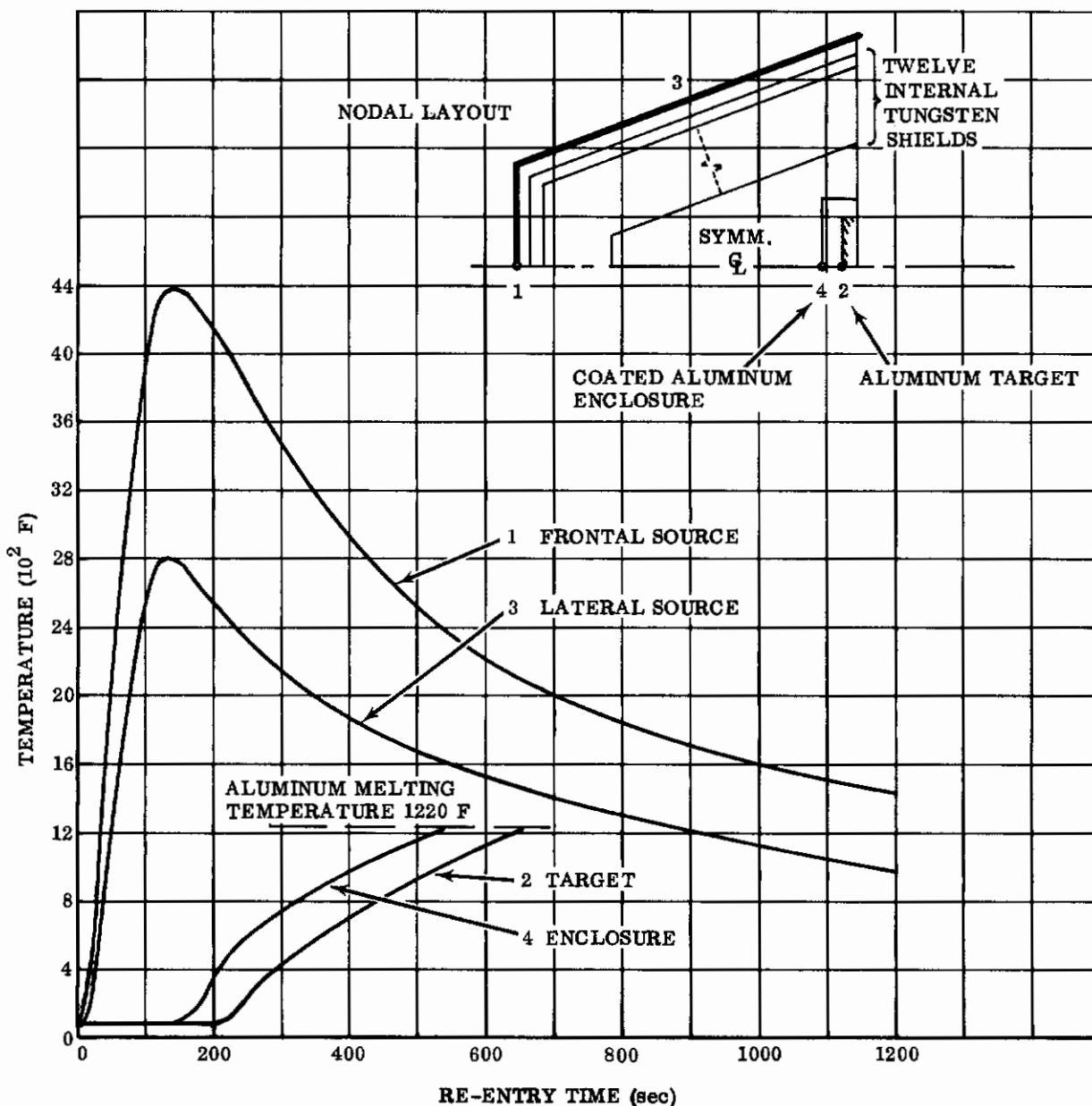


FIGURE 77. TEMPERATURE RESPONSE; Multiple Radiation Baffles

inadequate for internal temperature control with temperatures determined at the central aft target element exceeding 1000 F. From practical considerations, the additional weight and fabrication complexity are prohibitive. Without complementary insulation behind the outer refractory shell, heat control from high-temperature radiation baffles was disappointing.

The thermal response of the low-capacity target disc completely imbedded in an internal insulative packing of zirconia fibers is shown in Figure 78. The appropriate analog for this case was a pure conduction network. In addition to blocking internal

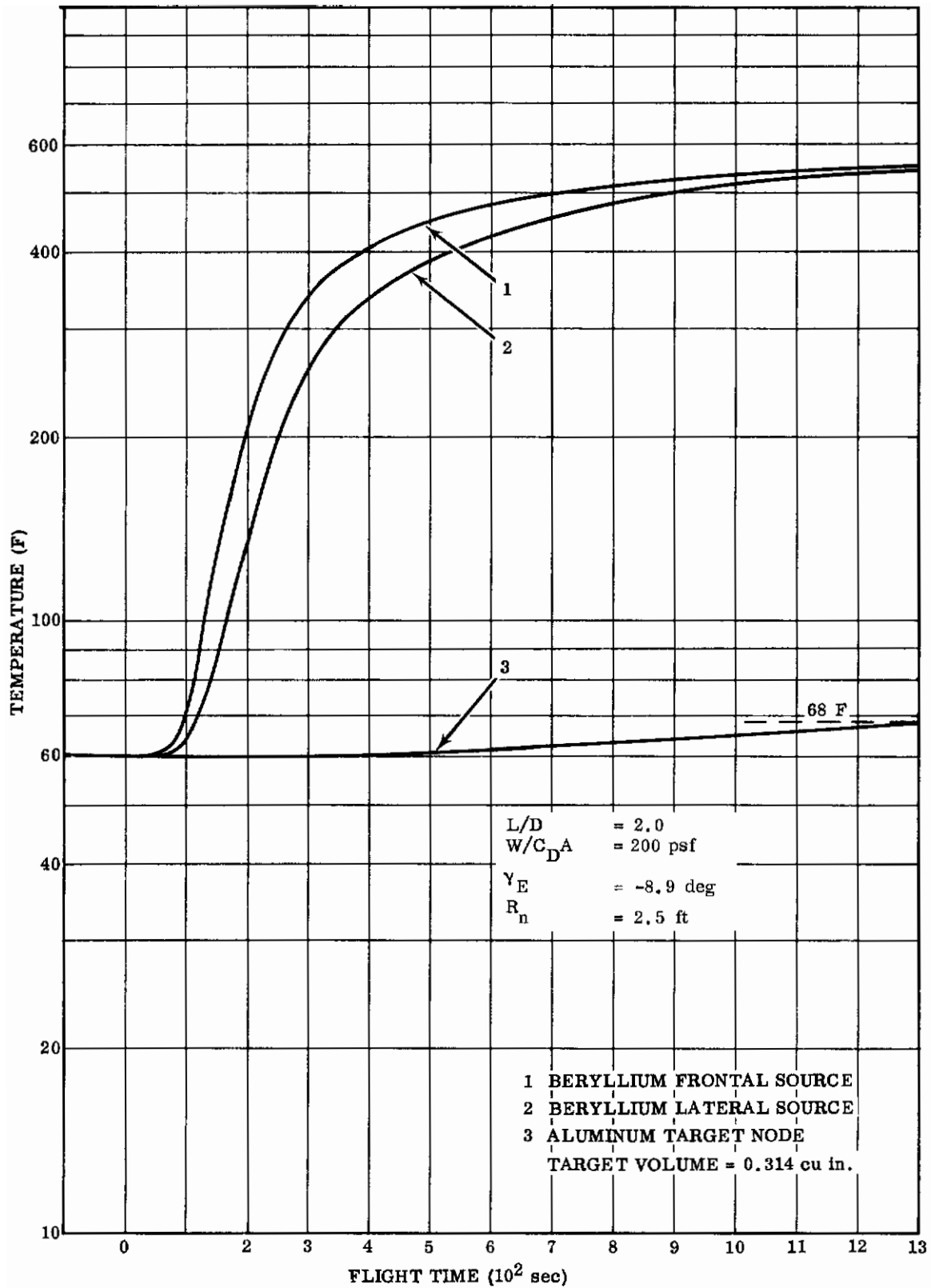


FIGURE 78. TEMPERATURE RESPONSE; Frontal Section Filled With Zirconia Fibers

radiation, the low thermal conductivity of the fibrous insulator, on the order of  $10^{-5}$  Btu/ft-sec-deg F, prevented the aluminum receptor at the rear from exceeding 68 F in 1300-second entry time. The additional weight contributed by the filling of fibrous zirconia for a compacted density of  $5 \text{ lb/ft}^3$  was less than 80 pounds.

In reviewing the various modes of internal temperature control, the insulation-filled system was by far the most promising from the standpoint of minimum weight and minimum target temperature rise. Drawbacks of the single and multiple shields, aside from weight, appear to be in the complexities of connecting the structural elements for adequate support and in minimizing heat leakage at the junctures.

The numerical solutions for internal heat blockage were based upon use of only two sources, frontal and lateral, to represent simply the non-uniform heating environment.

In previous solutions, however, manifold sources were employed to determine temperature distribution about the composite ellipsoid-cone outer shell structure (Sec. I). With reasonable assurance, the findings of the latter study are representative because: The two-point distribution was locally accurate, properly describing heating rate from source to source through the specific networks; trends from prior heating analyses indicated only a very limited dependence of composite backface temperatures reflected from changes in external heating.

Thermal response of the actual prototype configuration (all joints, reinforcements, bulkheads included) would possibly be less favorable than displayed here due to additional paths for heat flow aft, resulting in higher temperatures at a given node and given time. The results of the many detailed calculations of transient thermal distribution have emphasized the predominant characteristics of temperature control associated with long-duration lifting re-entry.



## V. STRUCTURAL INVESTIGATIONS

Structural analysis of the candidate frontal sections was limited to study of the tungsten substrate. Thermal analysis of the reinforced thoria overlay was not attempted, both because analytical techniques for such composites are not noted for accuracy, and because continued development of the thoria material throughout the program resulted in constantly changing properties. Value of the thoria coating was therefore assured experimentally, and optimization was conducted empirically.

This section summarizes the structural analyses performed. These analyses include:

- Shell thickness analysis
- Composite thermal stress analysis
- Unbonding pressure analysis.

### 5.1 STRENGTH AND STIFFNESS OF A THIN MONOCOQUE SHELL

Because an alloy of tungsten--with its attendant room-temperature brittleness and forming difficulties--is required for the primary shell structure of an ultra-high-temperature frontal section, it was considered mandatory to eliminate all stiffeners, internal bulkheads, and intermediate fasteners, all of which complicate fabrication. The remaining alternative is a thin, unstiffened (monocoque) shell section attached to the entry glider with fasteners which permit considerable freedom of thermal deformation.

An elastic stress analysis applicable to the common glider nose shape was formulated. The following assumptions apply in this analysis.

1. The ellipsoidal frontal cap is approximated by a shallow spherical cap with fixed edges (representing support from the conical afterbody).

2. A uniform load distribution is applied to the spherical cap, the magnitude of which corresponds to the stagnation pressure. There exists a hyper-sonic axisymmetric pressure distribution approximated for Newtonian flow by

$$\Delta p = \bar{q} \sin^2 \eta$$

where  $\Delta p$  = pressure differential from the ambient value

$\bar{q}$  = dynamic pressure at the stagnation point

$\eta$  = flow deflection angle.

But for the blunt frontal cap being considered,  $\sin^2 \eta \approx 1$ .

3. A uniform temperature distribution equal to the value at the stagnation point exists over the frontal cap. Previous data (Fig. 37 and 38) indicated the constant heat input for certain oblate spheroids. Moreover, streamwise gradients are diminished by internal radiation.

The reference ellipsoid had a semi-major axis of 0.994 foot and a semi-minor axis of 0.398 foot, giving an effective stagnation point radius

$$\rho_{sp} = a^2/b = 2.48 \text{ feet.}$$

The unstiffened ellipsoidal cap in the vicinity of the stagnation point was approximated by a spherical shell with radius of 2.2 feet, depth of 0.34 feet, and chord of 1.17 feet. With a small depth-to-radius ratio  $h/R = 0.155$ , shallow shell theory should apply, according to Reference 35.

### 5.1.1 First Criterion of Failure

The critical buckling pressure for shallow caps is determined from the formula

$$(\Delta p)_{cr} = K \left[ 1.212E \left( \frac{t}{R} \right)^2 \right], \quad \frac{h}{R} < \frac{1}{6}$$

The quantity inside the bracket (involving elastic modulus, shell thickness, and radius) is the classical expression for the elastic buckling pressure of a sphere. The K factor is a correction to account for discrepancies between theoretical and experimental data and in geometry. Values of K have been plotted as a function of the parameter C, which is defined as

$$C = \left[ 12(1-\nu^2) \right]^{1/4} \left[ R/t \right]^{1/2} \sin \theta$$

where

$\nu$  = Poisson's ratio

R = mean radius of shell

t = thickness of shell

h = haunched depth of shell

$\theta$  = half-angle of shell

## 5.1.2 Second Criterion of Failure

At higher temperatures, there is sufficient degradation of material properties that the nose shape may fail because of inadequate strength. The applicable equation is that of fundamental equilibrium, or hoop compressive pressure

$$(\Delta p)_{cr} = 2\sigma_T(t/R)$$

where  $\sigma_T$  is the compressive strength at elevated temperature.

With ultimate strength at temperature known, a safety factor of 1.5 will be applied. Thus

$$(\Delta p)_{cr} = \frac{4}{3} \sigma_{T_{ult}} (t/R)$$

If these equations are used with tungsten properties corresponding to various elevated temperatures, values of allowable pressures may be computed for each of the temperatures. Nominal shell thicknesses were selected and critical pressures were calculated for both of the foregoing criteria. The plots of these results are shown in Figure 79. The curves indicate that, for a given thickness, the elastic buckling stress decreases (with E) as temperature increases. The buckling allowable curves no longer control at the higher temperatures. Here, the material property cutoff lines are significant, and the high-temperature strength of shell governs the design thickness.

Time-dependent external loads and temperatures occur on the frontal structure during vehicle re-entry. Both the external pressure loading and the convective heating rates are functions of the super-orbital entry trajectory.

Two loading conditions were investigated for the glider nose configuration: maximum temperature and maximum dynamic pressure. For the simple hot-wall vehicle (the light glider), these maxima nearly coincide in time because of the

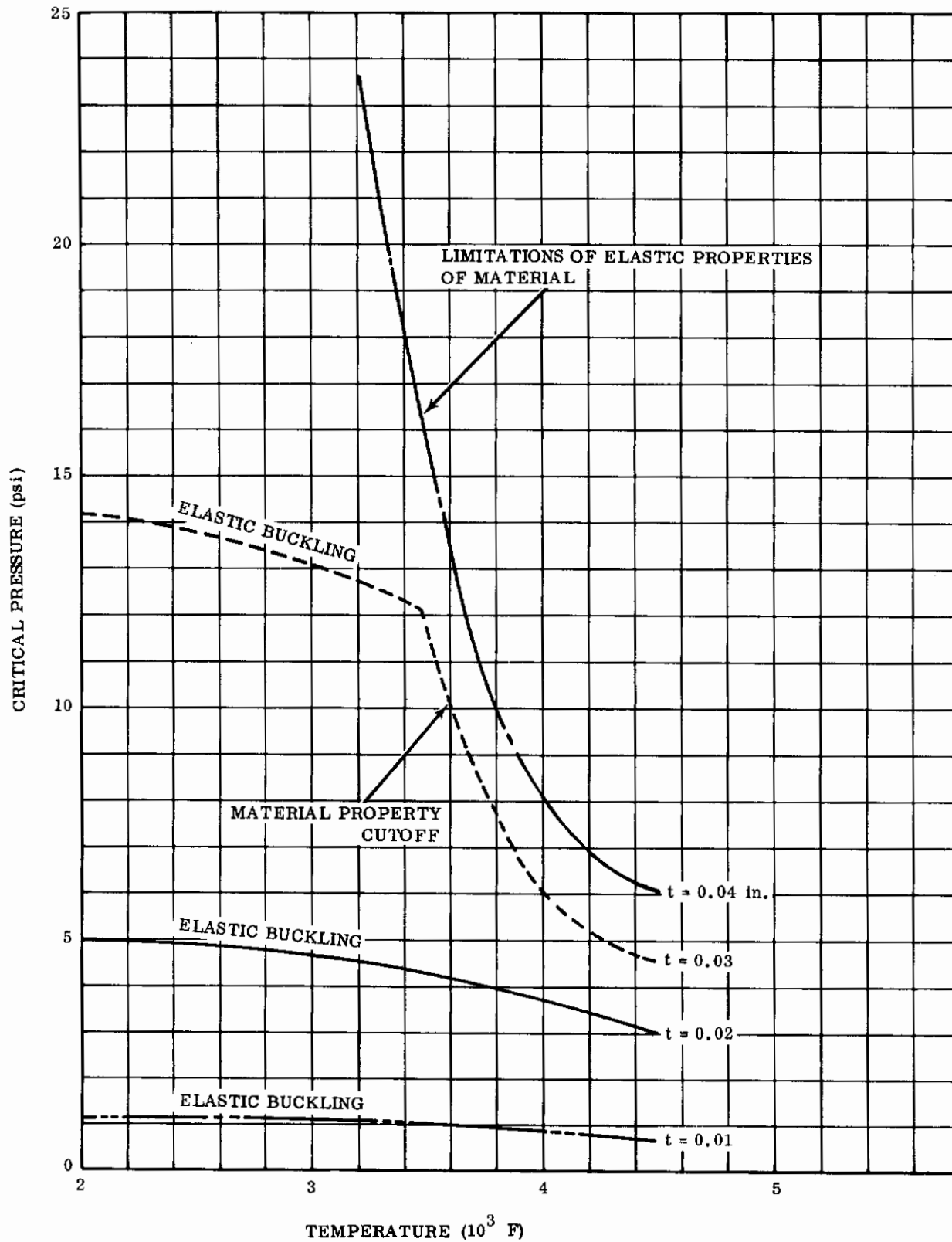


FIGURE 79. GLIDER NOSE SHELL; Tungsten Monocoque Construction

negligible heat storage capacity of the structure. For the composite ablative-radiative frontal, the nose is still relatively cool at peak dynamic pressure, depending upon the type and thickness of ablator selected. To define the material properties, a temperature of 2000 F (moderate for tungsten) was assumed at the time of peak pressure when utilizing transitory heat absorption. The probability of the substrate exceeding this temperature at peak pressure is remote for a receding ablative surface or for a high-capacitive absorptive coating.

Shell thickness must be based upon the complete history of heating and loading, including boost, passage through vacuum space, and super-orbital entry. Histories of dynamic pressure were derived for free-stream conditions ahead of the shock. Considering compressibility effects, the pressure at the stagnation point for Mach numbers greater than 10 will be higher than free-stream values by a factor of 1.84. Using an effective radius of curvature of 2.5 feet and true dynamic pressures on the body, the combination of conditions which govern the selection of the metallic shell thickness is tabulated in Table 5.

TABLE 5  
AIR LOADS AT ELEVATED TEMPERATURES

Vehicle	$t$ (sec)	$\bar{q}_{max}$ (psi)	$T_w$ (F)	$t_{200}$ (sec)	$\bar{q}_{200}$ (psi)	$T_w$ (F)
I. Glider (medium wing load)	55	11.6	2000	160	5.8	4500
II. Light Glider	80	0.36	4500	throughout re-entry	-	-

where

- $t$  = Time of peak dynamic pressure, sec
- $\bar{q}_{max}$  = Peak dynamic pressure at the stagnation point, psi
- $t_{200}$  = Time at which the nose may operate as a hot wall radiation structure, vis, when  $q_c = 200 \text{ Btu/ft}^2\text{-sec}$  is attained, sec
- $\bar{q}_{200}$  = Dynamic pressure at instant of zero ablation requirement, psi
- $T_w$  = Wall temperature of thin tungsten shell, F

For the winged glider, the re-entry design condition occurs at the instant of radiation structure capability as determined by entering Figure 79 with the tabular values. For the derived combination of temperature and dynamic pressure, a nominal shell thickness of nearly 0.04 inch is required for compressive strength.

For the light glider, a shell thickness of only 0.01 inch is required for buckling resistance. Considering launch and boost environment, that is, during powered ascent through the atmosphere with a typical large-scale lunar propulsion system, peak dynamic pressures would probably not exceed 5 psi. Lesser heating occurs during exit, and a small-amplitude buffeting would be expected near transonic flight. To withstand such conditions, plus lateral maneuver loads, a thickness of at least 0.03 inch is recommended for this flight article.

## 5.2 THERMAL STRESSES IN A FREE COMPOSITE SLAB

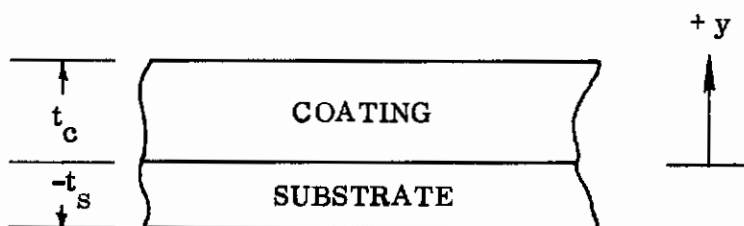
A simplified technique to evaluate thermal stress was developed for in-plane stresses induced in two-element composite slabs at elevated temperatures. The method has principal application in evaluating small coupons of hot-wall structure exposed, for example, to screening tests in a plasma tunnel. Under such circumstances refined, two-dimensional solutions including plasticity effects, creep, cyclical straining under transient temperatures, and attachment restraints are not warranted. Often, too, at the higher operating temperatures, the time-temperature-stress-strain characteristics of the materials, especially the ceramics, are unavailable.

The solutions for two different depthwise temperature profiles are presented. Case I represents a constant temperature change ( $\Delta T$ ) from an initial uniform condition throughout both elements of the composite slab. Case II represents a uniform temperature rise in the coating ( $\Delta T_c$ ) different from the uniform temperature change in the substrate ( $\Delta T_s$ ). The first case is applicable to steady-state conditions; attained temperatures are uniformly high throughout the thickness. The second case represents approximately the transient conditions early in re-entry when the temperatures throughout the structure are rising.

The following conditions were applied in formulating the thermal stress expressions:

1. A linear stress-strain relation was assumed.
2. The geometry approached that of a flat, unsupported plate (representing a shell of large radius-to-thickness ratio).
3. Specific uniform temperature profiles described above were assumed through the thicknesses of the slab.

The resultant stresses which are presented in the following examples are given in terms of Young's modulus and thermal expansion coefficient. The slab geometry is shown in the accompanying figure. The Y-axis originates at the interface and is positive toward the outer face.



Case 1. Uniform temperature change  $\Delta T$  throughout entire thickness

### Substrate Stress

$$\sigma_s = \alpha_s E_s \Delta T \left\{ \frac{\left[ \frac{j k (\ell - 1) (j + 1)}{2(jk + 1)} \right] \left[ \frac{y}{t_s} - \frac{(j^2 k - 1)}{2(jk + 1)} \right]}{\left[ \frac{j^3 k + 1}{3} - \frac{(j^2 k - 1)^2}{4(jk + 1)} \right]} + (\ell - 1) \left( \frac{jk}{jk + 1} \right) \right\} \quad (9)$$

### Coating Stress

$$\sigma_c = \alpha_c E_c \Delta T \left\{ \frac{\frac{1}{\ell} \left[ \frac{j k (\ell - 1) (j + 1)}{2(jk + 1)} \right] \left[ \frac{y}{t_c} - \frac{(j^2 k - 1)}{2(jk + 1)} \right]}{\left[ \frac{j^3 k + 1}{3} - \frac{(j^2 k - 1)^2}{4(jk + 1)} \right]} + \left( \frac{1}{\ell} - 1 \right) \left( \frac{1}{jk + 1} \right) \right\} \quad (10)$$

where

$$j = t_c/t_s; \quad k = E_c/E_s; \quad \ell = \alpha_c/\alpha_s$$

## Example

For a thoria coating ( $t_c = 0.20$  in.) on a tungsten substrate ( $t_s = 0.04$  in.), assume that the ratios of  $\alpha_c/\alpha_s$  and  $E_c/E_s$  will, for all temperatures, remain constant at the room temperature values,  $k = 0.45$  and  $\ell = 2.42$ . For a temperature increase ( $\Delta T$ ) of 5000 F over the entire composite thickness,

$$\sigma_c|_{y=t_c} = 1000 \quad \alpha_c E_c$$

$$\sigma_c|_{y=0} = -1800 \quad \alpha_c E_c$$

$$\sigma_s|_{y=0} = 2800 \quad \alpha_s E_s$$

$$\sigma_s|_{y=-t_s} = 1500 \quad \alpha_s E_s$$

Case 2. Uniform temperature change in coating  $\Delta T_c$  different from uniform Temperature change in substrate  $\Delta T_s$ .

### Substrate Stress

$$\sigma_s = \alpha_s E_s \Delta T_s \left\{ \frac{\left[ \frac{jk(\ell p - 1)(1 + 1)}{2(jk + 1)} \right] \left[ \frac{y}{t_s} - \frac{(j^2 k - 1)}{2(jk + 1)} \right]}{\left[ \frac{j^3 k + 1}{3} - \frac{(j^2 k - 1)^2}{4(jk + 1)} \right]} + (\ell p - 1) \left( \frac{jk}{jk + 1} \right) \right\} \quad (11)$$

### Coating Stress

$$\sigma_c = \alpha_c E_c \Delta T_c \left\{ \frac{\frac{1}{\ell p} \left[ \frac{jk(\ell p - 1)(1 + 1)}{2(jk + 1)} \right] \left[ \frac{y}{t_c} - \frac{(j^2 k - 1)}{2j(jk + 1)} \right]}{\left[ \frac{j^3 k + 1}{3} - \frac{(j^2 k - 1)^2}{4(jk + 1)} \right]} + \left( \frac{1}{\ell p} - 1 \right) \left( \frac{1}{jk + 1} \right) \right\} \quad (12)$$

where  $p = \Delta T_s / \Delta T_c$



Example

For a temperature increase in the tungsten substrate ( $\Delta T_s$ ) of 2200 F and a temperature increase in the protective coating ( $\Delta T_c$ ) of 3500 F.

$$\sigma_c|_{y = t_c} = -160 a_c E_c$$

$$\sigma_c|_{y = 0} = -1300 a_c E_c$$

$$\sigma_s|_{y = 0} = 450 a_s E_s$$

$$\sigma_s|_{y = -t_s} = 240 a_s E_s$$

**5.3 THERMAL STRESSES IN COMPOSITE AXISYMMETRIC THIN SHELLS**

The thermal stress analysis for a free composite slab (Sec. 5.2) was applicable to small test coupons, of possible interest in screening evaluations.

An analysis more nearly representing the conditions and geometry of the actual nose configurations is presented below.

With a given infinitesimal ring element subjected both to thermal strain and a strain arising from the restraint imposed by adjacent laminae, there is a radial line through the concentric laminae before heating which remains a straight unbroken line after heating. This represents a final strain line ( $\epsilon_o$ ), which is evaluated from an equilibrium of circumferential forces over each of the depthwise elements:

$$\epsilon_o = \frac{\sum_i E_i t_i \alpha_i \bar{T}_i / (1 - \mu_i)}{\sum_i E_i t_i / (1 - \mu_i)} \quad (13)$$

where

$\epsilon_0$  = final resultant strain

$E$  = elastic modulus

$\alpha$  = coefficient of thermal expansion

$t$  = thickness of shell element

$\mu$  = Poisson's ratio

$\bar{T}$  = average temperature rise in a given element, from an initial prevailing reference temperature

Subscript  $i$  = index for shell laminae, increasing from inner to outer elements.

With the subscripts  $a$  and  $b$  denoting, respectively, the inner and outer edges of a given element, the circumferential stresses for a general elemental layer of the shell are

$$\sigma_{i_a} = \frac{E_i}{1 - \mu_i} (\epsilon_0 - \alpha_i T_i - 1) \quad (14)$$

$$\sigma_{i_b} = \frac{E_i}{1 - \mu_i} (\epsilon_0 - \alpha_i T_i) \quad (15)$$

## Examples

Equations 6 and 7 may be used to determine thermal stresses in specific two-layer shell examples ( $i = 1, 2$ , with index 1 pertaining to the metallic substrate,  $s$ , and index 2 indicating the ceramic coating,  $c$ ). The nomenclature to be invoked is, namely

$$j = t_2/t_1 = t_c/t_s$$

$$k = E_2/E_1 = E_c/E_s$$

$$l = \alpha_2/\alpha_1 = \alpha_c/\alpha_s$$

$$p = \bar{T}_1/\bar{T}_2 = \bar{T}_s/\bar{T}_c$$

The resultant strain becomes

$$\epsilon_o = \frac{\frac{E_s t_s a_s \bar{T}_s}{1 - \mu_s} + \frac{E_c t_c a_c \bar{T}_c}{1 - \mu_c}}{\frac{E_s t_s}{1 - \mu_s} + \frac{E_c t_c}{1 - \mu_c}} \quad (16)$$

Dividing by  $(E_s t_s a_s \bar{T}_c)$  and assuming that  $\mu_s = \mu_c$

$$\epsilon_o = \frac{p + j k \ell}{1 + j k} a_s \bar{T}_c \quad (17)$$

The four thermal stresses (inner substrate; substrate-interface; ceramic-interface; outer ceramic) are

$$\sigma_{s \text{ inner}} = \frac{E_s}{1 - \mu_s} (\epsilon_o - a_s T_{s \text{ inner}}) \quad (18)$$

$$\sigma_{s \text{ outer}} = \frac{E_s}{1 - \mu_s} (\epsilon_o - a_s T_{s \text{ outer}}) \quad (19)$$

$$\sigma_{c \text{ inner}} = \frac{E_c}{1 - \mu_c} (\epsilon_o - a_c T_{c \text{ inner}}) \quad (20)$$

$$\sigma_{c \text{ outer}} = \frac{E_c}{1 - \mu_c} (\epsilon_o - a_c T_{c \text{ outer}}) \quad (21)$$

## Case 1: Uniform Temperature Change Throughout Entire Thickness

$$j = 5.0$$

$$k = 0.45$$

$$\ell = 2.42$$

$$p = 1.00 \quad (T_c = 5000 \text{ F})$$

$$\epsilon_o = \frac{1 + 5.0 (0.45) (2.42)}{1 + 5.0 (0.45)} (5000) a_s$$

$$= 9900 a_s = 9900 \frac{\alpha_c}{\ell} = 4090 a_c$$

$$\sigma_s = \frac{E_s}{1 - \mu_s} (9900 \alpha_s - 5000 a_s) = \underline{4900 \left( \frac{E a}{1 - \mu} \right)_s}$$

$$\sigma_c = \frac{E_s}{1 - \mu_c} (4090 \alpha_c - 5000 a_c) = \underline{-910 \left( \frac{E a}{1 - \mu} \right)_c}$$

Verify equilibrium of forces

$$\sigma_s + j \sigma_c = 4900 E_s a_s + 5.0 (-910) (0.45 E_s) (2.42 a_s)$$

$$= 4900 E_s a_s - 4900 E_s a_s = \underline{0}$$

## Case 2: Temperature Gradient Through Composite -- Thick Coating

$$T_o = 1900 \text{ F}; T_1 = 2500 \text{ F}; T_2 = 3900 \text{ F}$$

$$j = 5.0$$

$$k = 0.45$$

$$\ell = 2.42$$

$$p = (1900 + 2500) / (2500 + 3900) = 0.687$$

$$\left( \bar{T}_c = \frac{2500 + 3900}{2} = 3200 \text{ F} \right)$$

# Contrails

Equation 17 gives  $\epsilon_0 = \frac{0.687 + 5(0.45)(2.42)}{1 + 5(0.45)} (3200) a_s$

$$= 6050 a_s = 6050 \frac{a_c}{\ell} = 2500 a_c$$

Equations 18 through 21 yield

## Substrate

$$\sigma_{s_{\text{inner}}} = \frac{E_s}{1 - \mu_s} (6050 a_s - 1900 a_s) = \underline{\underline{4150 \left( \frac{E_s a}{1 - \mu_s} \right)_s}}$$

$$\sigma_{s_{\text{outer}}} = \frac{E_s}{1 - \mu_s} (6050 a_s - 2500 a_s) = \underline{\underline{3550 \left( \frac{E_s a}{1 - \mu_s} \right)_s}}$$

## Coating

$$\sigma_{c_{\text{inner}}} = \frac{E_c}{1 - \mu_c} (2500 a_c - 2500 a_c) = \underline{\underline{0}}$$

$$\sigma_{c_{\text{outer}}} = \frac{E_c}{1 - \mu_c} (2500 a_c - 3900 a_c) = \underline{\underline{-1400 \left( \frac{E_c a}{1 - \mu_c} \right)_c}}$$

Summing the tangential forces

$$\begin{aligned} \sigma_{s_{\text{avg}}} + j \sigma_{c_{\text{avg}}} &= \frac{4150 + 3550}{2} E_s a_s + 5 \left( \frac{0 - 1400}{2} \right) (0.45 E_s) (2.42 a_s) \\ &= 3800 E_s a_s - 3800 E_s a_s = \underline{\underline{0}} \end{aligned}$$

### 5.4 UNBONDING PRESSURE IN TWO-ELEMENT COMPOSITE SHELLS

In early techniques, holding the thoria coating to the tungsten substrate involved the welding of tungsten members to the substrate. An analysis was developed to determine the retention strength required to hold a reinforced ceramic overlay on a refractory metal shell. Retaining an intact protective refractory coating was of vital concern whether the attachment be an interfacial bonding, a spot welding of reinforcement to the substrate, a simple wiring-down of reinforcing mesh intersections, or these methods in combination. A thin-shell elastic solution was formulated to determine unbonding pressures between two laminae.

A simplified (thin-shell, elastic) solution for determining unbonding pressures between two laminae follows. The shell geometry is defined in Figure 80.

Line A represents the displaced inner face of Element 1 due to free (unbonded) thermal expansion. Line B represents the displaced outer face of Element 2 due to free (unbonded) thermal expansion.

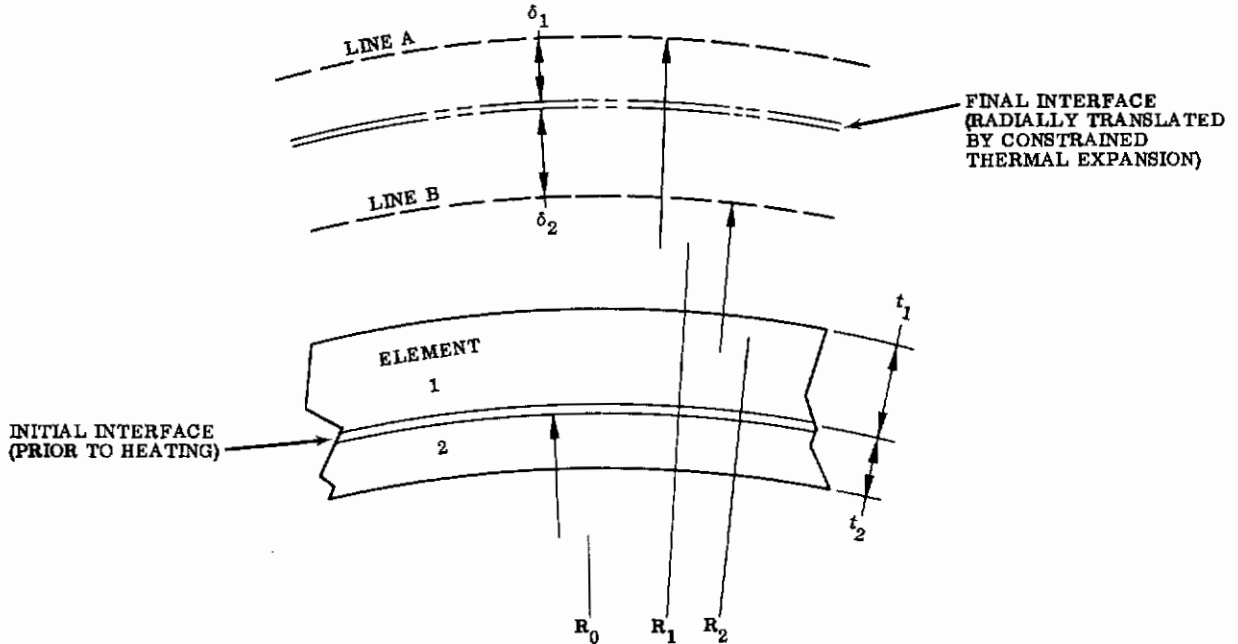


FIGURE 80. DESCRIPTION OF SHELL LAMINAE

If Elements 1 and 2 are detached at the interface and heated to their respective average temperatures ( $\Delta T_1$  and  $\Delta T_2$ ) from an initial condition of uniform temperature throughout, the final position of the bond surfaces for each of the elements, due to free thermal expansion, will be

$$R_1 = R_0 (1 + \alpha_1 \Delta T_1) \quad (22)$$

$$R_2 = R_0 (1 + \alpha_2 \Delta T_2) \quad (22a)$$

where the applicable coefficients of linear thermal expansion are denoted by  $\alpha$ .

The deflections required to re-attach each of the elements in their final bonded (equilibrium) position are  $\delta_1$  and  $\delta_2$ . Thus,

$$R_1 - R_2 = \delta_1 + \delta_2 \quad (23)$$

#### 5.4.1 Case 1; Spherical Shell

Considering the elemental rings to be cut from a sphere, the deflections are

$$\delta = \epsilon R.$$

But,

$$\epsilon = \frac{\sigma}{E} (1 - \nu) \text{ and } \sigma = pR/2t$$

where:

$\epsilon$  = strain

$R$  = thin-shell radius

$\sigma$  = membrane stress in spherical shell

$E$  = modulus of elasticity

$\nu$  = Poisson's ratio

$p$  = unbonding pressure

$t$  = shell thickness

The deflections are then

$$\delta_1 = \frac{pR_1^2 (1 - \nu_1)}{2E_1 t_1} \quad (24)$$

$$\delta_2 = \frac{pR_2^2 (1 - \nu_2)}{2E_2 t_2} \quad (24a)$$

The pressure term  $p$  may be considered as the external pressure acting on Element 1 or the internal pressure (same absolute magnitude) acting on Element 2 tending to deflect the rings to the attached equilibrium position.

Substituting Equations 22 and 24 into Equation 23 gives

$$R_o (\alpha_1 \Delta T_1 - \alpha_2 \Delta T_2) = \frac{p}{2} \left[ \frac{R_1^2 (1 - \nu_1)}{E_1 t_1} + \frac{R_2^2 (1 - \nu_2)}{E_2 t_2} \right]$$

To simplify the above expression, the initial interface radius is used, assuming for the thin shell that  $R_o \approx R_1 \approx R_2$ .

$$\text{Thus,} \quad \alpha_1 \Delta T_1 - \alpha_2 \Delta T_2 = \frac{pR_o}{2} \left[ \frac{1 - \nu_1}{E_1 t_1} + \frac{1 - \nu_2}{E_2 t_2} \right]$$

giving, for the unbonding pressure

$$p = \frac{2}{R_o} \left[ \frac{\alpha_1 \Delta T_1}{\frac{1 - \nu_1}{E_1 t_1}} + \frac{\alpha_2 \Delta T_2}{\frac{1 - \nu_2}{E_2 t_2}} \right] \quad (25)$$

#### 5.4.2 Case 2; Cylindrical Shell

Here,  $\epsilon = \frac{\sigma}{E} = \frac{1}{E} \frac{pR}{t}$  due to hoop stresses.

Proceeding as in Case 1, the unbonding pressure is

$$p = \frac{1}{R_o} \left[ \frac{\alpha_1 \Delta T_1 - \alpha_2 \Delta T_2}{\frac{1}{E_1 t_1} + \frac{1}{E_2 t_2}} \right] \quad (26)$$



## VI. SELECTION AND DESIGN OF FRONTAL SECTION

Prior analytical studies in this program dealt with necessary aerodynamic, thermodynamic, and structural aspects of designing a suitable refractory metal frontal structure for a lifting super-orbital entry vehicle. This section discusses the evaluation of selected frontal structures from diverse viewpoints — fabrication, weight, reliability, satisfying mission requirements — to justify a choice of final design structure. In brief review, the candidate vehicle configurations, due to their distinctive aerodynamic qualities, viz., lift-to-drag ratio and ballistic coefficient, and because they adhere to a unique maneuver program, descend with specific portions of an allowable flight corridor. The upper and lower bounds of this entry corridor are termed, respectively, the single-pass (grazing) skip-out limit and the deceleration limit. These extremes are approached whenever the entry flight path angle is either too shallow or too steep.

Oblate ellipsoidal frontal sections, each aligned at approximately pitch angle  $\alpha$  from the respective vehicle centerlines were chosen for the re-entry shapes. Actual external shell geometries for the various frontal sections were presented in Section 2.3. Since a constant positive trim attitude is maintained throughout descent, definite advantages accrue from a drooped nose alignment: the fixed stagnation point will coincide with their axes, and a symmetric distribution of load and temperature will exist about rotationally symmetric frontal caps. The principal advantages of a blunted frontal geometry are lowering of stagnation point convective heating and a more uniform input heating about the remainder of the nose cap; the convective input heating rate for a given flight velocity and air density varies inversely as the square root of effective nose radius at the stagnation point.

Rather than tailor a specific optimum (thermally and structurally) frontal section to a single parabolic entry routine, which from a strategic operational standpoint is over restrictive, a more attractive approach is to design a thermal protective system which has a broad range of capabilities. Such a frontal structure requires a built-in margin to survive possible extremes in hyperthermal environment induced by

# Contrails

maneuvers which unforeseen circumstances might demand of the system. A potential for flying a lifting vehicle through diverse entry conditions emphasizes the complementary role of man in the system and of his judgement in selecting suitable entry paths and maneuvering down-range and cross-range to alternate landing sites. Moreover, a design of general applicability makes the initial angle-velocity tolerances on atmospheric penetration less critical. Without a capacity for withstanding probable combinations of peak heat rates, moderate dynamic loads, and long-duration high integrated heat loads, the value of the aerospace vehicle to fulfill unpredictable entry missions upon return from flight in outer space becomes marginal.

Early in the program, four typical lifting vehicles were chosen as being a representative cross section of candidates, each characterized by distinctive and differing flight (and therefore, environmental) qualities. As studies progressed, the possibility of narrowing the frontal thermal protection system to one of two basic concepts became apparent — either a thin radiative (hot-wall) structure or a combined system embodying transitory absorption followed by prolonged radiation. With only the light glider demonstrating a possible potential for withstanding peak heating in the simple radiative mode, this selection was automatic. Alternatively, the fact became increasingly apparent during this evaluation that designing for the most severe peak heat rate in conjunction with a long-duration trailing pulse would also show merit; thus, the glider of medium wing loading was selected as the absorptive-radiative candidate. Both of these winged vehicles possess a hypersonic L/D of 2.0 with resultant favorable supersonic and subsonic glide characteristics.

Next, between the two winged vehicles a final design configuration was selected. With the primary objective being versatility of entry operation (return to earth at times and places chosen to support a selected mission), the medium glider (L/D = 2.0,  $W/C_D A = 200$  psf) was the principal choice. It displayed a combined capacity to resist the highest-amplitude heating rates or any lesser but extended values at shallower entry. The light glider, on the other hand, was restricted to entry near the skip-out limit (Fig. 4) for a controlling  $\dot{q}_{c_{max}}$  of 200 Btu/ft<sup>2</sup>-sec. With little or no tolerance on entry path, severe burdens are placed on accuracy of mid-course guidance and control, and limitations are imposed upon maneuvers within the air space. Other factors strongly suggest shortcomings in the light glider concept: for large surface areas, the ratio of gross payload-to-entry weight is substantially reduced; controlling

the weight of heat protection on the predominant surface areas elsewhere on the vehicle becomes difficult; the very thin protective refractory coatings recommended for a light glider are subject to cracking and spallation when undergoing low-temperature vibration during ascent or when exposed to high-velocity particle impingement in space; with large fixed aerodynamic surfaces atop a multi-stage boost configuration, flight stabilization during ascent would be difficult to achieve; and for a rigid re-entry vehicle, a wing loading of 15 psf is about the practical lower limit. Also, as shown in Figure 9, the winged glider may be operated at a variety of design points other than near  $L/D)_{\max}$ .

Since comparative weight determinations for various hyperthermal protective systems require integrated values of surface area and of volume enclosed by the nose shells, these data were derived for the frontal section selected above.

Figure 81 shows a plot of cumulative surface area as a function of vehicle stationing commencing from the stagnation zone. A plan view, side elevation, and rear view of the candidate nose section were presented in Figure 12. The overall length of the body was 46 inches. Values of area and volume were obtained by integration of a loft contour drawing for the external metallic shell surface of the common glider nose shape. The total shell surface, exclusive of the base, was 31.5 square feet. Surface area is required for assessing the weight contribution of a reinforced ceramic protective overlay graduated fore-to-aft in thickness.

Figure 82 shows a plot of variation in area of sections normal to the vehicle longitudinal axis. Integrating the area under this curve yielded the total enclosed volume as 16.3 cubic feet. This value is of importance in determining, for instance, weight of a high-temperature internal insulative system.

## 6.1 SELECTION OF FINAL DESIGN THERMAL PROTECTION SYSTEM

With the pure hot-wall concept no longer being considered, the remaining frontal system was the combined absorptive-radiative structure.

Adequate temporary heat absorption was assumed provided by either of the following:

1. A thin efficient coating of a conventional high-temperature char-forming ablator bonded to a coated refractory primary frontal structure.

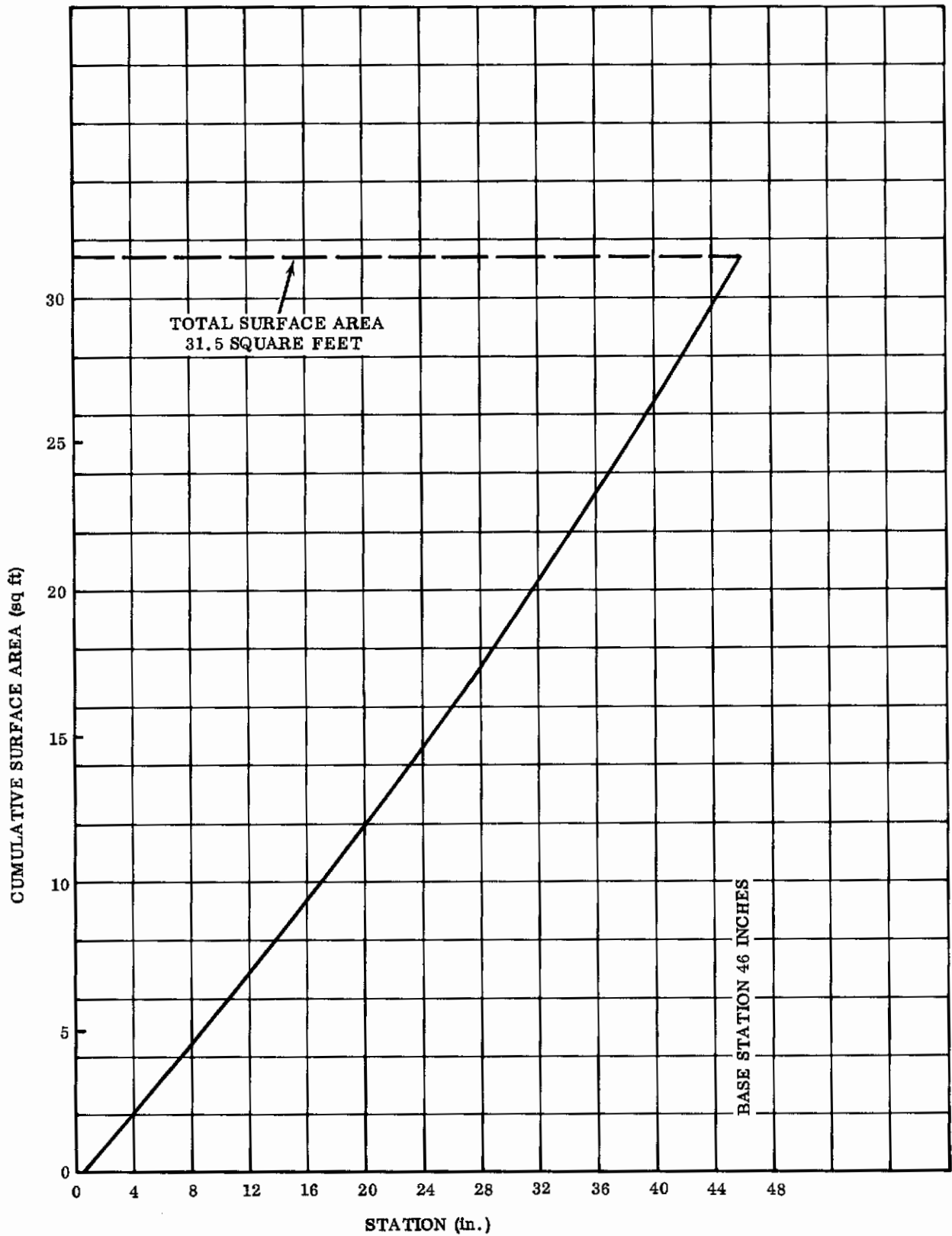


FIGURE 81. WINGED GLIDER FRONTAL SHELL; Cumulative Surface Area

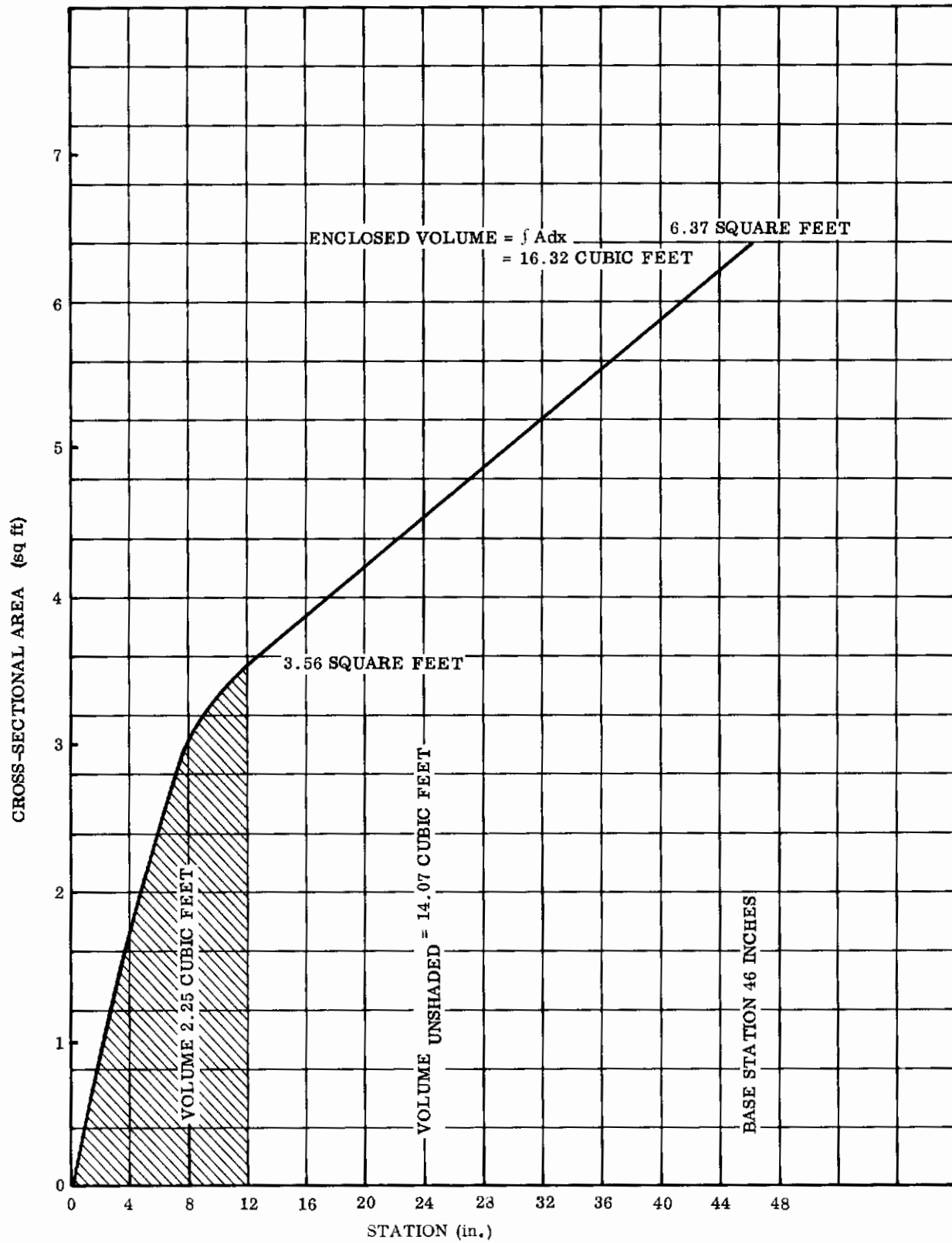


FIGURE 82. WINGED GLIDER FRONTAL SHELL; Area of Normal Sections

2. A composite of high heat-capacity reinforced ceramic attached to a tungsten alloy substrate.

Ablation of fused silica and magnesium oxide were also investigated, but both systems were found to be of questionable use. Softening and premature loss of unreinforced material as well as chemical attack of metallic base were the more-pronounced problems.

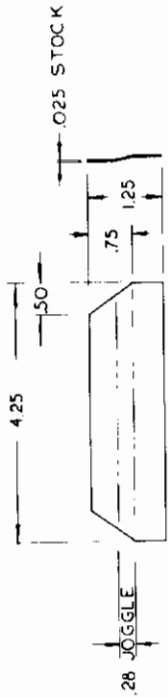
A severe demand upon the ablation systems, in general, was the criterion that the coating must disappear entirely at a relatively early time in Phase III flight. Such a situation precipitates high stresses and even a possible unpredictable early loss of the ablative shield. Thermal stresses were found to predominate by several orders of magnitude over stresses arising from inertia loading and applied airloads (normal forces and aerodynamic shear).

Since this program was to emphasize design approaches other than thermal shielding from the customary organic ablators, the high capacity-radiative frontal system in Item (2), above, was chosen for the final design structure. However, weights of both systems were calculated for comparative purposes.

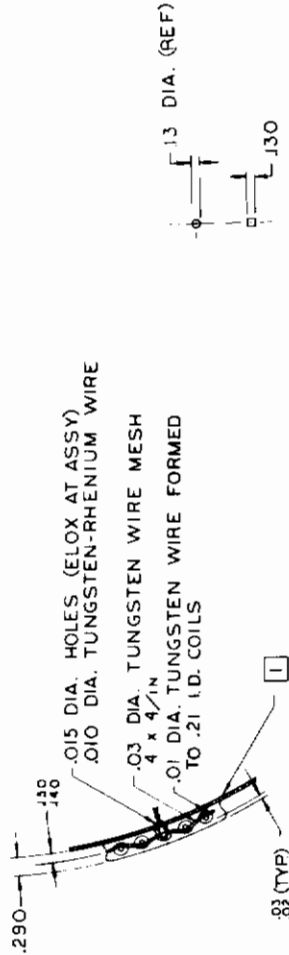
## 6.2 DESIGN OF FRONTAL SECTION

The final design of the frontal section closely follows the analysis presented in prior sections of this report, supported by materials development work discussed in Volume II, Materials and Composite Structure Development. Details of the design are shown in Figure 83. Since the full-scale frontal section was not to be fabricated, the design was performed in detail sufficient to allow a reasonable weight estimate.

Analyses presented in Sections 5.1 and 4.3.1 defined the required shell thickness to be 0.040 inch, and the thoria coating to be 0.29 inch at the stagnation point. Beyond the shoulder, thoria thickness is dropped to 0.10 inch as a practical minimum. Reinforcement of the thoria is accomplished by a tungsten screen in combination with fine tungsten coils. Attachment of the reinforcement system to the substrate is accomplished mechanically; either by pins, as was done during the program, or by wire loops. Fastening of the frontal section to the vehicle is accomplished through a series of metallic clips. These clips are designed to operate at elevated temperatures (approximately 3000 F) and to withstand base moments and axial loads as well as air loads. These clips allow freedom of thermal deformation radially, circumferentially, and rotationally.



DETAIL -21 GUSSET  
FULL SIZE



SECT A-A  
NO SCALE

8. ALL BEND RADIUS .12 UNLESS OTHERWISE NOTED.
7. ALL RIVET LOCATIONS NOT SHOWN, MAY BE SCALED.
6. ODD DASH NO SHOWN NEXT HIGHER EVEN NUMBER OPPOSITE.
- 5] QUANTITY AS REQUIRED
- 4] CONTOUR AND DIMENSIONS TO BE TAKEN FROM FRONTAL SECTION, LOFT DWG. NO R-58894
- 3] FAIR FROM .290 THICK AS PER SECT 'A-A' TO .100 THICK, CONSTRUCT AS PER DETAIL 'B', IN 2.00 LONG SURFACE OF REVOLUTION.
- 2] .290 THICK CONSTRUCTION AS PER SECT 'A-A'.
- 1] COAT ENTIRE INNER SURFACE WITH .002 THICK TUNGSTEN THEN .005 THICK THORIA.

NOTE:

QTY.	CODE	DESCRIPTION	NAME OR IDENTIFYING NO.	DATE	APPROVED	REVISION	SCALE
5		THORIA (T-O <sub>2</sub> )					
5		FIBROUS Zr O <sub>2</sub>					
		COILS					
		WIRE MESH .03 DIA. 4 x 4/IN (TUNG)					
		WIRE MESH .02 DIA. 10 x 10/IN (TUNG)					
		WIRE .010 DIA. TUNGSTEN-RH (25%)					
		RIVET 3/32					
		RIVET 1/8					
		RIVET 3/16					
		SPACER .025 SHT. TUNGSTEN					
5		PIN .13 DIA. TUNGSTEN ROD					
1		SUPPORT .01 DIA. TUNGSTEN WIRE 3 x 3/IN MESH					
1		ANGLE .032 SHT. MOLYBDENUM					
1		GUSSET .025 SHT. MOLYBDENUM					
2		GUSSET					
1		BINDER					
1		ANGLE					
2		BINDER					
2		ANGLE					
1		BEAM					
1		BEAM					
1		BEAM					
1		FLEXURE .050 SHT. MOLYBDENUM					
1		WEB .025 SHT. MOLYBDENUM					
1		SUPPORT .01 DIA. TUNGSTEN WIRE 3 x 3/IN MESH					
1		BODY					
1		INSULATION OR SUBSTRATE					

MISSILES & SPACE COMPANY 5000 AVENUE 100 BUREAU OF AERONAUTICS WASHINGTON, D.C. 20330	
ASSY - FRONTAL SECTION FOR RE-ENTRY VEHICLE	DRAWING NO. R-58895
SHEET NO. 06887 J	SHEET TOTAL 1 OF 1

FIGURE 83. FINAL DESIGN FRONTAL STRUCTURE; Detailed Drawing (Sheet 1 of 6)

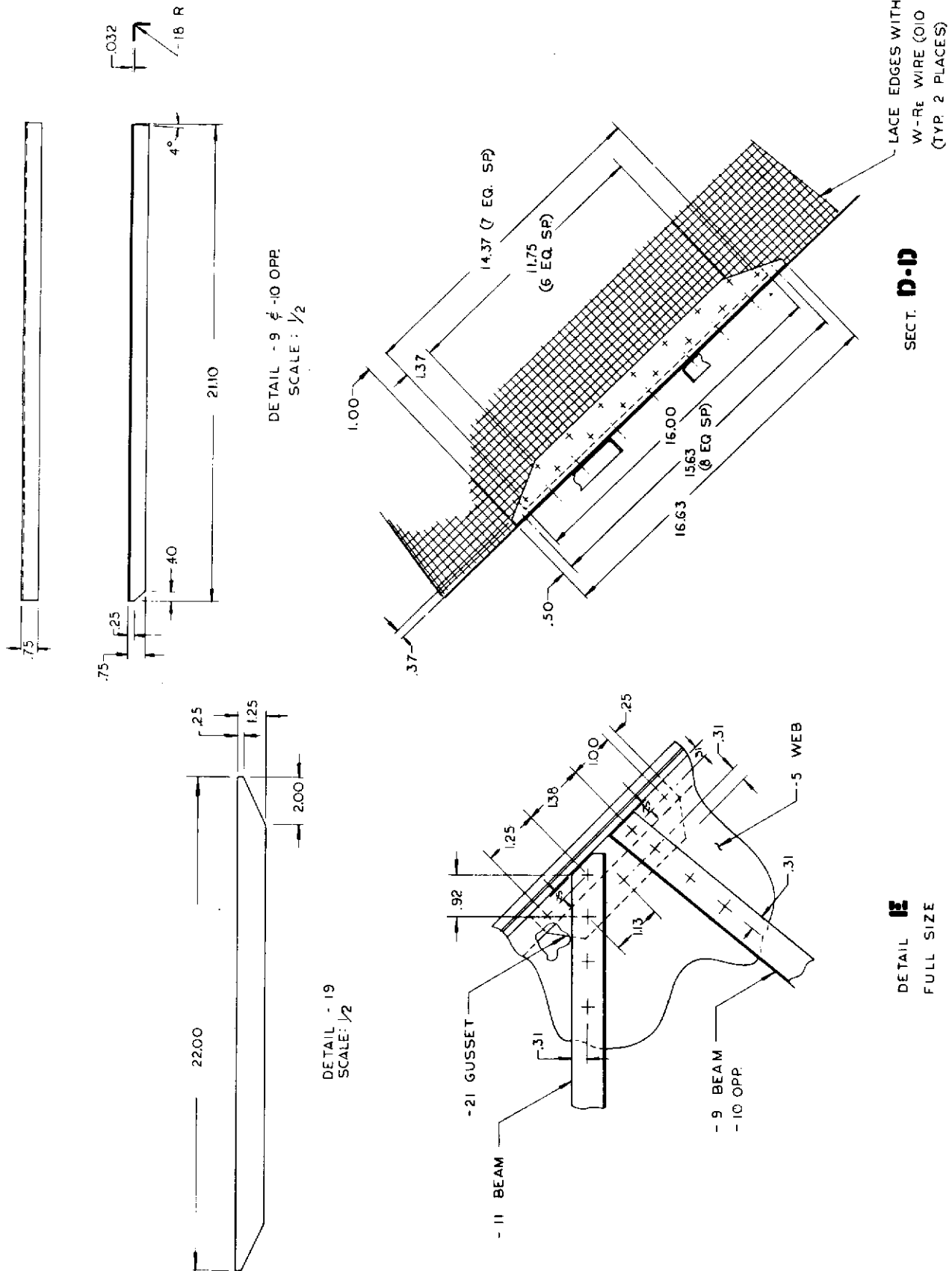


FIGURE 83. FINAL DESIGN FRONTAL STRUCTURE; Detailed Drawing (Sheet 2 of 6)



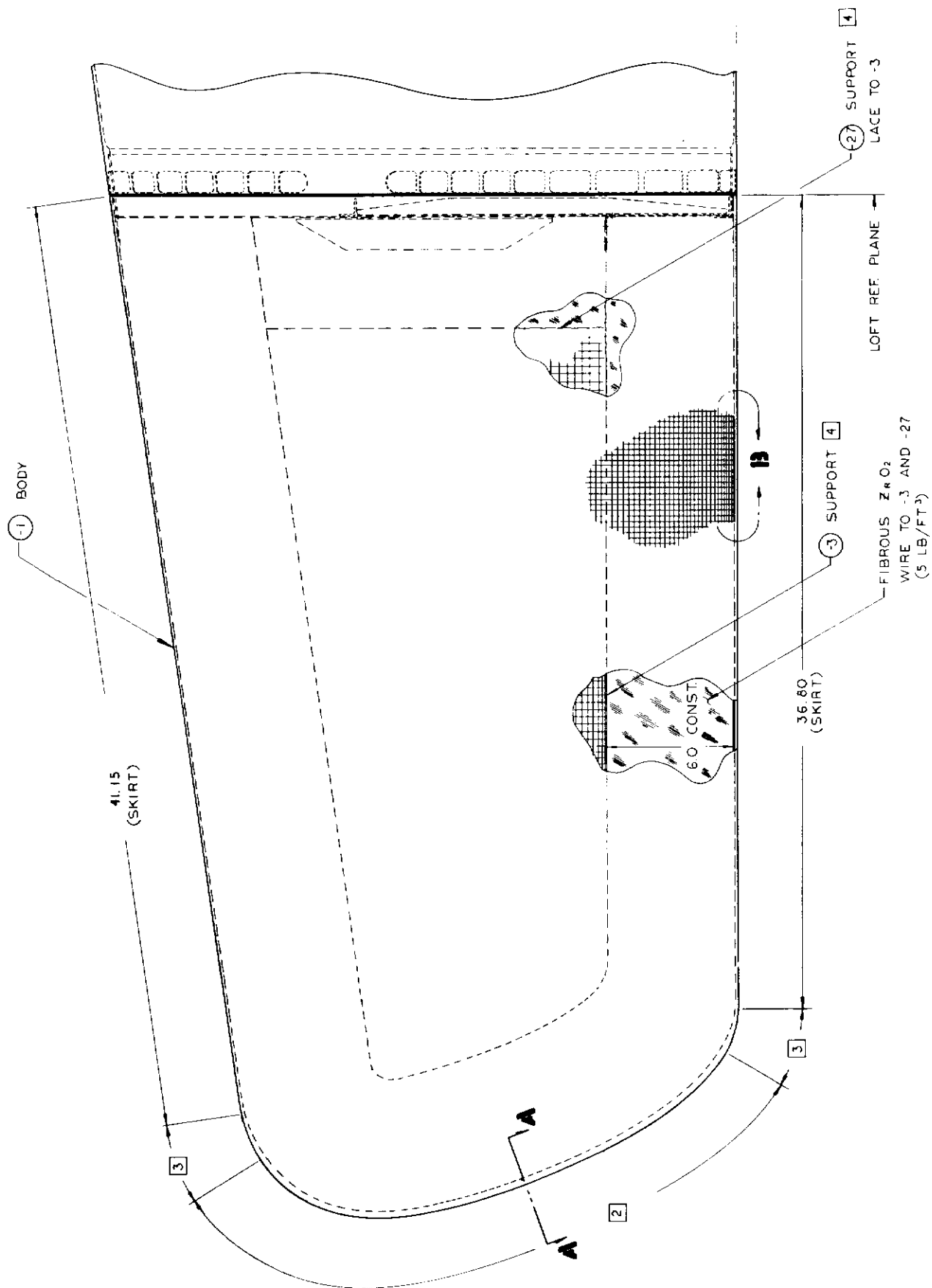


FIGURE 83. FINAL DESIGN FRONTAL STRUCTURE; Detailed Drawing (Sheet 3 of 6)

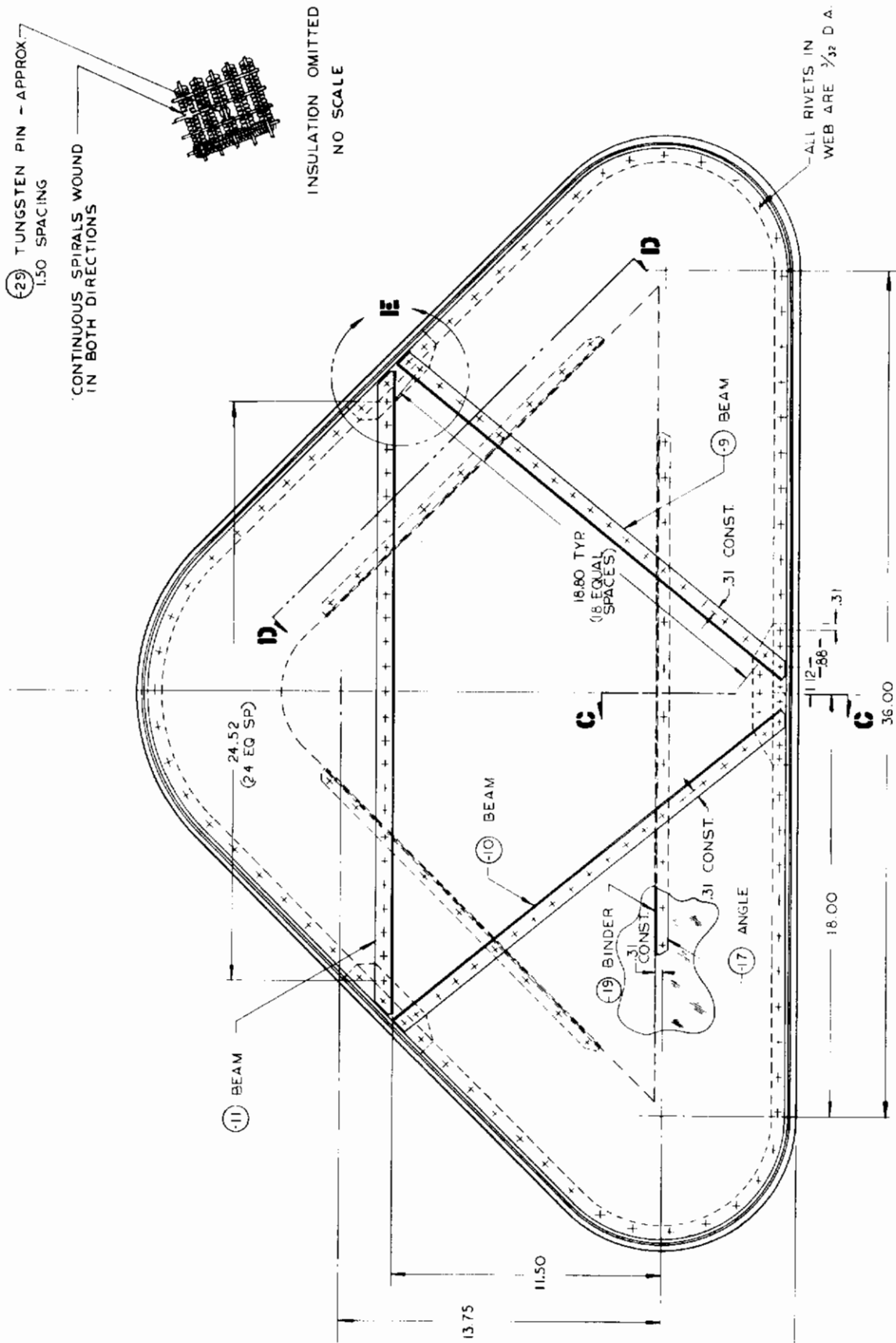
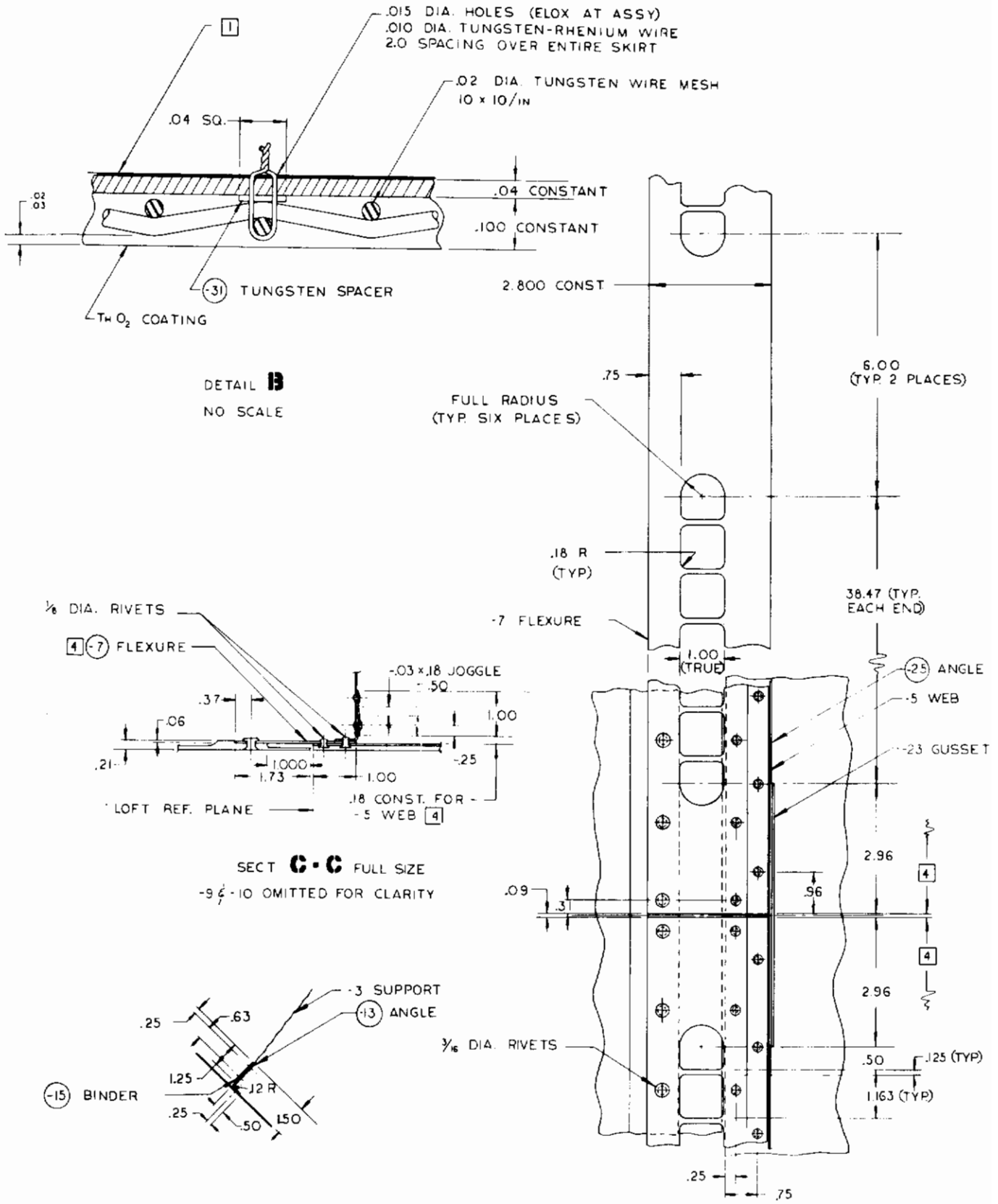


FIGURE 83. FINAL DESIGN FRONTAL STRUCTURE; Detailed Drawing (Sheet 4 of 6)



**FIGURE 83. FINAL DESIGN FRONTAL STRUCTURE; Detailed Drawing (Sheet 5 of 6)**

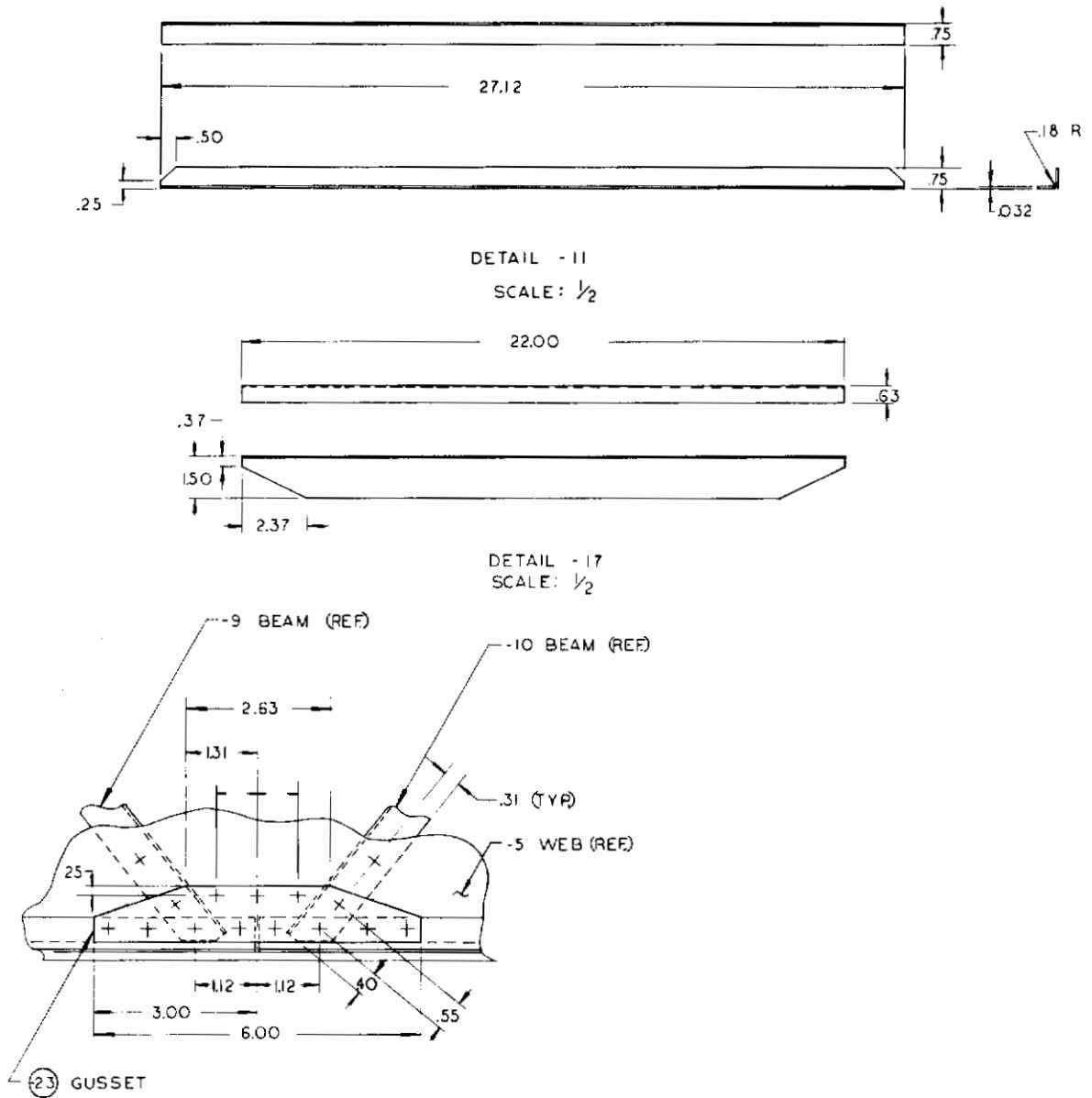
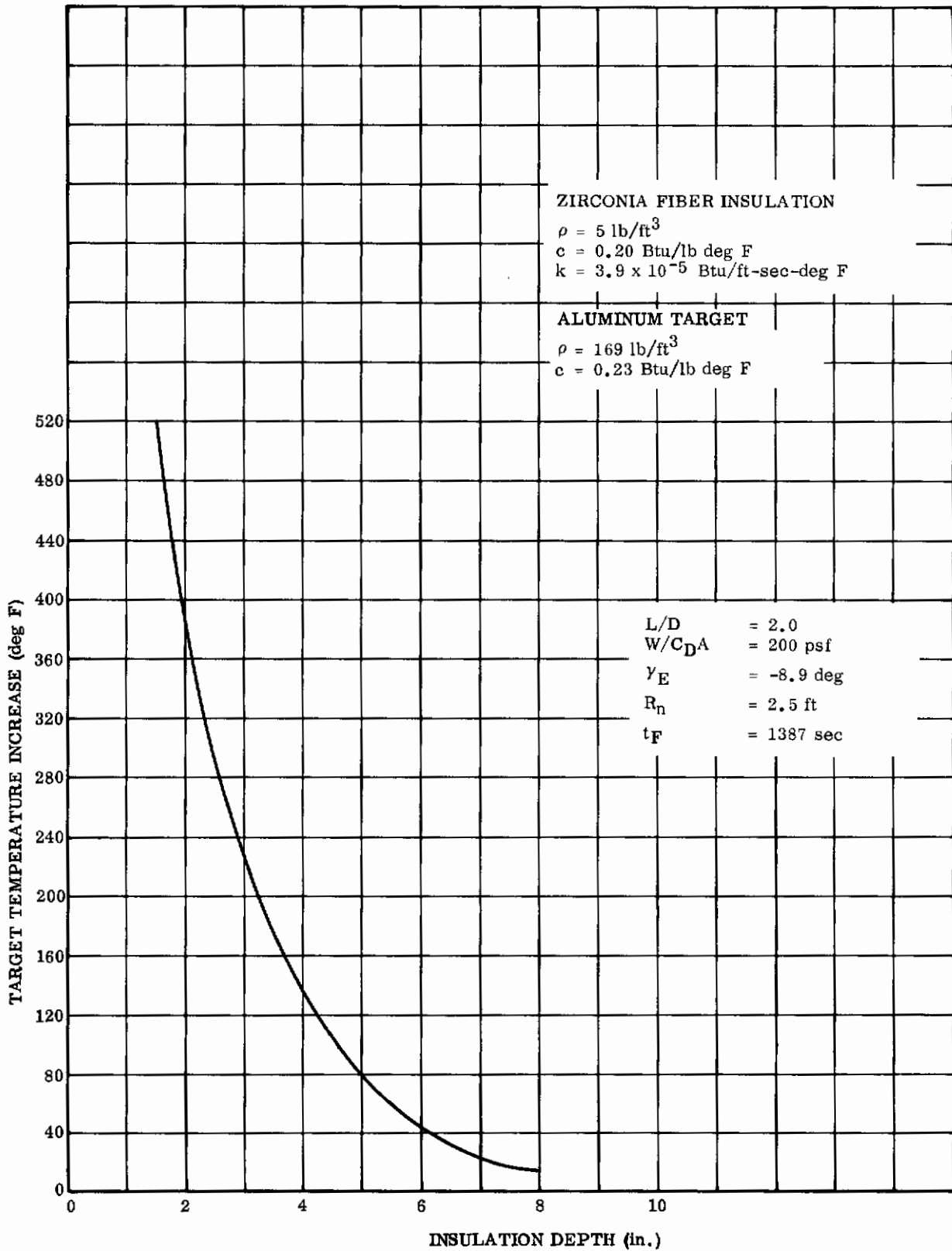


FIGURE 83. FINAL DESIGN FRONTAL STRUCTURE; Detailed Drawing (Sheet 6 of 6)

An efficient final design system for impeding heat flow into the nose section interior from the hot back surface of the refractory structural shell was selected based on analyses shown in Section 4.3.2. The rise in target temperature in the central base region was calculated for various thicknesses of a loosely compacted rear insulation of high-melting-temperature fibrous zirconia insulation. For minimum weight of insulation, a low value of  $\rho k/c$  is important (Fig. 84). For minimum weight of insulation, a low value of  $\rho k/c$  is important. From Figure 73, fibrous zirconia has a  $\rho k/c = 9.8 \times 10^{-4} \text{ lb}^2/\text{ft}^4\text{-sec}$  for temperatures greater than 2800 F. For prolonged low-level heat input, the unit weight of insulator depends more strongly on the heating duration and allowable temperature rise of the target rather than the heat load (Ref. 4). From Figure 84, a low-capacity aluminum target will be protected against a 100 F temperature increase by only a 5-inch thickness of ceramic matte which, for a density of  $5 \text{ lb}/\text{ft}^3$ , represents a unit weight of only  $2.1 \text{ lb}/\text{ft}^2$ . In the final design, a 6.0-inch layer will be recommended to preclude problems of variation in compacted fiber density after placement in the nose cone.

#### 6.2.1 Non-Coated Tungsten Conical Section

A study was conducted to consider the feasibility of utilizing a partially uncoated tungsten nose shell to conserve weight. The winged glider conceptual ellipsoid-cone employed in this analysis was the same as is shown in Figure 61. Oxidation recession was calculated for the thin-gage tungsten conical skirt with no protective ceramic overlay provided. The correlation equations of Figure 85 give oxidation rates, knowing the time-variation of local temperature and pressure. The history of the partial pressure of oxygen on the tungsten skirt and of the absolute surface temperature were computed in Reference 27 and the results are given in Figure 86 of this report. At the altitude corresponding to peak impact pressure, 173,500 feet, ambient pressure is insignificant. The rise in the pressure curve beyond 600-second entry time is due to the increasing ambient pressure of Phase IV flight. In the early high-temperature, low-pressure flight regime, no oxide scale adheres to the metallic surface of the tungsten, and a lower value of total normal emittance ( $\epsilon_W = 0.4$ ) is realized. In the later low-temperature, high-pressure regime, the surface emittance characteristics change due to retention of a red-violet oxide (Ref. 36) believed to be  $\text{W}_{18}\text{O}_{49}$ . Operation in this phase results in an increased total normal emittance, here assumed as 0.6.



**FIGURE 84. TARGET TEMPERATURE INCREASE FOR VARIOUS INTERNAL INSULATION DEPTHS**

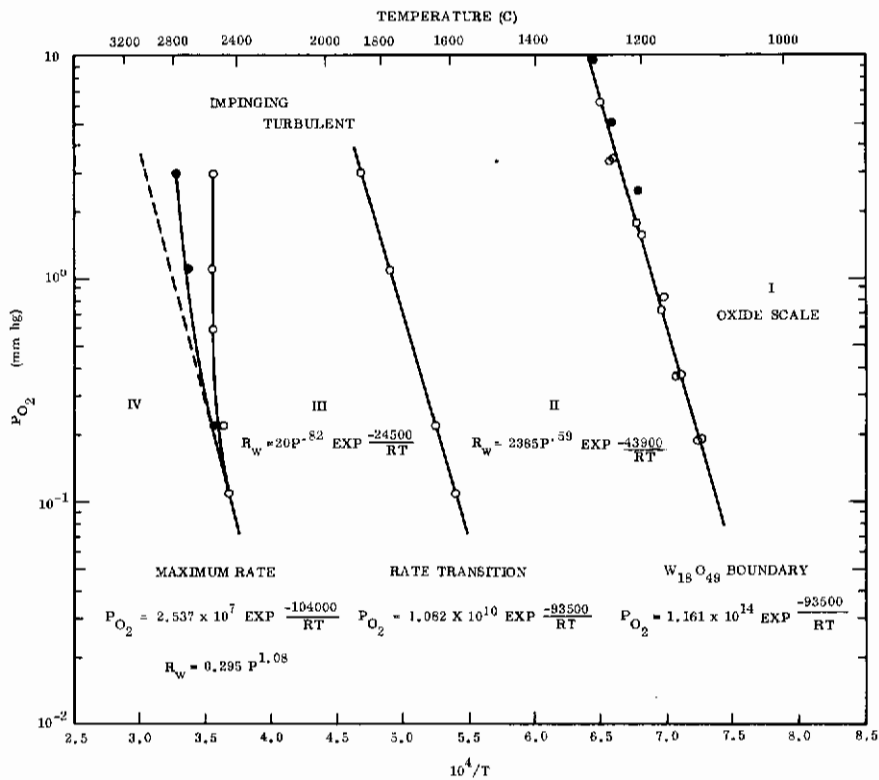


FIGURE 85. TUNGSTEN OXIDATION BEHAVIOR AT LOW PRESSURE AND HIGH TEMPERATURE

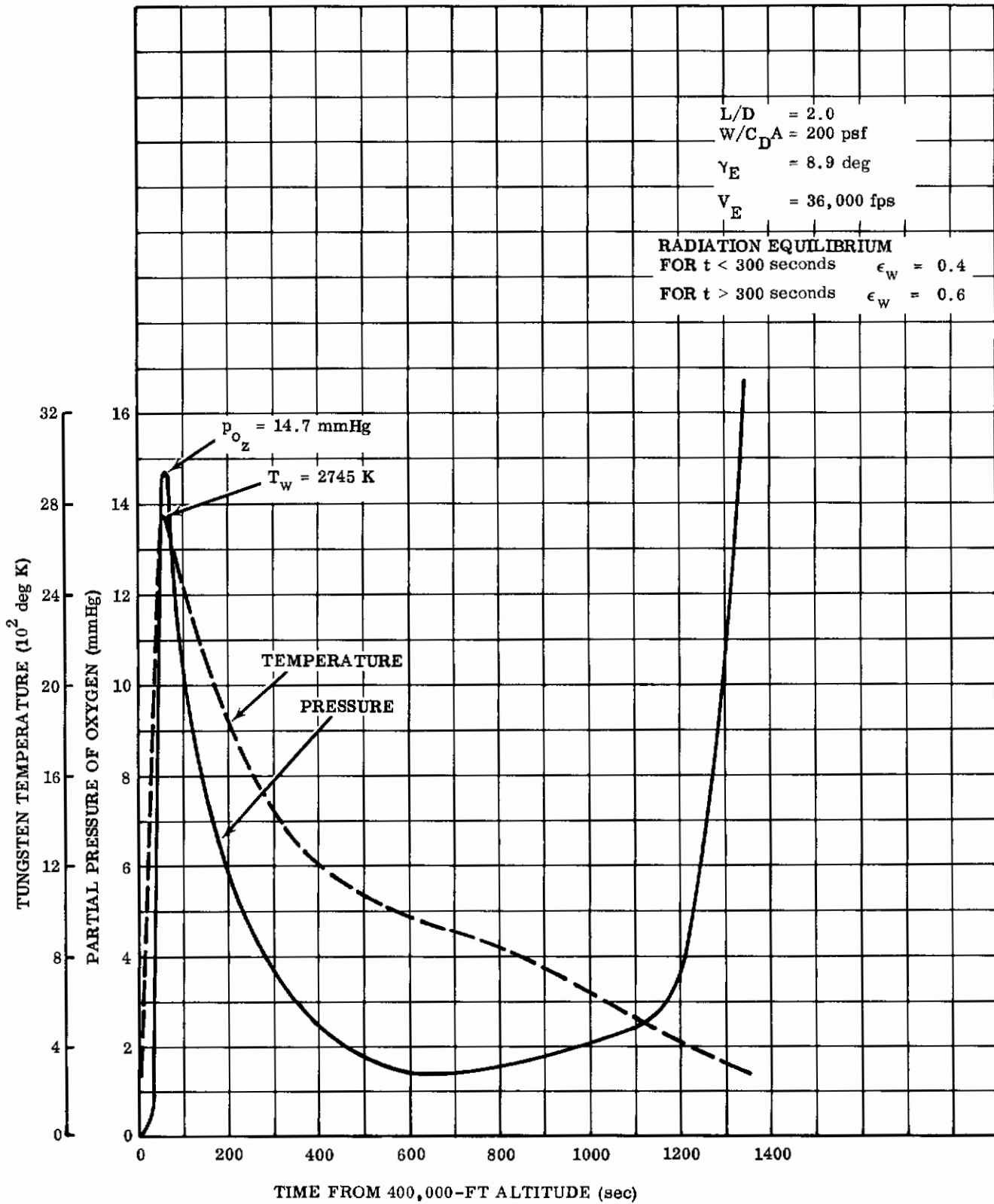


FIGURE 86. CONICAL SECTION TEMPERATURE-PRESSURE HISTORY



# Contrails

The recession rates shown in Figure 87 were obtained from the aforementioned correlation expressions. From the figure, the following observations may be made:

1. A peak recession rate of approximately 0.7 mil/sec occurs at 54 seconds after atmospheric entry.
2. A total integrated recession of approximately 0.040 inch occurs on the outer surface of the body. The inner surface presumably will remain at a much lower pressure — approaching the ambient value — and, furthermore, will not be readily accessible to attack by oxygen because of a fibrous insulative backing.
3. At a time when pressure-temperature magnitudes have decayed to a point where a residual film of oxide adheres to the tungsten (approximately 300 seconds), the surface recession rate becomes immeasurably small.

A statement of caution should be added to the preceding results. Correlation expressions upon which the results were obtained were based upon a radially inward flow of either cold oxygen or cold air about heated cylindrical tungsten test specimens. Two unanswered questions pertaining to the actual entry environment and its effect upon oxidation rate remain:

1. What is the effect if air within the boundary layer has a temperature greater than the body surface?
2. What is the effect of dissociation — in other words, is the recession rate increased by the presence of atomic oxygen rather than molecular oxygen?

A supplemental tungsten thickness of 0.04 inch for recession versus a 0.1-inch coating of tungsten-reinforced 80 percent-dense thoria (assuming a specific gravity of 19.3 for the former and 10.0 for the latter) have comparative unit weights of 4.0 psf and 5.2 psf, respectively, favoring the tungsten erosion. However, if this concept had been chosen, the resultant hardware would be restricted to a single re-entry before replacement. This factor, plus the presently unknown aspects of oxidation in a realistic hypervelocity environment, made the skirt aft section a more favorable design.

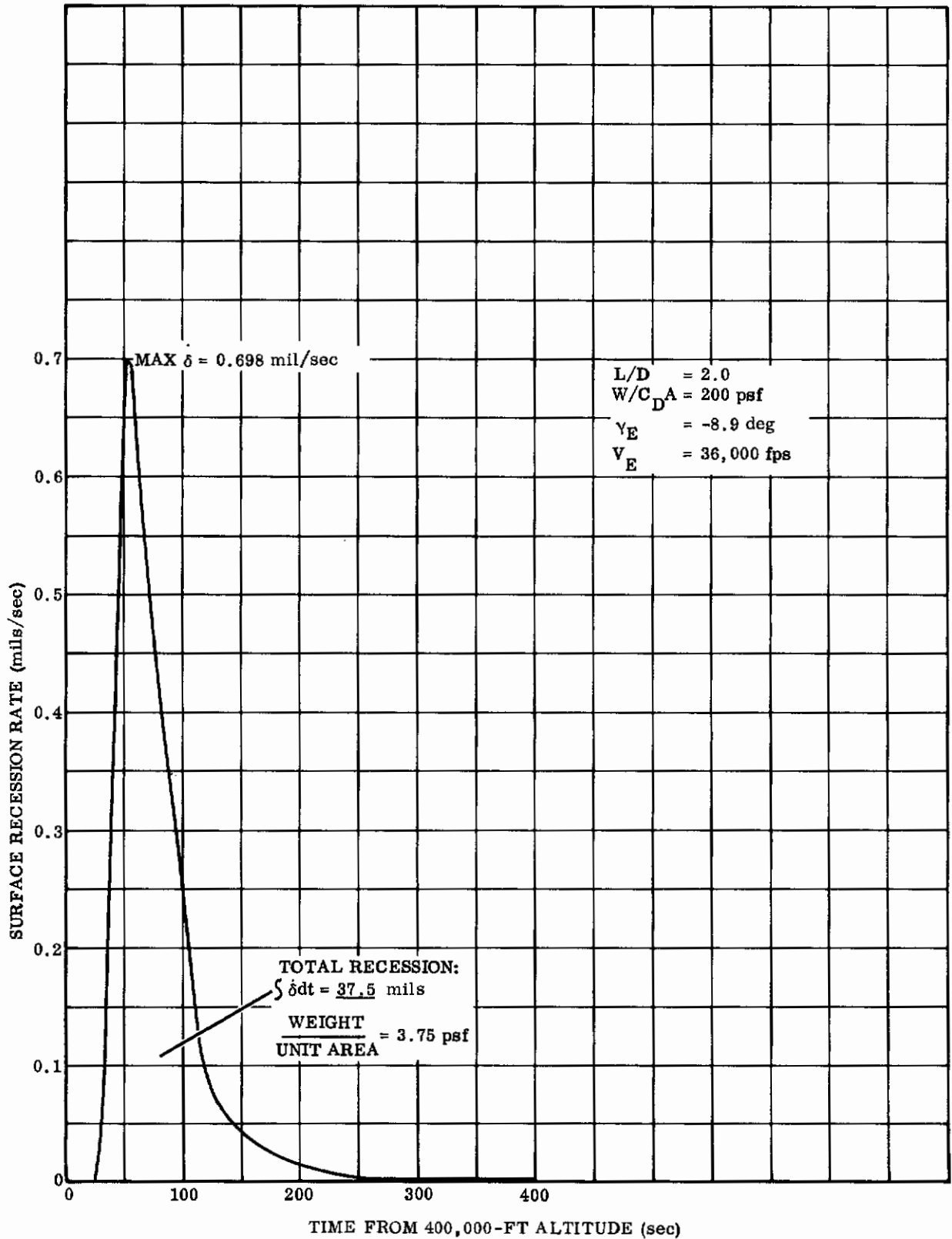


FIGURE 87. CONICAL SECTION TUNGSTEN OXIDATION RECESSION

### 6.3 UNIT WEIGHT COMPARISONS

The comparative average unit weights and total weights of the three most promising refractory frontal structure options are presented in Table 6. These weights were tabulated with the help of the cumulative surface area and volume curves (Fig. 81 and 82), but exclude weight of attachment hardware from the totals. For all three frontal systems, the same basic shell structure pertained — a uniform 0.040 inch tungsten alloy monocoque shell backed by 6-inch fibrous  $ZrO_2$  insulation. Only the outer absorptive and radiative coatings were varied. The unit and total weights of the basic structure are  $6.5 \text{ lb/ft}^2$  and 205 lb, respectively. The first and second weight columns of the table refer to the specific coating system; the final two columns include the basic structure weights.

TABLE 6  
COMPARATIVE FRONTAL SECTION WEIGHTS

$L/D = 2.0, W/C_D A = 200 \text{ psf}, \gamma_E = -8.9 \text{ deg}, R_n = 2.5 \text{ ft}$

Type Frontal System	Avg. W/A (psf)	W (lb)	Avg. $(W/A)_{tot}$ (psf)	$W_{tot}$ (lb)
1. Final Design, W-ThO <sub>2</sub> High-Capacity-Radiative	6.2	195	12.7	400
2. Ablative-Radiative (Oxidation Coating)	5.5	173	12.0	378
3. Ablative-Radiative (No Oxidation Coating)	4.6	145	11.1	350

The first thermal protective system, the selected final design, has an average weight per square foot of surface of 12.7 pounds. It consists of a 0.29-inch thickness of trowelled thoria in the cap region tapered to 0.10 inch on the skirt with the entire ceramic (80 percent dense) reinforced with a tungsten gridwork.

The other two systems are presented for comparison only. The ablative-radiative structure with oxidation coating consists of a 0.38-inch transitory nylon phenolic ablator on the cap area only, bonded to a uniform 0.10-inch plasma-sprayed,

# Contrails

90 percent-dense coating of tungsten- or tantalum-reinforced ceramic ( $\text{ThO}_2$  or  $\text{HfO}_2$ ) covering the entire basic structure. Since a 0.1-inch protective coating was sufficient on the skirt of the final design structure, it was here, also. The unit weight for this structure was slightly less, 12.0 psf.

The final ablative-radiative system (nylon phenolic ablator), bonded directly to the tungsten alloy shell, was again graduated in thickness meridionally, but here there was an insulative excess thickness of 0.4 inch carried to provide added protection until the metallic surface reached a temperature-pressure regime which no longer presented a danger of oxidation recession. This structure was lighter than either of the previous two, with a unit overall weight of 11.1 psf.

A fourth option, an ordinary char-former ablator over a cold-wall primary structure, was not considered in this study. With the present lengthly trailing thermal pulse and high heat load, active cooling concepts in conjunction with a beryllium or similar type primary structure (rather than the currently investigated high-temperature reradiation bodies) would not be competitive weightwise.

## VII. CONCLUSIONS

In addition to conclusions of a specific nature mentioned throughout this volume, the following overall conclusions can be drawn:

1. Lifting re-entry of manned vehicles at super-orbital speeds can be performed on trajectories that allow the use of radiation-cooled frontal sections. Corresponding vehicle aerodynamic parameters and re-entry corridors are reasonable.
2. The use of fibrous insulation fillers is an efficient method of limiting heat flow to the interior of the frontal section. Multiple radiation shields result in large weight penalties and additional structural complexity.
3. The refractory metal frontal section embodying a monocoque tungsten alloy shell protected externally by a graduated thorium oxide coating and internally by a uniform insulative blanket of zirconium oxide fibers appears to meet successfully the rigors of the most critical and relatively prolonged lifting entry environment.
4. With an average structural weight of  $12.7 \text{ lb/ft}^2$ , this system compares favorably with more-conventional absorptive-radiative structure employing char-type ablaters.

# *Contrails*

VIII. REFERENCES

1. Manning, L.A., Study of Lifting Re-Entry From Parabolic Velocity. Intra-departmental Communication IAD FM-52-20/AO13, Lockheed Missiles and Space Company, Sunnyvale, California (30 August 1962).
2. Detra, R.W., Kemp, N.H., and Riddell, F.R., "Addendum to Heat Transfer to Satellite Vehicles Re-entering the Atmosphere." Jet Propulsion (December 1957) pp 1256-1257.
3. Zierten, T.A., Comparison of Analytical Prediction Methods for Stagnation Point Heat Transfer for Typical Satellite Entry. Interdepartmental Communication TIAD 514, Lockheed Missiles and Space Company, Sunnyvale, California (16 October 1962).
4. Tellep, D.M. and Sheppard, T.D., "Insulation Requirements for Long-Time Low-Heat Rate Environments." AIAA Journal (July 1963) p 1670.
5. Thomas, P.D., "Air Emissivity and Shock-Layer Radiation." Journal of the Aerospace Sciences (April 1962) p 477.
6. Lees, L., "Laminar Heat Transfer Over Blunt-Nosed Bodies at Hypersonic Flight Speeds." Jet Propulsion (April 1956).
7. Hearne, L.F., Hines, F.L., and Rindal, R.A., Recommended Procedures for Prediction of the Reentry Convective Heating Environment. Interdepartmental Communication TIAD 201, Lockheed Missiles and Space Company, Sunnyvale, California (28 September 1960).
8. Vinokur, M., "Laminar Heat Transfer Distribution on Oblate Ellipsoidal Noses in Hypersonic Flow." Journal of the Aerospace Sciences (January 1962) p 113.
9. Vinokur, M., Inviscid Hypersonic Flow Around Blunt Bodies. LMSD-48454, Lockheed Missiles and Space Company, Sunnyvale, California (16 March 1959).
10. Collins, A., Arbitrary Node Temperature Prediction Program. TIAD/188, Lockheed Missiles and Space Company, Sunnyvale, California (24 August 1960).
11. Arras, R.P., The IBM 709 Thermal Analyzer Program. TIAD/192, Lockheed Missiles and Space Company, Sunnyvale, California (15 May 1961).
12. Brogan, J.J., "A Numerical Method of Solution for Heat Conduction in Composite Slabs with a Receding Surface." General Research in Flight Sciences, Technical Report 288139, Lockheed Missiles and Space Company, Sunnyvale, California (January 1960).

13. Arras, R.P. and Gallagher, L.W., Moving Boundary Program on the IBM 7090. Internal Report, Dept. 53-15 to G.A. Etemad, Lockheed Missiles and Space Company, Sunnyvale, California (24 March 1961).
14. Schneider, P.J., Conduction Heat Transfer. Palo Alto, California Addison-Wesley (1955).
15. Thomas, P.D. and Kruger, C.H., Radiant Energy Transfer from the Shock Layer to a Vehicle in Hypersonic Flight. Mechanical and Mathematical Sciences Laboratories Report 6-90-62-55, Lockheed Missiles and Space Company, Sunnyvale, California (May 1962).
16. Collins, J.A., Thermo-Physical Properties of Pure Metals, Alloys, Non-Metals, and Plastics. (A Survey), Avco Research & Advanced Development Division, Wilmington, Massachusetts (15 December 1958).
17. Adams, Mac C., "Recent Advances in Ablation." American Rocket Society Journal (September 1959).
18. Hanshaw, C.E., Jacobsen, W.E., and Strasser, G., Study of Structural Requirements of Re-Entry from Outer Space. WADD TR 60-886, Wright Air Development Depot, Wright-Patterson Air Force Base, Ohio (May 1961).
19. First Quarterly Progress Report on Frontal Section for Re-Entry Vehicle. Report Code 3-10-61-5, Lockheed Missiles and Space Company, Sunnyvale, California, Subcontract to Solar, a Division of International Harvester Company (1 December 1961).
20. Hoshizaki, H., "Heat Transfer from an Ionized, Equilibrium Boundary Layer at Super Satellite Speeds." Theoretical Research Papers in Fluid Mechanics for 1960, Lockheed Missiles and Space Company, Sunnyvale, California (18 May 1961).
21. Internal Data on Nylon Phenolic. Thermodynamics Section, Polaris and Satellite Systems, Lockheed Missiles and Space Company, Sunnyvale, California.
22. Georgiev, S., et al., On Ablating Heat Shields for Satellite Recovery. Avco Research Report 65, Avco Research & Advanced Development Division, Wilmington, Massachusetts (July 1959).
23. Bethe, H.A. and Adams, M.C., A Theory for the Ablation of Glassy Materials. Journal of the Aero/Space Sciences (June 1959).
24. Adams, M.C., et al., An Experimental and Theoretical Study of Quartz Ablation at the Stagnation Point. Avco Research Report 57, Avco Research & Advanced Development Division, Wilmington, Massachusetts (June 1959).
25. Third Quarterly Progress Report on Frontal Section for Re-Entry Vehicle. Report Code 3-10-61-13, Lockheed Missiles and Space Company, Sunnyvale, California, Subcontract to Solar, a Division of International Harvester Company (1 August 1962).



# Contrails

26. Hoshizaki, H., "Heat Transfer in Planetary Atmospheres at Super-Satellite Speeds." American Rocket Society Journal (October 1962).
27. Fourth Quarterly Progress Report on Frontal Section for Re-Entry Vehicle. Report Code 3-10-61-17, Lockheed Missiles and Space Company, Sunnyvale, California, Subcontract to Solar, a Division of International Harvester Company (1 December 1962).
28. Development of Frontal Section for Super-Orbital, Lifting, Re-Entry Vehicle. Quarterly Progress Report 3, Solar Report ER 1115-13, Solar, a Division of International Harvester Company, San Diego, California (1 August 1962).
29. Huber, P.W., Tables and Graphs of Normal-Shock Parameters at Hypersonic Mach Numbers and Selected Altitudes. NACA TN 4352, National Advisory Committee for Aeronautics, Washington, DC (September 1958).
30. Fourteenth Monthly Progress Letter on Frontal Section for Re-Entry Vehicle. Report Code 3-10-61-18, Lockheed Missiles and Space Company, Sunnyvale, California, Subcontract to Solar, a Division of International Harvester Company (1 January 1963).
31. Handbook of Thermophysical Properties of Solid Materials, Volume 5. New York, The MacMillan Company (1961).
32. Collins, J.A., Thermo-Physical Properties of Pure Metals, Alloys, Non-Metals, and Plastics. (A Survey), Avco Research & Advanced Development Division, Wilmington, Massachusetts (15 December 1958).
33. Hamilton, D.C. and Morgan, W.R., Radiant Interchange Configuration Factors. NACA TN 2836, National Advisory Committee for Aeronautics, Washington DC (December 1962).
34. McKellar, L.A., "Effects of Spacecraft Environment on Thermal Control Materials Characteristics." Spacecraft Thermodynamics Symposium, San Francisco, California, Holden-Day, Inc. (1962).
35. Structural Methods Handbook. LMSD-895078, Section 6.32, Lockheed Missiles and Space Company, Sunnyvale, California (February 1962).
36. Perkins, R.A., Price, W.L., and Crooks, D.D., Oxidation of Tungsten at Ultra-High Temperatures. Technical Report: Materials 6-90-62-90, Lockheed Missiles and Space Company, Sunnyvale, California (November 1962).

# *Contrails*